

# **PHYSICAL AND NUMERICAL ASPECTS OF AEROELASTIC SIMULATIONS**

**B.B. Prananta**



Stellingen  
behorende bij het proefschrift  
PHYSICAL AND NUMERICAL ASPECTS OF AEROELASTIC SIMULATIONS  
door  
Bonifacius Bima PRANANTA

1. Het streven naar een gelijkwaardige nauwkeurigheid in de beschrijving van aërodynamica en elastomechanica geeft binnen het vakgebied van aëro-elasticiteit aanleiding tot het gebruik van niet gelijkwaardige oplossingsmethoden en/of niet vergelijkbare rekenroosters.  
*In aeroelasticity, comparable accuracy requirements for aerodynamic and structural features leads, in most cases, to different solution methods and/or mesh densities.*
2. De conclusie van Lee [1], dat het bewegen van een schok tijdens buffet wordt veroorzaakt door Kutta-golven die tegen de stroming in bewegen, mag niet getrokken worden.  
*The conclusion of Lee [1], that the shock motion in a buffet condition is caused by Kutta waves moving upstream, is not correct.*  
[1] B.H.K. Lee. Transonic buffet on a supercritical aerofoil. *Aeronautical Journal*, 22(5):143-152, 1990.
3. Voor het uitvoeren van numerieke aëro-elastische simulaties ligt het gebruik van impliciete methoden meer voor de hand dan het gebruik van expliciete methoden.  
*In computational aeroelastic simulations the application of implicit methods is more appropriate than the use of explicit methods.*
4. Het succes van numerieke aëro-elastische simulaties wordt niet alleen bepaald door de kwaliteit van de aërodynamische en elastomechanische oplosmethoden. Het hangt net zo veel af van het vakmanschap van de aëro-elasticus om gegevens aangereikt door aërodynamici en constructeurs samen te voegen.  
*The success of computational aeroelastic simulations is not determined by the quality of the aerodynamic and structural dynamic tools only. It depends just as much on the skill of the aeroelastician in the merging the data supplied by aerodynamic and structural engineers.*
5. Relaxatie van instationaire residuen [1] en 'subcycling' [2] in tijdsimulatie waren ontwikkeld met het doel de numerieke aëro-elastische simulatie met grote tijdstappen te kunnen doen. De relaxatie van instationaire residuen is beter dan de 'subcycling' omdat de eerste numerieke stabiliteit garandeert terwijl de laatste juist numerieke instabiliteit veroorzaakt.  
*Relaxation of unsteady residuals [1] and subcycling [2] in time accurate simulations are developed for the same goal, namely to have a CAS method capable of using large time steps. The relaxation of the unsteady residual is better than the subcycling because the first ensures numerical stability whereas the latter introduces numerical instability.*  
[1] J.J. Alonso, L. Martinelli and A. Jameson. Multigrid Unsteady Navier-Stokes calculations with aeroelastic applications. AIAA paper 95-0048.  
[2] C. Farhat and Lesoinne. On the accuracy, stability and performance of the solution of three-dimensional nonlinear transient aeroelastic problems by partitioned procedures. AIAA paper 96-1388.
6. De grootte van de tijdstap voor tijdsintegratie van een instationair aërodynamisch probleem is bepaald door voortplantingsverschijnselen van golven. Een gelijkwaardige eis voor de elastomechanica is bepaald door de hoogste eigenfrequentie van de constructie. In de aëro-elasticiteit komen deze verschillende eisen toch uit op dezelfde tijdstapgrootte.  
*The time step size requirement for temporal integration of an unsteady aerodynamic problem is defined by wave propagation phenomena. The corresponding requirement for a structural dynamic problem is determined by the highest natural frequency of the structure. However, in aeroelasticity these two requirements result in the same time step size since the waves in the fluid are primarily generated by the vibration of the structure.*
7. Men leert veel door het maken van fouten; het is evenwel de kunst om nuttige fouten te maken omdat men daarvan het meeste leert.

*One learns a lot from making mistakes; however the art is how to make useful mistakes since one learns most from these useful mistakes.*

8. De enige stomme vraag is de vraag die niet gesteld wordt.

*The only stupid question is the unasked one.*

Aanhaling uit NET2-HOWTO (netwerk manual van Linux besturing system)

9. In Indonesië is de naam "Kantor Hukum" ('Court of Law') meer gepast dan de huidige naam "Kantor Pengadilan" ('Court of Justice').

*In Indonesia the name "Kantor Hukum" (Court of Law) is more appropriate than the current name "Kantor Pengadilan" (Court of Justice).*

10. Het onmiskenbare verschil tussen het Indonesische en Nederlandse klimaat komt op Indonesische nieuwkomers anders over dan op de Indonesiërs die al langer in Nederland wonen. De eersten zullen direct het verschil opmerken tussen de twee seizoenen in Indonesië en de vier seizoenen in Nederland. De anderen zullen echter beweren dat het in Indonesië een half jaar regent en in Nederland het hele jaar door.

*The undeniable difference between the Indonesian and Dutch climate leads to different opinions at Indonesian new-comers and Indonesians who have lived longer in The Netherlands. The first group distinguishes two seasons in Indonesia and four seasons in The Netherlands. The second group will state that it rains half a year in Indonesia but all year round in The Netherlands.*



719306-TR 3332  
3/14/67 3332

# PHYSICAL AND NUMERICAL ASPECTS OF AEROELASTIC SIMULATIONS

B.B. Prananta

Copyright © 1999 by B.B.Prananta, Delft, The Netherlands.

All rights reserved. No part of this thesis may be reproduced, stored in a retrieval system or transmitted in any form or by any means, electronic, mechanical, photocopying, recording or otherwise without the prior written permission of the author B.B. Prananta, Delft University of Technology, Faculty of Aerospace Engineering, P.O. Box 5058, 2600 GB Delft, The Netherlands

Printed in The Netherlands, typeset using  $\text{\LaTeX}$

# PHYSICAL AND NUMERICAL ASPECTS OF AEROELASTIC SIMULATIONS

Proefschrift



ter verkrijging van de graad van doctor  
aan de Technische Universiteit Delft,  
op gezag van de Rector Magnificus prof. ir. K.F. Wakker,  
in het openbaar te verdedigen ten overstaan van een commissie,  
door het College voor Promoties aangewezen,  
op maandag 17 mei 1999 te 13.30 uur

door

Bonifacius Bima PRANANTA

Sarjana Teknik Institut Teknologi Bandung  
geboren te Surakarta, Indonesië

Dit proefschrift is goedgekeurd door de promotoren:

Prof. ir. R.J. Zwaan

Prof. dr. ir. H.W.M. Hoeijmakers

Samenstelling promotiecomissie:

Rector Magnificus,

voorzitter

Prof. ir. R.J. Zwaan,

Technische Universiteit Delft, promotor

Prof. dr. ir. H.W.M. Hoeijmakers,

Universiteit Twente, promotor

Prof. ir. J.W. Slooff,

Technische Universiteit Delft &

Nationaal Lucht- en Ruimtevaart Laboratorium

Prof. dr. A.E.P. Veldman,

Rijksuniversiteit Groningen

Prof. H. Djodihardjo, Sc.D.,

Institut Teknologi Bandung (Indonesia)

Prof. dr. ir. P. Wesseling,

Technische Universiteit Delft

Prof. dr. ir. A.A. van Steenhoven,

Technische Universiteit Eindhoven

The research described in this thesis has been performed by the author at the Chair Aerospace Structures and Computational Mechanics, Faculty of Aerospace Engineering, Delft University of Technology. Financial assistance was provided by the Dutch-Indonesian cooperation program through the APERT Project.

ISBN 90-9012663-5

Keywords: aeroelasticity, time domain, transonic flow, viscous flow, Euler/Navier-Stokes equations, computational aeroelastic simulation, computational fluid dynamics, unsteady, deforming mesh, buffet, buffeting.

# CONTENTS

LIST OF FIGURES	XVI
LIST OF TABLES	XVII
LIST OF SYMBOLS	XXIV
1 INTRODUCTION	1
1.1 Aeroelasticity of Aircraft	3
1.1.1 Notions and definitions	3
1.1.2 Flutter calculations in aircraft design	4
1.1.3 Transonic flow effects	5
1.2 Progress in Aeroelastic Analysis	6
1.3 Background of the Study	10
1.4 Objectives and Scope of the Study	10
1.5 Outline of the Thesis	11
2 COMPUTATIONAL AEROELASTIC SIMULATIONS	13
2.1 Discretization Aspects of CAS Method	13
2.2 Temporal Integration Aspects of CAS, Aero-Structural Coupling	14
2.3 Literature Survey	16
2.3.1 Review of unsteady Euler/Navier-Stokes methods	16
2.3.2 Review of computational aeroelastic simulation methods	18
2.3.3 General directives in developing CAS methods	20
2.4 Equations of Motion of an Aeroelastic System	21
2.5 Unsteady Aerodynamics for Aeroelastic Applications	21
2.5.1 Aeroelastic requirements	22
2.5.2 Governing equations	24
2.5.3 Boundary Conditions	34
3 SOLUTION OF UNSTEADY NAVIER-STOKES EQUATIONS FOR FLOW PAST AIRFOILS	39
3.1 Discretization Aspects of Unsteady Flow with Shock Waves	40
3.1.1 Ensuring proper shock position and shock strength	40
3.1.2 Preventing the spurious subgrid frequency components	41

3.2	Computational Mesh . . . . .	42
3.2.1	Mesh topology . . . . .	42
3.2.2	Mesh generator . . . . .	43
3.2.3	Dynamic mesh algorithm . . . . .	43
3.3	Coordinate Transformation . . . . .	47
3.4	Discretization Methods . . . . .	50
3.5	Spatial discretization . . . . .	51
3.5.1	Calculation of metrics according to GCL . . . . .	52
3.5.2	Upwind discretization of inviscid flux . . . . .	53
3.5.3	Some considerations of the discretized inviscid flux . . . . .	61
3.5.4	Calculation of higher-order inviscid flux . . . . .	62
3.6	Application of Solid Boundary Conditions . . . . .	63
3.6.1	Velocity boundary condition . . . . .	63
3.6.2	Unsteady normal momentum equation on solid surface . . . . .	64
3.6.3	Flux formula at solid surface . . . . .	65
3.7	Temporal Integration . . . . .	65
3.7.1	Introduction . . . . .	65
3.7.2	Unsteady residual . . . . .	66
3.7.3	Relaxation method . . . . .	68
3.7.4	Nonstationary acceleration methods . . . . .	69
3.7.5	Other types of preconditioner . . . . .	70
3.8	Turbulence Modeling . . . . .	71
3.9	Summary of the Present CUA Method . . . . .	72
3.10	Numerical Results . . . . .	72
3.10.1	Test of dynamic mesh algorithms . . . . .	73
3.10.2	Comparison of inviscid flux methods . . . . .	74
3.10.3	Comparison of relaxation methods . . . . .	75
3.10.4	Steady viscous flow . . . . .	76
3.10.5	Unsteady flow . . . . .	77
3.10.6	Figures . . . . .	83
3.11	Conclusions Concerning the Two-Dimensional CUA Method . . . . .	96
4	SIMULATION OF UNSTEADY FLOW PHENOMENA AROUND AIRFOILS . . . . .	99
4.1	<b>Presentation of the Results</b> . . . . .	<b>99</b>
4.2	Transonic Flow About Pitching NLR 7301 Airfoil . . . . .	101
4.2.1	Figures . . . . .	103
4.3	Shock Wave Motions in Separated Flow About NACA 64A010 . . . . .	105
4.3.1	Figures . . . . .	108
4.4	Transonic Buffet of NACA 0012 Airfoil . . . . .	111
4.4.1	Figures . . . . .	116
4.5	Conclusions Concerning the Simulation of Unsteady Flow Phenomena Around Airfoils . . . . .	124

5	AEROLEASTIC SIMULATIONS USING CUA METHODS	125
5.1	Introduction . . . . .	125
5.2	Structural Model . . . . .	126
5.2.1	Equations of motion . . . . .	126
5.2.2	Temporal integration methods for structural dynamics . . . .	128
5.3	Loose Aero-Structural Coupling Methods . . . . .	131
5.3.1	Commonly used method . . . . .	131
5.3.2	Aerodynamic extrapolation . . . . .	133
5.3.3	Structural extrapolation . . . . .	135
5.3.4	Results . . . . .	136
5.4	Analysis of the Response . . . . .	142
5.5	Applications for Two-Degree-of-Freedom Airfoil . . . . .	143
5.5.1	Attached flow case . . . . .	143
5.5.2	Separated flow . . . . .	150
5.6	Conclusions Concerning the Two-Dimensional CAS Method . . . .	156
6	COMPUTATIONAL AEROELASTIC SIMULATION METHOD FOR THREE-DIMENSIONAL FLOW	157
6.1	Aerodynamic Model . . . . .	158
6.1.1	Mesh topology . . . . .	158
6.1.2	Dynamic Mesh Algorithm . . . . .	159
6.1.3	Governing equations . . . . .	160
6.1.4	Discretization . . . . .	164
6.2	Parallelization Strategy . . . . .	169
6.2.1	Domain decomposition . . . . .	170
6.2.2	Explicit subdomain coupling . . . . .	170
6.2.3	Implementations . . . . .	171
6.3	Results of CUA method for three-dimensional flow . . . . .	172
6.3.1	Results of parallelization . . . . .	172
6.3.2	Results of flow simulations . . . . .	174
6.4	Structural Model . . . . .	190
6.5	Aeroelastic Equations . . . . .	190
6.5.1	Conformity of aerodynamic and structural parameters . . . .	193
6.5.2	Results of CAS method for three-dimensional flow . . . . .	194
6.6	Conclusions of three-dimensional CUA and CAS methods . . . . .	200
7	CONCLUSIONS AND PROSPECTS OF CAS FOR APPLICATIONS IN PRACTICE	201
	BIBLIOGRAPHY	203
A	REYNOLDS-AVERAGED NAVIER-STOKES EQUATIONS	219
B	EIGENVALUES AND EIGENVECTORS OF EULER EQUATIONS	225

C	TURBULENCE MODELS	233
C.1	Baldwin-Lomax Algebraic Model . . . . .	233
C.2	Spallart-Allmaras One-Equation Model . . . . .	235
C.2.1	Discretization . . . . .	236
C.2.2	Gradient of production and destruction terms . . . . .	238
D	TRANSITION MATRIX METHOD	239
	SUMMARY	241
	SAMENVATTING IN HET NEDERLANDS	243
	ACKNOWLEDGMENT	245
	CURRICULUM VITAE	247



# LIST OF FIGURES

1	Two- and three-dimensional coordinate systems, $x$ -axis directed downstream along flight path . . . . .	xxiii
1.1	Structural failure of the T-tail of a Fokker F.28 wind tunnel model. The inset shows the model before the experiment (courtesy of NLR, Amsterdam) . . . . .	1
1.2	Transonic flutter dip phenomenon occurring in the SKV-5 test program. Results for $\alpha = -0.35, 0.85$ and $2.05$ deg. . . . .	2
1.3	Flutter calculations during an aircraft design process, after [185] . . .	4
1.4	Status in computational unsteady aerodynamic capability in 1995, from [59] . . . . .	9
2.1	Dependency of structural and aerodynamic parts in CAS . . . . .	15
2.2	Relation of CFL number to the reduced frequency of a specific problem for various numbers of time steps per cycle . . . . .	24
2.3	Change of control volume due to the motion of a surface element of the control volume . . . . .	31
2.4	Space-time plot on one-dimensional wave propagation . . . . .	35
3.1	Volume elements for fixed and deformed mesh . . . . .	41
3.2	Coordinate transformation from physical to computational domain . .	43
3.3	Overall picture of the grid around an RAE 2822 airfoil . . . . .	44
3.4	Grid close-up near an RAE 2822 airfoil . . . . .	44
3.5	Normal and tangential vectors for the definition of surface forcing function . . . . .	45
3.6	The spring analogy of the mesh . . . . .	46
3.7	The normals showing the closed computation cell . . . . .	49
3.8	Space-time area formed during mesh deformation . . . . .	53
3.9	Riemann's problem, shock tubes at rest and after the diaphragm has broken . . . . .	57
3.10	Definition of discontinuity at cell faces in Godunov's method . . . .	58
3.11	Definition of discontinuity at cell faces in the higher-order Godunov method . . . . .	62
3.12	The initial $160 \times 30$ mesh around RAE 2822 airfoil for the mesh deformation test . . . . .	83

3.13	The deformed $160 \times 30$ mesh around RAE 2822 airfoil using the elliptic method without surface forcing function . . . . .	83
3.14	The deformed $160 \times 30$ mesh around RAE 2822 airfoil using the elliptic method with surface forcing function to maintain orthogonality . . .	84
3.15	The deformed $160 \times 30$ mesh around RAE2822 airfoil using the spring analogy with extrapolation predictor . . . . .	84
3.16	The deformed $160 \times 30$ mesh around RAE2822 airfoil using the spring analogy with the new 'direct z-solve' predictor . . . . .	84
3.17	Comparison of pressure distributions and Mach number obtained with various inviscid flux methods for the inviscid flow test case. NACA 0012 airfoil at $M_\infty=0.85$ , $\alpha=1.00$ deg, $160 \times 60$ C-mesh . . . . .	85
3.18	Comparison of isobars obtained with various inviscid flux methods for the inviscid flow test case. NACA 0012 airfoil at $M_\infty=0.85$ , $\alpha=1.00$ deg, $160 \times 60$ C-mesh . . . . .	85
3.19	Comparison of isomach contours obtained from various inviscid flux methods for the inviscid flow test case. NACA 0012 airfoil at $M_\infty=0.85$ , $\alpha=1.00$ deg, $160 \times 60$ C-mesh . . . . .	86
3.20	Comparison of pressure distributions and skin friction obtained from various inviscid flux methods for the viscous test case. RAE 2822 airfoil at $M_\infty=0.729$ , $\alpha_{exp}=2.92$ deg and $Re_\infty=6.5 \times 10^6$ , $160 \times 60$ C-mesh . . . . .	86
3.21	Comparison of isobars obtained from various inviscid flux methods for the viscous flow test case. RAE 2822 airfoil at $M_\infty=0.729$ , $\alpha_{exp}=2.92$ deg and $Re_\infty=6.5 \times 10^6$ , $160 \times 60$ C-mesh . . . . .	87
3.22	Comparison of isomach contours obtained from various inviscid flux methods for the viscous flow test case. RAE 2822 airfoil at $M_\infty=0.729$ , $\alpha_{exp}=2.92$ deg and $Re_\infty=6.5 \times 10^6$ , $160 \times 60$ C-mesh . . . . .	87
3.23	Convergence rates of the lift coefficient against the iteration number and CPU time for various relaxation methods. RAE 2822 airfoil at $M_\infty=0.729$ , $Re_\infty=6.5 \times 10^6$ and $\alpha_{corr}=2.31$ deg, $160 \times 60$ C-mesh . . .	88
3.24	Convergence rates of the residual of the mass conservation equation against the iteration number and CPU time for various relaxation methods. RAE 2822 airfoil at $M_\infty=0.729$ , $Re_\infty=6.5 \times 10^6$ and $\alpha_{corr}=2.31$ deg, $160 \times 60$ C-mesh . . . . .	88
3.25	The mesh for the viscous flow calculation. RAE 2822 airfoil, $189 \times 60$ C-mesh . . . . .	89
3.26	Comparison of calculated and measured distributions of pressure and skin friction coefficients for RAE 2822 airfoil at $M_\infty=0.729$ , $\alpha_{exp}=2.92$ deg, $\alpha_{corr}=2.31$ deg and $Re_\infty=6.5 \times 10^6$ , $189 \times 60$ C-mesh . . . . .	89
3.27	Instantaneous Mach contours at four time levels ( $\Delta M = 0.10$ ) of 18% circular arc airfoil at $M_\infty=0.76$ and $Re_\infty=11 \times 10^6$ , the time is relative to $t_0 a_\infty/c=50$ , $140 \times 60$ C-mesh . . . . .	90
3.28	Time history of lift coefficient and moment coefficient about 0.25 chord of 18% circular arc airfoil at $M_\infty=0.76$ and $Re_\infty=11 \times 10^6$ , $140 \times 60$ C-mesh . . . . .	91

3.29	Comparison of $C_L$ and $C_{M,0.25}$ of NACA 0012 airfoil pitching about 0.25 chord at $M_\infty=0.754$ , $\alpha_{\text{mean}}=2.00$ , $\alpha_{\text{amp}}=2.50$ and $k=0.082$ , using rigid and dynamic mesh modeling, $140\times 30$ C-mesh . . . . .	91
3.30	Comparison of calculated $C_L$ and $C_{M,0.25}$ of NACA 0012 airfoil pitching about 0.25 chord at $M_\infty=0.754$ , $\alpha_{\text{mean}}=2.00$ deg , $\alpha_{\text{amp}}=2.50$ deg and $k=0.082$ , using different inviscid flow methods, $140\times 30$ C-mesh . . . . .	92
3.31	Comparison of calculated $C_L$ and $C_{M,0.25}$ of NACA 0012 airfoil pitching about 0.25 chord at $M_\infty=0.754$ , $\alpha_{\text{mean}}=2.00$ deg , $\alpha_{\text{amp}}=2.50$ deg and $k=0.082$ , using various iteration strategies, $140\times 30$ C-mesh . . . . .	92
3.32	Comparison of calculated and experimental $C_L$ and $C_{M,0.25}$ of NACA 0012 airfoil pitching about 0.25 chord at $M_\infty=0.754$ , $\alpha_{\text{mean}}=2.00$ deg, $\alpha_{\text{amp}}=2.50$ deg, $k=0.082$ and $Re_\infty=5.7\times 10^6$ , $140\times 60$ C-mesh . . . . .	93
3.33	Comparison of calculated and experimental $C_L$ and $C_{M,0.25}$ of NACA 0012 airfoil pitching about 0.25 chord at $M_\infty=0.60$ , $\alpha_{\text{mean}}=4.86$ deg, $\alpha_{\text{amp}}=2.44$ deg, $k=0.081$ and $Re_\infty=4.8\times 10^6$ , $140\times 60$ C-mesh . . . . .	93
3.34	Comparison of calculated $C_L$ and $C_{M,0.25}$ of NACA 0012 airfoil pitching about 0.25 chord at $M_\infty=0.60$ , $\alpha_{\text{mean}}=4.86$ deg , $\alpha_{\text{amp}}=2.44$ deg, $k=0.081$ and $Re_\infty=4.8\times 10^6$ , using various iteration strategies, $140\times 60$ C-mesh . . . . .	94
3.35	Comparison of calculated $C_L$ and $C_M$ of NACA 0015 airfoil pitching about 0.25 chord at $M_\infty=0.30$ , $\alpha_{\text{mean}}=15$ deg , $\alpha_{\text{amp}}=4.20$ deg, $k=0.10$ and $Re_\infty=2\times 10^6$ , $160\times 60$ C-mesh . . . . .	94
3.36	Instantaneous density contours at eight time steps of NACA 0012 airfoil pitching about 0.25 chord at $M_\infty=0.30$ , $\alpha_{\text{mean}}=15$ deg , $\alpha_{\text{amp}}=4.20$ deg, $k=0.10$ and $Re_\infty=1.93\times 10^6$ , $160\times 60$ C-mesh. The thickened contour is freestream density ( $\rho=1$ ) and $\Delta\rho=0.05$ . . . . .	95
4.1	Comparison of calculated and measured pressure distributions of an NLR 7301 airfoil at $M_\infty=0.70$ , $\alpha_{\text{calc}}=2.00$ deg , $\alpha_{\text{exp}}=3.00$ deg, and $Re_\infty=2.1\times 10^6$ using $160\times 60$ C-mesh . . . . .	103
4.2	Comparison of calculated and measured pressure distributions of an NLR 7301 airfoil pitching about 0.40 chord at $M_\infty=0.70$ , $\alpha_{\text{mean}}=2.00$ deg , $\alpha_{\text{amp}}=0.50$ deg, $k=0.192$ and $Re_\infty=2.1\times 10^6$ with transition strip at 0.30 chord, using two strategies using $160\times 60$ C-mesh . . . . .	104
4.3	Similar as figure 4.2 but expressed in magnitude $ C_P $ and phase angle, $\phi$ . . . . .	104
4.4	History of shock position for various excitation frequencies. NLR 7301 airfoil pitching about 0.40 chord at $M_\infty=0.70$ , $\alpha_{\text{mean}}=2.00$ deg , $\alpha_{\text{amp}}=0.50$ deg, $k=0.023, 0.072, 0.144$ and $0.192$ and $Re_\infty=2.1\times 10^6$ with transition strip at 0.30 chord . . . . .	105
4.5	Comparison of calculated and measured pressure distributions. NACA 64A010 airfoil at $M_\infty=0.80$ , $\alpha=4.00$ deg, and $Re_\infty=12\times 10^6$ using $160\times 60$ C-mesh . . . . .	108
4.6	Comparison of calculated and measured pressure distributions. NACA 64A010 airfoil pitching about 0.25 chord at $M_\infty=0.80$ , $\alpha_{\text{mean}}=4.00$ deg , $\alpha_{\text{amp}}=1.01$ deg, $k=0.051$ and $Re_\infty=12\times 10^6$ using $160\times 60$ C-mesh . . . . .	108

4.7	Comparison of calculated and measured pressure distributions. NACA 64A010 airfoil pitching about 0.25 chord at $M_\infty=0.80$ , $\alpha_{\text{mean}}=4.00$ deg, $\alpha_{\text{amp}}=1.01$ deg, $k=0.204$ and $Re_\infty=12\times 10^6$ using $160\times 60$ C-mesh . .	109
4.8	Comparison of calculated positions of the shock wave. NACA 64A010 airfoil pitching about 0.25 chord at $M_\infty=0.80$ , $\alpha_{\text{mean}}=4.00$ deg, $\alpha_{\text{amp}}=1.01$ deg, $k=0.204$ and $0.051$ and $Re_\infty=12\times 10^6$ using $160\times 60$ C-mesh . . .	109
4.9	History of $C_L$ and $C_M$ and magnitude of the Fourier components of $C_L$ . NACA 64A010 airfoil pitching about 0.25 chord at $M_\infty=0.80$ , $\alpha_{\text{mean}}=4.00$ deg, $\alpha_{\text{amp}}=1.01$ deg, $k=0.051$ and $Re_\infty=12\times 10^6$ . . . . .	110
4.10	History of $C_L$ and $C_M$ and magnitude of the Fourier components of $C_L$ . NACA 64A010 airfoil in a buffet condition at $M_\infty=0.80$ , $\alpha=4.50$ deg and $Re_\infty=12\times 10^6$ . . . . .	110
4.11	History of $C_L$ and $C_M$ of a NACA 0012 airfoil at $M_\infty=0.775$ , $\alpha=2.50$ deg (last steady solution), $\alpha=3.00$ deg (first unsteady solution), $\alpha=4.00$ deg (deep buffeting condition) and $Re_\infty=10^7$ using $160\times 60$ C-mesh .	116
4.12	Instantaneous Mach contours at four time levels of an NACA 0012 airfoil at $M_\infty=0.775$ , $\alpha=4.00$ and $Re_\infty=10^7$ , using $160\times 60$ C-mesh. Time is relative to $t_0 a_\infty/c=124.83$ . . . . .	116
4.13	Contours of pressure and skin friction plotted in space-time of an NACA 0012 airfoil at $M_\infty=0.775$ , $\alpha=4.00$ deg and $Re_\infty=10^7$ using $160\times 60$ C-mesh . . . . .	117
4.14	History of $C_L$ and $C_M$ of an NACA 0012 airfoil at $\alpha=0.00$ deg, $M_\infty=0.830$ (last steady solution), $M_\infty=0.840$ (small fluctuation unsteady solution), $M_\infty=0.845$ (unsteady solution) and $Re_\infty=10^7$ using $160\times 60$ C-mesh . . . . .	117
4.15	Instantaneous Mach contours at four time levels of an NACA 0012 airfoil at $M_\infty=0.845$ , $\alpha=0.00$ deg and $Re_\infty=10^7$ using $160\times 60$ C-mesh. Time is relative to $t_0 a_\infty/c=111.54$ . . . . .	118
4.16	Comparison of calculated and measured buffet boundaries of an NACA 0012 airfoil at $M_\infty=0.725\sim 0.845$ and $Re_\infty=10^7$ . . . . .	118
4.17	Comparison of calculated and measured dominant buffet reduced frequency of an NACA 0012 airfoil at $M_\infty=0.775$ , $\alpha=2.00$ to $4.00$ deg and $Re_\infty=10^7$ . . . . .	119
4.18	Cross-correlation function of pressures on the surface of a Whitcomb <b>supercritical airfoil showing the propagation of disturbances during heavy buffet</b> , taken from the experiment of Roos [147] . . . . .	119
4.19	Cross-correlations of pressures on the surface of an NACA 0012 airfoil at a heavy buffet condition of $M_\infty=0.775$ , $\alpha=4.00$ deg and $Re_\infty=10^7$ using $160\times 60$ C-mesh . . . . .	120
4.20	Self-sustained shock oscillation model of Lee [100] . . . . .	120
4.21	Self-sustained shock oscillation model of Stanewsky and Basler [159] .	121
4.22	Cross-correlations of pressures outside the separated region of an NACA 0012 airfoil at a heavy buffet condition of $M_\infty=0.775$ , $\alpha=4.00$ deg and $Re_\infty=10^7$ using $160\times 60$ C-mesh . . . . .	121

4.23	Contours of constant time lag, obtained from applying cross-correlation, of pressures behind the shock wave of an NACA 0012 airfoil at a heavy buffet condition of $M_\infty=0.775$ , $\alpha=4.00$ deg and $Re_\infty=10^7$ using $160\times 60$ C-mesh . . . . .	122
4.24	History of $C_L$ and the magnitude of the Fourier components of $C_L$ for three cases of a stationary NACA 0012: $M_\infty=0.775$ , $\alpha=4.00$ deg using Baldwin-Lomax turbulence model and Spalart-Allmaras turbulence model and $M_\infty=0.845$ , $\alpha=0.00$ deg using Baldwin-Lomax turbulence model, all at $Re_\infty=10^7$ . . . . .	122
4.25	History of $C_L$ and the magnitude of the Fourier components of $C_L$ for the forced pitching oscillation about 0.25 chord of an NACA 0012 at $M_\infty=0.775$ , $\alpha=4.00$ deg, $k=0.10, 0.18, 0.40$ , calculated using Spalart-Allmaras turbulence model . . . . .	123
5.1	Typical section of a wing, CG is the center of gravity, EA is the elastic axis, $K_h$ is the translational stiffness, $K_\alpha$ is rotational stiffness . . . .	126
5.2	Vibration modes of Isogai's typical section . . . . .	130
5.3	Comparison of the results between the matrix transition method, equation (5.9), and the Newmark- $\beta$ method, equation (5.7), for small time step . . . . .	131
5.4	Comparison of the results between the matrix transition method, equation (5.9), and the Newmark- $\beta$ method, equation (5.7), for large time step . . . . .	132
5.5	Comparison of the results between the transition matrix method, equation (5.9), and the Newmark- $\beta$ method, equation (5.7), for large time step and very long simulation time . . . . .	133
5.6	Comparison of time response of $h$ and $\alpha$ for small time step simulations of Isogai's case A at $M_\infty=0.85$ . . . . .	138
5.7	Comparison of time responses between small and large time step simulations for extrapolation method of [52], Isogai's case A at $M_\infty=0.775$	138
5.8	Comparison of time responses between small and large time step simulations for the present aerodynamic extrapolation method, Isogai's case A at $M_\infty=0.775$ . . . . .	139
5.9	Comparison of time responses between small and large time step simulations for the present structural extrapolation method, Isogai's case A at $M_\infty=0.775$ . . . . .	139
5.10	Comparison of time response of $h$ and $\alpha$ for small time step simulations of Isogai's case A at $M_\infty=0.85$ . . . . .	140
5.11	Comparison of time responses between small and large time step simulations for aerodynamic extrapolation method of [52], Isogai's case A at $M_\infty=0.85$ . . . . .	140
5.12	Comparison of time responses between small and large time step simulations for the present aerodynamic extrapolation method, Isogai's case A at $M_\infty=0.85$ . . . . .	141

5.13	Comparison of time responses between small and large time step simulations for the present structural extrapolation method, Isogai's case A at $M_\infty=0.85$ . . . . .	141
5.14	Time responses close to the flutter boundary for inviscid flow case. Isogai's case A . . . . .	145
5.15	Time responses close to the flutter boundary for the viscous flow case. Isogai's case A . . . . .	146
5.16	Comparison of calculated speed indices and nondimensional frequency at the flutter boundaries for inviscid flow cases. Isogai's case A . . . .	147
5.17	Comparison of calculated speed indices and nondimensional frequency at the flutter boundaries of the viscous and inviscid flow cases. Isogai's case A . . . . .	147
5.18	Time responses at $M_\infty=0.85$ for increasing speed indices for inviscid flow case. Isogai's case A . . . . .	148
5.19	Time responses at $M_\infty=0.85$ for increasing speed indices for the viscous flow case. Isogai's case A . . . . .	149
5.20	Typical section of a wing with nonzero mean angle of attack . . . . .	150
5.21	History of translational and rotational displacement about the elastic axis at various speed indices for Isogai case A of NACA 64A010, $M_\infty=0.70$ , $\alpha=4$ deg, $Re_\infty=12\times 10^6$ . . . . .	152
5.22	History of translational and rotational displacement about the elastic axis at various speed indices for Isogai case A of NACA 64A010, $M_\infty=0.80$ , $\alpha=4$ deg, $Re_\infty=12\times 10^6$ . . . . .	153
5.23	History of translational and rotational displacement about the elastic axis at various speed indices for Isogai case A of NACA 64A010, $M_\infty=0.825$ , $\alpha=4$ deg, $Re_\infty=12\times 10^6$ . . . . .	154
5.24	Results of aeroelastic simulations for Isogai case A of NACA 64A010, $M_\infty=0.650-0.825$ , $\alpha=4$ deg, $Re_\infty=12\times 10^6$ . The isomach contours are at steady flow conditions, $\Delta M=0.10$ and the thickened contour is $M=1155$	
5.25	Buffeting of NACA 0012 at $M_\infty=0.775$ , $\alpha=4.0$ deg, $Re_\infty=10\times 10^6$ . . .	155
6.1	Geometrical transformation from Cartesian physical domain to computational domain with CH-topology for isolated wing configurations	159
6.2	Geometrical transformation from Cartesian physical domain to computational domain with CO-topology for wing-body configurations . .	160
6.3	<b>Geometrical transformation from Cartesian physical domain to computational domain with HO-topology . . . . .</b>	<b>161</b>
6.4	A deformed mesh for viscous flow calculations around an isolated wing, the mesh follows the deformation of the wing using the spring analogy method with the implicit predictor . . . . .	162
6.5	A three-dimensional volume cell . . . . .	165
6.6	Relaxation sweep along the planes of constant $\xi$ . . . . .	167
6.7	Relaxation sweep along the planes of constant $(\xi + \eta)$ . . . . .	168
6.8	Relaxation sweep along the planes of constant $(\xi + \eta + \zeta)$ . . . . .	169
6.9	Artificial boundary condition between two subdomains using ghost cells	170

6.10	Mesh around LANN wing with CH topology, number of mesh points $\approx 220,000$ . . . . .	179
6.11	Steady pressure distributions on LANN wing, case CT5 . . . . .	180
6.12	Convergence of lift coefficient and residual in mass conservation equation . . . . .	180
6.13	Speed-up of parallelization of steady flow calculation for LANN wing, case CT5, fixed mesh problem . . . . .	181
6.14	Performance of parallelization of unsteady flow calculation for LANN wing, case CT5, fixed mesh problem . . . . .	181
6.15	Mesh around ONERA M6 wing with CH topology for calculations involving the Navier-Stokes equations . . . . .	182
6.16	Comparison of steady pressure distribution on ONERA-M6 wing calculated with FP and Euler methods at $M_\infty = 0.84$ , $\alpha = 3.06$ deg . . .	182
6.17	Comparison of experimental and calculated steady pressure distributions for ONERA-M6 wing at $M_\infty=0.84$ , $\alpha=3.06$ deg and $Re_\infty=14.6 \times 10^6$	183
6.18	Comparison of experimental and calculated steady pressure distributions for ONERA-M6 wing at $M_\infty=0.84$ , $\alpha=5.06$ deg and $Re_\infty=14.6 \times 10^6$	183
6.19	Comparison of experimental and calculated steady pressure distributions for fighter type wing at $M_\infty=0.90$ , $\alpha=0$ deg and $Re_\infty=12 \times 10^6$ .	184
6.20	Comparison of real part of experimental and calculated (Euler) first harmonic pressure distributions for fighter type wing at $M_\infty=0.90$ , $\alpha_{amp}=0.25$ deg and $k=0.274$ . . . . .	184
6.21	Comparison of imaginary part of experimental and calculated (Euler) first harmonic pressure distributions for fighter type wing at $M_\infty=0.90$ , $\alpha_{amp}=0.25$ deg and $k=0.274$ . . . . .	185
6.22	Comparison of experimental and calculated steady pressure distributions on LANN wing at $M_\infty=0.82$ , $\alpha=0.6$ deg and $Re_\infty=7.3 \times 10^6$ . .	185
6.23	Comparison of real part of experimental and calculated first-harmonic pressure distributions on LANN wing at $M_\infty=0.82$ , $\alpha_{mean}=0.6$ deg, $\alpha_{amp}=0.25$ deg and $k=0.102$ . . . . .	186
6.24	Comparison of imaginary part of experimental and calculated first harmonic pressure distributions on LANN wing at $M_\infty=0.82$ , $\alpha_{mean}=0.6$ deg, $\alpha_{amp}=0.25$ deg and $k=0.102$ . . . . .	186
6.25	Convergence history of lift and residual for the DLR-F4 wing-body test case at $M_\infty=0.75$ , $\alpha=0.93$ deg, $Re_\infty=12.49 \times 10^6$ . . . . .	187
6.26	Comparison of experimental and calculated pressure distributions on the wing of DLR-F4 wing-body configuration at $M_\infty=0.75$ , $\alpha=0.93$ deg	187
6.27	Mesh around wing-body-tail fighter type configuration with HO topology, number of mesh points $\approx 200,000$ . . . . .	188
6.28	Comparison of experimental and calculated steady pressure distributions on the the upper side of the wing of fighter type configuration at $M_\infty = 0.92$ , $\alpha = 6.00$ deg, $\alpha_{amp} = 0.50$ deg . . . . .	188
6.29	Comparison of the real part of experimental and calculated unsteady pressure distributions on the upper side of the wing of fighter type configuration at $M_\infty = 0.92$ , $\alpha = 6.00$ deg, $\alpha_{amp} = 0.50$ deg . . . . .	189

6.30	Comparison of the imaginary part of experimental and calculated unsteady pressure distributions on the upper side of the wing of fighter type configuration at $M_\infty=0.92$ , $\alpha=6.00$ deg, $\alpha_{amp}=0.50$ deg . . .	189
6.31	Different types of discretization and geometrical modeling of the aerodynamic (finite volume) and structural (finite element) part of AGARD wing 445.6 . . . . .	191
6.32	Control point incompatibility between the structural computational model and the aerodynamic computational model . . . . .	192
6.33	The first four mode shapes prolonged from the structural nodes to the aerodynamic surface control points of AGARD 445.6 wing. Note that for clarity not all mesh lines have been plotted . . . . .	193
6.34	Comparison of forced vibration case of 445.6 wing at $M_\infty=0.96$ between small 48/period and large 10/period time steps runs . . . . .	197
6.35	Comparison of time responses between the aerodynamic extrapolation method of [52] and the present structural extrapolation method for small 48/period time steps, 445.6 wing at $M_\infty=0.96$ . . . . .	197
6.36	Comparison of time responses between small 48/period and large 8/period time steps simulation for aerodynamic extrapolation method of [52], 445.6 wing at $M_\infty=0.96$ . . . . .	198
6.37	Comparison of time responses between small 48/period and large 8/period time steps simulation for the present structural extrapolation method, 445.6 wing at $M_\infty=0.96$ . . . . .	198
6.38	Time responses of the first four modes of 445.6 wing at $M_\infty=0.96$ for three speed indices . . . . .	199
6.39	Flutter boundaries of AGARD I-wing 445.6 . . . . .	199



# LIST OF TABLES

2.1	Accuracy of the components of aeroelastic equation of motion, from a practical point of view [186] . . . . .	22
2.2	Dimensionless value of flow variables at freestream condition . . . . .	30
3.1	Coefficients for the linear multistep method . . . . .	67
3.2	Comparison of the aerodynamic coefficients of the present method, the NLR MUTU2D and the experiment of [38]. RAE 2822 airfoil at $M_\infty=0.729$ , $Re_\infty=6.5\times10^6$ $\alpha_{exp}=2.92$ deg . . . . .	77
3.3	Comparison of reduced frequency obtained using the present method with the experiment of [108]. Circular arc airfoil, 18% thickness ratio at $M_\infty=0.76$ and $Re_\infty=11\times10^6$ , $140\times60$ C-mesh . . . . .	79
3.4	CPU time comparison of running strategies shown in figure 3.31 . . . .	80
3.5	CPU time comparison of running strategies shown in figure 3.34 . . . .	81
4.1	Comparison of calculated and measured phase angles of the shock motion lagging the airfoil motion . . . . .	102
5.1	Aeroelastic parameters of a typical section (Isogai's case A) used for the example of structural temporal integration methods . . . . .	129



# NOMENCLATURE

## SYMBOLS

$a$	speed of sound
$b$	semichord
$A, B$	system dynamic matrix
$A^I$	Jacobian of flux $F^I$
$A^V$	Jacobian of flux $F^V$
$c$	chord; wave velocity of model equation
$C$	convective part of the inviscid flux
$C$	matrix of structural damping
$C_L$	lift coefficient
$C_M$	moment coefficient, positive nose up
$c_p$	specific heat at constant pressure
$c_v$	specific heat at constant volume
$e$	specific internal energy
$E$	specific total energy
$\mathbf{F}^I = [F_x^I, F_y^I, F_z^I]^T$	inviscid flux vectors
$\mathbf{F}^V = [F_x^V, F_y^V, F_z^V]^T$	viscous flux vectors
$F_\zeta^V$	thin-layer flux in $\zeta$
$h, H$	enthalpy, total enthalpy
$h$	inverse Jacobian of the transformation, $J^{-1} = \partial(x, y, z)/\partial(\xi, \eta, \zeta)$
	translational displacement
$J$	Jacobian of the transformation, $h^{-1} = \partial(\xi, \eta, \zeta)/\partial(x, y, z)$
$I_\alpha$	mass moment of inertia of typical wing section
$k$	reduced frequency, $\omega b/U_\infty$
	specific kinetic energy, $\frac{1}{2}(u^2 + v^2 + w^2)$
	stiffness of the spring for mesh deformation
$K$	structural stiffness matrix
$\mathbf{l}, \mathbf{m}$	tangential vectors
$L, R$	matrix of left and right eigenvectors of the inviscid flux
$m$	mass of typical wing section
$M$	Mach number; structural mass matrix
$\mathbf{n}$	normal vector
$n_{\text{cyc}}$	number of time steps per cycle
$P, Q$	source functions of elliptic grid generation

$p$	static pressure
$\mathcal{P}$	pressure part of the inviscid flux
$Pr$	Prandtl number, $\mu c_p / \kappa$
$q$	dynamic pressure, $\frac{1}{2} \rho_\infty U_\infty^2$ ; generalized coordinate
$\mathbf{q}$	heat flux vector
$Q$	generalized aerodynamic force; vector of conservative variables
$R$	gas constant; matrix of right eigenvectors; residual of discretized equation
$R^+, R^-$	Riemann variables
$r_\alpha$	dimensionless radius of gyration of typical section
$Re, \bar{Re}$	Reynolds numbers, $\rho U_\infty c / \mu_L$ , $\rho a_\infty c / \mu_L$
$s$	limiter function
$S$	reference area
$t$	physical time
$T$	temperature (K); period of harmonic motion
$T_s$	Sutherland's constant
$\mathbf{u} = [u, v, w]^T$	Cartesian velocity components
$U, V, W$	contravariant velocity components
$U_\infty =  \mathbf{u}_\infty $	magnitude of freestream velocity
$U$	excitation vector, $[C_L, C_M]^T$
$V^*$	speed index, $U / (\omega b \sqrt{\mu})$
$V_F^*$	flutter speed index
$X$	state variable, $[q, \dot{q}]^T$
$\mathbf{x} = [x, y, z]^T$	Cartesian coordinate system
$\mathbf{x}$	structural state vector
$x_\alpha$	dimensionless static imbalance of typical section
$\alpha$	angle of attack; rotational displacement
$\gamma$	ratio of specific heats, $\gamma = 1.4$
$\zeta$	mode damping
$\theta_5$	dimensionless Sutherland's constant, $T_s / T_\infty$
$\kappa$	coefficient of thermal conductivity
$\lambda$	eigenvalues of the inviscid flux second coefficient of viscosity
$\Lambda$	diagonal matrix of eigenvalues of the inviscid flux
$\mu$	<b>coefficient of viscosity, <math>\mu = \mu_L + \mu_T</math></b> mass ratio
$\mu_E$	coefficient of eddy viscosity
$\xi = [\xi, \eta, \zeta]^T$	transformed coordinates
$\rho$	air density
$\sigma$	damping decay coefficient, equation (5.23)
$\tau$	viscous stresses
$\tau$	transformed aerodynamic time, $(a_\infty / c)t$
$\tau_s$	structural time, $t / \omega_\alpha$
$\phi$	natural mode shape

$\Phi$	transition matrix
$\omega$	natural frequency
$\omega^*$	characteristic frequency
$\Omega, \partial\Omega$	control volume, control volume boundary

## ADDITIONAL SUB/SUPERSCRIPTS

'	real part of complex quantity
"	imaginary part of complex quantity
$L, T$	laminar, turbulent
$n, (n)$	time level, $n$ -th Fourier component
$p$	Newton iteration level
$\infty$	freestream
$i, j, k$	$\xi$ -, $\eta$ -, $\zeta$ -direction

## MISCELLANEOUS

$\hat{\bullet}$	$h\bullet$ , unscaled with respect to $J^{-1}$
$\hat{\kappa}_k$	$h\kappa_k$ , unscaled with respect to $J^{-1}$
$\bullet$	$\bullet/ \nabla \bullet $ , normalized
$\tilde{\kappa}_k$	$\kappa_k/ \nabla \kappa $ , normalized
$\bullet$	special case, see the text

## ABBREVIATIONS

AF	Approximate Factorization
ALE	Arbitrary Lagrangian Eulerian
AUSM	Advection Upstream Splitting Method
BL	Baldwin-Lomax
CAS	Computational Aeroelastic Simulation
CFL	Courant-Friedrichs-Lewy
CG	Center of Gravity
CGS	Conjugate Gradient Squared
CUA	Computational Unsteady Aerodynamics
DNS	Direct Numerical Simulation
DUT	Delft University of Technology
EA	Elastic Axis

EE	Euler Equations
FDS	Flux Difference Splitting
FNS	Full Navier-Stokes
FP	Full Potential
FVS	Flux Vector Splitting
GAF	Generalized Aerodynamic Force
GCL	Geometric Conservation Law
GMRES	Generalized Minimal Residual
GVT	Ground Vibration Test
HST	High Speed Tunnel, NLR, Amsterdam
HUS	Hybrid Upwind Scheme
LCO	Limit Cycle Oscillation
LES	Large Eddy Simulation
LLU-SGS	Line Lower-Upper Symmetric Gauss Seidel
LU-ADI	Lower-Upper Alternating Direction Implicit
LU-SGS	Lower-Upper Symmetric Gauss Seidel
MUSCL	Monotonic Upwind Scheme for Conservation Law
NACA	National Advisory Committee for Aeronautics
NAL	National Aerospace Laboratory, Tokyo
NLR	National Aerospace Laboratory, Amsterdam
NS	Navier-Stokes
PGS	Point Gauss Seidel
PSOR	Point Successive OverRelaxation
RANS	Reynolds-Averaged Navier-Stokes
RB	Red-Black
SA	Spalart-Allmaras
SGS	Symmetric Gauss-Seidel
SKV	Supercritical Wing
SLOR	Successive Line OverRelaxation
SSOR	Symmetric Successive OverRelaxation
TLNS	Thin-Layer Navier-Stokes
TSP	Transonic Small Perturbation
TVD	Total Variation Diminishing

# AXIS SYSTEM

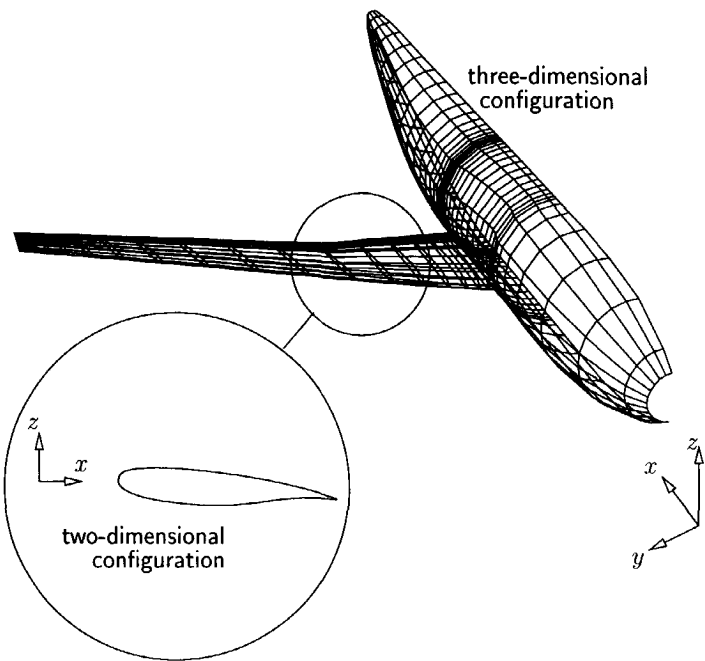


Figure 1: Two- and three-dimensional coordinate systems,  $x$ -axis directed downstream along flight path

What I want to see is a new kind of government, one that is not controlled by the few, but by the many.



# CHAPTER 1

## INTRODUCTION

The danger of unstable dynamic or static deformations of aircraft structures in an airflow has been recognized since the early days of powered flight. An illustrative example of the result of such an instability phenomenon can be seen in figure 1.1, which shows a wind tunnel model of a Fokker F.28 transport aircraft. This model was used in a series of exploratory tests at the National Aerospace Laboratory (NLR), Amsterdam, The Netherlands [180]. At a certain test condition<sup>1</sup>, the T-tail of the model vibrated with a growing amplitude until the structure could not withstand the load and broke. Figure 1.1 shows the disastrous result after the test. This kind

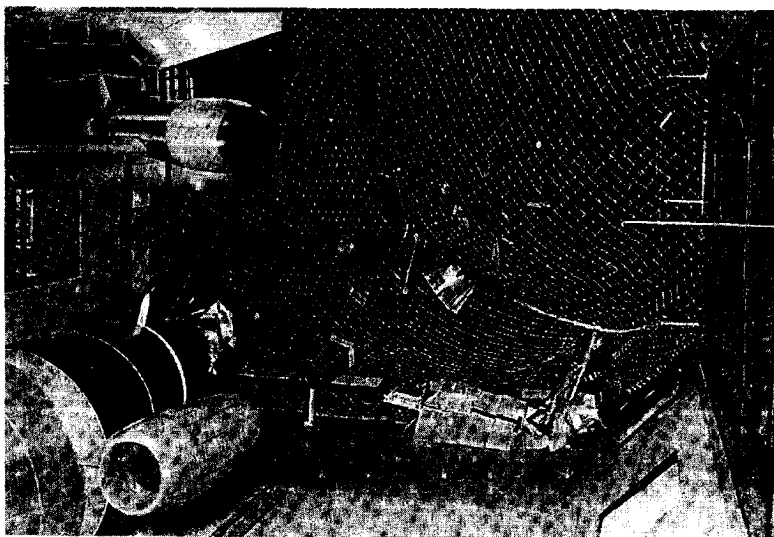


Figure 1.1: Structural failure of the T-tail of a Fokker F.28 wind tunnel model. The inset shows the model before the experiment (courtesy of NLR, Amsterdam)

of instability, called flutter, certainly may not occur during the service life of an aircraft. Airworthiness regulations deliver the requirements which have to be met

---

<sup>1</sup>It should be emphasized that the model did not represent the full-scale vibration characteristics for this flow condition.

in the design of the aircraft to guarantee freedom of flutter.

In the past years the awareness of this instability phenomenon, which is caused by the interaction between the airflow and the structure, has increased mainly due to two reasons: first, the advanced design approach striving for a lighter aircraft, which leads to a more flexible structure, and second, the higher flight speeds deep into the transonic speed regime. The complex nature of transonic flow interacting with the flexible aircraft structure presents a special problem. Figure 1.2 shows results of wind tunnel flutter tests at the NLR, Amsterdam obtained during the so-called SKV-5 program [184]. The test article was a semispan model of a supercritical wing of a

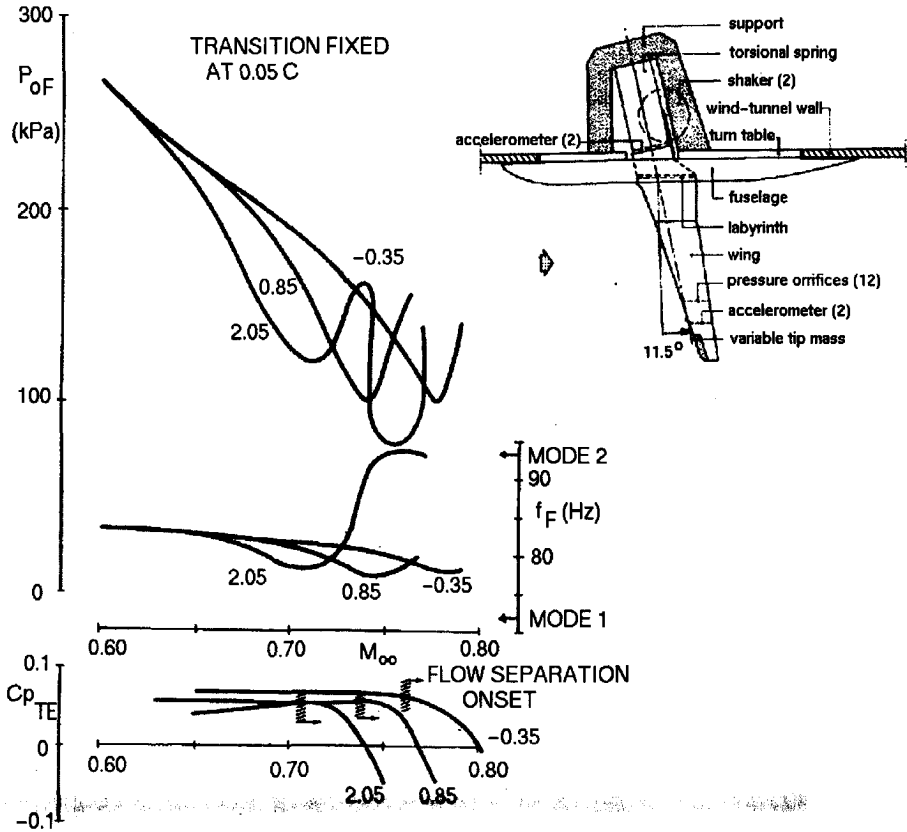


Figure 1.2: Transonic flutter dip phenomenon occurring in the SKV-5 test program. Results for  $\alpha = -0.35, 0.85$  and  $2.05$  deg.

transport aircraft. The main elements of the test setup are shown in the upper right figure. The curves in the upper left diagram represent the flutter dynamic pressure at three angles of attack, plotted against the freestream Mach number. The flutter dynamic pressures exhibit a distinct reduction at high subsonic Mach numbers. This phenomenon is called the transonic dip. Increasing the angle of attack shifts the dip

to lower Mach numbers. At the highest angle of attack, where viscous effects are most significant, the flutter dynamic pressure experiences another dip at a higher Mach number. Note the change in the flutter mode from the first dip to the second dip, as indicated by the increase of the flutter frequency from a low value close to the first wing bending frequency to a higher value close to the frequency of the second mode (wing rotation around pitch axis). This second dip turned out to be caused by flow separation [184], as indicated by the trailing edge pressure shown in the lowest diagram. Flutter boundaries of a full-scale aircraft flying at transonic flight speeds generally show transonic flutter dips as well, which has been confirmed by calculation many times. These dips form the most critical part of the flutter boundary and should therefore be carefully considered in the aircraft design stage.

This thesis describes a study of aircraft flutter at transonic flight by means of computational aeroelastic simulation. This introductory chapter presents some notions of the aeroelasticity of aircraft as well as the background and the scope of the study.

## 1.1 AEROELASTICITY OF AIRCRAFT

### 1.1.1 NOTIONS AND DEFINITIONS

Aeroelasticity is a discipline focusing on the class of fluid-structure interaction problems dealing with the deformations of elastomechanic bodies in an airflow. The flow and the structure are coupled in a closed loop system. The deformations interact with the flow through a change of the interface, i.e. the surface of the body, leading to a change of the aerodynamic loads exerted by the flow on the body, which contribute to the deformations. So, in an aeroelastic system the aerodynamic loads induced by the deformations are considered as part of the system and not as an independent excitation of the structure. In this interaction mainly the most flexible parts of the aircraft structure are involved, like the wings, tail surfaces and canard.

Besides the deformation-induced aerodynamic loads other aerodynamic loads are active in general, which do not depend on the deformations. Well-known examples of such loads are those due to atmospheric disturbances (gust) and flow separation at wing stall. The latter is known as the buffeting problem, see e.g. Nixon [119].

The flow and the structure form an aeroelastic system of which the properties are characterized by its stability (static or dynamic) and its response to an excitation. The important aerodynamic parameters in analyzing the stability of an aeroelastic system are Mach number,  $M_\infty$ , Reynolds number,  $Re_\infty$ , and dynamic pressure,  $q_\infty$ , where the subscript  $\infty$  refers to undisturbed flow conditions. At a certain Mach number and Reynolds number an increase of the dynamic pressure may lead to deformations of the aircraft structure which become unstable. If the deformations have an almost static character, the instability is called divergence, and when they are of an oscillatory nature the instability is called flutter. The speed of the first occurrence of flutter or divergence is called flutter or divergence speed, respectively.

The present study concentrates on the dynamic aeroelasticity in the transonic flight regime, i.e. at conditions where the flow is characterized by a mixed subsonic-

supersonic flow and is dominated by the physics of both types of flows [13]. This flow condition occurs at high subsonic up to low supersonic speeds. Experience shows that transonic flow usually presents the most critical flutter problems.

### 1.1.2 FLUTTER CALCULATIONS IN AIRCRAFT DESIGN

Figure 1.3 shows a typical procedure of the aeroelastic certification in an aircraft design process [185]. Without discussing the activities in detail, the role of flutter calculations and the associated development of analytical models is noticed, which proceeds through all stages of the design process. The results of these calculations

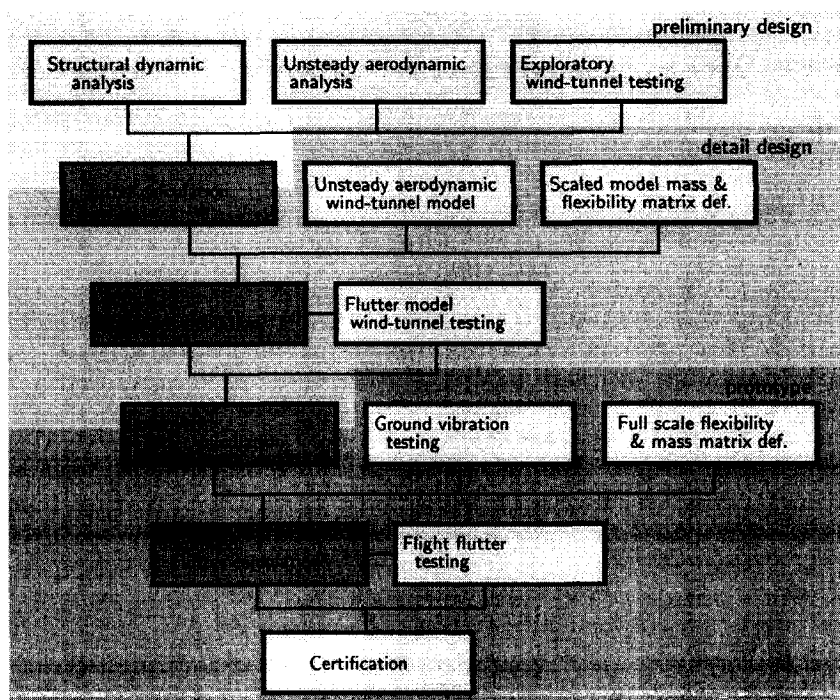


Figure 1.3: Flutter calculations during an aircraft design process, after [185]

provide support to the preparation of the expensive wind tunnel and flight flutter tests. The final results obtained by using the most updated analytical models in combination with the flight flutter test results provide the evidence for the flutter certification.

Advancing through the design stages implies the obvious needs of increasingly accurate data, analytical models and calculation methods for the flutter analysis. Usually also the number of required flutter calculations increases. The majority of these calculations is performed using standard methods, e.g. the aeroelastic module of the finite element analysis program MSC-NASTRAN<sup>®</sup>. The structural

and aerodynamic models in these standard methods have been reduced usually to a very minimum. Although acceptable in the first stages of the design process, these models often fall short in the final stage, and sometimes also earlier when special aeroelastic characteristics have to be investigated. For this situation the need to apply more accurate aerodynamic models is quite obvious. However, to maintain efficiency in the design process, it is of utmost importance to consider continuously the balance between the required accuracy and the acceptability in the design office in terms of cost and turn-around times.

### 1.1.3 TRANSONIC FLOW EFFECTS

For subsonic flow, at speeds up to  $M_\infty \approx 0.70$ , a relatively simple linear aerodynamic model, based on the classical lifting surface theory, is practiced. At this condition the aerodynamic forces respond linearly to the structural deflections and the influence of the mean steady flow, caused by the angle of attack and thickness and camber of the lifting surfaces on the unsteady flow can be neglected.

At transonic speeds, however, the assumption underlying this linear model is violated for several reasons: the interference between the steady flow and the unsteady flow is significant and can not be neglected [167, 184], the relationship between the aerodynamic forces and the structural deflections has become essentially nonlinear [47, 48], and in certain cases viscosity plays a vital role [89, 184]. In the following this is explained further.

The obvious situation in transonic flow is the mixed subsonic-supersonic flow. The immediate consequence is that disturbances in the flow, generated by the structural motion, are prevented to travel upstream in the supersonic flow regions and retarded in the (high) subsonic flow regions, leading to a substantial increase of the phase lag between the aerodynamic loading and the structural motion. When the supersonic flow region is terminated by a shock wave another consequence arises: the oscillating shock creates a shock pulse acting on the aircraft structure which may excite certain vibration modes. A thorough description of the phase lag and the shock pulse effects was given by Tijdeman [167].

The phenomena mentioned above are the cause of the aforementioned transonic dip shown already in figure 1.2. As pointed out in [184], which describes an extensive investigation of transonic flutter of an advanced transport wing, an analysis using a linear model would lead to a dangerous nonconservative prediction. This is the main reason which makes the transonic flutter characteristic as one of the most critical issues in the design of a transonic aircraft.

Concerning the effect of viscosity in transonic flow, a shock wave thickens the downstream boundary layer and in some cases may induce flow separation. In the case where the shock on the upper wing surface is weak and the flow is still mainly attached, the boundary layer will effect a decambering of the wing which reduces the unsteady aerodynamic loading. For a relatively thin wing a good approximation can still be provided by an inviscid flow model. For high performance wings of modern transport aircraft an inviscid flow model usually leads to a too conservative prediction of the flutter speed. In the case where the shock wave induces a large

---

region of flow separation, which dominates the aerodynamic loading behavior, the resulting instability is usually called buffeting flutter or buzz [119]. Buffeting flutter often constitutes the operational limit of aircraft.

Modern transonic aircraft are usually designed to fly quite close to the buffet boundary to gain performance. Due to atmospheric turbulence or pilot input, the aircraft angle of attack can increase momentarily inducing a (partly) separated flow condition. The problems of aeroelastic stability and response under these circumstances belong also to the aeroelastic discipline.

## 1.2 PROGRESS IN AEROELASTIC ANALYSIS

In the field of aeroelasticity of aircraft it is generally accepted that the level of structural deflections allows the assumption of a linear relationship between these deflections and the inertial, damping and stiffness forces in the structure. This simplifies the application of structural models substantially. However, it is clear from the preceding section that such an assumption is not always appropriate for the aerodynamic forces, especially in transonic flow. Therefore, research activities in the computational aeroelasticity in the past years focused mainly on the development of unsteady aerodynamic models with various levels of sophistication. These developments are well-documented, e.g. in the proceedings of the AGARD Structures and Materials Panel (SMP) specialists' meetings [2, 5, 6, 7] and of the Forums on Aeroelasticity and Structural Dynamics [15, 45, 150]. This section presents a concise review of the progress of aeroelastic analysis and focuses on flutter calculations since it constitutes the major portion of aeroelastic analysis in industrial practice.

Almost all flutter calculation methods are based on the assumption that each vibratory motion can be described by a series of predefined vibration modes, orthogonal or not. Each vibration mode is considered as an independent degree of freedom. The methods can be categorized into two types: frequency domain and time domain methods. In the frequency domain approach the further assumptions are that the equations of motion can be linearized and that use can be made of unsteady aerodynamic forces valid for harmonic motions. These assumptions enable the formulation of a complex eigenvalue problem, of which each eigenvalue can be associated with the frequency and the damping of an eigenmode. The flutter speed is defined as the speed at which the damping is zero. The flutter calculations are **carried out for a mainly large number of flight speeds and altitudes. Well-known** methods in this category are the classical k- or U-g-method [33], the p-k-method [73] and the modern methods in which the unsteady aerodynamic forces are approximated by rational functions of a Laplace variable [146]. In the time domain approach an initial condition is prescribed and the equations of motion—linear or not—are solved by numerical integration for various values of the flight speed and altitude. The resulting time traces are analyzed to obtain the frequency and damping of the responses. The flutter speed is then obtained by extrapolation or interpolation of the flight speed to the speed where the damping is zero. In this approach less assumptions are made than in the frequency domain approach. The consequence is

that the approach has been strongly computerized. For this reason the time domain approach is often referred to as computational aeroelastic simulation (CAS).

As stated above, for a frequency domain flutter calculation, unsteady aerodynamic data for harmonic oscillations are required. In the early days these data were calculated using a two-dimensional flow method, applied in a stripwise manner for each wing span station. Closed form solutions of the two-dimensional linearized potential-flow equation are available, see e.g. [33]. The solution for the flow about three-dimensional isolated wings was made possible by the advent of computing power. Two well-known methods which are based on the numerical solution of an integral equation are the kernel function method [98] and the doublet lattice method [9]. These methods were further developed for handling more complex geometries, like interfering surfaces and wings with control surfaces [168] and wing-body configurations [144, 148]. Nowadays, the doublet lattice-method is still considered as the principal tool by the industry [36, 59]. However, the employment of the underlying linearized potential-flow equation limits the method to pure subsonic or supersonic flows.

To handle transonic flows the transonic small perturbation (TSP) equation for the velocity potential has to be employed as a minimum. Since the TSP equation is nonlinear several ways have been proposed to proceed in the flutter calculations:

1. Prescribe a harmonic motion of the structure with frequency  $\omega$  and assume the solution to be  $\phi(\mathbf{x}, t) = \phi_0(\mathbf{x}) + \phi_1(\mathbf{x})e^{i\omega t} + \phi_2(\mathbf{x})e^{2i\omega t} + \dots$ . Assuming that the unsteady perturbations are small the TSP equation can be solved subsequently for  $\phi_0(\mathbf{x})$ ,  $\phi_1(\phi_0, \mathbf{x})$  and so on. This procedure is called time-linearization. The calculation of the unsteady aerodynamic forces is limited to solving  $\phi_0$  and  $\phi_1$ , see e.g. [176];
2. Solve the equation in the time domain for a prescribed motion, harmonic, pulse or diverging, and extract the frequency domain data. For the input of harmonic motion and pulse motion the frequency domain data are obtained from the Fourier transform of the aerodynamic forces divided by the Fourier transform of the input motion [30, 92]. In case of a diverging motion several data are first fitted using a Padé approximation technique and assuming analytical continuation of the aerodynamic forces the result can be used to calculate the data in the frequency domain, see [78, 131];
3. Solve the unsteady flow equations and structural dynamic equations simultaneously in the time domain [51, 52].

The results of the first two techniques can be directly applied in the linear frequency domain flutter calculation methods. It should be noted that the aeroelastic simulation of the third technique provides the possibility to appropriately handle the nonlinearity in the aeroelastic system.

The development of methods for solving the unsteady TSP equations was pioneered by NASA [19]. The solution technique is completely different from that of the integral equation method, as it employs finite differences, in other words it is

a method belonging to the field of computational fluid dynamics (CFD). Both the frequency domain approach [77, 92, 176] and the time domain approach [25] for the TSP equation were developed afterwards to handle more complex configurations and also to include effects of viscosity through coupling with a boundary-layer equation. Currently, this method is considered by industry to be the state-of-the-art of computational unsteady aerodynamics (CUA) [36]. Methods with a higher-level of physical modeling, viz. full-potential (FP) equation, Euler equations and Navier-Stokes (NS) equations, are still considered as methods of the future.

The aeroelastic analysis using an unsteady aerodynamic model which is of higher level than TSP usually takes at once the direction of an aeroelastic simulation technique, e.g. [25, 29, 66, 85, 178]. This is mainly due to the following two reasons: first, a proper modeling of the nonlinearity requires a time-marching approach, and second, the technique is just a straightforward extension of current Euler/Navier-Stokes methods for steady flows. There are, however, a few exceptions: Isogai [88] and Hounjet and Meijer [82] for FP and M. Lesoinne and C. Farhat [106] and Mortchelewicz [114] for the Euler equations, who applied the frequency domain approach through time linearization. A further review of CAS methods employing the Euler/Navier-Stokes equations is presented in the next chapter. In the following paragraphs the status of CAS methods is discussed in view of their significance as practical tools in the flutter certification of aircraft.

The development of CUA methods for aeroelastic applications was summarized in the review papers of Edwards and Malone [53] and Försching [59]. Many complicated flow problems can now be solved using the Euler or Navier-Stokes equations: the effect of the mean flow on the flutter speed, the limit cycle oscillations of an airfoil, control surface buzz, dynamic stall, shock stall, etc. However, the survey paper of Edwards and Malone [53] also shows that the aeroelastic application lags far behind the development of unsteady aerodynamic methods. Moreover, most of these aeroelastic applications employed potential-flow methods (particularly TSP) and only a very few of the aeroelastic applications were carried out by industry. The status presented three years later by Försching in [59], depicted in figure 1.4, shows practically the same situation.

Figure 1.4 makes clear that in 1995 CAS methods employing higher-level flow models were mostly in the development/research stage. Although an almost similar conclusion was reported in the technical evaluation of the 1997 AGARD SMP specialists' meeting [96], there is actually some obvious progress in the application **of advanced CUA/CAS methods in industry**. Baker [17] applied a CFD method indirectly, namely as correction for the classical linear flutter calculation. Franzen et al. [60] applied Euler/Navier-Stokes methods for checking the discrepancy between the results of flight tests and linear flutter calculations. Further, Henshaw et al. [75] pointed out the strong relationship between the extent of the modeling and analysis effort and the cost savings through reduced flight testing and reduced risk of redesign. Most importantly, they mentioned the justification of spending cost for advanced CAS methods with a reward of greater savings of the wind tunnel and flight flutter tests. Thus, although for routine applications aeroelasticians still use the potential-flow model [7, 59, 96], the need for higher-level flow models in the



		Airfoil	Wing+ Stores	Full Configuration
Panel	Linear Potential Theory	●	●	●
	Time-Linearized Transonic Potential	●	●	●
Unsteady CFD	Nonlinear TSD	●	●	●
	Nonlinear FP	●	●	●
	TSD/FP+ Boundary Layer	●	●	○
	Euler Equations	●	●	
	Euler Equations+ Boundary Layer	○	○	
	Navier-Stokes Equations	○		
		● Engineer	○ Researcher/Developer	

Figure 1.4: Status in computational unsteady aerodynamic capability in 1995, from [59]

industry exists, because during the design process specific conditions often occur for which the application of potential-flow methods would lead to doubtful results, while wind tunnel tests are very expensive and offer limited alternatives.

Currently the application of CAS in the industry is still limited. The causes pointed out by Lacabanne and Zwaan [96] are the high computing cost, the significant implementation effort and the need for sufficient validation of the methods. Burt [36] indicated that the first cause is the most important one with the computing time as the major part. In addition, preprocessing (grid generation) contributes substantially to the cost and effort related to the applications of Euler/Navier-Stokes methods. He also offered a view on industrially-accepted CUA methods, which rests heavily on the available steady flow CFD methods to be extended/modified for unsteady flow applications. This is perhaps the most feasible way in view of the startup costs, but this approach certainly requires substantial CFD expertise which may not or insufficiently be available for CAS design tasks, or may not be effective in taking account of typical aeroelastic requirements. Experience has learned that in such cases the availability of special CUA/CAS facilities provide a viable way out. It is the author's opinion that the CUA/CAS method proposed in the following chapters has a potential of such a facility.

Concerning the problem of long computing times one can argue that relief can be found in the implementation of CAS/CUA on supercomputers of parallel vector processors (PVP), which currently have enormous computing power. However, the question remains whether industry can afford the use of these PVP supercomputers. Actually the price/performance of the supercomputer has reduced noticeably by the introduction of the massively parallel processor (MPP) supercomputers. This type of supercomputers usually utilizes a large number of commodity processors instead of a small number of expensive vector processors. Meanwhile the computing power of

relatively cheap workstations and personal computers, which are presumably available in large numbers in industry, is also considerably improved. The power of MPP machines and that of the cheap computers can be harnessed by introducing parallel computation methodology into the CUA/CAS methods. The development of the CUA/CAS method proposed here has taken due account of this methodology.

### 1.3 BACKGROUND OF THE STUDY

Summarizing the preceding discussion, the background and motivation of the present study can be formulated as follows:

1. There exists a need in industry for affordable CAS methods employing high-level aerodynamic models as complementary tools to linear methods in order to support the flutter clearance during the design of a transonic aircraft;
2. So far, the developments in CUA and CAS have mainly concentrated on improving the flow modeling without adequate consideration of industrial acceptability of the methods, in terms of accuracy, robustness, turn-around times and hardware facilities. This has contributed to the reluctance of industry to employ high-level unsteady aerodynamic modeling;
3. The most important aspect therein is the high computational cost, with the required computing times of the simulations as the major component;
4. The availability of MPP machines and also clusters of workstations promise an enormous computing power at reasonable price.

### 1.4 OBJECTIVES AND SCOPE OF THE STUDY

The present study is a search for opportunities to make higher-level flow modeling (i.e. the Euler and Navier-Stokes equations) in CUA and CAS more attractive for aeroelastic applications, especially in industry. The interest in such opportunities is expanding at several places (see e.g. [96]). In The Netherlands this type of work was started already at the NLR, Amsterdam, on the basis of FP flow modeling [80, 81]. The present study makes use of this development and focuses on the introduction of a higher-level flow modeling. The scope of the present study is:

1. **Development of a two-dimensional CUA method for solving the Euler/Navier-Stokes equations based on CAS requirements.** Besides its applicability to two-dimensional configurations, the objective of this part of the study is to investigate the feasibility of extension to three-dimensional configurations;
  2. Development of a CAS method using the developed CUA method. In this part of the work an appropriate structural model is selected and coupling methods between the aerodynamic and the structural models are developed;
  3. Application of the method to two-dimensional unsteady aerodynamic phenomena in transonic flow and aeroelastic simulations;
-

4. Extension of the two-dimensional flow method to a three-dimensional flow method. This method is intended for applications to simple isolated wings and to wing-body configurations. The most important step to make computing times affordable is the application of a parallel computational method to distribute the work to many processors. The implementation of the method should be portable to a variety of platforms;
5. Applications of the three-dimensional method to realistic configurations.

Representative results of the present investigation were reported at several conferences and in a scientific journal [111, 132, 133, 134, 135, 136].

## 1.5 OUTLINE OF THE THESIS

The thesis is organized as follows: Chapter 2 presents a review and a discussion of CAS methods employing Euler/Navier-Stokes equations. CUA methods for solving the unsteady Euler/Navier-Stokes equations are also briefly reviewed. Further, in this chapter the requirements for the solution method from the point of view of aeroelasticians are discussed. Lastly, the governing equations and boundary conditions are introduced.

Chapter 3 presents an extensive study on numerically solving the two-dimensional unsteady Euler/Navier-Stokes equations on a deforming mesh. Many aspects are discussed: the deforming mesh, the temporal integration, inviscid flux discretization, solution of the set of linear equations and the results of some test cases to demonstrate the applicability of the method.

In chapter 4 the method is applied to investigate the unsteady flow phenomena occurring in the flow field around oscillating airfoils. Both attached and separated flow conditions are considered and computational results are compared to available data from experiments. A study concerning the flow characteristics is also presented.

Chapter 5 discusses a method of applying the CUA method developed in chapter 3 for aeroelastic analysis. The structural model, coupling procedures and the solution of the coupled equations are discussed. Validation test cases and other applications of the method are also presented.

Chapter 6 presents a three-dimensional CUA and CAS method based on the studies described in the previous chapters. An important provision in the three-dimensional flow method which is not present in the two-dimensional flow method is the parallelization. Some applications are presented ranging from a simple isolated wing to a more realistic configuration.

Finally Chapter 7 summarizes the capability of the CUA/CAS methods developed in this study, presents concluding remarks and offers recommendations for further studies.

Figure 1.1: A diagram illustrating the relationship between the number of nodes and the number of edges in a graph. The x-axis represents the number of nodes (n) and the y-axis represents the number of edges (m). The graph shows a linear relationship where the number of edges increases proportionally with the number of nodes.

---

## CHAPTER 2

# COMPUTATIONAL AEROELASTIC SIMULATIONS

The development of CAS methods follows mainly the progress of CUA methods because a CUA method can be considered as a prerequisite for a successful CAS method. The development of CUA methods has been one of the major research topics in aeroelasticity as well as in CFD in general. In the following sections some aspects of discretization in CAS are discussed, then a concise review of current CUA and CAS methods is presented. This review focuses on methods employing the Euler/Navier-Stokes equations. After presenting the general approach taken for the present study, the governing equations are described in the last section.

### 2.1 DISCRETIZATION ASPECTS OF CAS METHOD

Established methods to describe the motion of particles which constitute the continuum of either the structure or the fluid are the Lagrangian and the Eulerian description methods. In the Lagrangian or material description the observation point is attached to a specific particle and one observes the state of that particle during its motion. This method is mainly applied in the structural dynamics where the motion of each particle takes place in a neighborhood of the point where the motion started. In the Eulerian or spatial description the observation point is fixed in space and particles are passing this point. One observes not only the state of motion of each passing particle but also its convective change (flux). This method is preferred in fluid dynamics where the motions of particles are usually large and the convective changes dominate in the motions. In certain situations, like the one discussed hereafter, a generalized description, called the mixed/arbitrary/hybrid Lagrangian-Eulerian description (abbreviated to ALE), is needed. In the arbitrary Lagrangian-Eulerian description one observes the state and the flux of particles passing the observation point of which its time-dependent position can be defined independently of the motion of the particles.

In an aeroelastic simulation system both structural and aerodynamic parts are involved, interfaced by the surface of the structure. Since the deformation of the structure is assumed to be relatively small, the common Lagrangian approach can be applied for the discretization of the structural part. For the aerodynamic part the boundary of the domain in which the aerodynamic problem is solved has to adapt

itself to the continuously changing fluid-structure interface, caused by the deformation of the structure. Consequently, the boundary of the mesh in the aerodynamic domain is defined by the state of the structure. In the approach where the mesh in the field deforms according to the deformation of the mesh boundary, a method based on the ALE description has to be applied for the aerodynamic part<sup>1</sup>. Another approach, which is valid for small displacements of the interface, is the linearization of the boundary condition of the aerodynamic equations around the mean position of the interface. Thus, the boundary condition is applied at the mean position of the interface, so that the adaption of the aerodynamic domain is not necessary and the common Eulerian approach may be applied for the aerodynamic part.

At the interface, the surface of the structure, an interchange of data takes place. The structural part defines the position and velocity of the boundary of the aerodynamic mesh and the aerodynamic part provides the load to the structural part. Two important aspects concerning the transfer of the data can be identified: the spatial/geometrical aspect and the temporal aspect. The spatial/geometrical aspect concerns the compatibility of the geometrical representation of the interface by the structural and the aerodynamic part. An incompatibility can be easily caused by the employment of different discretization methods for the two domains and/or the different requirements upon the mesh density for the two domains to reach a comparable accuracy. In this case a correct transfer of data has to imply a conserved transfer of work. This aspect will be elaborated further in section 2.5.1. The temporal aspect of the transfer of the data concerns the availability of the data at a certain time during the simulation. This aspect is not trivial since the states of the two domains depend on each other. The following section discusses this aspect in more detail, reviews the available methods in the literature and presents the current approach.

## 2.2 TEMPORAL INTEGRATION ASPECTS OF CAS, AERO-STRUCTURAL COUPLING

The interdependency/coupling between the aerodynamic part and the structural part in a CAS system is illustrated in figure 2.1. In order to solve the structural equations to obtain the structural state, and subsequently the state of the interface, the aerodynamic loading on the interface is needed. Meanwhile the aerodynamic loading on the interface can only be calculated from the aerodynamic state when **the state of the interface is known and the mesh has been generated**. This coupling constitutes the main problem in the temporal integration of a CAS system. In the sequel the manner in which this dependency is treated is called the aero-structural coupling procedure.

Various methods were proposed to solve this problem. Bendiksen [27, 28] applied the explicit Runge-Kutta (RK) method to both the structural and aerodynamic equations. The application of an explicit method implies that the updates of the structural and the aerodynamic states depend on the states at the previous time,

---

<sup>1</sup>In the field of structures, there are similar situations where application of ALE is a necessity. An example is the analysis of a metal-forming process, see e.g. Atzema and Huétink [16]

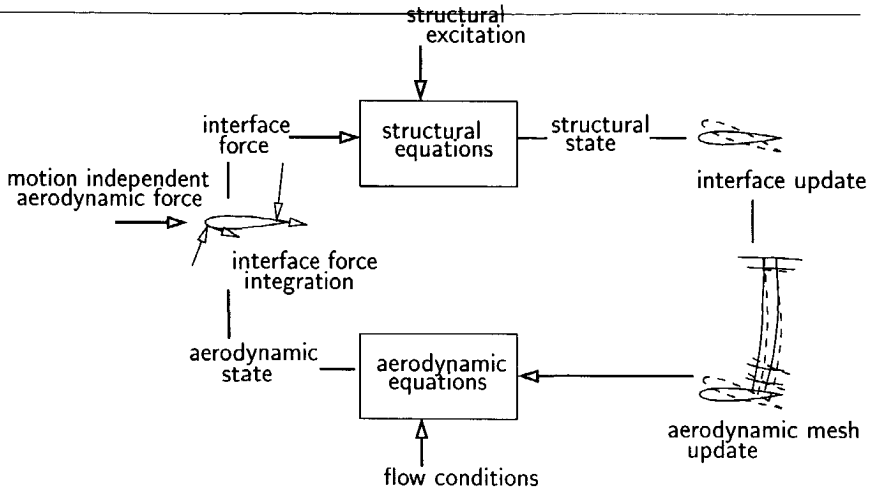


Figure 2.1: Dependency of structural and aerodynamic parts in CAS

which is a very convenient situation. Since the aerodynamic and the structural equations are treated in the same manner and their solutions proceed at the same pace in time, the method is called a fully coupled method. This method is probably the ideal way from the point of view of physical modeling. The main drawback is the small time step which has to be taken due to stability limits of the explicit method. This also has repercussions for the aerodynamic mesh to be regenerated or deformed and subsequently the calculation of the mesh metrics. The turn-around time of this method might therefore be prohibitive for practical problems.

A fully coupled method using an implicit temporal integration method, which allows larger time steps, needs an iterative scheme to solve the coupled equations simultaneously. The iteration scheme may be of an explicit type, using dual time stepping, e.g. in Alonso and Jameson [10], or an implicit type, e.g. in Weeratunga and Pramono [172]. An implicit type iteration is rather difficult to construct since the gradient matrix has an unfavorable form, which might also lead to ill-conditioning, see Farhat and Lesoinne [58]. Therefore in [172] an explicit treatment of the fluid-structure coupling during the iteration is applied. Both types of iteration schemes need certainly mesh updates during the iterations within each time step. Since mesh updating, and the subsequent metrics calculation, is expensive in term of CPU time, this reduces the advantage of these implicit fully coupled methods.

The so-called loose aero-structural coupling method (also known as staggered or partitioned method) in Edwards et al. [52], and [58] is more widely accepted due to the clear separation of the solution of the aerodynamic and the structural equations. The method proceeds by extrapolation of either the fluid state, called aerodynamic extrapolation method, or the structural state, called structural extrapolation method, to be used as an input for the other field. An advantage of this method is that a limited number of meshes have to be regenerated or deformed

within each time step. An important consideration in introducing mesh updates during the subiteration is whether having  $n$  updates in the subiteration with time step  $\Delta\tau$  is more efficient than just one update with time step  $\Delta\tau/n$  at a comparable accuracy. Another important advantage of this method is that it is suited for most of the methods developed for the flow and structural parts. Thus, it can benefit by the existence of efficient solution methods, corresponding software and experiences in each of the parts of CAS.

Various loose aero-structural coupling strategies for two-dimensional configurations are discussed in chapter 5. One of these strategies will also be applied to three-dimensional configurations.

## 2.3 LITERATURE SURVEY

### 2.3.1 REVIEW OF UNSTEADY EULER/NAVIER-STOKES METHODS

From the class of Lax-Wendroff methods (methods with a combined space-time discretization) the MacCormack method [107] is the most popular one for solving the Euler/Navier-Stokes equations. The combined space-time discretization, which provides a natural numerical stabilization for the class of Lax-Wendroff methods, is efficiently applied in the MacCormack method by using a time splitting.

Next to the MacCormack method, the most important pioneering methods for solving the Euler/Navier-Stokes equations for practical flow problems are without doubt the methods based on the central difference scheme related to the implicit approximate factorization (AF) method of Beam and Warming [26] and the explicit multi-stage RK method of Jameson et al. [91]. Many codes in use today are based on these methods.

For steady flow problems the application of an explicit RK method appears to be much more popular than the use of an implicit AF method. This is due to the simplicity of the explicit RK method compared to the implicit AF method. Although in its original form the method is not efficient due to its low numerical stability limit, when acceleration techniques are applied it can still compete with the implicit AF method. For unsteady flow problems, however, the explicit RK method is less popular because of its strict numerical stability limitation which in terms of a Courant number is of  $\mathcal{O}(10)$  (five-stage RK with implicit residual smoothing). Unlike steady flow calculations where for faster convergence the time step can be defined **locally, i.e. proportional to the local speed of the waves**, unsteady flow simulations require a uniform time step to be used in the whole field. This time step, called global time step, is determined by the computational cell with the highest local Courant number. Examples of unsteady flow methods with a deforming mesh capability which employ the explicit RK method are given by Bendiksen and Kousen [29], Bendiksen and Hwang [28], Damodaran [40] and Gaitonde and Fiddes [61]. Note that an explicit method is mostly applied when unstructured meshes are employed. In such a case it is difficult to construct an implicit method.

Many papers on steady flow problems confirm that the implicit AF method has proven to be a very efficient method. It is highly vectorizable or parallelizable due to



the splitting which brings independence between the equations in each dimensional direction or mesh lines. Application of the central-difference method with an implicit AF method for an unsteady moving mesh problem was already initiated by Steger and Warming [160]. For unsteady flow applications, although linear analysis suggests unconditional stability, the implicit AF method is known to have a severe time step limitation due to the factorization error. The maximum global time step that can be employed in time-accurate two-dimensional flow simulations corresponds to a Courant number of  $\mathcal{O}(500)$ . For the three-dimensional flow case, where simple linear analysis indicates unconditional instability, this limitation is even more severe. This makes the implicit AF method to have poor efficiency for unsteady flow problems. Nevertheless, many well-known unsteady flow methods are based on this technique, examples are ENSAERO [68], CFL3D [12] and the Navier-Stokes method of NAL [116].

For upwind methods there are more possibilities for approximately factorizing the Jacobian matrix, see Pulliam [138]. The most successful factorization for unsteady flow applications uses the sign of eigenvalues of the Jacobian of the flux, the so-called two-factor scheme. For three-dimensional flow, unlike the AF method, the two-factor scheme retains its stability property. The drawback of the two-factor scheme is its sequential character when the equation is solved by sweeping in a natural order. A vectorizable ordering can be constructed but the resulting scheme becomes quite complicated. This is one of the reasons that many upwind methods still apply the implicit AF method based on the dimensional direction factorization (two-factor in two-dimensional and three-factor in three-dimensional flow). The stability boundary of an upwind method applying implicit AF is not significantly different from its central difference counterpart. The methods of Rumsey and Anderson [151] and Lee-Rausch and Batina [102] belong to this category. Guruswamy [68] showed that an improvement of the stability boundary of an AF method is achieved by applying a hybrid of directional and eigenvalue-sign factorizations, called lower-upper alternating direction implicit (LU-ADI). Although the work in each time step increases, a better overall efficiency is achieved due to the possibility to use a larger time step.

Facilitated by the possibility of constructing a positive and diagonally dominant Jacobian matrix by using an upwind method, some authors take a different approach in solving the Euler/Navier-Stokes equations, namely by using relaxation. This approach has been traditionally applied in methods for solving the potential flow equation, i.e. TSP and FP. A relaxation approach is not sensitive to the time step limitation. Steady flow problems, which were traditionally modeled using the unsteady form of the Euler/Navier-Stokes equations and solved using a time marching approach, can be solved directly using a relaxation method applied to the steady form of the Euler/Navier-Stokes equations. Examples of this approach are presented by Dick [46], Eberle [49], Koren [94], Spekreijse [158], Thomas et al. [164], Venkatakrishnan [171]. Surprisingly, there are only a few applications of this procedure for unsteady flow cases involving deforming meshes. Two possible explanations are: the belief that the nonlinear nature of transonic flow problems can not be represented by methods employing a large time step and the notorious complexity of the im-

PLICIT method. The work of Brenneis and Eberle [35] is an example of this approach, where a point Gauss-Seidel (PGS) iteration scheme is employed to drive the residual of the unsteady flow equations to zero, i.e. the time derivative (first-order accurate) is included in the residual. This method is actually an extension of a steady flow method for solving the Euler equations, see [49].

A paper which constitutes an important development in unsteady flow methods was presented by Jameson [90], namely an efficient application of an explicit RK scheme for unsteady flow problems. A pseudo-time was introduced to redefine the unsteady flow problem into a steady flow problem, with the physical time derivative included in the discretized equations. The method is called the dual time-stepping method. A decisive advantage is that acceleration methods, which were traditionally developed for steady flows, i.e. the local time stepping, the implicit residual smoothing and the multigrid method, can now be utilized for unsteady flow applications. This is the main feature of Jameson's method, since without acceleration techniques the explicit method can not compete with the implicit method in terms of efficiency. Following the popularity of the explicit RK method for steady flow applications this method also became very popular. In a short time after its introduction in 1991 the method was adopted by many authors and became more or less a standard method to transform a steady flow solver into an unsteady flow method. The discussion concerning the application of either explicit or implicit methods for unsteady flow calculations, which was in favor of implicit methods, became once more open.

Concerning the upwind flux modeling for two- and three-dimensional flow problems, the most common method to date is the application of a one-dimensional splitting method to the inviscid flux normal to the cell face. This makes the method, the so-called quasi-one-dimensional splitting method, to depend on the orientation of the mesh. Recently, several modern upwind methods of a real multi-dimensional character have been developed to solve the Euler/Navier-Stokes equations, see e.g. Hussaini et al. [84], Struijs et al. [162]. A multi-dimensional upwind method has a mesh-independent character, which is ideal for an unstructured mesh method. Most of the multi-dimensional upwind methods are in the development state and still have to mature with respect to their accuracy and robustness, see Paillere et al. [126], Zhang et al. [182]. So far, multi-dimensional splitting has not been applied to unsteady flow problems with moving boundaries.

### 2.3.2 REVIEW OF COMPUTATIONAL AEROELASTIC SIMULATION METHODS

The application of the two-dimensional Euler equations for aeroelastic analysis in transonic flow was initiated by Bendiksen and Kousen [29] with a modified explicit RK method of Jameson et al. [91]. The aero-structural coupling employs an aerodynamic extrapolation method. The method was used to study nonlinear aeroelasticity in transonic flow by Kousen and Bendiksen [95], which showed the possible occurrence of limit-cycle oscillations (LCO). Later, Bendiksen [27] improved the aero-structural coupling into a fully coupled one using the explicit RK method. Wu et al. [178] presented results for two-dimensional configurations using the Navier-Stokes

equations in the aerodynamics. The solution method applies Jameson's central difference scheme and the implicit AF method with the aerodynamic extrapolation coupling procedure. Time-marching aeroelastic solutions were given for an NACA 0012 airfoil near stall conditions.

The recent paper of Alonso and Jameson [10] pays attention to the efficiency in the time-marching aeroelastic solution method by applying an implicit method with an explicit subiteration scheme based on the work of Jameson [90]. The structural state is updated during the subiteration to obtain a full convergence of the aeroelastic equations. They show results of aeroelastic simulations with the Euler equations using relatively large time steps with an adequate temporal accuracy and conclude that the method has gained efficiency in time-marching aeroelastic analyses through its ability to march with large time steps. Later on Alonso et al. [11] also presented some time-marching aeroelastic results using the laminar Navier-Stokes flow model.

The three-dimensional CAS method using the Euler/Navier-Stokes aerodynamics was pioneered by Guruswamy [65, 66]. The method utilized a central difference scheme and implicit AF and LU-ADI methods for the aerodynamic part. The aero-structural coupling of the method was an aerodynamic extrapolation method. The aeroelastic equations were integrated in time using a linear acceleration method. The mesh was adapted to the motion of the surface using a shearing technique. The method, called ENSAERO, was later improved by the introduction of an upwind method by Obayashi et al. [122].

Recently, numerous authors have presented three-dimensional CAS methods employing the Euler/Navier-Stokes equations, e.g. by Batina [24] and Rausch et al. [141] with the Euler equations on unstructured meshes, by Bendiksen and Hwang [28], Farhat and Lesoinne [58] and Robinson et al. [143] with the Euler equations on structured meshes and by Guruswamy [66] and Lee-Rausch and Batina [102] with the Navier-Stokes equations on structured meshes. The flow considered in these papers is mostly transonic attached flow. Strongly nonlinear cases are considered by Nakamichi et al. [117] for separated flow resulting in LCO, and Guruswamy [67] for vortex flow.

The aero-structural coupling procedures applied in these papers are mostly the aerodynamic extrapolation method. The exceptions are [28] where a fully coupled method with an explicit RK temporal integration is used like in [27], and [58] where aerodynamic as well as structural extrapolation methods are used. The temporal integration methods for the loose aero-structural coupling scheme varies from the Newmark- $\beta$  method [58], the linear acceleration method [66, 67], the Wilson- $\theta$  method [117] and the transition matrix method [102, 141, 143].

Most of these papers which present loose aero-structural coupling methods in combination with aerodynamic extrapolation report that the numerical stability boundary of the methods applied for the aerodynamic part determines the time step for the whole aeroelastic simulation. Since larger time steps are desired for efficiency reasons, Farhat and Lesoinne [58] applied the so-called subcycling in which the structural part is updated only after a number of aerodynamic steps. For example, an  $n$ -subcycling means that the time step size of the aerodynamic part is  $1/n$  of the aeroelastic or structural time step size. Unfortunately, subcycling is reported to

---

introduce numerical instability when  $n$  is too large, see e.g. [58] and Grisval et al. [64].

The deforming mesh algorithm applied in these references, in general, may be categorized into two groups: the algebraic method and the spring analogy method. In the algebraic method of Guruswamy [66, 67], Nakamichi et al. [117] the mesh is sheared in one direction (usually the normal,  $\zeta$ , direction) to follow the deformation of the structure. As reported in [117] this method fails to produce a mesh with adequate quality when the deformation is relatively large. To overcome this problem, in [117] a new mesh is generated using an online algebraic mesh generator each time the deformation reaches a certain level. The spring analogy was first introduced by Batina [24] to model the mesh deformation. Originally the method was employed for a mesh adaption by Nakahashi and Deiwert [115]. The mesh segments are represented by a spring system which reacts to the deformation on the boundary of the mesh. This technique is very general in terms of its capability to follow the motion of the interface and its applicability to both structured [24] or unstructured [58, 141] meshes.

### 2.3.3 GENERAL DIRECTIVES IN DEVELOPING CAS METHODS

Several important issues have now been identified from the past research in the field of CUA/CAS. Based on these issues the following general directives for the present study in developing a CAS method are summarized:

- The loose aero-structural coupling method has been used successfully in two-dimensional and three-dimensional CAS and is applied in the present study. This method offers the possibility to consider the approaches for the aerodynamic and structural parts relatively independently. The aerodynamic extrapolation method, required for a loose aero-structural coupling method, appears to be well explored whereas the structural extrapolation method has been less applied. Thus both extrapolation methods should be explored;
- Numerical stability, which allows the time step to be determined by the flow physics, is important in order to achieve overall efficiency. This is confirmed in [10, 65, 90]. Therefore, also in the present study the numerical methods to be applied for solving the aerodynamic and structural equations should be stable enough to allow the time step to be determined by flow physics. **Two possible methods for the aerodynamic part have been identified: the dual-time stepping method of [90] and the relaxation method;**
- Subcycling, as a technique to allow large time steps for the aeroelastic simulation, introduces a numerical instability when the aerodynamic time step is too small compared to the structural time step [58, 64]. This approach should not be applied;
- The spring analogy method for deforming the mesh offers generality in handling the motion of the structure. This method should be applied here;

- Most methods presented in the literature thus far employ relatively small time steps. The applicability of some procedures of their CAS, i.e. the loose aero-structural coupling method and the mesh deformation method, has still to be investigated for simulations employing large time steps which are determined solely by the physics.

## 2.4 EQUATIONS OF MOTION OF AN AEROELASTIC SYSTEM

In general the equations of motion of the aeroelastic system can be represented by:

$$M\ddot{\mathbf{x}} + C\dot{\mathbf{x}} + K\mathbf{x} = q_\infty S \mathbf{C}_A(M_\infty, Re_\infty, \dot{\mathbf{x}}, \mathbf{x}), \quad (2.1)$$

where  $M$ ,  $C$  and  $K$  are the mass matrix, structural damping matrix and stiffness matrix, respectively.  $\mathbf{x}$  is the vector of the physical displacements,  $q_\infty$  is the freestream dynamic pressure,  $S$  is the reference area and  $\mathbf{C}_A$  is the aerodynamic force coefficient. In aeroelasticity usually the high-frequency vibration modes are hardly important and are therefore omitted in the analysis. To take advantage of this, the motion of the structure is represented by a finite number of modes obtained from solving:

$$M\ddot{\mathbf{x}} + K\mathbf{x} = 0. \quad (2.2)$$

By assuming the solution to be  $\mathbf{x}(t) = \boldsymbol{\phi} e^{i\omega t}$ , a standard eigenvalue problem is obtained which can be solved for the natural mode shapes  $\boldsymbol{\phi}_i$  and their natural frequencies  $\omega_i$ . The resulting mode shapes are normalized with respect to the mass matrix:

$$\boldsymbol{\phi}^T M \boldsymbol{\phi} = I, \quad \boldsymbol{\phi}^T K \boldsymbol{\phi} = \omega_i. \quad (2.3)$$

Substituting  $\mathbf{x} = \boldsymbol{\phi} \mathbf{q}$  into equation (2.1), using equation (2.3) and assuming a diagonal damping (e.g. proportional damping), results in the following set of equations:

$$\ddot{q}_i + 2\zeta_i \omega_i \dot{q}_i + \omega_i^2 q_i = q_\infty S Q_i, \quad i = 1..N, \quad (2.4)$$

where  $\zeta_i$  is the mode damping and  $Q_i$  is the  $i$ -th dimensionless generalized aerodynamic force (GAF) defined as:

$$Q_i = \frac{1}{S} \int_S p \boldsymbol{\phi} \cdot \mathbf{n} dS. \quad (2.5)$$

$N$  is the number of normal modes which are retained in the simulation. Most of the time  $N$  is much smaller than the number of degrees of freedom employed in solving equation (2.2).

## 2.5 UNSTEADY AERODYNAMICS FOR AEROELASTIC APPLICATIONS

In this section some aspects of unsteady aerodynamics for CAS applications are presented. First the requirements upon accuracy and capability of CUA methods for CAS applications are discussed. The governing equations employed for the present study are also presented.

### 2.5.1 AEROELASTIC REQUIREMENTS

**SPATIAL ACCURACY** The interaction between the fluid and the structure occurs at the solid surface. In practice the parameters acting in the aero-structural coupling may differ according to the type of solution method. For example, the loading on the structure can be expressed directly in the form of pressures and viscous stresses [27] or in the form of forces [58]. In the present approach, where a modal decomposition of the structural part is applied, the load parameters are the GAFs, defined by equation (2.5). The total of GAFs represents the work of the fluid performed on the structure. To obtain accurate values of the generalized forces, an accurate prediction of the pressure is essential at the locations with large structural displacements normal to the surface. This implies that the computational mesh should be generated according to this requirement. It should be noted that the accuracy requirement for the GAFs should also take into account the physical uncertainties involved in the structural modeling. Table 2.1, presented by Zwaan [186], about the order of accuracy of the components in equation (2.1) considered from a practical point of view, makes clear that a somewhat relaxed accuracy requirement is acceptable. The

force	order	accuracy	remarks
$M\ddot{\mathbf{x}}, K\mathbf{x}$	1	$\pm 0.05$	
$C\dot{\mathbf{x}}$	0.05	$\pm 0.01$	available after GVT
$q_\infty SC_A(M_\infty, Re_\infty, \dot{\mathbf{x}}, \mathbf{x})$	0.20	$\pm 0.05$	assuming balanced accuracy

Table 2.1: Accuracy of the components of aeroelastic equation of motion, from a practical point of view [186]

accuracy of the aerodynamic forces is assumed to be in balance with that of the structural forces (inertial, damping and stiffness). From table 2.1 then, it can be concluded that the required accuracy of the aerodynamic force is  $\pm 25\%$ . This level of required accuracy is relatively low compared to that needed in steady aerodynamic problems, which is dictated mainly by the prediction of lift and drag forces. The values presented in table 2.1 are of course not universal and their significance is only to make clear that pursuing increased accuracy in the aerodynamics of CAS should not be an isolated goal.

**TEMPORAL ACCURACY AND NUMERICAL STABILITY** The important issues related to temporal accuracy are: the time scales involved in the simulations, the time step size, the order of accuracy and the numerical stability boundary of the temporal integration method. By specifying the number of time steps per cycle the time step can be related to the frequency as:

$$\omega^* = \frac{2\pi}{\Delta\tau^* n_{\text{cyc}}}, \quad (2.6)$$

where  $\omega^*$  is the characteristic frequency of the problem,  $\Delta\tau^*$  is the characteristic time step of the problem and  $n_{\text{cyc}}$  is the number of time steps per cycle. As stated in the general directives, section 2.3.3, the time step size should be determined solely

by the physics, i.e. the frequency scales involved in the aeroelastic simulation. In the following these frequency scales will be discussed and the requirements, in terms of accuracy and numerical stability, upon the temporal integration method for the flow equations will be defined. The frequency parameter that is commonly used in unsteady aerodynamics is the so-called reduced frequency, defined as:

$$k = \frac{\omega b}{U_\infty}. \quad (2.7)$$

The structural motions involved in aeroelastic analyses are restricted to a number of natural vibration modes (see section 2.4). The specification of the highest frequency of the natural vibration modes is based on experience, defined here as  $\omega_r$ . Because of the truncation of the number of vibration modes, the structure may be considered as a low-pass filter to the aerodynamic input signals. Aliasing of higher frequency signals will be disturbing only if the aliased frequencies coincide with physically present natural frequencies. This situation is not expected in practice, so it may be concluded that the highest reduced frequency of interest for the unsteady aerodynamics is  $k_r = \omega_r c / U_\infty$ . From an accuracy point of view  $k_r$  is of interest since the temporal integration method for the flow equations has to be able to capture the flow behavior only up to this reduced frequency:

$$k < k_r. \quad (2.8)$$

Note that flow behavior with a characteristic frequency  $k < k_r$  will be more accurately resolved since it is sampled with more time steps per cycle.

The numerical stability of a temporal integration method is usually expressed in terms of the Courant number, also called the CFL number, which can be related to the reduced frequency as:

$$\text{CFL} = \frac{c}{\Delta x} \frac{2\pi}{kn_{\text{cyc}}}, \quad (2.9)$$

where  $c$  is the local convection speed and  $\Delta x$  is a typical measure of the mesh size. The requirement to ensure numerical stability everywhere in the aerodynamic domain is:

$$\text{CFL} < \text{CFL}_{\text{stab}}, \quad (2.10)$$

where the value of  $\text{CFL}_{\text{stab}}$  depends on the type of temporal integration method.

In a typical aeroelastic case the relation between CFL (related to numerical stability) and  $k$  (related to physics) for several values of  $n_{\text{cyc}}$  is shown in figure 2.2. The curves showing the accuracy limit of the first and second order temporal integration method are concluded from various results in the literature. Setting the frequency scale based on physics to be  $k_r \approx 0.20$ , the various temporal integration method can now be associated with different requirements upon  $n_{\text{cyc}}$  to be used. Explicit methods usually have a stability limit in terms of CFL number of  $\mathcal{O}(1)$  which require  $n_{\text{cyc}} = \mathcal{O}(10^5)$ . Traditional implicit AF methods, like that of Beam and Warming

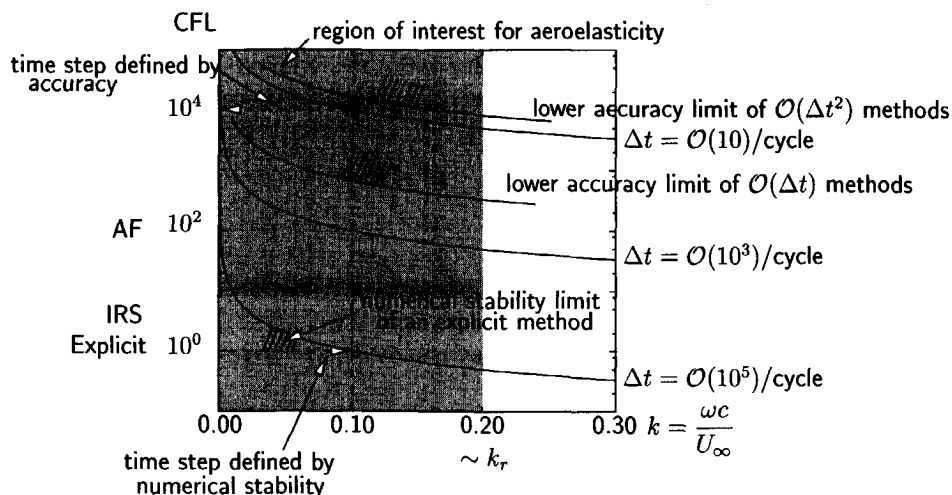


Figure 2.2: Relation of CFL number to the reduced frequency of a specific problem for various numbers of time steps per cycle

[26], require  $n_{cyc} = \mathcal{O}(10^3)$ , see e.g. [68]. Experience has shown that an accurate integration of the structural equations needs a number of time steps per cycle of  $\mathcal{O}(10)$ , see Hounjet and Eussen [80]. Requiring also  $n_{cyc}$  for the aerodynamic part to be of  $\mathcal{O}(10)$  defines the requirement upon CFL to be  $\mathcal{O}(10^4)$ . In practice more difficult situations occur in which the highest frequency of interest for a certain case is lower than  $k_r$  leading to even higher value of CFL. For example a typical transonic aeroelastic case characterized by relatively low frequencies, say  $k = 0.10$ , a medium sized mesh and a high subsonic Mach number, the CFL number in the unsteady aerodynamic calculation can easily exceed  $\mathcal{O}(10^4)$ . In general, the region of interest starts already at  $k=0$ , so that it may be concluded that a method has to be applied which is not sensitive to a CFL restriction.

Brenneis and Eberle [35] showed that an implicit temporal integration method of first-order accuracy required  $n_{cyc}$  of  $\mathcal{O}(100)$  to simulate a typical aeroelastic problem in transonic flow. Therefore, to use time steps of  $\mathcal{O}(10)$  per cycle, at least a second-order accurate temporal integration method has to be applied.

## 2.5.2 GOVERNING EQUATIONS

The equations governing the fluid flow are derived from the fundamental principles in mechanics, namely mass and energy are conserved and the fluid motion satisfies Newton's second law. The application of these principles to fluid flows can be carried out in several ways. The issues relevant to a numerical method are related to the flow physics of the problem and to the method of solution.

Due to the ability to automatically determine discontinuities in the flow field, a shock-capturing method is more convenient in practice than a shock-fitting method



for the present problem of flows with shock structures that are a priori unknown, or varying in time. This means that the governing equations have to be considered in a conservation form.

### COMPRESSIBLE VISCOUS FLOW

The Navier-Stokes equations are the most general set of equations representing compressible viscous fluid flow. Originally the designation 'Navier-Stokes equations' was attributed to the momentum equation for viscous incompressible flow, but it has become common, especially in the CFD field, to use this designation for the whole system of equations including the conservation of mass and energy. Supplemented by constitutive laws and thermodynamic equations of the state describing the nature of the fluid, the Navier-Stokes equations completely define the characteristics of compressible viscous flows. In practice, however, the so-called Direct Numerical Simulation (DNS) methods have an important limitation for application to turbulent flow. The time and length scales of turbulence range from almost a molecular motion up to the motion of relatively large vortices (eddies). To capture all these turbulent flow phenomena the spatial and temporal discretizations have to be extremely fine. A less computationally demanding approach (the approximation next to DNS) is the Large Eddy Simulation (LES) which takes into account the large eddies only. The effect of the eddies which are smaller than those captured by the spatial grid is represented by a sub-grid scale model. Even with this sub-grid scale model a large number of grid points is still needed. For most practical problems in aerodynamics the practical use of these two methods is not feasible as yet due to the limited capacity of the available computers, at least at this moment and in the near future.

A straightforward approach for describing turbulent flows is representing the flow variables as the sum of quantities averaged over a certain representative period of time and their fluctuations around this averaged state. The representative period must be long enough compared to that of the turbulent fluctuation, but relatively small compared to the time scale of the unsteady flow phenomena of interest. The equations resulting from substituting this decomposition into the Navier-Stokes equations and subsequently time averaging the equations are referred to as the Reynolds-Averaged Navier-Stokes (RANS) equations for the averaged quantities. The terms in the averaged equations originating from the averaging process of the nonlinear terms need additional relations to close the mathematical model. These relations constitute the so-called turbulence model. Turbulence models are usually developed from theoretical considerations supplemented with empirical relations. Their forms vary from algebraic relations between the turbulence variables and the averaged flow quantities up to a turbulence model involving one or more partial differential equations.

Both the integral form and differential form of the governing equations are used in the present study. First the governing equations in the integral form are presented. The integral form is more fundamental than the differential form since discontinuities may exist in the field where the solution would not be differentiable. Solutions of

---

the integral form of the governing equations which are not differentiable are called *weak solutions*. The differential form of the governing equations is then obtained from the integral form.

The Navier-Stokes equations consist of two scalar equations and one vector equation. The first scalar equation expresses the conservation of mass for the fluid flow in a moving finite control volume  $\Omega$  with  $\partial\Omega$  as the boundary,

$$\frac{\partial}{\partial t} \iiint_{\Omega} \rho dV + \iint_{\partial\Omega} \rho(\mathbf{u} - \dot{\mathbf{x}}) \cdot \mathbf{n} dS = 0, \quad (2.11)$$

where  $\rho$  is the density of the fluid,  $\mathbf{u} = [u, v, w]^T$  is the flow velocity vector and  $\dot{\mathbf{x}} = [\dot{x}, \dot{y}, \dot{z}]^T$  is the the surface velocity vector at the boundary  $\partial\Omega$  of the control volume  $\Omega$ . The vector equation expresses conservation of momentum and is obtained by applying Newton's second law to a moving finite control volume,

$$\frac{\partial}{\partial t} \iiint_{\Omega} \rho \mathbf{u} dV + \iint_{\partial\Omega} \rho \mathbf{u}(\mathbf{u} - \dot{\mathbf{x}}) \cdot \mathbf{n} dS = - \iint_{\partial\Omega} p \mathbf{n} dS + \iint_{\partial\Omega} \boldsymbol{\tau} \cdot \mathbf{n} dS \quad (2.12)$$

where  $p$  is the pressure and  $\boldsymbol{\tau}$  is the viscous stress tensor acting at the boundary of the control volume. Body forces, such as gravitational or electromagnetic forces, are not considered. Finally, conservation of energy, as stated by the first law of thermodynamics, applied to a moving finite control volume leads to:

$$\begin{aligned} \frac{\partial}{\partial t} \iiint_{\Omega} \rho E dV + \iint_{\partial\Omega} \rho E(\mathbf{u} - \dot{\mathbf{x}}) \cdot \mathbf{n} dS = & - \iint_{\partial\Omega} p \mathbf{u} \cdot \mathbf{n} dS + \\ & \iint_{\partial\Omega} (\boldsymbol{\tau} \cdot \mathbf{u}) \cdot \mathbf{n} dS - \iint_{\partial\Omega} \mathbf{q} \cdot \mathbf{n} dS. \end{aligned} \quad (2.13)$$

Here  $E$  is the specific total energy ( $E = e + k$ ),  $e$  is the specific internal energy,  $k = \frac{1}{2}(u^2 + v^2 + w^2)$  is the specific kinetic energy and  $\mathbf{q}$  is the heat flux vector, volumetric heat sources are not considered.

This system of equations still needs supplementary relationships as there are now more variables, i.e.  $\rho$ ,  $\mathbf{u}$ ,  $E$ ,  $p$ ,  $\boldsymbol{\tau}$  and  $\mathbf{q}$ , than the number of equations, i.e. five. For a gas of a fixed composition the thermodynamic state principle states that the complete thermodynamic state is determined by two variables. The other thermodynamic variables then follow from so-called equations of state. For air at normal **temperature and pressure, the perfect gas relation defines the relation between the thermodynamic properties of the flow as the following thermal equations of state:**

$$p = \rho RT, \quad (2.14)$$

where  $T$  is the absolute temperature and  $R$  is the gas constant. In the international unit system (SI)  $R=0.287$  kJ/kgK. For a calorically perfect gas the internal energy and enthalpy are unique functions of temperature, i.e.:

$$\begin{aligned} e &= c_v T \\ h &= c_p T, \end{aligned} \quad (2.15)$$

where  $h$  is the enthalpy,  $c_v$  and  $c_p$  are the specific heat at constant volume and the specific heat at constant pressure, respectively. Both  $c_v$  and  $c_p$  are constant and thus internal energy and enthalpy are linear functions of temperature. Using these relations, the pressure is obtained as:

$$p = (\gamma - 1)\rho e, \quad (2.16)$$

where  $\gamma = c_p/c_v$  is the ratio of the specific heats.

The constitutive equation for heat conduction is the Fourier law:

$$\mathbf{q} = -\kappa \nabla T, \quad (2.17)$$

with  $\kappa$  as the coefficient of thermal conductivity of the gas. For a calorically perfect gas equation (2.17) can be expressed as:

$$\mathbf{q} = -\frac{\gamma\mu}{Pr} \nabla e. \quad (2.18)$$

Here  $\mu$  is the coefficient of viscosity and  $Pr$  is the Prandtl number defined as  $Pr = \mu c_p / \kappa$ . The Prandtl number can be interpreted as the ratio of the diffusivity of the momentum and the diffusivity of the heat. If  $Pr < 1$  the thermal boundary layer is thicker than the velocity boundary layer. For air  $Pr$  is usually assumed to be constant, equal to 0.70.

The stresses,  $\tau$ , can be linearly related to the gradients in the velocity field since the gas is considered to be a Newtonian fluid:

$$\begin{aligned} \tau_{xx} &= \lambda \nabla \cdot \mathbf{u} + 2\mu \frac{\partial u}{\partial x}, & \tau_{xy} &= \tau_{yx} = \mu \left( \frac{\partial v}{\partial x} + \frac{\partial u}{\partial y} \right), \\ \tau_{yy} &= \lambda \nabla \cdot \mathbf{u} + 2\mu \frac{\partial v}{\partial y}, & \tau_{yz} &= \tau_{zy} = \mu \left( \frac{\partial w}{\partial y} + \frac{\partial v}{\partial z} \right), \\ \tau_{zz} &= \lambda \nabla \cdot \mathbf{u} + 2\mu \frac{\partial w}{\partial z}, & \tau_{zx} &= \tau_{xz} = \mu \left( \frac{\partial w}{\partial x} + \frac{\partial u}{\partial z} \right), \end{aligned} \quad (2.19)$$

where  $\lambda$  is the second coefficient of viscosity.  $\mu$  and  $\lambda$  are related through Stokes' theorem namely that the bulk viscosity is zero, i.e.  $\lambda + 2/3\mu = 0$ . The coefficient of viscosity can be accurately approximated using Sutherland's empirical law:

$$\frac{\mu}{\mu_\infty} = \left( \frac{T}{T_\infty} \right)^{\frac{3}{2}} \frac{1 + T_5/T_\infty}{T/T_\infty + T_5/T_\infty}. \quad (2.20)$$

where  $T$  is in Kelvin. The constant,  $T_5 = 110K$ , is known as Sutherland's constant.

By expressing  $p$ ,  $\tau$ ,  $\mu$  and  $\mathbf{q}$  as functions of  $\rho$ ,  $\rho\mathbf{u}$  and  $\rho E$  using equations (2.15) to (2.20), the number of variables is now equal to the number of equations, i.e. two scalars,  $\rho$  and  $\rho E$ , and one vector,  $\rho\mathbf{u}$ .

#### NONDIMENSIONALIZATION AND SIMILARITY PARAMETERS

The development of a solution method for the Navier-Stokes equations in the form of equations (2.11) to (2.20), and the analysis of the results are facilitated by nondimensionalization and introduction of similarity parameters. The solution depends

on five physical parameters: the size of the airfoil (represented by  $c$ ), the freestream velocity ( $\mathbf{u}_\infty$ ), the freestream coefficient of viscosity ( $\mu_\infty$ ), the freestream density ( $\rho_\infty$ ) and the freestream speed of sound ( $a_\infty$ ). According to the so-called Pi theorem [13] the number of similarity parameters which can be defined to completely describe the flow is the number of physical parameters subtracted by the number of fundamental dimensions required to describe the physics. The fundamental dimensions required to describe the physics are mass, length and time (three dimensions). Note that the temperature has been eliminated from the governing equations through the employment of equations (2.14) to (2.18) and equation (2.20). Thus two similarity parameters can be defined. These similarity parameters can be obtained by nondimensionalization of the governing equations.

There are many possibilities for the nondimensionalization where at least three basic nondimensionalization variables have to be chosen (at least equal to the number of the fundamental dimensions required to describe the physics). More than three nondimensionalization variables can be employed, e.g. for convenience, which will introduce proportionality constants. Here  $\rho$ ,  $\mathbf{u}$ ,  $\mathbf{x} = [x, y, z]^T$  and  $\mu$  are used as the basic nondimensionalization parameters with  $\rho_\infty$ ,  $a_\infty$ ,  $c$  and  $\mu_\infty$  as the reference conditions, respectively. In two-dimensional configurations  $c$  represents the chord length, while in three-dimensional configurations it is usually set equal to the root chord. The nondimensionalization parameters for the remaining variables are derived from the main parameters: time by  $c/a_\infty$ , specific energy by  $a_\infty^2$  and pressure by  $\rho_\infty a_\infty^2$ . After this nondimensionalization the Navier-Stokes equations can be written in a matrix form as (using the overbar to indicate dimensionless variables):

$$\frac{\partial}{\partial t} \iiint_{\Omega} \bar{Q} dV + \iint_{\partial\Omega} (\bar{\mathbf{F}}^I - \bar{Q}\hat{\mathbf{x}}) \cdot \mathbf{n} dS = \iint_{\partial\Omega} \bar{\mathbf{F}}^V \cdot \mathbf{n} dS, \quad (2.21)$$

where  $\bar{Q}$  is the vector of conservative variables<sup>1</sup>,  $\bar{\mathbf{F}}^I$  and  $\bar{\mathbf{F}}^V$  are the inviscid and viscous flux vectors, respectively. In a Cartesian coordinate system the vector of conservative variables is:

$$\bar{Q} = \begin{bmatrix} \bar{\rho} \\ \bar{\rho}\bar{u} \\ \bar{\rho}\bar{v} \\ \bar{\rho}\bar{w} \\ \bar{\rho}\bar{E} \end{bmatrix}, \quad (2.22)$$

while the inviscid fluxes are:

$$\bar{\mathbf{F}}_x^I = \begin{bmatrix} \bar{\rho}\bar{u} \\ \bar{\rho}\bar{u}^2 + \bar{p} \\ \bar{\rho}\bar{u}\bar{v} \\ \bar{\rho}\bar{u}\bar{w} \\ (\bar{\rho}\bar{E} + \bar{p})\bar{u} \end{bmatrix} \quad \bar{\mathbf{F}}_y^I = \begin{bmatrix} \bar{\rho}\bar{v} \\ \bar{\rho}\bar{v}\bar{u} \\ \bar{\rho}\bar{v}^2 + \bar{p} \\ \bar{\rho}\bar{v}\bar{w} \\ (\bar{\rho}\bar{E} + \bar{p})\bar{v} \end{bmatrix} \quad \bar{\mathbf{F}}_z^I = \begin{bmatrix} \bar{\rho}\bar{w} \\ \bar{\rho}\bar{w}\bar{u} \\ \bar{\rho}\bar{w}\bar{v} \\ \bar{\rho}\bar{w}^2 + \bar{p} \\ (\bar{\rho}\bar{E} + \bar{p})\bar{w} \end{bmatrix}. \quad (2.23)$$

<sup>1</sup>Note that although  $\bar{Q}$  is introduced here as a vector, its symbol is indicated by a normal letter to distinguish it from a spatial vector which has components in the coordinate directions.

The viscous fluxes are:

$$\bar{F}_x^V = \begin{bmatrix} 0 \\ \bar{\tau}_{xx} \\ \bar{\tau}_{yx} \\ \bar{\tau}_{zx} \\ \bar{u}\bar{\tau}_{xx} + \bar{v}\bar{\tau}_{xy} + \bar{w}\bar{\tau}_{xz} - \bar{q}_x \end{bmatrix}, \quad \bar{F}_y^V = \begin{bmatrix} 0 \\ \bar{\tau}_{xy} \\ \bar{\tau}_{yy} \\ \bar{\tau}_{zy} \\ \bar{u}\bar{\tau}_{yx} + \bar{v}\bar{\tau}_{yy} + \bar{w}\bar{\tau}_{yz} - \bar{q}_y \end{bmatrix} \quad (2.24)$$

and:

$$\bar{F}_z^V = \begin{bmatrix} 0 \\ \bar{\tau}_{xz} \\ \bar{\tau}_{yz} \\ \bar{\tau}_{zz} \\ \bar{u}\bar{\tau}_{zx} + \bar{v}\bar{\tau}_{zy} + \bar{w}\bar{\tau}_{zz} - \bar{q}_z \end{bmatrix}. \quad (2.25)$$

The stresses are:

$$\begin{aligned} \bar{\tau}_{xx} &= \frac{\bar{\mu}}{\hat{Re}_\infty} \left( 2 \frac{\partial \bar{u}}{\partial \bar{x}} - \frac{2}{3} \nabla \cdot \bar{\mathbf{u}} \right) & \bar{\tau}_{xy} = \bar{\tau}_{yx} &= \frac{\bar{\mu}}{\hat{Re}_\infty} \left( \frac{\partial \bar{v}}{\partial \bar{x}} + \frac{\partial \bar{u}}{\partial \bar{y}} \right), \\ \bar{\tau}_{yy} &= \frac{\bar{\mu}}{\hat{Re}_\infty} \left( 2 \frac{\partial \bar{v}}{\partial \bar{y}} - \frac{2}{3} \nabla \cdot \bar{\mathbf{u}} \right) & \bar{\tau}_{yz} = \bar{\tau}_{zy} &= \frac{\bar{\mu}}{\hat{Re}_\infty} \left( \frac{\partial \bar{w}}{\partial \bar{y}} + \frac{\partial \bar{v}}{\partial \bar{z}} \right), \\ \bar{\tau}_{zz} &= \frac{\bar{\mu}}{\hat{Re}_\infty} \left( 2 \frac{\partial \bar{w}}{\partial \bar{z}} - \frac{2}{3} \nabla \cdot \bar{\mathbf{u}} \right) & \bar{\tau}_{zx} = \bar{\tau}_{xz} &= \frac{\bar{\mu}}{\hat{Re}_\infty} \left( \frac{\partial \bar{u}}{\partial \bar{z}} + \frac{\partial \bar{w}}{\partial \bar{x}} \right), \end{aligned} \quad (2.26)$$

and the heat flux vector is:

$$\bar{\mathbf{q}} = -\frac{\gamma \bar{\mu}}{Pr \hat{Re}_\infty} \nabla \bar{e}. \quad (2.27)$$

The freestream Reynolds number based on the speed of sound,  $\hat{Re}_\infty$ , is defined as  $\rho_\infty a_\infty c / \mu_\infty = Re_\infty / M_\infty$  and the Mach number as  $M_\infty = U_\infty / a_\infty$  with  $U_\infty = |\mathbf{u}_\infty|$ . The Reynolds number represents the ratio between the inertial force and the viscous force. The Mach number measures the compressibility of the flow. Note that the similarity analysis could have been started already directly after equation (2.19), excluding equations (2.16) and (2.18). Then the number of physical parameters had to be extended with  $c_p$ ,  $c_v$ ,  $\kappa$  and  $T_5$  and the fundamental dimension by  $T$ . The analysis would have yielded the ratio of specific heats ( $\gamma$ ), Prandtl number ( $Pr$ ) and ( $\theta_5 = T_5 / T_\infty$ ) as the additional similarity parameters.

The viscosity coefficient is obtained directly from the dimensionless Sutherland law, equation (2.20). The temperature can be calculated using equation (2.14) as  $T / T_\infty = \bar{a}^2$ . The dimensionless freestream values of various flow quantities are tabulated in table 2.2, where  $\alpha$  is the angle of attack. Note that in the present study the side slip angle  $\beta$  is assumed to be zero, so that a  $y$ - $z$  symmetry plane can be defined and only a half three-dimensional space needs to be considered. The extension to cases with a nonzero side-slip angle needs only a minor modification.

flow quantity	symbol	freestream value
density	$\bar{\rho}_\infty$	1
speed of sound	$\bar{a}_\infty$	1
coefficient of viscosity	$\bar{\mu}_\infty$	1
$x$ component of velocity	$\bar{u}_\infty$	$M_\infty \cos \alpha$
$y$ component of velocity	$\bar{v}_\infty$	0
$z$ component of velocity	$\bar{w}_\infty$	$M_\infty \sin \alpha$
static pressure	$\bar{p}_\infty$	$1/\gamma$
internal energy	$\bar{e}_\infty$	$\bar{p}_\infty/(\gamma - 1)$
total energy	$\bar{E}_\infty$	$\bar{e}_\infty + \frac{1}{2}M_\infty^2$

Table 2.2: Dimensionless value of flow variables at freestream condition

### GEOMETRIC CONSERVATION LAW

The appearance of a control volume surface velocity,  $\dot{\mathbf{x}}$ , in equation (2.21) is of importance since a deforming computational flow domain will be treated. The moving control volume surface should not disturb the physics which is modeled by the governing equations. This requirement can be checked easily by realizing that the freestream condition should be a solution of equation (2.21). This requirement is called the freestream consistency check, see e.g. [121, 165].

Consider first the steady part of equation (2.21) applied to the freestream condition:

$$(\bar{\mathbf{F}}_\infty^I - \bar{\mathbf{F}}_\infty^V) \cdot \iint_{\partial\Omega} \mathbf{n} dS = 0, \quad (2.28)$$

which results in the first geometrical identity:

$$\iint_{\partial\Omega} \mathbf{n} dS = 0. \quad (2.29)$$

The other geometrical identity is obtained by applying the unsteady equation to the freestream condition:

$$\bar{Q}_\infty \frac{\partial}{\partial t} \iiint_{\Omega} dV - \bar{Q}_\infty \iint_{\partial\Omega} \dot{\mathbf{x}} \cdot \mathbf{n} dS + (\bar{\mathbf{F}}_\infty^I - \bar{\mathbf{F}}_\infty^V) \cdot \iint_{\partial\Omega} \mathbf{n} dS = 0, \quad (2.30)$$

which results in the second geometrical identity, known as the Geometric Conservation Law (GCL) in an integral form:

$$\frac{\partial}{\partial t} \iiint_{\Omega} dV - \iint_{\partial\Omega} \dot{\mathbf{x}} \cdot \mathbf{n} dS = 0. \quad (2.31)$$

Essentially, equation (2.29) is the requirement that the control volume is closed and equation (2.31) is the requirement that the rate of change of the volume is balanced by the velocity of the surface of the control volume, see figure 2.3. Equation (2.29) and equation (2.31) have to be satisfied simultaneously with solving equation (2.21) to avoid the occurrence of nonphysical sources in the method. Note that for a steady flow method, involving a fixed mesh, only equation (2.29) has to be satisfied.

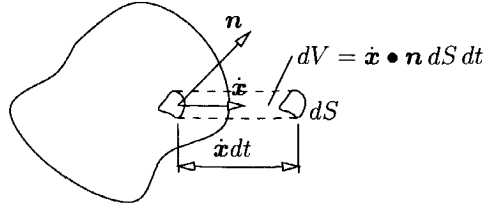


Figure 2.3: Change of control volume due to the motion of a surface element of the control volume

### DIFFERENTIAL FORM OF THE NAVIER-STOKES EQUATIONS

The surface integrals in equation (2.21) can be converted into volume integrals, using Gauss's theorem:

$$\iiint_{\Omega} \left( \frac{\partial \bar{Q}}{\partial t} + \nabla \cdot \bar{\mathbf{F}}^I \right) dV + \iiint_{\Omega} \bar{Q} \frac{\partial dV}{\partial t} - \iint_{\partial\Omega} \bar{Q} \dot{\mathbf{x}} \cdot \mathbf{n} dS = \iiint_{\Omega} \nabla \cdot \bar{\mathbf{F}}^V dV. \quad (2.32)$$

The second and third integrals on the left-hand side cancel out according to the GCL. Since the control volume element is arbitrary, equation (2.32) can also be applied to a differential element resulting in the differential form of the Navier-Stokes equations:

$$\frac{\partial \bar{Q}}{\partial t} + \nabla \cdot \bar{\mathbf{F}}^I = \nabla \cdot \bar{\mathbf{F}}^V. \quad (2.33)$$

For the sake of convenience the overbars of all variables are dropped and all variables represent from now on the dimensionless variables.

### REYNOLDS-AVERAGED NAVIER-STOKES EQUATIONS

For turbulent flow the Navier-Stokes equations are averaged in time. The set of equations for the time-averaged Navier-Stokes equations is obtained by defining a flow variable  $f$  as the sum of its average value and its fluctuation. The formal definition of the time-averaging is:

$$\begin{aligned} f(x, y, z, t) &= \lim_{T \rightarrow \infty} \frac{1}{T} \int_{-T/2}^{T/2} f(x, y, z, t + \tau) d\tau + f'(x, y, z, t) \\ &= \bar{f}(x, y, z, t) + f'(x, y, z, t). \end{aligned} \quad (2.34)$$

In practice a finite value is taken for  $T$  and the time-averaging process is valid if the time scale of the simulated unsteady flow phenomena remains large compared to  $T$ . For compressible flow the mass-weighted, the so-called Favre-averaging, is introduced as:

$$\begin{aligned} f(x, y, z, t) &= \frac{\overline{\rho(x, y, z, t) f(x, y, z, t)}}{\bar{\rho}(x, y, z, t)} + f''(x, y, z, t), \\ &= \bar{f}(x, y, z, t) + f''(x, y, z, t), \end{aligned} \quad (2.35)$$

in order to simplify the resulting equations. The final form of the equations is obtained by applying the time-averaging, equation (2.34), to  $\rho$  and  $p$ , applying the Favre-averaging, equation (2.35), to  $\mathbf{u}$  and  $E$  and subsequently time-averaging the equations. The resulting equations will contain the so-called Reynolds stresses which are expressed as functions of the averaged variables using the Boussinesq's approximation. The detailed derivation of the equations for turbulent flow may be found in Appendix A. The result is summarized here:

$$\frac{\partial Q}{\partial t} + \nabla \cdot \mathbf{F}^I = \nabla \cdot \mathbf{F}^V, \quad (2.36)$$

where the conservative variables and inviscid fluxes are (and note that the overbars have now the meaning of time-average values, as defined by equation (2.34)):

$$Q = \begin{bmatrix} \bar{\rho} \\ \bar{\rho}\bar{u} \\ \bar{\rho}\bar{v} \\ \bar{\rho}\bar{w} \\ \bar{\rho}\bar{E} \end{bmatrix}, \quad \mathbf{F}_x^I = \begin{bmatrix} \bar{\rho}\bar{u} \\ \bar{\rho}\bar{u}^2 + \bar{p} + \frac{2}{3}\bar{\rho}k \\ \bar{\rho}\bar{u}\bar{v} \\ \bar{\rho}\bar{u}\bar{w} \\ (\bar{\rho}\bar{E} + \bar{p} + \frac{2}{3}\bar{\rho}k)\bar{u} \end{bmatrix} \quad (2.37)$$

$$\mathbf{F}_y^I = \begin{bmatrix} \bar{\rho}\bar{v} \\ \bar{\rho}\bar{v}\bar{u} \\ \bar{\rho}\bar{v}^2 + \bar{p} + \frac{2}{3}\bar{\rho}k \\ \bar{\rho}\bar{v}\bar{w} \\ (\bar{\rho}\bar{E} + \bar{p} + \frac{2}{3}\bar{\rho}k)\bar{v} \end{bmatrix}, \quad \mathbf{F}_z^I = \begin{bmatrix} \bar{\rho}\bar{w} \\ \bar{\rho}\bar{w}\bar{u} \\ \bar{\rho}\bar{w}\bar{v} \\ \bar{\rho}\bar{w}^2 + \bar{p} + \frac{2}{3}\bar{\rho}k \\ (\bar{\rho}\bar{E} + \bar{p} + \frac{2}{3}\bar{\rho}k)\bar{w} \end{bmatrix}. \quad (2.38)$$

The turbulent viscous fluxes are,

$$\mathbf{F}_x^V = \begin{bmatrix} 0 \\ \tau_{xx} \\ \tau_{yx} \\ \tau_{zx} \\ \bar{u}\tau_{xx} + \bar{v}\tau_{xy} + \bar{w}\tau_{xz} - q_x \end{bmatrix}, \quad \mathbf{F}_y^V = \begin{bmatrix} 0 \\ \tau_{xy} \\ \tau_{yy} \\ \tau_{zy} \\ \bar{u}\tau_{yx} + \bar{v}\tau_{yy} + \bar{w}\tau_{yz} - q_y \end{bmatrix} \quad (2.39)$$

and

$$\mathbf{F}_z^V = \begin{bmatrix} 0 \\ \tau_{xz} \\ \tau_{yz} \\ \tau_{zz} \\ \bar{u}\tau_{zx} + \bar{v}\tau_{zy} + \bar{w}\tau_{zz} - q_z \end{bmatrix}. \quad (2.40)$$

The stresses are:

$$\begin{aligned} \tau_{xx} &= \frac{\mu_T}{\hat{Re}_\infty} \left( 2 \frac{\partial \bar{u}}{\partial x} - \frac{2}{3} \nabla \cdot \bar{\mathbf{u}} \right) & \tau_{xy} = \tau_{yx} &= \frac{\mu_T}{\hat{Re}_\infty} \left( \frac{\partial \bar{v}}{\partial x} + \frac{\partial \bar{u}}{\partial y} \right), \\ \tau_{yy} &= \frac{\mu_T}{\hat{Re}_\infty} \left( 2 \frac{\partial \bar{v}}{\partial y} - \frac{2}{3} \nabla \cdot \bar{\mathbf{u}} \right) & \tau_{yz} = \tau_{zy} &= \frac{\mu_T}{\hat{Re}_\infty} \left( \frac{\partial \bar{w}}{\partial y} + \frac{\partial \bar{v}}{\partial z} \right), \\ \tau_{zz} &= \frac{\mu_T}{\hat{Re}_\infty} \left( 2 \frac{\partial \bar{w}}{\partial z} - \frac{2}{3} \nabla \cdot \bar{\mathbf{u}} \right) & \tau_{zx} = \tau_{xz} &= \frac{\mu_T}{\hat{Re}_\infty} \left( \frac{\partial \bar{u}}{\partial z} + \frac{\partial \bar{w}}{\partial x} \right), \end{aligned} \quad (2.41)$$



and the heat flux vector is:

$$\mathbf{q} = -\frac{\mu_T}{\hat{Re}_\infty} \frac{\gamma(\mu Pr_T + \mu_E Pr)}{Pr Pr_T(\mu + \mu_E)} \nabla \tilde{e}, \quad (2.42)$$

where  $\mu_T = \mu + \mu_E$ , with  $\mu_E$  being the eddy viscosity coefficient. Note that an overbar is used to designate time averaged variables, defined by equation (2.34), and a tilde is used to designate mass-weighted averaged variables, defined by equation (2.35). It can be seen that the governing equations for the averaged flow quantities have exactly the same form as the original equations except that the flow variables are now,  $\bar{\rho}$  for the density,  $\tilde{\mathbf{u}}$  for the velocity,  $\tilde{E}$  for the total energy,  $\tilde{p} = \bar{p} + \frac{2}{3}\bar{\rho}k$  for the pressure and the coefficient of viscosity is replaced by its turbulent value.

Again the tildes and overbars are dropped for convenience and from now on the flow variables represent time and mass-weighted averaged values, respectively, when dealing with turbulent flow.

### INVISCID COMPRESSIBLE FLOW

The system of equations governing inviscid compressible flow is, like the Navier-Stokes equations, named after its momentum equation namely the Euler equations. They are obtained by neglecting the viscous and heat-conducting terms in equation (2.33):

$$\frac{\partial Q}{\partial t} + \nabla \cdot \mathbf{F}^I = 0. \quad (2.43)$$

There are two important mathematical properties of the Euler equations: the hyperbolic character of the unsteady Euler equations and the existence of discontinuities in the solution, i.e. shock waves, vortex sheets and contact discontinuity surfaces. The latter property is in contrast with the Navier-Stokes equations where in principle the density, pressure and velocity fields are continuous due to the presence of elliptic viscosity and heat conduction terms. The numerical methods to solve the system of Euler equations are based on these mathematical properties.

The hyperbolic character of the Euler equations is demonstrated by the existence of wave-like solutions in the form of, see e.g. Hirsch [76]:

$$Q(\mathbf{x}, t) = \hat{Q} e^{i(\mathbf{n} \cdot \mathbf{x} - \omega t)}, \quad (2.44)$$

where  $i = \sqrt{-1}$ ,  $\mathbf{x}$  is the position vector and  $\mathbf{n}$  is a vector normal to the wave front surface (surface which separates the region which has been and the one which has not been influenced by the wave). Substitution of equation (2.44) into the Euler equations in the so-called quasi-linear form,

$$\frac{\partial Q}{\partial t} + \mathbf{A}^I \cdot \nabla Q = 0, \quad \text{where} \quad \mathbf{A}^I = \frac{\partial \mathbf{F}^I}{\partial Q}, \quad (2.45)$$

yields the condition for a nontrivial solution of  $\hat{Q}$ , which is  $|\omega I - \mathbf{A}^I \cdot \mathbf{n}| = 0$ . The condition for hyperbolicity then is the existence of real eigenvalues of the Jacobian

$\mathbf{A}^I \cdot \mathbf{n}$ . It is shown in appendix B that the eigenvalues are indeed all real. This means that the eigenvalues represent the speed of propagation of the waves in the direction of  $\mathbf{n}$ . This information is very important in discretizing the governing equations because the domain of dependence of the discrete equations has to cover the domain of dependence of the continuous equations.

It was already mentioned that the governing equations in an integral conservation form allow weak solutions containing discontinuities to exist. When the Euler equations in integral form are applied across a moving surface of discontinuity they become:

$$([\mathbf{F}^I] - \mathbf{C}[Q]) \cdot \mathbf{n}_{\text{disc}} = 0, \quad (2.46)$$

where  $[\cdot]$  represents a jump across a surface of discontinuity,  $\mathbf{C}$  is the velocity of the surface of discontinuity and  $\mathbf{n}_{\text{disc}}$  is the normal to the surface of discontinuity. Equation (2.46) relates two states separated by the surface of discontinuity. For a more detailed discussion, see [76]. Equation (2.46) is known as the Rankine-Hugoniot relation in which  $\mathbf{c}$  represents the velocity of the discontinuity surface. Satisfaction of this jump condition ensures the correct position and strength of the discontinuity. Thus it is very important that the discretized Euler equations render this same property across discontinuities. The discretized equations in a nonconservation form do not have this property, which makes the nonconservation form invalid to use in flows containing discontinuities, or alternatively the jump condition, i.e. equation (2.46), has to be introduced explicitly across the discontinuities.

### 2.5.3 BOUNDARY CONDITIONS

Boundary conditions have to be imposed in order to obtain a well-posed problem. Since the Navier-Stokes equations and the Euler equations represent problems of propagating waves (in the case of the Euler equations the waves are undamped, while in the case of the Navier-Stokes equations the waves are damped by the diffusive terms), the information concerning the direction of propagation of the waves plays a very important role in determining the correct boundary conditions. This can be illustrated using a simple scalar model of the Euler equations, i.e. consider

$$\frac{\partial u}{\partial t} + \frac{\partial f}{\partial x} = 0, \quad (2.47)$$

with the flux function  $f = cu$  and  $c$  a positive constant, which is solved in the domain of  $x = [0, 1]$  and  $t \geq 0$ , see figure 2.4. The solution of equation (2.47) represents a right running wave with velocity  $c$ ,  $u(x, t) = u(x - ct)$  with  $c$  as the characteristic direction. Thus it is clear that a point in the domain is influenced only by the part of the domain which resides on the left side of this point. For example, see figure 2.4,  $u(x_B, t_B)$  depends on  $u(x_A, t_A)$  or precisely  $u(x_B, t_B) = u(x_A, t_A)$ . Consequently, at  $x = 0$  a boundary condition has to be specified at all time, while specifying a boundary condition at  $x = 1$  will violate the nature of the problem. Instead, to obtain the value at  $x = 1$  one has to extrapolate  $u$  from the domain towards  $x = 1$ .

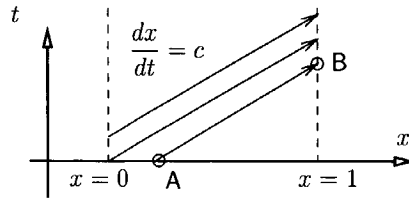


Figure 2.4: Space-time plot on one-dimensional wave propagation

For a system of hyperbolic equations, i.e. the Euler equations, there is more than one wave. By examining the eigenvalues of the Euler equations the direction of propagation of each wave can be determined. At the boundary a value associated with each wave can then be specified or extrapolated depending on the sign of the corresponding eigenvalue.

#### FAR-FIELD BOUNDARY

To set up a proper condition at the far-field boundary the direction of propagation of the waves is identified. To facilitate this identification the Euler equations are expressed in the characteristic variables on the  $[\mathbf{l}, \mathbf{m}, \mathbf{n}]$  coordinate system with  $\mathbf{n}$  normal to the boundary surface pointing outward. Assuming homentropic flow, i.e. a uniform entropy everywhere, the Euler equations become:

$$\begin{aligned}
 \frac{\partial R_1}{\partial t} + \lambda_1 \cdot \nabla R_1 &= 0 \\
 \frac{\partial R_2}{\partial t} + \lambda_2 \cdot \nabla R_2 &= -\frac{1}{\rho}(\mathbf{l} \cdot \nabla)p \\
 \frac{\partial R_3}{\partial t} + \lambda_3 \cdot \nabla R_3 &= -\frac{1}{\rho}(\mathbf{m} \cdot \nabla)p \\
 \frac{\partial R_4}{\partial t} + \lambda_4 \cdot \nabla R_4 &= -a\mathbf{l} \cdot (\mathbf{l} \cdot \nabla)\mathbf{u} - a\mathbf{m} \cdot (\mathbf{m} \cdot \nabla)\mathbf{u} \\
 \frac{\partial R_5}{\partial t} + \lambda_5 \cdot \nabla R_5 &= a\mathbf{l} \cdot (\mathbf{l} \cdot \nabla)\mathbf{u} + a\mathbf{m} \cdot (\mathbf{m} \cdot \nabla)\mathbf{u}.
 \end{aligned} \tag{2.48}$$

where  $\lambda = [\mathbf{u}, \mathbf{u}, \mathbf{u}, \mathbf{u} + a\mathbf{n}, \mathbf{u} - a\mathbf{n}]^T$ ,  $a$  is the local speed of sound,  $R = [s, u_l, u_m, R^+, R^-]^T$ ,  $s$  is the entropy,  $\mathbf{l}$  and  $\mathbf{m}$  are the tangential vectors perpendicular to the normal vector at the boundary ( $\mathbf{n}$ ),  $u_l = \mathbf{u} \cdot \mathbf{l}$  and  $u_m = \mathbf{u} \cdot \mathbf{m}$  are the tangential components of the flow velocity and  $R^\pm = u_n \pm 2a/(\gamma - 1)$ .  $R$  is called the Riemann variable. Equations (2.48) are usually referred to as the compatibility equations. The right-hand side of the first equation is zero, which means that  $s$  is invariant in the direction  $d\mathbf{n}/dt = \mathbf{u}$ . The other equations have nonzero right-hand sides, but if the far-field boundary is set to a constant freestream condition, the right-hand sides will also be zero, leaving  $u_l$ ,  $u_m$ ,  $R^+$  and  $R^-$  invariant along the associated paths.

At the boundary the direction of propagation of each Riemann variable can be decomposed into a normal and a tangential direction. The tangential direction

carries information which does not enter nor leave the domain, while the normal direction of propagation carries information which effectively enters or leaves the domain. Since the direction of propagation of the waves is represented by the sign of the eigenvalues of the Jacobian of the flux, i.e.  $\lambda$ , the boundary conditions are determined by examining locally the eigenvalues of the flux normal to the boundary.

Here a simple technique is adopted to calculate the boundary values. When a wave leaves the domain, the associated Riemann variable at the boundary is obtained by extrapolation. When a wave propagates into the domain, the associated Riemann variable takes the freestream value. Note that this approach will satisfy the non-reflecting condition if the flow at the boundary is close to the freestream condition. The possible cases are then:

- subsonic  $|u_n| < a$ 
  - inflow  $u_n < 0$ :  $s$ ,  $u_m$  and  $u_l$  are set to their freestream values and since  $u_n + a > 0$  and  $u_n - a < 0$  the  $R^+$  is extrapolated from inside the domain to the boundary and  $R^-$  takes the freestream value.
  - outflow  $u_n > 0$ :  $s$ ,  $u_l$  and  $u_m$  are extrapolated from the values inside the domain to the boundary and again since  $u_n + a > 0$  and  $u_n - a < 0$  the  $R^+$  is extrapolated from inside the domain to the boundary and  $R^-$  takes the freestream value.
- supersonic  $|u_n| > a$ 
  - inflow  $u_n < 0 < -a$ : all eigenvalues are negative, all variables are set at the freestream values.
  - outflow  $u_n > 0 > a$ : all eigenvalues are positive, all variables are extrapolated from the the values inside the domain towards the boundary.

Note that in the supersonic case conservative variables, see equation (2.22) may be used directly rather than the Riemann variables.

Since equations (2.48) are not valid across discontinuities, as they were derived using the assumption of infinitesimal wave amplitude and homentropic flow, shock waves and other discontinuities may not be present at the boundary.

The above boundary condition holds formally for the Euler equations. The boundary conditions for the Navier-Stokes equations are less clear than those for the Euler equations. **Although the equation for the conservation of mass is still hyperbolic the second-order diffusive terms in the momentum and energy equations introduce elliptic behavior with respect to the space coordinates, which suggests a Dirichlet type condition at the boundary.** Usually it is hypothesized that far from the airfoil the viscous terms become vanishingly small and the boundary conditions for the Euler equations remain valid. However, this assumption can not be applied for the far-field condition downstream of a solid body where the wake shear layers are present. Nordstrom [120] suggested to extrapolate all variables at the downstream outflow for a time-dependent Navier-Stokes calculation when sufficiently large transverse gradients of the velocity are present.

## SOLID BOUNDARY

For the Euler equations the normal velocity at a solid boundary is set to zero in agreement with the slip boundary condition. This implies that only one eigenvalue is positive so that only one variable may be prescribed, viz. the normal velocity. The other three variables have to be extrapolated from the interior of the flow domain to the surface. In the present study the method of the normal momentum equation due to Rizzi [142], modified to account for the moving boundary, is used to obtain the pressure at the surface. The tangential velocity and density are obtained by extrapolation.

In viscous flow problems the no-slip condition is applied implying that the velocity is zero at the surface. The density is obtained either via a constant temperature condition at the wall or by specifying the heat flux at the wall. For the constant temperature condition usually the stagnation temperature is taken which leads to the condition for the dimensionless speed of sound as:

$$a_{\text{wall}} = \sqrt{1 + \frac{\gamma - 1}{2} M_{\infty}^2}, \quad (2.49)$$

while in case the heat flux boundary condition is applied, one has:

$$-\kappa \frac{\partial T}{\partial \mathbf{n}} = \mathbf{q}_{n \text{ wall}}.$$

For an adiabatic wall the heat flux  $q_{\text{wall}}$  is set equal to zero leading to the following relation at the wall:

$$\frac{1}{\rho} \frac{\partial \rho}{\partial \mathbf{n}} = \frac{\partial p}{\partial \mathbf{n}}. \quad (2.50)$$



## CHAPTER 3

# SOLUTION OF UNSTEADY NAVIER-STOKES EQUATIONS FOR FLOW PAST AIRFOILS

For most of the problems in practice requiring the solution of the Navier-Stokes equations a numerical approach is the only obvious way. The two main reasons for that are the nonlinearity of the equations and the often arising geometrical complexity in the application. This chapter presents the approach taken to solve the Navier-Stokes equations for the unsteady flow past stationary and oscillating airfoils. Various results are also presented to establish the validity of the method and to demonstrate its capability.

The usual building blocks of a method to solve numerically the unsteady Navier-Stokes equations are: the construction of the mesh, the spatial discretization and the temporal integration. The methods studied for each of them were selected here mainly on the basis of efficiency in aeroelastic simulations. From the author's experience, in a cooperation with NLR, gained in solving the full-potential equation [77, 79, 131] and considering the literature survey in the previous chapter, some general directives can be identified:

- An implicit method is applied for the temporal integration due to its favorable numerical stability characteristics. The method should have at least second-order accuracy in time because simulations with large time step are desired. One-step implicit methods, which solve a linearized equation at each time step, show lack of accuracy for large time steps. Therefore an implicit method which solves the nonlinear unsteady equation using a subiteration scheme should be applied;
- It has been identified that there are two possible temporal integration methods which can be applied for the present study: dual-time stepping method with explicit subiterations and implicit method employing relaxations. It has been known that acceleration methods, i.e. multigrid, implicit residual smoothing, and local time stepping, are indispensable for efficient methods employing explicit subiterations. On the other hand, a basic implicit method employing a simple relaxation scheme usually gives already satisfactory efficiency, provided the relaxation matrix/Jacobian is carefully designed. This advantage

outweighs the complexity commonly referred to in the implementation of an implicit method. Application of a multigrid method for an implicit method will improve further its efficiency. Furthermore, with the fast development of acceleration techniques for implicit methods, like conjugate gradient-based methods, a further development of an implicit method appears to be still open. Therefore, an implicit subiteration method employing a relaxation scheme is preferred and should be applied. Acceleration methods will not be applied in the present study and are left for future research;

- Since flows at high Reynolds number are considered the viscous effects will be concentrated in thin shear layers close to the solid surface. The Thin-Layer approximation of the Navier-Stokes equations (TLNS) is therefore valid and should be applied because it will simplify the numerical method considerably;
- A structured mesh method should be applied for the following reasons. (a) Given the application of an implicit method, the ordered structure of the Jacobian matrix in a structured mesh method will facilitate the application of various relaxation schemes. (b) The implementation of the thin-layer approximation of the viscous terms is trivial in a structured mesh method. (c) A quasi-one-dimensional upwind method is employed in the present study. The mesh dependency of a quasi-one-dimensional method is likely to be less severe in the case of a structured mesh method than for an unstructured mesh method, provided that the mesh topology is carefully selected. In this case the mesh orientation should be chosen to align with the direction of propagation of the dominant waves.

In the following sections, some basic discretization aspects of the unsteady Euler/Navier-Stokes equations for flows with shock waves are presented, followed by the discussion of the computational mesh handling for moving boundaries and the transformation of the governing equations from the physical domain into the computational domain. Subsequently the solution methods: spatial discretization and temporal integration are presented.

### 3.1 DISCRETIZATION ASPECTS OF UNSTEADY FLOW WITH SHOCK WAVES

Two important aspects in developing a shock-capturing method are: ensuring a **correct shock position and shock strength** and **preventing the spurious subgrid frequency components** due to discontinuities (for which additional numerical dissipation to damp the oscillations is required). These basic aspects, considered here for unsteady flow problems, are discussed in the following sections.

#### 3.1.1 ENSURING PROPER SHOCK POSITION AND SHOCK STRENGTH

It was shown by Lax [99] that a proper shock strength and shock location can be computed using the conservation form of the governing equations. In steady flow calculations this means maintaining conservation of the spatial discretization.

---



In calculations of the more general unsteady flows, which might include a moving mesh, also the temporal coordinate has to be taken into account.

Consider the Euler equations in the integral form, i.e. the inviscid part of equation (2.32). Treating the temporal coordinate in a similar manner as the spatial coordinates, and applying the Gauss' integral theorem, one obtains:

$$\iiint_{\tilde{\Omega}} \nabla' \cdot \tilde{\mathbf{F}}^I d\tilde{V} = \iint_{\partial\tilde{\Omega}} \tilde{\mathbf{F}}^I \cdot \tilde{\mathbf{n}} d\tilde{S} = 0, \quad (3.1)$$

where  $\nabla'$  is a nabla operator for a space-time coordinate system and  $\tilde{\mathbf{F}}^I$  is the flux including the conservative variable which acts in the temporal direction as  $\tilde{\mathbf{F}}^I = [Q, F_x^I, F_y^I, F_z^I]^T$ . A conservative discretization for general unsteady flow cases implies maintaining the conservation property of equation (3.1). Discretizing equation (3.1) in a conservative manner includes the satisfaction of the GCL which was introduced in equation (2.32).

The effect of the conservation property for a deforming mesh can be seen clearly from figure 3.1, which for clarity shows a one-dimensional flow problem.

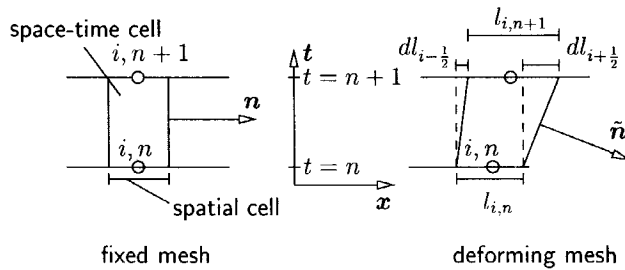


Figure 3.1: Volume elements for fixed and deformed mesh

The normal direction of the space-time cell for the fixed mesh and hence the flux component  $Qe_x$  remains perpendicular to the temporal axis, whereas for the deforming mesh a component in the temporal axis appears so that the flux component  $Qe_t$  has to be taken into account. The GCL condition, equation (2.31), in this one-dimensional case can also be seen from figure 3.1, and is simply:

$$\frac{l_{i,n+1} - l_{i,n}}{\Delta t} = \frac{dl_{i+1/2}}{\Delta t} - \frac{dl_{i-1/2}}{\Delta t}. \quad (3.2)$$

The detailed application of the GCL in the calculation of two-dimensional flows using the Navier-Stokes equations will be presented in section 3.3.

### 3.1.2 PREVENTING THE SPURIOUS SUBGRID FREQUENCY COMPONENTS

Considering the solution of the flow equations as decomposable into frequency components, a shock discontinuity can be related typically to the high-frequency components of the solution. However, a discrete system represented by a finite number

of mesh points is able to support only a finite number of frequencies ( $\lambda_{\min} = 2\Delta$ ,  $\lambda_{\max} = 2N\Delta$ , where  $\lambda$  is the wave length,  $\Delta$  is a typical measure of the mesh size and  $N$  is the number of mesh points). Hence, the components contained in a solution with a frequency higher than the highest supported frequency can not be represented by the discrete system. These components will appear as lower frequencies through aliasing. High-frequency components are continuously produced when shock waves occur in the solution. Those which can not be accommodated by the mesh are called subgrid components. They may harm the overall solution if they are not carefully considered.

In central difference methods of Beam and Warming [26], Jameson et al. [91] a diffusive term is explicitly added to the discretized equations to prevent the subgrid components affecting the solution. The diffusive term has a user-specified scalar artificial viscosity coefficient. In upwind methods, the hyperbolic character of the Euler equations is exploited to arrive at a stable scheme enabling oscillation-free solutions (also called monotonic), see Hussaini et al. [84]. The resulting schemes, in a certain sense, are similar to the schemes with explicit artificial viscosity, but now with the coefficient in the form of a matrix.

## 3.2 COMPUTATIONAL MESH

The aspects concerning the mesh for an unsteady flow calculation are the topology of the mesh, the initial mesh generator and the treatment of the mesh when the boundaries move. In the present study a standard algebraic-elliptic method is used to generate the initial mesh. To deform the mesh in order to follow the moving boundaries an elliptic method is introduced and the spring analogy method of Batina [24] is modified to enable the method to handle large deformations.

### 3.2.1 MESH TOPOLOGY

The choice for the topology of the mesh should not only be based on the geometrical features, but also on the expected solution (the flow features). In viscous flow boundary layers are generated along solid surfaces which continue as a wake upon leaving the airfoil at the trailing edge. These thin shear layers are the regions where viscous effects are dominant, which suggests that one member of the family of coordinate lines should run along the airfoil surface and continue onto the wake.

Furthermore, in transonic flow shock waves can be properly captured if another member of the family of coordinate lines runs more or less parallel to the shock wave. Boundary-fitted meshes with a C-type or an H-type topology meet all these requirements. Here the C-type mesh is used since it is more efficient in terms of mesh points needed to wrap around an airfoil and does not have a singularity at the leading edge like the H-type mesh. The coordinate transformation from the physical to the uniform computational domain is illustrated in figure 3.2.

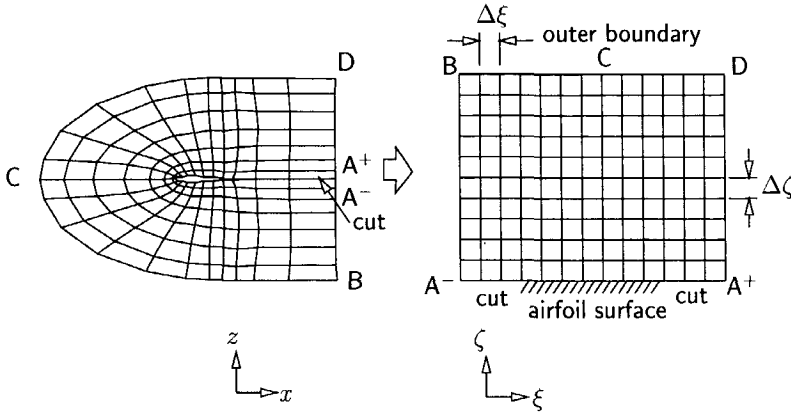


Figure 3.2: Coordinate transformation from physical to computational domain

### 3.2.2 MESH GENERATOR

The mesh generator used in this study is an improved version of the one presented by the author in [131], which is based on an algebraic method with a smoother based on an elliptic method.

The target applications presented in [131] are flow calculations employing the full-potential equation. For the present applications, which utilize the Navier-Stokes equations only minor modifications turned out to be necessary. The method to distribute the points in the normal direction had to be modified. The original method used a one-parameter exponential function to distribute the mesh points in the normal direction. For a mesh to be used for solving the Navier-Stokes equations, however, it is preferred to prescribe the distance from the airfoil surface to the first mesh point. This is required to properly capture the viscous sublayer. For this purpose a two-parameter stretching function is used. The stretching is controlled by specifying the lengths of the first and the last segment. An example of the grid generated using this method is presented in figure 3.3 and figure 3.4. The airfoil is the RAE 2822 airfoil section, the dimension of the mesh is  $161 \times 60$ , with 120 points on the surface of the airfoil. Around the nose of the airfoil the distance between the surface and the first point away from the surface is  $4 \times 10^{-6}$  chords and close to the trailing edge it is  $8 \times 10^{-6}$  chords. The outer boundary was set at 20 chords away from the airfoil.

### 3.2.3 DYNAMIC MESH ALGORITHM

To consistently take into account the moving solid surface of the airfoil section, the inner boundary of the mesh at which the solid surface resides has to conform to the motion of the airfoil surface at all times. The other part of the mesh inner boundary, i.e. the cut, see figure 3.2, has to follow the motion of the trailing edge. The mesh outer boundary is free to move or is fixed as long as it stays in the far-

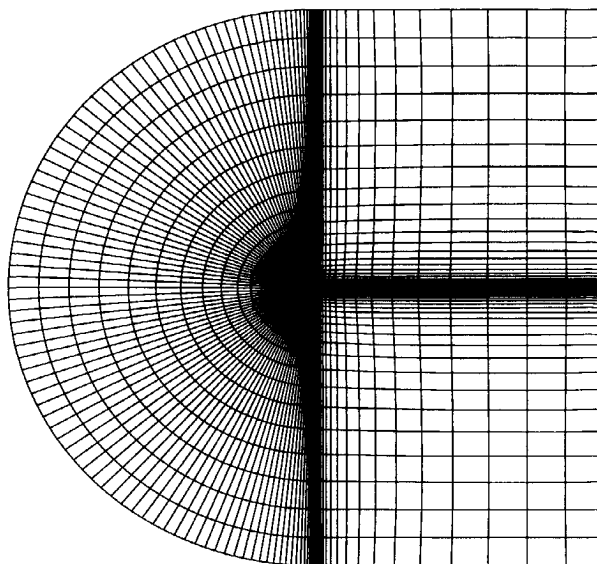


Figure 3.3: Overall picture of the grid around an RAE 2822 airfoil

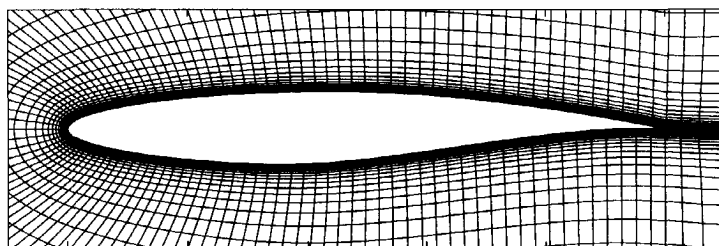


Figure 3.4: Grid close-up near an RAE 2822 airfoil

field. For motions of a rigid airfoil the whole mesh may be attached to the airfoil and move along with the airfoil. When the airfoil deforms (control surface oscillation, chordwise bending) the mesh has to deform in order to follow the motion of the **solid surface**. **The deforming airfoil is the most general situation, which means** that a method developed for this type of motion can certainly be applied also to rigid motions. In three dimensions, even for a simple isolated wing, the sectional deformation is most likely to vary in spanwise direction, so that a deformed mesh capability is definitely required.

In the present study some basic properties of the dynamic mesh algorithm are required: it should be efficient, robust, independent of the initial mesh, suitable for general types of motion and conservative, i.e. the property that the initial mesh is recovered when the moving boundary returns to its initial position. In general, the procedure to deform the mesh includes:

1. Read the initial mesh, extract some quality parameters of the mesh and store these quality parameters, so that they can be used during the calculation of the mesh.
2. Deform the mesh to follow the moving boundary, while keeping the quality parameters constant.

Two methods have been investigated in the the present study: the elliptic method and the spring analogy.

### ELLIPTIC METHOD

Although the initial mesh can be generated by any method, in the elliptic dynamic mesh method the mesh points are assumed to be solutions of a system of Poisson equations, see e.g. Thompson [166]:

$$\begin{aligned}\xi_{xx} + \xi_{zz} &= P(\xi, \zeta) \\ \zeta_{xx} + \zeta_{zz} &= Q(\xi, \zeta).\end{aligned}$$

$P$  and  $Q$  are the source functions which control the mesh spacing during the mesh deformation. Function  $P$  controls the mesh point distribution in  $\xi$ -direction and function  $Q$  the mesh point distribution in  $\zeta$ -direction.  $P$  and  $Q$  serve as quality parameters and are extracted from the initial mesh and stored. The procedure to calculate  $P$  and  $Q$  from a given mesh can be found in [131].  $P$  and  $Q$  are very effective in preserving the mesh point distribution during the deformation, which means that the deformed mesh will have a similar quality in the mesh point distribution as the initial mesh. However, these quality parameters fail to preserve local orthogonality which is important at the solid surface. A simple method to maintain orthogonality at a solid surface is proposed by introducing an additional forcing function at the surface as:

$$\tilde{P}(\xi) = - \left[ \frac{\mathbf{t}(\xi) \cdot \mathbf{n}(\xi)}{|\mathbf{t}(\xi)| |\mathbf{n}(\xi)|} \right]^n + \left[ \frac{\mathbf{t}(\xi) \cdot \mathbf{n}(\xi)}{|\mathbf{t}(\xi)| |\mathbf{n}(\xi)|} \right]^0, \quad (3.3)$$

where  $\mathbf{t}(\xi)$  and  $\mathbf{n}(\xi)$  are a vector tangential to the surface and a vector connecting the point on the surface and the first mesh point away from the surface, respectively, see figure 3.5. Function  $Q$  is kept unchanged since it is not necessary to change the mesh point distribution in the  $\zeta$ -direction. Superscript  $n$  and 0 represent the

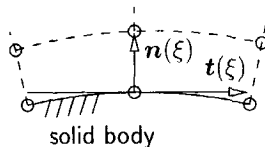


Figure 3.5: Normal and tangential vectors for the definition of surface forcing function

conditions at time level ( $n$ ) and the initial mesh, respectively. This surface forcing function is blended with the field forcing function as follows:

$$\bar{P}(\xi, \zeta) = f(\bar{\zeta}) \tilde{P}(\xi) + [1 - f(\bar{\zeta})]P(\xi, \zeta), \quad (3.4)$$

where  $f(\bar{\zeta})$  is some monotonic function of  $\bar{\zeta} = [0, 1]$ , the normalized  $\zeta$ , which satisfies the condition  $f(0) = 1$  and  $f(1) = 0$ . Using these forcing functions, equations (3.2.3–3.4) are solved to obtain the mesh points at each time step using a point Gauss-Seidel (PGS) relaxation method. The initial guess of the mesh points is calculated using an algebraic method. Some 4 to 5 PGS iterations are usually sufficient to ensure a mesh of good quality.

### SPRING ANALOGY

The mesh is modeled as a system of springs connecting each pair of mesh points. The stiffness of each spring is set proportional to the inverse of the length of the segment which connects the pair of points. The stiffnesses of the springs are the quality parameters of the spring analogy method. At its mean steady position the

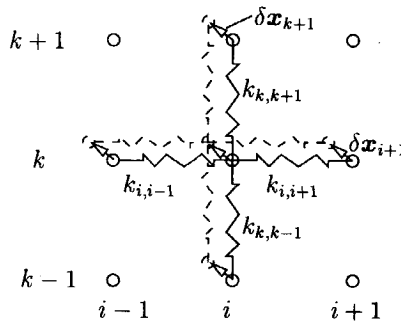


Figure 3.6: The spring analogy of the mesh

system is statically balanced. Then, when the airfoil moves while the outer boundary is fixed, the points in the field will also move to reach another equilibrium position. As no masses are involved in this mesh, the deformations follow instantaneously the airfoil motion. This means that the spring system will not introduce some spurious dynamic characteristics to the system. The static balance of the spring forces for the mesh deformation at  $(i, k)$  in the new position is expressed by the equation:

$$\begin{aligned} k_{k,k-1}^r (\delta \mathbf{x}_k - \delta \mathbf{x}_{k-1}) + k_{k,k+1}^r (\delta \mathbf{x}_k - \delta \mathbf{x}_{k+1}) + \\ k_{i,i-1}^r (\delta \mathbf{x}_i - \delta \mathbf{x}_{i-1}) + k_{i,i+1}^r (\delta \mathbf{x}_i - \delta \mathbf{x}_{i+1}) = 0, \end{aligned} \quad (3.5)$$

in which  $k$  is the stiffness of a mesh segment and  $\delta \mathbf{x}$  is the displacement of a mesh point. The power  $r$  of the stiffness coefficients serves as a control parameter of the mesh deformation. To prevent large deformations of the mesh close to the airfoil, a relatively large value of  $r$  is used, whereas close to the outer boundary a small  $r$  is applied. In between, a linear interpolation is used.

In contrast to the elliptic method, which employs a system of coupled nonlinear equations, the equations of the spring analogy are linear and uncoupled, being a strong advantage over the elliptic method. Originally, a predictor-corrector type method was used to solve the static balance equation, see Batina [24]. The predictor step employed a linear extrapolation from the displacements at the previous time and the corrector step used the Jacobi iteration method. This relaxation method worked satisfactorily for the cases considered in [24] where meshes for the Euler equations were deformed and relatively small time steps were employed in the calculations. In the present study, where a relatively large time step is pursued, the method did not give a satisfactory convergence rate, even for meshes for the Euler equations. The number of Jacobi iterations grew very rapidly with the magnitude of the deformations. The situation was even worse for the stiff meshes commonly used in viscous flow calculations. To overcome this problem, the original method has been modified by replacing the predictor step by a solution of the static balance equations in  $\zeta$  direction only:

$$k_{k,k-1}^r(\delta \mathbf{x}_k - \delta \mathbf{x}_{k-1}) + k_{k,k+1}^r(\delta \mathbf{x}_k - \delta \mathbf{x}_{k+1}) = 0, \quad (3.6)$$

called here the implicit predictor. Equation (3.6) is a simple scalar tridiagonal system of equations which can be solved efficiently. This predictor scheme also relieves the need to store the deformations of the previous time step. The corrector step employs the PGS relaxation method and usually not more than two iterations are needed.

Both methods are applied in the present study. A test case involving large displacements will be presented later in this chapter to investigate the applicability of these methods.

### 3.3 COORDINATE TRANSFORMATION

The flow equations discussed in chapter 2 are expressed in a Cartesian coordinate system. For reason of convenience in working with deforming structured meshes the flow equations are transformed in a time-dependent curvilinear coordinate system. The transformation and its inverse transformation are written as:

$$\begin{aligned} x &= x(\xi, \zeta, \tau) & \xi &= \xi(x, z, t) \\ z &= z(\xi, \zeta, \tau) & \zeta &= \zeta(x, z, t) \\ t &= \tau. \end{aligned}$$

A time transformation is not necessary since for time-accurate calculations a uniform time step is used in the whole domain.

The differentials in the Cartesian and in the curvilinear coordinate systems can be calculated using the chain rule as:

$$\begin{bmatrix} dt \\ dx \\ dz \end{bmatrix} = \begin{bmatrix} 1 & 0 & 0 \\ x_\tau & x_\xi & x_\zeta \\ z_\tau & z_\xi & z_\zeta \end{bmatrix} \begin{bmatrix} d\tau \\ d\xi \\ d\zeta \end{bmatrix} \quad \text{and} \quad \begin{bmatrix} d\tau \\ d\xi \\ d\zeta \end{bmatrix} = \begin{bmatrix} 1 & 0 & 0 \\ \xi_t & \xi_x & \xi_z \\ \zeta_t & \zeta_x & \zeta_z \end{bmatrix} \begin{bmatrix} dt \\ dx \\ dz \end{bmatrix}.$$

Comparing the above two equations, the so-called metrics of the transformation can be easily derived:

$$\begin{aligned}\xi_x &= Jz_\zeta, & \zeta_x &= -Jz_\xi, \\ \xi_z &= -Jx_\zeta, & \zeta_z &= Jx_\xi, \\ \xi_t &= -J(x_\tau z_\zeta - z_\tau x_\zeta), & \zeta_t &= -J(-x_\tau z_\xi + z_\tau x_\xi).\end{aligned}\quad (3.7)$$

The Jacobian of the mesh transformation,  $J = \partial(\xi, \zeta)/\partial(x, y)$ , can be calculated from  $J = h^{-1}$ , where:

$$h = \left| \frac{\partial \mathbf{x}}{\partial \xi} \right| = x_\xi z_\zeta - x_\zeta z_\xi, \quad (3.8)$$

which represents the ratio of the areas of an element (in two-dimensional flow) in the computational and in the physical domain. The metrics  $\zeta_x$  and  $\zeta_z$  represent the components of the normal to the line of constant  $\xi$  scaled by the Jacobian, and  $\zeta_t$  represents the velocity in the same normal direction and again scaled by the Jacobian. A similar interpretation holds for  $\xi_x$ ,  $\xi_z$  and  $\xi_t$  for the line of constant  $\zeta$ . For brevity, total fluxes are defined to consist of the inviscid and viscous fluxes as  $F_x = F_x^I - F_x^V$  and  $F_z = F_z^I - F_z^V$ . After the transformation the Navier-Stokes equation (2.21) will be in the following nonconservation form:

$$\frac{\partial Q}{\partial \tau} + \xi_t \frac{\partial Q}{\partial \xi} + \zeta_t \frac{\partial Q}{\partial \zeta} + \xi_x \frac{\partial F_x}{\partial \xi} + \zeta_x \frac{\partial F_x}{\partial \zeta} + \xi_z \frac{\partial F_z}{\partial \xi} + \zeta_z \frac{\partial F_z}{\partial \zeta} = 0. \quad (3.9)$$

Peyret et al. [129] showed that a conservation form of the Navier-Stokes equations in a general curvilinear coordinate system may be obtained with the help of the following transformation invariants:

$$\frac{\partial \hat{\xi}_x}{\partial \xi} + \frac{\partial \hat{\zeta}_x}{\partial \zeta} = 0, \quad (3.10)$$

$$\frac{\partial \hat{\xi}_z}{\partial \xi} + \frac{\partial \hat{\zeta}_z}{\partial \zeta} = 0. \quad (3.11)$$

and

$$\frac{\partial h}{\partial \tau} + \frac{\partial \hat{\xi}_t}{\partial \xi} + \frac{\partial \hat{\zeta}_t}{\partial \zeta} = 0. \quad (3.12)$$

The hat ( $\hat{\bullet}$ ) above the metrics means that they are not scaled by the Jacobian. Using these invariants, the conservation form of the Navier-Stokes equations in the curvilinear coordinate system is obtained:

$$\frac{\partial \hat{Q}}{\partial \tau} + \frac{\partial \hat{F}_\xi}{\partial \xi} + \frac{\partial \hat{F}_\zeta}{\partial \zeta} = 0, \quad (3.13)$$

where the new conservative variable is  $\hat{Q} = hQ$  and the fluxes in the curvilinear coordinate system are given by:

$$\hat{F}_\xi = \hat{F}_\xi^I - \hat{F}_\xi^V = \hat{\xi}_t Q + \hat{\xi}_x F_x^I + \hat{\xi}_z F_z^I - (\hat{\xi}_x F_x^V + \hat{\xi}_z F_z^V) \quad (3.14)$$

$$\hat{F}_\zeta = \hat{F}_\zeta^I - \hat{F}_\zeta^V = \hat{\zeta}_t Q + \hat{\zeta}_x F_x^I + \hat{\zeta}_z F_z^I - (\hat{\zeta}_x F_x^V + \hat{\zeta}_z F_z^V). \quad (3.15)$$



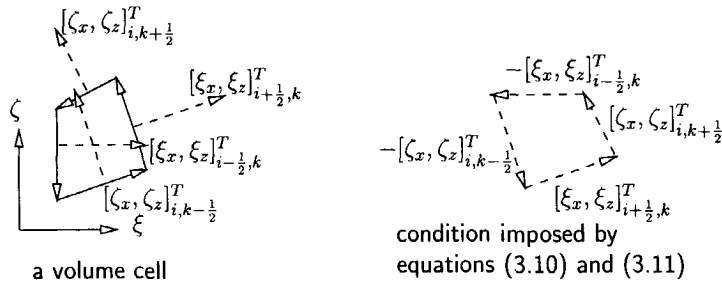


Figure 3.7: The normals showing the closed computation cell

The physical interpretation of the two transformation invariants, equations (3.10) and (3.11), can be seen from figure 3.7. The left picture shows a volume cell with its normal vectors on its cell faces, denoted by vectors with dashed lines. The right picture visualizes the condition imposed by equations (3.10) and (3.11), which can be interpreted as the condition of the volume cell being closed. These two equations are actually the differential form of equation (2.29). The other invariant relates the rate of change of the area of a volume cell and the velocities normal to the cell faces. This is actually a statement of the GCL, equation (2.31), in a differential form. As mentioned in section 2.5.2, a failure to satisfy these invariants may result in non-physical sources disturbing the solution.

The inviscid fluxes can be written in a more compact form by defining the so-called contravariant velocity components as  $U = \xi_t + \xi_x u + \xi_z w$  and  $W = \zeta_t + \zeta_x u + \zeta_z w$ .  $U$  is the component perpendicular to lines of constant  $\xi$ , and  $W$  is the component perpendicular to lines of constant  $\zeta$ . The inviscid fluxes, as defined by equations (3.14) and (3.15), may then be written as:

$$\hat{F}_\xi^I = \begin{bmatrix} \rho \hat{U} \\ \rho u \hat{U} + \hat{\xi}_x p \\ \rho w \hat{U} + \hat{\xi}_z p \\ \rho E \hat{U} + \hat{U}' p \end{bmatrix} \quad \hat{F}_\zeta^I = \begin{bmatrix} \rho \hat{W} \\ \rho u \hat{W} + \hat{\zeta}_x p \\ \rho w \hat{W} + \hat{\zeta}_z p \\ \rho E \hat{W} + \hat{W}' p \end{bmatrix}, \quad (3.16)$$

where  $U' = \xi_x u + \xi_z w$  is the scaled absolute velocity perpendicular to the lines of  $\zeta$  constant. A similar definition applies to  $W'$ . The hat has the same meaning as before. The viscous fluxes, as defined by equation (3.14) and equation (3.15), are written accordingly as

$$\hat{F}_\xi^V = \begin{bmatrix} 0 \\ \hat{\xi}_x \tau_{xx} + \hat{\xi}_z \tau_{xz} \\ \hat{\xi}_x \tau_{xz} + \hat{\xi}_z \tau_{zz} \\ \hat{\xi}_x u \tau_{xx} + \hat{U}' \tau_{xz} + \hat{\xi}_z w \tau_{zz} - q_\xi \end{bmatrix} \quad (3.17)$$

$$\hat{F}_\zeta^V = \begin{bmatrix} 0 \\ \hat{\zeta}_x \tau_{xx} + \hat{\zeta}_z \tau_{xz} \\ \hat{\zeta}_x \tau_{xz} + \hat{\zeta}_z \tau_{zz} \\ \hat{\zeta}_x u \tau_{xx} + \hat{W}' \tau_{xz} + \hat{\zeta}_z w \tau_{zz} - q_\zeta \end{bmatrix}. \quad (3.18)$$

### THIN-LAYER APPROXIMATION

The Thin-Layer approximation can be implemented very conveniently in the transformed equations. It keeps only the dissipation terms in the normal direction since large gradients of the velocity are expected in this direction. This means that  $F_\xi^V$ , i.e. equation (3.17), is dropped and the flux in  $\xi$  direction has only an inviscid contribution. Furthermore, the gradients of the velocity in  $\xi$  direction are also neglected because these are assumed to be small compared to the gradients in  $\zeta$  direction, which results in very simple expressions for the stresses. This approximation may be interpreted as modifying the chain rule into:

$$\frac{\partial u}{\partial x} = \xi_x \frac{\partial u}{\partial \xi} + \zeta_x \frac{\partial u}{\partial \zeta} \approx \zeta_x \frac{\partial u}{\partial \zeta} \quad \text{and} \quad \frac{\partial u}{\partial z} = \xi_z \frac{\partial u}{\partial \xi} + \zeta_z \frac{\partial u}{\partial \zeta} \approx \zeta_z \frac{\partial u}{\partial \zeta}.$$

Using these expressions, equation (3.17) for the Thin-Layer Navier-Stokes equations become simply:

$$\hat{F}_\zeta^V = \frac{\mu}{Re} \begin{bmatrix} 0 \\ m_1 u_\zeta + m_2 w_\zeta \\ m_2 u_\zeta + m_3 w_\zeta \\ \frac{m_1}{2}(u^2)_\zeta + m_2(uw)_\zeta + \frac{m_3}{2}(w^2)_\zeta + m_4 \frac{\gamma}{Pr} e_\zeta \end{bmatrix}, \quad (3.19)$$

where the metric functions are:

$$\begin{aligned} m_1 &= h \left( \frac{4}{3} \zeta_x^2 + \zeta_z^2 \right) & m_2 &= \frac{h}{3} \zeta_x \zeta_z \\ m_3 &= h \left( \zeta_x^2 + \frac{4}{3} \zeta_z^2 \right) & m_4 &= h (\zeta_x^2 + \zeta_z^2). \end{aligned}$$

Note that this form is slightly different from the one commonly presented in the literature, e.g. Steger [160]. The reason to use this form is to separate the geometric terms (the metrics) from the flow variables in order to facilitate an easy derivation of the Jacobian.

### 3.4 DISCRETIZATION METHODS

After having obtained the set of flow equations expressed in the curvilinear coordinate system, viz. equation (3.13), (3.16) and (3.19), this section presents the discretization methods to solve them. The objective is to develop a numerically stable and accurate simulation method, applicable for large time step unsteady flow simulations.

A natural choice for a conservative discretization method is the finite volume method. Two possible schemes can be considered, namely cell-centered and vertex-centered schemes. Based on a formal error analysis of a numerical scheme the vertex-centered scheme, where the unknowns are stored at the vertices and the secondary cell is used as the control volume, is more accurate than the cell-centered scheme, where the unknowns are stored at the cells and the primary cell is used as the control volume, see e.g. Radespiel et al. [139], Rossow [149]. In practice, however, the difference in accuracy is not significant as shown by Swanson and Radespiel [163]. In the present study, the choice to adopt a cell-centered scheme over a vertex-centered scheme has been primarily based on convenience in applying the scheme. A vertex-centered scheme needs a special treatment in the region close to the mesh boundary, while a cell-centered scheme can be applied throughout the field.

Following the first directive presented at the beginning of this chapter, an implicit temporal integration method with implicit subiteration employing relaxation is applied. This has been implemented using the method of lines, where the spatial discretization and temporal integration are considered separately. At each time step a set of discretized unsteady Navier-Stokes equations is solved using a relaxation scheme. To ensure the convergence of that scheme, the relaxation matrix has to be positive and preferably diagonally dominant. As will be shown later in this section, an upwind difference method can be constructed to possess these properties, while a central difference method can not, so an upwind difference method is applied. Another consideration is that an upwind difference method is in general more accurate in modeling shear layers than a central difference scheme, which of course is a very important feature of methods for solving Navier-Stokes equations. It should be noted that not all upwind difference methods can model shear layer accurately, thus only the class of upwind methods which has this property will be considered in the present study. The main disadvantage of an upwind difference method, however, is that it is more expensive in terms of CPU time, than a central difference scheme.

### 3.5 SPATIAL DISCRETIZATION

The cell-centered finite-volume method is applied for the spatial discretization of the Navier-Stokes equations. This can be done conveniently in the transformed coordinates, i.e. equation (3.13). Since this equation is valid in the whole domain, the following integral form may be used:

$$\frac{\partial}{\partial \tau} \int_{\mathcal{V}} hQ \, d\xi d\zeta + \int_{\mathcal{V}} \left( \frac{\partial}{\partial \xi}, \frac{\partial}{\partial \zeta} \right)^T \cdot \hat{\mathbf{F}} \, d\xi d\zeta = 0, \quad (3.20)$$

where  $\mathcal{V}$  is the control volume in the transformed coordinates. Expressing the second volume integral as a surface integral and expanding the time derivative, one obtains:

$$\int_{\mathcal{V}} h \frac{\partial Q}{\partial \tau} \, d\xi d\zeta + \int_{\mathcal{V}} Q \frac{\partial h}{\partial \tau} \, d\xi d\zeta + \int_{\partial \mathcal{V}} \hat{\mathbf{F}} \cdot [d\xi, d\zeta]^T = 0. \quad (3.21)$$

In the cell-centered method, the average value of  $Q$  is defined as a discrete value representing the flow variables in cell  $(i, k)$ . According to the average integral theorem it holds:

$$Q_{i,j} = \frac{1}{S_{i,j}} \int_{S_{i,j}} Q dV. \quad (3.22)$$

However, the position to locate  $Q_{i,j}$  is not known in general. Evaluating equation (3.21) in a uniform computational domain, defining  $\Delta\xi = \Delta\zeta = 1$ , the semi-discrete form<sup>1</sup> of equation (3.13) becomes simply:

$$h^{n+1} \frac{\partial Q}{\partial \tau} + Q^n \frac{\partial h}{\partial \tau} + \hat{F}_{\xi, i+\frac{1}{2}, j}^{I, n+1} - \hat{F}_{\xi, i-\frac{1}{2}, j}^{I, n+1} + \hat{F}_{\zeta, i, j+\frac{1}{2}}^{n+1} - \hat{F}_{\zeta, i, j-\frac{1}{2}}^{n+1} = 0. \quad (3.23)$$

The form of equation (3.23) where all fluxes are defined at the cell faces is called a discrete conservation form and the fluxes are called conservative fluxes. At each cell face only the flux normal to the face has a contribution to the equation, so that its computation may be considered as a locally one-dimensional problem. At cell face  $i \pm \frac{1}{2}, j$  only flux  $\hat{F}_{\xi}^I$  is involved, hence at this cell face only  $\xi_t$ ,  $\xi_x$  and  $\xi_z$  are calculated. For the same reason at cell face  $i, j \pm \frac{1}{2}$  only  $\zeta_t$ ,  $\zeta_x$  and  $\zeta_z$  are calculated.

### 3.5.1 CALCULATION OF METRICS ACCORDING TO GCL

Consider first the transformation invariants defined by equations (3.10) and (3.11). The discretized form of equations (3.10) and (3.11) which conforms to the discrete equation for the flow, i.e. equation (3.23), is:

$$\begin{aligned} \hat{\xi}_{x, i+\frac{1}{2}, j} - \hat{\xi}_{x, i-\frac{1}{2}, j} + \hat{\zeta}_{x, i, j+\frac{1}{2}} - \hat{\zeta}_{x, i, j-\frac{1}{2}} &= 0 \\ \hat{\xi}_{z, i+\frac{1}{2}, j} - \hat{\xi}_{z, i-\frac{1}{2}, j} + \hat{\zeta}_{z, i, j+\frac{1}{2}} - \hat{\zeta}_{z, i, j-\frac{1}{2}} &= 0. \end{aligned}$$

These equations have to be satisfied to avoid the presence of nonphysical sources. The metrics satisfying the transformation invariants are calculated as:

$$\begin{aligned} \hat{\xi}_{x, i+\frac{1}{2}, j} &= z_{i+\frac{1}{2}, j+\frac{1}{2}} - z_{i+\frac{1}{2}, j-\frac{1}{2}} & \hat{\zeta}_{x, i, j+\frac{1}{2}} &= -(z_{i+\frac{1}{2}, j+\frac{1}{2}} - z_{i-\frac{1}{2}, j+\frac{1}{2}}) \\ \hat{\xi}_{z, i+\frac{1}{2}, j} &= -(x_{i+\frac{1}{2}, j+\frac{1}{2}} - x_{i+\frac{1}{2}, j-\frac{1}{2}}) & \hat{\zeta}_{z, i, j+\frac{1}{2}} &= x_{i+\frac{1}{2}, j+\frac{1}{2}} - x_{i-\frac{1}{2}, j+\frac{1}{2}}. \end{aligned} \quad (3.24)$$

This is the only condition required for a calculation involving a fixed mesh.

**The rate of change of the cell volume,  $\partial h / \partial \tau$ , is calculated from the contravariant mesh speed using the GCL statement equation (3.12) as:**

$$\frac{\partial h}{\partial \tau} = -\frac{\partial \hat{\xi}_t}{\partial \xi} - \frac{\partial \hat{\zeta}_t}{\partial \zeta}.$$

The contravariant mesh speeds,  $\hat{\xi}_t$  and  $\hat{\zeta}_t$ , are calculated from the deformation of the mesh caused by the motion of the airfoil. This motion is prescribed in case

<sup>1</sup>Semi-discrete form means one of either the spatial discretization or temporal integration has, while the other has not been applied.

of a forced vibration and for an aeroelastic simulation case it is determined by the solution of the elasto-mechanical equations. In case the elasto-mechanical equations are solved using a two-level scheme, e.g. the Newmark method or the transition matrix method, the contravariant mesh speed at a cell face,  $\hat{\xi}_t^{n,n+1}$  or  $\hat{\zeta}_t^{n,n+1}$ , is calculated on the 'space-time' (swept) area formed by a cell face at two structural levels, see figure 3.8. For example,  $\hat{\xi}_{t,i+\frac{1}{2}}^{n,n+1}$  at cell face [2-4] of figure 3.8 is calculated

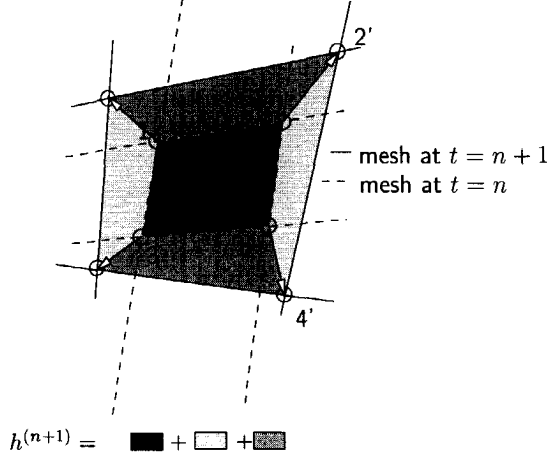


Figure 3.8: Space-time area formed during mesh deformation

as  $-\nabla \hat{\xi} \cdot \hat{\mathbf{x}}$  in the swept area [2-2'-4'-4], in which:

$$\begin{aligned} \nabla \hat{\xi} &= \frac{1}{2}(\nabla \hat{\xi}^{n+1} + \nabla \hat{\xi}^n) \\ \hat{\mathbf{x}} &= \frac{1}{2\Delta\tau}(\mathbf{x}_{i+\frac{1}{2},j+\frac{1}{2}}^{n+1} + \mathbf{x}_{i+\frac{1}{2},j-\frac{1}{2}}^{n+1} - \mathbf{x}_{i+\frac{1}{2},j+\frac{1}{2}}^n - \mathbf{x}_{i+\frac{1}{2},j-\frac{1}{2}}^n). \end{aligned} \quad (3.25)$$

For a three-level scheme, e.g. the second-order implicit backward Euler scheme,  $\hat{\xi}_t$  is calculated as:

$$\hat{\xi}_t = \frac{3}{2}\hat{\xi}_t^{n,n+1} - \frac{1}{2}\hat{\xi}_t^{n-1,n}. \quad (3.26)$$

The above way of calculating the contravariant mesh speed was shown by Obayashi [121] to be consistent with the rate of change of the cell volume, which implies that equation (3.12) is implicitly satisfied. The GCL ensures that the area of the cell at time level  $n+1$  of figure 3.8 is the area of the cell at time level  $n$  plus the area of the cell faces swept during the following time step.

### 3.5.2 UPWIND DISCRETIZATION OF INVISCID FLUX

The inviscid flux is a crucial element in the discretization of the Navier-Stokes equations since it requires artificial viscosity for stabilization which may not disturb the

physical viscosity. The conservative methods which are used in this study are discussed in this section. Aspects which determine the usability for the current problem are presented.

Pulliam [137] showed that in general an upwind scheme can be written as a central scheme plus a damping term. Hence, constructing an upwind scheme may also be regarded as constructing a proper artificial viscosity for a set of centrally-discretized Euler equations. However, the original reason is to discretize the equations in an appropriate manner according to the direction of propagation of the information.

Consider again the simple hyperbolic equation, equation (2.47) from section 2.5.3, where the velocity  $c$  can now be positive or negative. The case of  $c=0$  is not considered because it would not contribute to the change of  $u$ . When  $c$  is positive, equation (2.47) models a right-running wave and thus a backward difference is appropriate. For negative  $c$  the wave is running to the left and a forward difference is appropriate. Thus a proper differencing can be set up by separating  $c$  into a positive and a negative component as:

$$c = c^+ + c^-, \quad (3.27)$$

where  $c^+ = \frac{1}{2}(c + |c|)$  and  $c^- = \frac{1}{2}(c - |c|)$ , and discretize them using a backward and forward differencing, respectively. Applying this separation and a first-order backward difference in time one obtains for equation (2.47):

$$u_i^{n+1} - u_i^n + \frac{c\Delta t}{2\Delta x}(u_{i+1}^{n+1} - u_{i-1}^{n+1}) - \frac{\Delta t}{2\Delta x}|c|(u_{i+1}^{n+1} - 2u_i^{n+1} + u_{i-1}^{n+1}) = 0. \quad (3.28)$$

The last term is a second-order diffusive term which brings stabilization to the central difference of the third term. The conservative flux definition of equation (3.28) at a cell face is:

$$f_{i+\frac{1}{2}} = \frac{1}{2}c(u_{i+1} + u_i) - \frac{1}{2}|c|(u_{i+1} - u_i). \quad (3.29)$$

In the neighborhood of a shock wave the central difference methods tend to produce spurious oscillations in their solution. These oscillations are a purely numerical behavior since they are not observed in experiments. The behavior of the solution of the Euler equations should be monotonic, like for instance the solution of the Laplace equation. The notion of monotonicity for upwind differences was introduced in an attempt to obtain a solution which is free from wiggles. Writing equation (3.28) as:

$$C_{i-1}^{n+1}u_{i-1}^{n+1} + C_i^{n+1}u_i^{n+1} + C_{i+1}^{n+1}u_{i+1}^{n+1} = u_i^n, \quad (3.30)$$

where:

$$C_{i-1}^{n+1} = -\frac{\Delta t}{2\Delta x}(c + |c|), \quad C_i^{n+1} = (1 + \frac{\Delta t|c|}{\Delta x}), \quad C_{i+1}^{n+1} = \frac{\Delta t}{2\Delta x}(c - |c|),$$

one can see that  $C_i^{n+1} > 0$ ,  $C_{i-1}^{n+1} \leq 0$  and  $C_{i+1}^{n+1} \leq 0$ . The form of this first-order scheme, i.e. equation (3.30), is called 'positive', which has a monotonic solution, see e.g. Dick [46]. A monotone scheme does not have oscillations in the solution.

A weaker condition for a method to be free of wiggles is the Total Variation Diminishing (TVD) condition, see Hirsch [76], Hussaini et al. [84] for an excellent reference. A higher-order upwind scheme, which can be obtained from variable or flux extrapolation, needs to be limited to preserve the monotonicity of the first-order scheme. Since a TVD scheme preserves monotonicity, this criterion is used to limit the flux/variable extrapolation. This section presents upwind methods which have a monotonic behavior.

### FLUX VECTOR SPLITTING (FVS)

The solution of a system of hyperbolic equations represents in general more than one wave. Each wave may have a different direction of propagation. Flux vector splitting is a method to split the inviscid flux into positive (moving forward) and negative (moving backward) contributions.

The first FVS was proposed by Steger [161]. He splits the inviscid flux like in equation (3.27). Although the method became popular, it contained a lack of differentiability of the flux at sonic and shock points causing a glitch in the flow variables.

**VAN LEER FVS** An ingenious direct solution of the discontinuity problem of Steger's splitting [161] was introduced by van Leer. The flux is split based on polynomial expansions in Mach number for which the requirement is put, amongst others, that no discontinuities are present. For example, the mass flux may be written as a function of Mach number as:

$$\bar{F}_{\xi m}^I = \rho \bar{U} = \rho \bar{M}_{\xi} a, \quad \text{where} \quad \bar{M}_{\xi} = \frac{\bar{U}}{a}, \quad (3.31)$$

where  $a$  is the speed of sound. Since the symmetry property of the mass flux is  $F_{\xi m}^I(M) = -F_{\xi m}^I(-M)$  and at a supersonic condition  $F_{\xi m}^{I+}(M) = F_{\xi m}^I(M)$  and  $F_{\xi m}^{I-}(-M) = F_{\xi m}^I(-M)$ , then the symmetry property of the split mass flux should also be:

$$F_{\xi m}^{I+}(M) = -F_{\xi m}^{I-}(-M).$$

With the conditions that  $F_{\xi}^{I+} + F_{\xi}^{I-} = F_{\xi}^I$  and that  $F_{\xi}^I$  be continuous at  $M = \pm 1$  the proper choice would be:

$$\bar{F}_{\xi m}^{I\pm} = \pm \frac{\rho a}{4} (\bar{M}_{\xi} \pm 1)^2. \quad (3.32)$$

The detailed description of the van Leer splitting may be found in the original paper of van Leer [103] or in [76] and for applications with moving meshes it is described in [128] and [12]. In the moving mesh case the Mach number defined in equation (3.31) is the Mach number relative to the speed of the cell face,  $\bar{M}_{\xi} =$

$[(u - \hat{x})\tilde{\xi}_x + (w - \hat{z})\tilde{\xi}_z]/a$ . The inviscid flux written as a function of  $\tilde{M}_\xi$  is:

$$\hat{F}_\xi^I = |\nabla \xi| \begin{bmatrix} \rho a \tilde{M}_\xi \\ \rho u a \tilde{M}_\xi + \hat{\xi}_x p \\ \rho w a \tilde{M}_\xi + \hat{\xi}_z p \\ \rho E a \tilde{M}_\xi + p(a \tilde{M}_\xi - \hat{\xi}_t) \end{bmatrix}. \quad (3.33)$$

The tilde means that the quantity is normalized with the magnitude of the normal to the cell surface. Following the approach of [12] the van Leer flux for  $|\tilde{M}_\xi| < 1$  is:

$$\hat{F}_\xi^{I\pm} = |\nabla \hat{\xi}| F_{\xi m}^{I\pm} \begin{bmatrix} 1 \\ \tilde{\xi}_x(-\tilde{U} \pm 2a)/\gamma + u \\ \tilde{\xi}_z(-\tilde{U} \pm 2a)/\gamma + w \\ (\gamma \tilde{U}' + \tilde{\xi}_t)(-\tilde{U} \pm 2a)/(\gamma - 1) + 2a^2/(\gamma^2 - 1) + k \end{bmatrix},$$

where the mass flux  $F_{\xi m}^{I\pm}$  is taken from equation (3.32) and  $k$  is the kinetic energy per unit mass. For a supersonic flow condition the flux returns to its unsplit form, i.e. equation (3.16). Unfortunately the superiority of van Leer's splitting in capturing shock discontinuities does not extend to its performance in capturing contact discontinuities, which is necessary for resolving viscous layers. This is due to the convective term which does not vanish when the contact discontinuity is at rest. This drawback makes van Leer's FVS not a proper choice for a Navier-Stokes solver. The van Leer's FVS is applied here in conjunction with the hybrid method which will be presented later in this section.

**ADVECTION UPSTREAM SPLITTING METHOD FVS (AUSM)** This FVS has been designed to have the performance of flux-difference splitting (FDS, see next subsection) in capturing contact discontinuities while maintaining the simplicity of FVS. The essence of the method is the separation of the flux into a convective term and a pressure term as:

$$\hat{F}_\xi^I = |\nabla \xi| \tilde{U} \begin{bmatrix} \rho a \\ \rho u a \\ \rho w a \\ \rho H a \end{bmatrix} + p \begin{bmatrix} 0 \\ \hat{\xi}_x \\ \hat{\xi}_z \\ -\hat{\xi}_t \end{bmatrix} \equiv |\nabla \xi| \tilde{U} \mathcal{C}_\xi + p \mathcal{P}_\xi, \quad (3.34)$$

where  $H = E + p/\rho$ . The convective term is treated in an FDS style while the pressure term is split as in van Leer's FVS. In the original paper of Liou [105], splitting based on the polynomial in Mach number is used for both convective and pressure terms as:

$$\tilde{F}_{\xi i+\frac{1}{2}}^I = [\tilde{M}_{\xi i+\frac{1}{2}}^+(Q_{i+\frac{1}{2}}^-) + \tilde{M}_{\xi i+\frac{1}{2}}^-(Q_{i+\frac{1}{2}}^+)] [a \mathcal{C}_\xi]_{i+\frac{1}{2}} + [p_i^+ + p_{i+1}^-] \mathcal{P}_\xi, \quad (3.35)$$



where:

$$[a\mathcal{C}_\xi]_{i+\frac{1}{2}} = \begin{cases} [a\mathcal{C}_\xi]_i & \text{if } [\tilde{M}_{\xi i+\frac{1}{2}}^+(Q_{i+\frac{1}{2}}^-) + \tilde{M}_{\xi i+\frac{1}{2}}^-(Q_{i+\frac{1}{2}}^+)] \geq 0 \\ [a\mathcal{C}_\xi]_{i+1} & \text{otherwise} \end{cases}$$

$$M^\pm = \begin{cases} \pm 0.25 (M \pm 1)^2 & \text{if } |M| \leq 0 \\ 0.50 (M \pm |M|) & \text{otherwise} \end{cases}$$

$$p^\pm = \begin{cases} 0.50 p(1 \pm M) & \text{if } |M| \leq 0 \\ 0.50 p(M \pm |M|)/M & \text{otherwise.} \end{cases}$$

In this manner the convective flux vanishes when the contact discontinuity is at rest. Application of AUSM FVS for solving the Navier-Stokes equations leads to accurate solutions in shear layers. The application of AUSM FVS for moving mesh problems is obtained automatically when defining the Mach number to be relative to the speed of the cell face.

AUSM FVS is applied here because it seems very suitable for the present application. The results of this scheme will be compared with results of the other methods to demonstrate the potential of this scheme.

#### GODUNOV'S METHOD, FLUX DIFFERENCE SPLITTING (FDS)

Although more complicated than the FVS method, the FDS method is considered in the present study since it has a very good performance in capturing the contact discontinuities. Thus a natural choice for use in a Navier-Stokes method.

The original Godunov method is a semi-analytical method. An analogy may be drawn with the panel methods for the linearized potential flow equation. The fundamental solutions in a panel method are the singularities (source, sink, dipole, etc.), while in the Godunov method it is the solution of the Riemann problem of the flow in a shock tube, see figure 3.9. At rest,  $t \leq 0$ , the pressure on the right

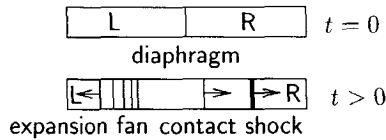


Figure 3.9: Riemann's problem, shock tubes at rest and after the diaphragm has broken

side of the diaphragm is lower than the one on the left side. After the diaphragm breaks, a shock wave moves to the right, a contact discontinuity also moves to the right with different (lower) speed and an expansion fan moves to the left. The state at time  $t > 0$  is a function of the initial state at  $t = 0$ , namely  $Q_L$  and  $Q_R$ . For a more detailed discussion about the Riemann problem, see standard books on gas dynamics, e.g. Liepmann and Roshko [104].

The Godunov method for solving a hyperbolic equation proceeds as follows. At a certain time level the continuous state of the flow is replaced by a piecewise constant

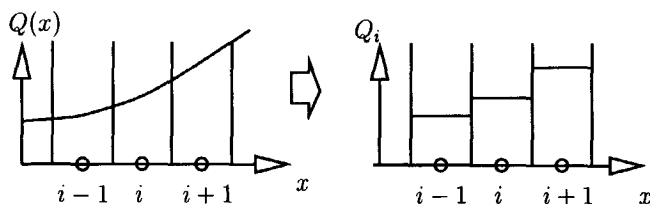


Figure 3.10: Definition of discontinuity at cell faces in Godunov's method

distribution, see figure 3.10. The state in a cell is obtained by averaging the values in a cell as:

$$\bar{Q}_i = \frac{1}{\Delta x} \int_{i-\frac{1}{2}}^{i+\frac{1}{2}} Q(x, t) dx. \quad (3.36)$$

Consequently the outcome is a discontinuity at every cell face. These discontinuities are then considered as a Riemann problem with the cell face as the diaphragm of a shock tube and the current time level as  $t = 0$ . For example: at cell face  $i + \frac{1}{2}$  the states are  $Q_L = Q_i$  and  $Q_R = Q_{i+1}$ . The state at the next time level is obtained by solving the Riemann problem at time  $t = \Delta t$ . This step is the physical step of the Godunov method. After solving the Riemann problem, the state in a cell will obtain contributions from two neighboring cells. The state at the next time level in a cell is obtained by averaging these contributions. The averaging processes, the first and the third stage, are of numerical nature. They can be considered to be independent from the physical stage.

The exact solution of Riemann's problem for the Euler equations requires the solution of a set of nonlinear algebraic equations. This is considered to be time-consuming because it has to be done for each cell face. Hence, an approximate Riemann solver is usually applied which should be able to represent the important features of the problem, but at less computational effort. This approach is also justified because even when using the exact Riemann solver, the solution is averaged in the cell. Up to now, the approximate Riemann solvers which are considered to be amongst the best are Osher's and Roe's approximate Riemann solvers.

**OSHER'S FDS** Osher's approximate Riemann solver [124] for the Euler equations is a generalization of the Engquist-Osher method [56] for potential flow. Their method is an improvement of the Murman-Cole method which recognizes only a shock transition, but not a sonic point. The application of Osher's method to the Euler equations leads to the definition of the numerical flux at the cell face as:

$$F_{\xi, i+\frac{1}{2}}^I = \frac{1}{2} [F_{\xi, i+\frac{1}{2}}^I(Q_{i+\frac{1}{2}}^+) + F_{\xi, i+\frac{1}{2}}^I(Q_{i+\frac{1}{2}}^-)] - dF_{\xi, i+\frac{1}{2}}^I, \quad (3.37)$$

where the last term, which is usually called the flux difference, for Osher's scheme is:

$$dF_{\xi, i+\frac{1}{2}}^I = \frac{1}{2} \int_{Q_i}^{Q_{i+1}} |A_{\xi}^I(Q)| dQ. \quad (3.38)$$

The integration of  $|A_\xi^I(Q)|$  implies a continuous flux with respect to the conservative variable. The evaluation of the integral is carried out by taking the path in the  $Q$  space according to the simple wave decomposition [124]. Using a set of Riemann's invariants, an exact integration (in this sense) may be carried out but the resulting expression is very complicated. Moreover, when an implicit scheme is employed, the Jacobian of the flux with respect to the conservative variables will be very complex and thus undesirable from a computational point of view. Many authors sacrifice some convergence, and perhaps also some stability, by using a simplified flux Jacobian.

The pure Osher's FDS method is not applied in the present study due to its complexity, which was already found by many authors to be very CPU time consuming. The mixed one, with FVS, is applied in the present study and will be described later in this section.

**ROE'S FDS** Roe's approximate Riemann solver employs much less complicated expressions. It constitutes an exact Riemann solution for the following linearized equation:

$$\frac{\partial \hat{Q}}{\partial \tau} + \hat{A}_\xi^I \frac{\partial Q}{\partial \xi} + \hat{A}_\zeta^I \frac{\partial Q}{\partial \zeta} = 0, \quad (3.39)$$

in which each dimensional direction is treated independently. Since a local linearization is assumed for  $\hat{A}_\xi^I(Q)$  and  $\hat{A}_\zeta^I(Q)$ , the numerical flux at a cell face follows equation (3.29):

$$\hat{F}_{\xi, i+\frac{1}{2}}^I = \frac{1}{2} [\hat{F}_{\xi, i+\frac{1}{2}}^I(Q_{i+\frac{1}{2}}^+) + \hat{F}_{\xi, i+\frac{1}{2}}^I(Q_{i+\frac{1}{2}}^-)] - \frac{1}{2} |\hat{A}_\xi^I(\bar{Q})| (Q_{i+\frac{1}{2}}^+ - Q_{i+\frac{1}{2}}^-), \quad (3.40)$$

The superscripts  $+$  and  $-$  represent the states at the right and left side of the cell face (diaphragm of the Riemann problem), respectively. The flux difference can be written in a more efficient way by using the definition of characteristic variables,  $\delta W_\xi = L_\xi \delta Q$ , and the diagonalization of the flux Jacobian,  $A_\xi^I = R_\xi |\Lambda_\xi| L_\xi$ , where  $L_\xi$  and  $R_\xi$  is the matrix of the left and right eigenvector of the flux Jacobian, respectively, and  $\Lambda_\xi$  is a diagonal matrix with the eigenvalue of the flux Jacobian as the entry:

$$|A_\xi^I| \delta Q = \sum_{k=1}^4 |\lambda_k| \delta w_k \mathbf{r}_k, \quad (3.41)$$

where  $\delta Q = Q^+ - Q^-$ . Equation (3.41) is more convenient than the flux difference of equation (3.40) because it shows a decomposition of the flux difference  $dF_\xi^I = |A_\xi^I| \delta Q$  into simple waves described by the right eigenvectors,  $\mathbf{r}_k$ , with amplitude  $\delta w_k$ . This representation of the flux difference was first used by Roe in [145].

Equation (3.39) is actually in a nonconservation form which can not be used across a discontinuity. The novel feature of Roe's approach lies in the definition of the Jacobian at the cell face,  $|A_\xi^I(\bar{Q})|$ , where a special type of averaging process, which became known as Roe's averaging, is used for defining  $\bar{Q}$  out of  $Q_{i+\frac{1}{2}}^+$  and

$Q_{i+\frac{1}{2}}^-$  at a cell face. The Rankine-Hugoniot relation across a discontinuity, equation (2.46), written specifically as:

$$F_{\xi i+1}^I - F_{\xi i}^I = A_{\xi i+\frac{1}{2}}^I (Q_{i+1} - Q_i), \quad (3.42)$$

is satisfied in this averaging process. This makes equation (3.39) also valid across discontinuities. A set of variables is introduced which together with the inviscid flux renders a similar quadratic behavior of the flux of Burgers' equation. The Roe variables and the associated inviscid flux as functions of Roe's variables are:

$$Q^{Roe} = \begin{bmatrix} r_1 \\ r_2 \\ r_3 \\ r_4 \end{bmatrix} = \begin{bmatrix} \sqrt{\rho} \\ \sqrt{\rho}u \\ \sqrt{\rho}w \\ \sqrt{\rho}H \end{bmatrix} \quad \hat{F}_{\xi}^I = \begin{bmatrix} r_1(r_1\hat{\xi}_t + r_2\hat{\xi}_x + r_3\hat{\xi}_z) \\ r_2(r_1\hat{\xi}_t + r_2\hat{\xi}_x + r_3\hat{\xi}_z) + \hat{\xi}_x p \\ r_3(r_1\hat{\xi}_t + r_2\hat{\xi}_x + r_3\hat{\xi}_z) + \hat{\xi}_z p \\ r_1 r_4 - \hat{\xi}_t p \end{bmatrix}, \quad (3.43)$$

where  $p = (\gamma - 1)[r_1 r_4 - \frac{1}{2}(r_2^2 + r_3^2)]/\gamma$ . A direct calculation will show that this expression of the inviscid flux has a quadratic property with respect to Roe's variables. This property remains valid when it is transformed back to the conservative variables using  $\delta Q = (\partial Q / \partial Q^{Roe}) \delta Q^{Roe}$ . After the Roe variables have been averaged at a cell face, the Jacobian  $A_{\xi i+\frac{1}{2}}^I$  is calculated using these averaged values. In practice, however, the calculation of the flux difference is carried out using equation (3.41) since it is more efficient.

The right eigenvectors, the eigenvalues and the fundamental state of the amplitude (variation of characteristic variables) are calculated using the Roe averaged value at the cell face. The Roe averaging process is efficiently calculated by defining  $r = \sqrt{\rho^+/\rho^-}$  and then:

$$\rho_{i+\frac{1}{2},j} = \rho^- r \quad , \quad u_{i+\frac{1}{2},j} = \frac{u^+ r + u^-}{r + 1} \quad , \quad w_{i+\frac{1}{2},j} = \frac{w^+ r + w^-}{r + 1} \quad , \quad H_{i+\frac{1}{2},j} = \frac{H^+ r + H^-}{r + 1}.$$

The speed of sound at the cell face can be obtained from these values. The eigenvalues  $\lambda$  are  $\tilde{U}$ ,  $\tilde{U}$ ,  $\tilde{U} - a$ ,  $\tilde{U} + a$ , the amplitude of the wave which is the characteristic variable depends on the choice of normalization of the eigenvectors. In appendix B the normalization is chosen such as to have a very simple expression of the right eigenvectors. The detailed expression of the right and left eigenvectors can be found in appendix B.

**HYBRID FDS AND FVS** This approach was introduced by Coquel and Liou [39] to take advantage of both FVS and FDS methods. As mentioned before, FVS, especially van Leer's FVS, is superior in capturing shocks (nonlinear field) but less accurate in the shear layer (linearly degenerate field). Exactly the reverse is true for FDS. The idea of hybridization will be clear when both FVS and FDS are written as equation (3.37), with the flux differences, see [39]:

$$dF_{\xi FVS}^I = \frac{1}{2} \int_0^1 |A_{\xi}^I| [\Phi(s; Q^-, Q^+)] \frac{\partial \Phi(s; Q^-, Q^+)}{\partial s} ds \quad (3.44)$$

$$dF_{\xi FDS}^I = \frac{1}{2} \int_0^1 |A_{\xi}^I| [s, \Phi(s; Q^-, Q^+)] \frac{\partial \Phi(s; Q^-, Q^+)}{\partial s} ds, \quad (3.45)$$

where  $\Phi(s, Q^-, Q^+)$  is a family of paths in the phase space, which connects  $Q^-$  and  $Q^+$ , with  $s$  as the parameter.  $s$  is  $[0, 1]$ , where  $\Phi(0, Q^-, Q^+) = Q^-$  and  $\Phi(1, Q^-, Q^+) = Q^+$ . Equations (3.44) and (3.45) show that FDS is path dependent, while FVS is not. A flux formula which has superiority in capturing shocks as well as accuracy in capturing contact discontinuities can be constructed by combining both methods as follows:

$$dF_{\xi}^I{}_{\text{HUS}} = \frac{1}{2} \int_{\text{NL}} |A_{\xi}^I|_{\text{FVS}}[\Phi(s; Q^-, Q^+)] \frac{\partial \Phi(s; Q^-, Q^+)}{\partial s} ds + \frac{1}{2} \int_{\text{LD}} |A_{\xi}^I|_{\text{FDS}}[s, \Phi(s; Q^-, Q^+)] \frac{\partial \Phi(s; Q^-, Q^+)}{\partial s} ds, \quad (3.46)$$

where subscript HUS means hybrid upwind scheme, subscript NL nonlinear fields (shock) and subscript LD linearly degenerate fields (contact discontinuity). Equation (3.46) can also be written in a more convenient form as:

$$F_{\xi}^I{}_{\text{HUS}} = F_{\xi}^I{}_{\text{FVS}} + \frac{1}{2} \int_{\text{LD}} (|A_{\xi}^I|_{\text{FVS}} - |A_{\xi}^I|_{\text{FDS}})[\Phi(s; Q^-, Q^+)] \frac{\partial \Phi(s; Q^-, Q^+)}{\partial s} ds, \quad (3.47)$$

which shows the FVS flux plus an anti-diffusive flux. When  $Q^-$  and  $Q^+$  are connected only by a shock, then equation (3.47) represents a pure FVS. When  $Q^-$  and  $Q^+$  are connected only by a contact discontinuity, then equation (3.47) represents a pure FDS. This remarkable behavior of equation (3.47) is used to improve van Leer's FVS using Osher's FDS as:

$$F_{\xi}^I{}_{\text{HUS}} = F_{\xi}^I{}_{\text{VL}} \begin{cases} -F_{\xi}^I{}_{\text{VL}}(Q_i^*) - F_{\xi}^I{}_{\text{VL}}(Q_{i+1}^*) & \text{if } |M| \leq 0 \\ +F_{\xi}^I{}_{\text{VL}}(Q_i^*) - F_{\xi}^I{}_{\text{VL}}(Q_{i+1}^*) & \text{otherwise.} \end{cases} \quad (3.48)$$

The Riemann invariants for calculating  $Q^{*, -}$  from  $Q^-$  are:  $p/\rho^\gamma$ ,  $\bar{W}$  and  $\bar{U} + 2a/(\gamma - 1)$ , while the Riemann invariants for calculating  $Q^{*, +}$  from  $Q^+$  are  $p/\rho^\gamma$ ,  $\bar{W}$  and  $\bar{U} - 2a/(\gamma - 1)$ . It should be noted that  $\bar{U}^{*, +} = \bar{U}^{*, -}$  is the speed of the contact discontinuity.

### 3.5.3 SOME CONSIDERATIONS OF THE DISCRETIZED INVISCID FLUX

The upwind methods described in the previous sections, van Leer's FVS, AUSM-FVS, Roe's FDS and the hybrid method of van Leer-Osher FV/DS, have been implemented and studied. Concerning the implementation, the simplest ones are AUSM FVS and van Leer's FVS. The Roe FDS and the hybrid method are comparably complex. It is noticeable that concerning the derivation and implementation of the Jacobian of the flux all methods are comparably complex. The most complex one, however, is the hybrid method.

Although the van Leer FVS and AUSM-FVS have very simple expressions for the flux formula, their Jacobian is far from simple due to the presence of functions of the Mach number. This suggests to use a different set of unknowns than the

usual conservative variables. However, since unsteady flows are considered and consequently the time derivative of the conservative variables will always be present in the residual, working with variables other than the conservative variables is not efficient.

It is also noticeable that constructing an approximation for the Jacobian of the AUSM flux is not trivial. Some approximations were tried to keep the expression simple, thereby maintaining the simplicity of the flux formula and reducing CPU time, but none resulted in a robust approximation. On the other hand, it is relatively simple to construct an approximation for the Jacobian of Roe's FDS. Finally, since the exact Jacobian of the hybrid method is very complex and expensive to calculate, the Jacobian of van Leer's FVS is employed. In section 3.10.2 these methods will be applied to a set of test cases. The results will be compared to determine the most suitable method for CAS applications. This method will be extended and applied for three-dimensional configurations in chapter 6.

### 3.5.4 CALCULATION OF HIGHER-ORDER INVISCID FLUX

The calculation of fluxes at a cell face involves: calculation of the metrics, definition of the variables at the two sides of the cell face, calculation of the inviscid flux according to the FVS or FDS approach and calculation of the viscous flux. The calculation of the metrics has to meet the transformation invariants requirement (GCL). For the presented upwind methods, when the flux is calculated in a first-order manner, the resulting scheme is TVD. For example: at cell face  $(i + \frac{1}{2})$   $Q^+ = Q_{i+1}$  and  $Q^- = Q_i$ . A higher-order flux definition at a cell face is obtained by defining the averaged state in a cell to be linear instead of constant, see figure 3.11. This involves an extrapolation which can be applied to the flow variables or directly to the flux itself. The first is called the variable extrapolation method and the latter

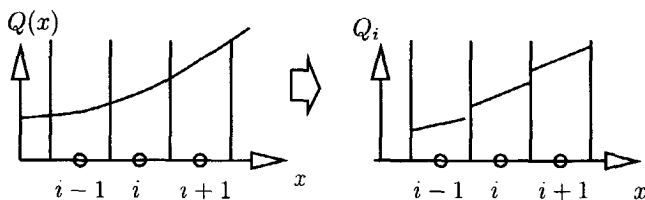


Figure 3.11: Definition of discontinuity at cell faces in the higher-order Godunov method

is called the flux extrapolation method.

In the present study the higher-order inviscid flux is obtained by defining the flow variables on the two sides of the face using the variable extrapolation scheme of van Leer, which is usually called the Monotonic Upwind Scheme for Conservation Law (MUSCL scheme). The general form of the MUSCL scheme is:

$$\begin{aligned} Q_{i+\frac{1}{2}}^+ &= Q_{i+1} - \frac{s}{4}[(1 - \kappa s)dQ_{i+1}^+ + (1 + \kappa s)dQ_{i+1}^-] \\ Q_{i+\frac{1}{2}}^- &= Q_i + \frac{s}{4}[(1 - \kappa s)dQ_i^- + (1 + \kappa s)dQ_i^+], \end{aligned} \quad (3.49)$$

where  $dQ_i^+ = Q_{i+1} - Q_i$ ,  $dQ_i^- = Q_i - Q_{i-1}$ .  $\kappa$  controls the accuracy of the extrapolation,  $\kappa = -1$  is the second-order fully upwind scheme,  $\kappa = 1/3$  is the third-order upwind biased scheme and  $\kappa = 1$  is the second-order central scheme. The limiter function  $s$  serves to limit the higher-order gradients to preserve the monotone behavior of the scheme. A non-monotone scheme would result in an overshoot due to higher-order gradients when the variable extrapolation equation (3.49) is applied close to shock waves. Since the first-order scheme has a monotone property, the limiter maintains the monotonicity of the solution by reducing the order of the extrapolation scheme equation (3.49) into first-order when it is necessary, namely in the vicinity of shock waves. Although there are many choices for the limiters, here the one of Albada et al. [8] is applied, primarily because of its continuous behavior which is indispensable for an implicit method:

$$s = \frac{2dQ^+dQ^- + \epsilon}{(dQ^+)^2 + (dQ^-)^2 + \epsilon}. \quad (3.50)$$

The small quantity  $\epsilon$  ensures the limiter to behave properly in smooth flow regions.

### 3.6 APPLICATION OF SOLID BOUNDARY CONDITIONS

The surface boundary condition is applied by introducing two layers of ghost-points along the interior side of the airfoil. The first ghost point is related to the first layer in the computational domain and the second ghost point is related to the second layer in the computational domain. In this manner the higher-order MUSCL variable extrapolation can be used throughout the domain without having to modify the scheme in the vicinity of solid surfaces.

#### 3.6.1 VELOCITY BOUNDARY CONDITION

For inviscid flows, the boundary condition at the solid surface requires the normal velocity to vanish at all time. For the Euler equations this condition is the only one which may be specified at the solid surface because only one eigenvalue at the surface has a positive sign (leaving the solid surface represents a positive direction). The other quantities have to be extrapolated from the computational domain onto the surface.

The application of the boundary condition is carried out in a very simple manner. The velocity in each ghost point consists of two components: the normal component and the tangential component. The normal component is determined from the corresponding mirrored value in the computational domain and the tangential component is obtained from extrapolation from the computational domain. The normal component in the ghost point has to cancel the mirrored normal component making the normal velocity zero at the solid surface. Thus the normal component in the ghost point is:

$$\mathbf{u}_{n,ghost} = -[(\mathbf{u}_{comp} - 2\dot{\mathbf{x}}) \cdot \mathbf{n}]\mathbf{n}, \quad (3.51)$$

where  $\dot{\mathbf{x}} = [x_\tau, z_\tau]^T$  is the velocity of the solid surface. The extrapolation of the tangential velocity to the ghost points may not affect the condition given in equation (3.51). The simplest way to satisfy this condition is by removing the normal component from the extrapolated velocity. If the extrapolated velocity at the ghost points is denoted by  $\mathbf{u}_{\text{ext}}$ , its tangential component becomes:

$$\mathbf{u}_{\text{t,ghost}} = \mathbf{u}_{\text{ext}} - [(\mathbf{u}_{\text{ext}} - \dot{\mathbf{x}}) \cdot \mathbf{n}] \mathbf{n}.$$

Using the usual notation for the transformed equations, very simple formulas are obtained for the velocity in the ghost points:

$$\mathbf{u}_{\text{ghost}} = \mathbf{u}_{\text{ext}} - w[\tilde{\zeta}_x, \tilde{\zeta}_z]^T, \quad (3.52)$$

where  $w = \tilde{W}_{\text{ext}} + \tilde{W}_{\text{comp}} + \tilde{\zeta}_t$ ,  $\tilde{W}$  is the contravariant velocity in the  $\zeta$  direction using the geometric data of the surface.

The velocity boundary condition for viscous flows, for which the normal velocity as well as the tangential velocity vanish, is much simpler:

$$\mathbf{u}_{\text{ghost}} = 2\dot{\mathbf{x}} - \mathbf{u}_{\text{comp}}. \quad (3.53)$$

In this manner the velocity at the ghost points is obtained without having to solve a system of equations.

### 3.6.2 UNSTEADY NORMAL MOMENTUM EQUATION ON SOLID SURFACE

To extrapolate the pressure from the field to the ghost points, the normal momentum equation method of Rizzi [142] is applied. The normal momentum equation used here is derived from the scalar product of the normal direction  $\nabla \hat{\zeta} = [\hat{\zeta}_x, \hat{\zeta}_z]^T$  and the momentum equations:

$$\frac{\partial}{\partial \tau} \begin{bmatrix} \rho h u \\ \rho h w \end{bmatrix} + \frac{\partial}{\partial \xi} \begin{bmatrix} \rho u \hat{U} + \hat{\xi}_x p \\ \rho w \hat{U} + \hat{\xi}_z p \end{bmatrix} + \frac{\partial}{\partial \zeta} \begin{bmatrix} \rho u \hat{W} + \hat{\zeta}_x p \\ \rho w \hat{W} + \hat{\zeta}_z p \end{bmatrix} = \frac{\partial}{\partial \zeta} \begin{bmatrix} \hat{\zeta}_x \tau_{xx} + \hat{\zeta}_x \tau_{xz} \\ \hat{\zeta}_x \tau_{xz} + \hat{\zeta}_z \tau_{zz} \end{bmatrix}. \quad (3.54)$$

For inviscid flows, inserting the condition  $\hat{W} = 0$  in the normal momentum equations, omitting the stresses and substituting the continuity equation leads to:

$$(\nabla \hat{\zeta} \cdot \nabla \hat{\xi}) \frac{\partial p}{\partial \xi} + (\nabla \hat{\zeta} \cdot \nabla \hat{\zeta}) \frac{\partial p}{\partial \zeta} = \rho \left( h \frac{\partial \hat{\zeta}_t}{\partial \tau} + u \frac{\partial \hat{\zeta}_x}{\partial \tau} + w \frac{\partial \hat{\zeta}_z}{\partial \tau} \right) + \rho \hat{U} \left( \frac{\partial \hat{\zeta}_t}{\partial \xi} + u \frac{\partial \hat{\zeta}_x}{\partial \xi} + w \frac{\partial \hat{\zeta}_z}{\partial \xi} \right). \quad (3.55)$$

For viscous flow, inserting also the condition  $\hat{U} = 0$ , one obtains:

$$(\nabla \hat{\zeta} \cdot \nabla \hat{\xi}) \frac{\partial p}{\partial \xi} + (\nabla \hat{\zeta} \cdot \nabla \hat{\zeta}) \frac{\partial p}{\partial \zeta} = \rho h \frac{\partial \hat{\zeta}_t}{\partial \tau}. \quad (3.56)$$

The viscous stresses at the surface have been omitted since they are small compared to the other terms, especially in high Reynolds number flows.



## 3.6.3 FLUX FORMULA AT SOLID SURFACE

Due to the vanishing normal velocity at the solid surface, the flux has only pressure terms. Applying the usual flux formula to the surface flux does in general not guarantee vanishing convective terms. The flux at the surface is therefore calculated using the pressure part of the van Leer splitting:

$$\hat{F}_{\zeta \text{ wall}} = p_{\text{wall}} \begin{bmatrix} 0 \\ \hat{\xi}_x \\ \hat{\xi}_z \\ -\hat{\xi}_t \end{bmatrix}, \quad (3.57)$$

where the splitting of the pressure follows equation (3.35):

$$p_{\text{wall}} = p^+(Q_{\text{ghost}}) + p^-(Q_{\text{comp}}) \quad \text{and} \quad p^\pm = \frac{1}{2} p(1 \pm M),$$

provided that the Mach number normal to the solid surface is smaller than one. Equation (3.57) is stable and performs well in conjunction with all flux formula used in the present study.

## 3.7 TEMPORAL INTEGRATION

As has been mentioned previously, in the method of lines the spatial discretization and the temporal integration are treated separately. This section discusses the temporal integration method for the semi-discretized equations which result from the spatial discretizations presented in the previous sections. The temporal integration, complying with the directive at the beginning of in this chapter, employs an implicit method with subiteration. The section will begin with some introductory notes followed by the formulation of the subiteration and discussions of the methods to solve the resulting set of nonlinear algebraic equations.

## 3.7.1 INTRODUCTION

For simplicity consider again the model equation, i.e. equation (2.47). Applying only the spatial discretization which was presented in section 3.5.2 results in an ordinary differential equation:

$$\frac{du_i}{dt} = \tilde{C}_{i-1}u_{i-1} + \tilde{C}_i u_i + \tilde{C}_{i+1}u_{i+1}, \quad (3.58)$$

where:

$$\tilde{C}_{i-1} = \frac{c + |c|}{2\Delta x}, \quad \tilde{C}_i = -\frac{|c|}{\Delta x}, \quad \tilde{C}_{i+1} = -\frac{c - |c|}{2\Delta x}.$$

Equation (3.58) is the semi-discrete equation for an interior point. At the boundary either  $u_{i-1}$  or  $u_{i+1}$  is known (from extrapolation or a fixed value depending on the

sign of  $c$ , see section 2.5.3). The semi-discrete equation for the whole field can be written as:

$$\frac{dU}{dt} = CU + B, \quad (3.59)$$

where  $U$  is the vector of the unknown,  $C$  is the matrix representing the spatial discretization and  $B$  is the vector of the nonhomogeneous term including the boundary conditions. The nonhomogeneous and homogeneous terms determine the steady and transient state, respectively. The condition for well-posedness or stability of equation (3.59) is that the real part of all eigenvalues of  $C$  is negative, see Hirsch [76]<sup>1</sup>. In the case of a first-order upwind method, like equation (3.59), the eigenvalue of matrix  $C$  is  $-|c|/\Delta x$ . A proper temporal integration method of equation (3.58) must have a stability region in the complex plane which includes the whole spectrum of the eigenvalues of  $C$ . A temporal integration method is called A-stable, see Gear [62], if its stability region includes the whole negative complex plane, including the imaginary axis. This implies that an A-stable method is appropriate for any type of proper spatial discretizations.

### 3.7.2 UNSTEADY RESIDUAL

In the present study an implicit linear multistep method is applied to equation (3.23). If a strictly A-stable scheme is desired at most a second-order accurate discretization may be applied to  $\partial Q/\partial \tau$  [62]. Experience gained during the course of the study revealed that a second-order scheme gives satisfactory results in most cases, thus it is adopted as the default scheme of the present method. However, third-order accurate backward differencing for  $\partial Q/\partial \tau$ , which is defined as stiffly stable by Gear [62], is also applied and employed for some cases presented later in this chapter. The stability region of a stiffly stable temporal integration method does not cover the imaginary axis. This may give problems when central differencing is applied for the spatial discretization. This is one of the reasons for not considering the central schemes in the present study. Another—and the most important—reason is that a diagonally dominant Jacobian matrix can only be expected from an upwind method.

The residual at a certain time level is defined by equation (3.23). The time derivative of  $Q$  is approximated using backward differences as:

$$\frac{\partial Q}{\partial \tau} \approx \frac{1}{\Delta \tau} (c_0 \Delta Q^n + c_1 \Delta Q^{n-1} + c_2 \Delta Q^{n-2}), \quad (3.60)$$

where the coefficients  $c_i$  are presented in table 3.1.

After selecting the temporal discretization from one of the schemes presented in table 3.1, the discretization of the unsteady Navier-Stokes equations is complete,

---

<sup>1</sup>Note: If one is only interested in the steady state a large negative value of the real part of the eigenvalues is preferred. When the ratio of the maximum and the minimum of the eigenvalues is very large the problem is said to be stiff.

method	$c_0$	$c_1$	$c_2$
1st order	1	0	0
2nd order	3/2	-1/2	0
3rd order	11/6	-7/6	2/6

Table 3.1: Coefficients for the linear multistep method

which reads:

$$h^{n+1} \left( \frac{c_0 \Delta Q^n + c_1 \Delta Q^{n-1} + c_2 \Delta Q^{n-2}}{\Delta \tau} \right) - Q^n \left( \frac{\partial \hat{\xi}_t}{\partial \xi} + \frac{\partial \hat{\zeta}_t}{\partial \zeta} \right) + \hat{F}_{\xi, i+\frac{1}{2}, j}^{I, n+1}(Q^{n+1}) - \hat{F}_{\xi, i-\frac{1}{2}, j}^{I, n+1}(Q^{n+1}) + \hat{F}_{\zeta, i, j+\frac{1}{2}}^{n+1}(Q^{n+1}) - \hat{F}_{\zeta, i, j-\frac{1}{2}}^{n+1}(Q^{n+1}) = 0, \quad (3.61)$$

where  $\Delta Q^n = Q^{n+1} - Q^n$ . Equation (3.61) represents a set of nonlinear algebraic equations which have to be solved for  $Q^{n+1}$ , the state of the flow at the next time step. Newton's method is employed to solve this set of nonlinear equations:

$$\frac{\partial R(Q^p)}{\partial Q} \Delta Q^p = -R(Q^p), \quad (3.62)$$

where  $p$  is the subiteration level,  $Q^p$  is the  $p$ -th iteration of the solution  $Q^{n+1}$ ,  $\Delta Q^p$  is  $Q^{p+1} - Q^p$  and the residual is defined as:

$$R(Q^p) = \frac{c_0 h^{n+1} Q^p}{\Delta \tau} + S(Q^n, Q^{n-1}, Q^{n-2}) + \bar{R}(Q^p). \quad (3.63)$$

$\bar{R}(Q^p)$  is the residual of the steady equation:

$$\bar{R}(Q^p) = \hat{F}_{\xi, i+\frac{1}{2}, j}^{I, n+1}(Q^p) - \hat{F}_{\xi, i-\frac{1}{2}, j}^{I, n+1}(Q^p) + \hat{F}_{\zeta, i, j+\frac{1}{2}}^{n+1}(Q^p) - \hat{F}_{\zeta, i, j-\frac{1}{2}}^{n+1}(Q^p),$$

and  $S(Q^n, Q^{n-1}, Q^{n-2})$  is the source term, which does not change during the iteration:

$$S(Q^n, Q^{n-1}, Q^{n-2}) = h^{n+1} \left( \frac{-c_0 Q^n + c_1 \Delta Q^{n-1} + c_2 \Delta Q^{n-2}}{\Delta \tau} \right) - Q^n \left( \frac{\partial \hat{\xi}_t}{\partial \xi} + \frac{\partial \hat{\zeta}_t}{\partial \zeta} \right).$$

Starting from an initial guess,  $Q^{p=0}$ , equation (3.62) is solved iteratively until the residual reaches a certain norm, which means that the discrete unsteady Navier-Stokes equations are satisfied at time step  $(n+1)$ . This iteration is called the subiteration. The accuracy of the subiteration scheme, i.e. equation (3.62), is determined only by the right-hand side (RHS), while the left-hand side (LHS) determines the rate of convergence. In a full Newton method, where the LHS is the exact Jacobian of the RHS and is inverted exactly to obtain the correction, a quadratic convergence of the residual can be expected [123, 170, 171]. An inexact LHS and/or an approximate inversion may be used at the cost of loosing the quadratic convergence property of Newton's method. In this case the method is called the quasi Newton method, see e.g. [123, 170]. In the present study a quasi Newton method is constructed and presented in the following subsection.

### 3.7.3 RELAXATION METHOD

In devising the relaxation scheme some issues are considered: efficiency, in terms of CPU time and storage per iteration, robustness and good convergence. In most cases, approximations to the LHS, which reduce the work and storage per iteration, slow down the convergence. Therefore, the LHS should not be too far away from the exact Jacobian of the RHS.

Based on these issues, the LHS is set to be the Jacobian of a first-order accurate residual. The residual itself can be of higher order accuracy. Several advantages of this approximation over the Jacobian of a second-order accurate residual are: (a) the LHS has three entries in each coordinate direction instead of five, which reduces the storage significantly, (b) it allows application of the efficient block tridiagonal solver for the equations in a mesh line, (c) positivity and diagonal dominance of the LHS, which improves convergence and robustness, are always guaranteed for any time step and (d) a first order upwind method as previously shown produces monotonic solution thus a limiter does not have to be applied, keeping the LHS simple. The equation for the subiterations reads:

$$[L_i^-] \Delta Q_{i-1}^p + [L_i] \Delta Q_i^p + [L_i^+] \Delta Q_{i+1}^p = -R(Q^p, Q^n, Q^{n-1}), \quad (3.64)$$

where the  $[L]$ 's represent the entry of a line:

$$[L_i^-] \Delta Q_{i-1} = -[A_{\xi, i-\frac{1}{2}, j}^+] \Delta Q_{i-1, j} \quad (3.65)$$

$$[L_i] \Delta Q_i = -[A_{\xi, i, j-\frac{1}{2}}^+] \Delta Q_{i, j-1} + [D_{i, j}] \Delta Q_{i, j} + [A_{\xi, i, j+\frac{1}{2}}^-] \Delta Q_{i, j+1} \quad (3.66)$$

$$[L_i^+] \Delta Q_{i+1} = [A_{\xi, i+\frac{1}{2}, j}^-] \Delta Q_{i+1, j}, \quad (3.67)$$

and where the diagonal entry,  $[D_{i, j}]$ , is:

$$[D_{i, j}] = [c_0 \frac{h^{n+1}}{\Delta \tau} + A_{\xi, i+\frac{1}{2}, j}^+ - A_{\xi, i-\frac{1}{2}, j}^- + A_{\xi, i, j+\frac{1}{2}}^+ - A_{\xi, i, j-\frac{1}{2}}^-],$$

with  $c_0$  from table 3.1. The Jacobian of van Leer's FVS and AUSM-FVS are calculated in an exact manner using the chain rule of differentiation. For the hybrid van Leer-Osher FV/DS method the exact flux Jacobian of van Leer's FVS is used. The exact Jacobian of the inviscid flux using Roe's FDS is very complicated and expensive to calculate, see [22], so that a simplified Jacobian is used instead. There are many possible approximations for the Jacobian: from  $A^\pm = A \pm \max(|\lambda|)I$ ,  $A^\pm = A(Q) \pm |A(Q)|$  (without Roe's averaging) up to a finite-difference type. The following form, which was found to be very robust and reasonably efficient, is used here:

$$A^{I \pm} = \frac{1}{2} A^I(Q^\pm) \pm \frac{1}{2} |A^I(\bar{Q})|. \quad (3.68)$$

It may be expected that due to these approximations the convergence rate will diminish, but numerical experiments revealed that, as far as convergence of the iteration procedure is concerned, the method performed well and turned out to be very robust.

When a local time step is applied to the LHS the time stepping method becomes similar to the approach of Jameson [90] in which an explicit subiteration scheme is employed. In this case the local time step should be set equal to:

$$\Delta\tau = \min(\Delta\tau_{\text{global}}, \Delta\tau_{\text{ref}}/\lambda), \quad \lambda = |U| + |W| + \alpha(|\nabla\xi| + |\nabla\zeta|). \quad (3.69)$$

Here temporal integration with a local time step is only needed to start the calculation. After a number of time steps, a very large global time step may be used to obtain fast convergence to the steady state.

In solving equation (3.64) a line relaxation is employed with direct inversion along  $\zeta$ -lines. The direct inversion should resolve stiffness due to the mesh stretching and implicitly handles the viscous terms which have an elliptic behavior. To account for the nature of signal propagation and for reasons of stability when the RHS is higher-order accurate, forward and backward sweeps are carried out in  $\xi$  direction. The forward sweep from  $\xi_1$  to  $\xi_{\max}$  is:

$$[L_i]\Delta\bar{Q}_i^{p+1} = -R_i - [L_i^-]\Delta\bar{Q}_{i-1}^{p+1} - \omega_l[L_i^+]\Delta Q_{i+1}^p, \quad (3.70)$$

which results in an intermediate solution  $\Delta\bar{Q}$ , followed by the backward sweep:

$$[L_i]\Delta Q_i^{p+1} = -R_i - \omega_l[L_i^-]\Delta\bar{Q}_{i-1}^{p+1} - [L_i^+]\Delta Q_{i+1}^p, \quad (3.71)$$

where  $\omega_l = 0.80$  to  $0.90$ . Due to the differences of the LHS from the exact Jacobian of the RHS only a part of the correction is used to update  $Q$ :  $Q^{p+1} = Q^p + \omega\Delta Q$ , where  $\omega = 0.30$  to  $0.60$ . Since in each sweep the equations along lines are solved this method may be called successive line over-relaxation (SLOR) and since forward and backward sweeps are carried out the method is also called symmetric successive over-relaxation (SSOR).

When the iteration is started from a poor initial guess (e.g. the freestream condition) more than one iteration is needed before the residual is updated. After a number of time steps the residual is updated after every sweep to obtain faster convergence. In this case the scheme represents a nonlinear relaxation method and  $\omega_l$  should be reduced to  $\omega_n = 0.30$  to  $0.40$ . The subiteration is stopped once  $|R^{n+1,p}|$  drops below a prescribed value. This criterion is different from the one applied in [90] where  $|R^{n+1,p}|/|R^{n+1,0}|$  is used. The present choice has been made after having observed that sometimes in the beginning of a subiteration the value of the unsteady residual is already very small, so that setting the convergence criterion relative to this level yields an unnecessarily stringent condition.

#### 3.7.4 NONSTATIONARY ACCELERATION METHODS

This method was developed from an optimization approach called the conjugate-gradient method. In this method the iteration matrix changes in each iteration level for which reason the method is called a nonstationary method. The original conjugate-gradient method applies only to a symmetric positive definite matrix. Starting from a zero initial guess the method will converge to the exact solution after  $N$  iterations, where  $N$  is the dimension of the iteration matrix. Therefore

the method is essentially a noniterative method. In practice, however, after several iterations the residual is expected to be lower than a prescribed tolerance and the iteration is stopped.

In the present study three types of nonstationary acceleration methods were applied [20]: Conjugate Gradient Squared (CGS), Bi-Conjugate Gradient Stabilized (Bi-CGSTAB) and Generalized Minimal Residual (GMRES). All these methods are applicable to nonsymmetric linear systems.

In this type of methods a sequence of orthogonal vectors is generated and used for searching the solution along this direction, which is obtained after an initial approximation of the solution is made and the correction to this approximation is made to be orthogonal to all base vectors. The base of these vectors, which is called a Krylov subspace, is  $(r, Ar, A^2r, \dots)$ , where  $r = b - Ax$ ,  $A$  is the Jacobian matrix and  $b$  is the RHS. The generated vectors are orthogonal to all vectors generated in the preceding iteration steps. In CGS and Bi-CGSTAB these vectors are generated using a simple recurrence relation involving the preceding iterations. In GMRES the Krylov subspace is explicitly generated using a modified Gram-Schmidt orthogonalization, similar to equation (3.52). This means that all generated vectors have to be stored to generate new ones. This constitutes the main drawback of the GMRES method. Although the CGS and Bi-CGSTAB do not suffer from this storage problem, the convergence of these methods is often irregular, especially for the CGS. The reader should refer to Barret et al. [20] for an excellent presentation of the methods.

In practical applications these methods are too expensive to use directly. A preconditioned problem is considered instead:

$$M^{-1}Ax = M^{-1}b, \quad (3.72)$$

where  $M$  is the preconditioner matrix. The preconditioner can have the form of the previously mentioned relaxation method or other types of iterative methods which will be presented later in this section. Because these nonstationary iterative methods are applied on top of the 'traditional' method, they may be regarded as an acceleration method. Since the linear equation does not need to be solved perfectly, only a small number of iterations is applied in the linear iteration loop. This in turn suggests that a method with a better uniformity of the convergence rate should be chosen. After considering this criterion, the CGS method, which has a highly irregular convergence rate, was dropped and was not elaborated further. The best acceleration is obtained using GMRES. In practice the linear iteration is stopped after 4 to 8 steps, implying that the penalty in the storage of all orthogonal vectors at each iteration step when using the GMRES method may be considered as moderate.

### 3.7.5 OTHER TYPES OF PRECONDITIONER

By relying on the acceleration obtained by applying the aforementioned nonstationary acceleration methods, a less CPU intensive preconditioner can be employed. Two types of preconditioners have been applied, namely the incomplete lower-upper decomposition (ILU) and the PGS iteration. The ILU sweeps follow equations (3.70

3.71), but with a different definition of the equation in a line  $[L_i]$ , as follows:

$$\begin{aligned} [L_i^{\text{fwd}}]\Delta Q_i &= -[A_{\zeta, i, j-\frac{1}{2}}^+]\Delta Q_{i, j-1} + [D_{i, j}]\Delta Q_{i, j} \\ [L_i^{\text{bwd}}]\Delta Q_i &= [D_{i, j}]\Delta Q_{i, j} + [A_{\zeta, i, j+\frac{1}{2}}^-]\Delta Q_{i, j+1}, \end{aligned}$$

leading to forward-backward sweeps:

$$\begin{aligned} [L_i^{\text{fwd}}]\Delta \bar{Q}_i^{p+1} &= -R_i - [A_{\zeta, i, j+\frac{1}{2}}^-]\Delta \bar{Q}_{i, j+1} - [L_i^-]\Delta \bar{Q}_{i-1}^{p+1} - [L_i^+]\Delta Q_{i+1}^p \\ [L_i^{\text{bwd}}]\Delta Q_i^{p+1} &= -R_i + [A_{\zeta, i, j-\frac{1}{2}}^+]\Delta Q_{i, j-1}^{p+1} - [L_i^-]\Delta \bar{Q}_{i-1}^{p+1} - [L_i^+]\Delta Q_{i+1}^{p+1}. \end{aligned}$$

The PGS sweep is a very simple relaxation in which only the block-diagonal matrix is taken as the iteration matrix:

$$\begin{aligned} [D_{i, j}]\Delta \bar{Q}_i^{p+1} &= -R_i + [A_{\zeta, i, j-\frac{1}{2}}^+]\Delta Q_{i, j-1}^{p+1} - [A_{\zeta, i, j+\frac{1}{2}}^-]\Delta Q_{i, j+1}^{p+1} \\ &\quad - [L_i^-]\Delta Q_{i-1}^{p+1} - [L_i^+]\Delta Q_{i+1}^{p+1}, \end{aligned} \quad (3.73)$$

where the latest value of  $\Delta Q$  is always used in the RHS. Equation (3.73) is used to sweep forward and backward.

### 3.8 TURBULENCE MODELING

Based on Bussinesq's approximation of the Reynolds stresses (see Appendix A), for turbulent flows the coefficient of viscosity consists of the coefficient of laminar viscosity and coefficient of eddy viscosity, see equation (2.41). The laminar coefficient of viscosity is calculated from the temperature using Sutherland's empirical law, i.e. equation (2.20). The coefficient of eddy viscosity has to be calculated from a turbulence model. In the present study two types of turbulence model have been applied: the algebraic turbulence model of Baldwin and Lomax [18] (BL) and the one-equation model of Spalart and Allmaras [157] (SA).

Mainly due to its simplicity, the BL turbulence model is perhaps the most applied turbulence model. By definition this turbulence model is not complete, which means that it requires a prior knowledge of the flow condition to tune the parameters involved in the model. The BL turbulence model was originally designed for two-dimensional turbulent boundary layers. It gives satisfactory results for attached flows, but less satisfactory results for separated flows. Advanced turbulence models, which require much more effort to obtain the coefficient of eddy viscosity, sometimes do not bring clear and definitive improvement compared to the BL turbulence model. Therefore, it is quite common that the BL model is used as a first step for further research in the application of a more advanced turbulence model. Concerning the way the turbulence length scale and velocity scale are calculated the BL turbulence model is usually called 'not local'. It means that the coefficient of eddy viscosity at a certain point depends to a large extent on the flow and geometrical data at other locations. The calculation of the length and velocity scale requires the normal distance to the wall, or to the center of the wake in case of wake flow, and the

maximum value of a certain function, the so-called BL  $F$ -function, i.e. equation (C.7), in the boundary layer or wake. The detailed explanation concerning the application in the present study is presented in appendix C.

The SA turbulence model [157] is relatively new compared to the BL model. It requires the solution of a transport equation for the working variable  $\tilde{\nu}$ , simultaneously with the flow equations of section 2.5.2, from which the coefficient of eddy viscosity can be calculated in a simple way. Compared to the BL turbulence model the SA model may be considered as 'local'. The traditional one-equation turbulence models solve the transport equation for the turbulent kinetic energy  $k$ , which still requires a 'non local' method to calculate the eddy viscosity, see e.g. Wilcox [175]. The SA turbulence model was designed based on empiricism and dimensional analysis [157]. Contrary to BL this model is complete, i.e. does not require a prior knowledge of the flow. For attached flows the SA turbulence model sometimes gives less accurate results than the BL model [175]. For separated flows mixed success has been reported by Bartels [21], Ekaterinaris et al. [55], Rumsey et al. [152], Rumsey and Vatsa [153], but in general the SA model is better than the BL model. The description of the SA model as applied in the present study is also discussed in appendix C.

### 3.9 SUMMARY OF THE PRESENT CUA METHOD

Summarizing the developments presented in the previous sections, the following methods have been adopted in the present CUA method:

- A second/third-order accurate implicit temporal integration method employing an implicit subiteration scheme. The subiteration scheme employs linear or nonlinear line relaxation methods and a nonstationary iteration method, i.e. Bi-CGSTAB and GMRES with ILU or Jacobi preconditioners.
- A second-order spatial discretization, which reduces to first-order in the vicinity of discontinuities, employing a cell-centered finite volume method. The inviscid flux is discretized using either van Leer's FVS, AUSM FVS, Roe's FDS or the hybrid van Leer-Osher FV/DS. The viscous term is discretized, using the thin-layer approximation, in a central manner.
- The mesh deformation is handled using either an elliptic method or the spring analogy method.

### 3.10 NUMERICAL RESULTS

This section presents some results of the present CUA methods including those of flow simulation and mesh deformation. An extreme test case for the mesh deformation has been selected to demonstrate its robustness and therewith its applicability to routine applications.

Subsequently various aspects of methods for flow simulation will be validated: relaxation method, inviscid flux method, moving mesh method, time accuracy, steady



and unsteady flows in an inviscid as well as in a viscous mode. Some demanding test cases have been selected to demonstrate the robustness of the present method. Results of the inviscid flow test case will be compared to results of well-known methods employing a similar flow model. The viscous flow results will be compared to both numerical results and experimental data.

### 3.10.1 TEST OF DYNAMIC MESH ALGORITHMS

The purpose of this section is to test the dynamic mesh algorithms of the present method in deforming the initial mesh. The chosen quality parameters are tested to show their effectiveness. The most important characteristic is the robustness and efficiency: the dynamic mesh deformer should not produce mesh folding and should preserve the quality of the mesh point distribution, and all this without requiring an excessive effort. The orthogonality at the solid surface is desirable but in general it is not a strict requirement.

A mesh for calculations employing the Euler equations for the flow around the RAE2822 airfoil is considered. The dimensions of the mesh are  $160 \times 30$ . The main reason to use a mesh for the Euler method is the experience that it is more difficult to maintain the quality of a relatively coarse mesh than of a fine mesh. Certainly it is more difficult to solve equation (3.2.3) and equation (3.5) on a fine mesh but the method employed in the present study, which is of an implicit type, performs efficiently for both coarse and fine meshes.

Figure 3.12 shows the initial mesh for the present test case. The details around the nose, which shows the orthogonality of the mesh near the surface, are presented on the right. Starting from this zero angle of attack, the airfoil is forced to pitch nose-up about the 0.25 chord point in two steps of 5 deg displacement. In the following paragraphs the meshes at the last position, i.e. 10 deg pitch angle, are presented.

Figure 3.13 shows the results using the elliptic method without the surface forcing function. The solution of the elliptic equation, equation (3.2.3), proceeds by generating a first guess using an algebraic method and subsequently 5 PGS iterations are carried out. The mesh distribution is preserved by the method but the orthogonality is less preserved. Figure 3.14 shows the results using the elliptic method with the surface forcing function. It can be seen that the mesh orthogonality near the airfoil surface has been improved relative to the case without surface forcing function.

Figure 3.15 shows the results using the spring analogy with the original solution method of Batina [24]. Although a relatively large number of iterations has been applied the result is still not satisfactory. Near the trailing edge mesh folding occurs which would certainly cause a breakdown in the flow calculation. This situation is improved using the proposed modification of the predictor step by solving the spring equation in the  $\zeta$ -direction. Subsequently only two iterations have been applied for the complete equations. The result is shown in figure 3.16. Now a better distribution of points has been obtained near the leading edge and mesh folding close to the trailing edge does not occur.

From these exercises some conclusions may be drawn: the source functions

$P(\xi, \zeta)$  and  $Q(\xi, \zeta)$  are indeed the proper quality parameters to maintain the mesh point distribution and the proposed surface forcing function improves the orthogonality close to the surface. Similarly, the spring stiffnesses preserve the mesh point distribution of the initial mesh. Against expectation, the elliptic method only needs slightly more CPU time compared to the spring analogy method. This may be explained by the geometry and the motion being quite simple so that the initial guess made by the algebraic method, a transfinite method using the Hermite polynomial, already gives a good mesh. Therefore only a small number of iterations is required to smooth the mesh. Furthermore, the results using the elliptic method (with surface forcing function) has a better quality especially close to the solid surface. This suggests that the elliptic method is better for two-dimensional cases. However, for three dimensional cases, where the boundaries and the motion of the surface are complex, the spring analogy may be better on the whole than the elliptic method.

### 3.10.2 COMPARISON OF INVISCID FLUX METHODS

In this section the performance of the various inviscid flux methods is discussed. The comparison is carried out in both the Euler mode as well as in the Navier-Stokes mode. The important parameters are the shock position and the shock strength, which can be seen from the pressure or Mach number distribution. Another aspect which is of paramount importance for viscous flow calculations is the performance in capturing viscous layers. This is judged by observing the skin friction and the isomach contours. A more detailed inspection, looking at the boundary layer profile, is not carried out because from the two parameters some conclusive results can be already obtained.

For the test case in the Euler mode the flow past an NACA 0012 airfoil at  $M_\infty=0.85$  and  $\alpha=1$  deg is considered. Results from the AGARD Compendium of Test Cases [4] are used as a reference. In this test case two shock waves are present. This test case has been chosen because the position of the shocks is obviously very sensitive, as appearing from the various results in [4] for this test case. The result which was concluded in [4] as the best result is used here as a reference. The dimensions of the mesh for the present calculation are  $140 \times 30$ , with 100 points on the surface of the airfoil.

Figure 3.17 shows the comparison of the chordwise distributions of the pressure coefficient and the Mach number. All methods show a good agreement for the shock position and the shock strength. No significant difference is shown as far as the pressure distribution is concerned. For the Mach number distribution the results still show some differences downstream of the shock. The possible explanation for this difference is the incompatibility between the flux formula at the solid surface and the flux formula in the field.

Figure 3.18 and figure 3.19 show the isobars and isomach contours for this test case. The isobars obtained by the various methods do not show significant differences. Inspecting the lower side shock wave, the weak one, the FVS schemes and the hybrid scheme seem to capture the shock somewhat sharper than the Roe FDS. The isomach contours also show some differences. The van Leer FVS result shows a sort

of numerical boundary layer which can be seen from the way the contours approach the solid surface. The AUSM-FVS result shows wiggles close to the solid surface which suggests that the numerical dissipation is too low. The possible explanation of this deficiency is that the stabilizing term of the AUSM FVS is a function of Mach number. Close to the surface the flow is almost parallel to the lines of constant  $\zeta$  which implies that the Mach number variation in the  $\zeta$ -direction is very small. This may have caused the stabilizing term of AUSM FVS to be ill-defined. Finally the results of Roe FDS and the hybrid method are almost identical.

The viscous flow case is the transonic flow past the RAE 2822 airfoil at  $M_\infty=0.729$ ,  $\alpha_{\text{exp}}=2.92$  deg and  $Re_\infty=6.5\times 10^6$ . As a reference the results of the NLR MUTU2D Navier-Stokes method presented by Haase et al. [69] are used. The dimensions of the mesh are  $160\times 60$ , with 100 points on the airfoil surface. The calculations have been carried out at a corrected angle of attack,  $\alpha_{\text{corr}}=2.31$  deg, which was suggested by Cook et al. [38].

Figure 3.20 shows the comparison of chordwise distributions of the pressure and skin friction coefficients for the viscous flow case. Except the result using van Leer's FVS, all methods show a good agreement concerning the shock position and shock strength. The shock strength using van Leer's FVS is a bit weaker and the position is slightly in front of the other results, which suggests that the dissipation is too high. The inferiority of van Leer's scheme can be seen clearly in the skin friction coefficient.

Figures 3.21 and 3.22 show the isobars and isomach contours, respectively. The isobars again show no significant differences between the methods. The differences in the isomach lines can only be seen in the result using van Leer's FVS. The deficiency of the amount of dissipation of the AUSM FVS, which is observed in the inviscid test case, does not seem to affect the results.

The results of the test cases of this section lead to the following conclusions. For inviscid flow applications, as far as the surface pressure distribution is concerned, all methods give satisfactory results. However, the flow field data reveal the inadequacy of the dissipation of the AUSM FVS and the excessive dissipation of van Leer's FVS. For viscous flow applications all methods except van Leer's FVS give satisfactory results. This means that only Roe's FDS and the hybrid van Leer/Osher FV/DS perform consistently well for both inviscid and viscous flow applications. Because the hybrid method is much more complex than Roe's FDS method, it is concluded that Roe's FDS is the most suitable method for the present study. The Roe FDS will be used throughout the rest of this chapter.

### 3.10.3 COMPARISON OF RELAXATION METHODS

The steady viscous flow case considered in the previous section is again used for the comparison of the relaxation methods. The efficiency, in terms of convergence rate, of the various relaxation methods applied in this study has been investigated. The global time step has been set at a very large value,  $\Delta\tau=10^6$ , since only the steady state is of interest. The combination of the stiff viscous mesh and the large time step makes the test case very hard. For this reason the results would also indicate

the robustness of the methods.

The results obtained using the standard SSOR method are compared to the ones obtained using the nonstationary iteration methods of GMRES and Bi-CGSTAB. The CGS method has not been included since the convergence rate is very nonuniform and the result is almost useless. The CGS method gives a reasonable result when a moderate time step size is used. The preconditioner for the nonstationary iteration methods is ILU.

Figure 3.23 shows the convergence of the lift coefficient and figure 3.24 shows the convergence of the residual of the mass conservation equation. Each of them are plotted against the iteration number and the CPU time. The indicated CPU time is normalized with respect to the one required for the calculation of the residual. Thus it more or less represents the CPU time of a step of an explicit method. The figures indicate that the Bi-CGSTAB can not even let converge the residual, thus it is not appropriate for this large time step case. From the plots against the iteration number, GMRES clearly shows a faster convergence compared to the standard SSOR method. But since the computational work per iteration of the GMRES method is higher than that of the SSOR method, this advantage does not show up strongly in the plots against CPU time. The other aspect of GMRES is the higher memory requirement compared to the SSOR method since the solutions of the former linear iterations have to be stored to form the appropriate Krylov-space.

From the test case presented in this section it is concluded that the SSOR method is in general superior to the GMRES method. SSOR is a good approximation to the perfect inversion of the Jacobian matrix in that a nonlinear relaxation can be applied (only one sweep of the SSOR method is necessary before the nonlinear residual is updated). The fact that the Jacobian matrix is not a true Jacobian of the residual, which means that even with a perfect inversion quadratic convergence would not be achieved, may have contributed to this situation.

#### 3.10.4 STEADY VISCOUS FLOW

The validation of the method in predicting the pressure and sectional coefficients for steady flow is presented in this section. The flow past an RAE2822 airfoil is considered at  $M_\infty=0.729$ ,  $\alpha_{\text{exp}}=2.92$  deg and  $Re_\infty=6.5\times 10^6$ . Geometrical data and experimental data for this condition, which is known as case 6.1, are available in Cook et al. [38]. The transition was forced at 3% chord from the leading edge **on both upper and lower surface. A comparison with another method is provided** by the result of the NLR MUTU2D Navier-Stokes method described in Haase et al. [69]. All calculations have been performed at a corrected angle of attack accounting for tunnel wall effects,  $\alpha_{\text{corr}}=2.31$  deg.

The calculation has been carried out on a C-mesh of  $189\times 60$ , with 150 points on the airfoil. The outer boundary is 40 chords away which from the experience already gives converged values of aerodynamic forces. Figure 3.25 shows the part of the mesh close to the airfoil section. The distance away from the solid wall to the first mesh point in normal direction is about  $10^{-6}$  at the leading edge and  $10^{-5}$  at the trailing edge. This results in the maximum  $y_1^+$  that is  $\mathcal{O}(1)$  during the calculation.

The result of MUTU2D is obtained using a C-mesh of  $240 \times 72$ , with 209 points on the airfoil and with the outer boundary placed only 10 chords away. The short distance of the outer boundary for NLR MUTU2D is allowed due to the embedding of a vortex correction in the far-field boundary conditions.

Figure 3.26 shows the comparison of the present results, the experimental data and the NLR MUTU2D results. Overall, good agreement has been obtained regarding the shock position and the shock strength. The pressure distributions on the lower surface of both calculation methods are in excellent agreement with experimental data. The shock position predicted by the present method is a bit forward, which is closer to the experimental data, than the one of NLR MUTU2D. The latter method captures the pressure peak at the leading edge better. The comparison of the aerodynamic coefficients is shown in table 3.2.

	$C_L$	$C_M$	$C_D$
present method	0.748	-0.098	0.0150
NS-NLR (MUTU2D)	0.777	-0.105	0.0149
experiment	0.743	-0.095	0.0127

Table 3.2: Comparison of the aerodynamic coefficients of the present method, the NLR MUTU2D and the experiment of [38]. RAE 2822 airfoil at  $M_\infty=0.729$ ,  $Re_\infty=6.5 \times 10^6$   $\alpha_{\text{exp}}=2.92$  deg

The lift and the moment coefficients of the present method are closer to the experimental data, which can be explained by the better prediction of the shock position. Although the present method captures the pressure peak at the leading edge less satisfactorily than the MUTU2D, it seems that it does not give much contribution to the lift and moment because of the misalignment of the normal vector at this part of the surface. The predicted drag coefficient is less satisfactory, probably because the mesh is not fine enough. The difference between the results of the present method and of MUTU2D may be attributed to the difference in the CFD modeling, the size of the mesh and the outer boundary conditions.

It may be concluded that the present method gives satisfactory results in predicting the aerodynamic forces for this steady flow case.

### 3.10.5 UNSTEADY FLOW

The most important application for which the method has been developed is unsteady flow. This section presents the validation of many aspects of the present method. First the applications using large time steps are validated for a fixed mesh, after that for a deforming mesh and finally the robustness and efficiency of the method are demonstrated.

#### STATIC MESH

The well-known test case for unsteady flow is the 18% thick circular arc airfoil of Seegmiller et al. [156] and McDevitt et al. [108]. This case is a good validation

test for the time accuracy of the basic temporal integration method, since no airfoil motion is present. This type of flow is usually called transonic buffet or shock induced oscillation (SIO). As shown in the experiment, at a certain range of Mach number the flow is unsteady with a distinct reduced frequency component.

This case has been suggested also by many authors as a good test case for the implementation of turbulence models. The flow condition is  $\alpha=0$  deg,  $M_\infty=0.76$  and  $Re_\infty=11\times 10^6$ . The present result is obtained using a C-mesh of  $140\times 60$  with 100 points on the airfoil. The experiment was carried out in a wind tunnel with upper and lower walls that were contoured to match the inviscid streamlines at  $M_\infty=0.775$ . Wall interference effects were reduced thereby, although not completely eliminated. The result of the calculation is influenced strongly by the distance of the outer boundary, where the freestream condition is imposed. Some authors, e.g. Arnone et al. [14], suggest 10 chords to be a good distance, so this is used here as well.

The instantaneous Mach contours at eight time levels during the simulation are presented in figure 3.27 showing the shocks, strengthening when moving upstream and weakening when moving downstream, and the waving wake. The time histories of the lift and moment coefficients are shown in figure 3.28. This result was obtained using a time step of 0.10 with 8 subiterations per time step producing a maximum CFL number of about 20,000. The simulation was carried out up to a dimensionless time of 50. Subsequently, another 10 time steps were simulated to record the field data. The symbols in figure 3.28 show the time levels at which the instantaneous Mach contours have been plotted in figure 3.27. Note that the time step of 0.10 is much larger than that commonly presented in the literature.

The chronology of the flow simulation can be summarized as follows. The simulation is started from a freestream initial condition. Proceeding in time, symmetric shock waves are formed at the two sides of the airfoil. For a short time the flow remains symmetric. After the shocks have strengthened and caused shock-induced separation which spreads up to the trailing edge, a nonsymmetric flow is started. This suggests that the wake is the main means of communication between the two shock waves. Proceeding further in time, the nonsymmetric condition continues, characterized by a weakening of one shock, strengthening of the other and a deflection of the wake. The sequence in figure 3.27 starts at  $ta_\infty/c=50.5$  when the airfoil upper side has a strong shock together with a massive shock-induced separation which deflects the wake to its side. This deflection of the wake causes the flow at the **other side (lower side) to fully reattach and thus to create a strong shock, figure 3.27** at  $ta_\infty/c=50.5\sim 53.5$ . After that this shock in turn starts massive shock-induced separation which deflects the wake toward the upper side at  $ta_\infty/c=54.5\sim 56.0$ . The wake deflection then causes full reattachment of the flow on the upper side, and so the phenomenon repeats itself. The alternating massive shock-induced separation sheds vorticity downstream in a manner similar to the von Kármán vortex street for low speed flow about bluff bodies. Although the flow is highly unsteady, the airfoil is stationary, so that the simulated flow may be considered as an natural aerodynamic mode of the flow.

The reduced frequency which is calculated by identifying the period of oscillation,

is presented in table 3.3. This value of the reduced frequency is well inside the range

freestream condition		$k$
present method	outer boundary at 10 chords away	0.250
experiment	curved-wall tunnel	0.245

Table 3.3: Comparison of reduced frequency obtained using the present method with the experiment of [108]. Circular arc airfoil, 18% thickness ratio at  $M_\infty=0.76$  and  $Re_\infty=11\times 10^6$ ,  $140\times 60$  C-mesh

of calculation results commonly presented in the literature, [105, 156]. This suggests the validity of the present temporal integration method and turbulence model.

#### FORCED VIBRATION

The response of a rigid NACA 0012 airfoil to forced oscillations is analyzed here to assess the performance of the computational method. The inviscid flow results were obtained using a mesh with dimensions of  $140\times 30$  and the viscous flow calculations were carried out on a mesh of  $140\times 60$ . Both meshes have 100 points on the airfoil surface. The outer boundary is placed at 40 chords away from the airfoil. For the viscous flow calculations the average distance away from the solid wall to the first mesh point in the normal direction is about  $6\times 10^{-6}$  chord.

**VALIDATION OF DYNAMIC MESH ALGORITHM** To validate the dynamic mesh algorithm an inviscid flow case of an oscillating NACA 0012 airfoil is considered. The oscillation is a pitching motion about 0.25 chord at  $M_\infty=0.754$ ,  $\alpha_{\text{mean}}=2.00$  deg,  $\alpha_{\text{amp}}=2.50$  deg and  $k=0.082$  based on semichord. The coefficients  $C_L$  and  $C_{M,0.25}$  at the two dynamic mesh strategies, the rigid mesh and the spring analogy are compared. In the case of the spring analogy, the outer boundary of the mesh is held fixed. Since the airfoil does not deform, both methods should give similar results.

Figure 3.29 shows a comparison of  $C_L$  and  $C_{M,0.25}$  for the two dynamic mesh strategies as a function of the angle of attack. Virtually no difference can be observed. It should be noted that the moment loop reveals a strong nonlinearity in the flow with a shock moving over a significant trajectory.

The present results were obtained using a relatively large time step, 24 steps per cycle, thus an error in the mesh handling and the outer boundary would be noticed immediately. Therefore the conclusion may be drawn that the current treatment of the time-dependent metrics and the outer boundary is correct.

**UNSTEADY INVISCID FLOW** An example of an unsteady inviscid flow application is shown in figure 3.30 for the conditions mentioned before. This is the case which is used for the validation of the dynamic mesh algorithm. Results of the present method are compared with those of TULIPS, an FP method described by Schippers [154], an extended version of TULIPS described by Westland and Hounjet [173] and the DLR-Euler method of Polz [130]. The extended TULIPS method employs the

Clebsch potential with entropy and vorticity corrections for modeling strong shock waves. The DLR-Euler method uses van-Leer's FVS for the inviscid flux modeling and an explicit method to march in time. Figure 3.30 shows the comparison of the lift and moment coefficients.

The results of the present method, the DLR-Euler method and the extended TULIPS method agree very nicely. The TULIPS result shows a consistent difference when compared to the results of the Euler methods. The hardly noticeable difference between the results of the present implicit method and the explicit method of DLR-Euler confirms the applicability of the present temporal integration strategy. The present result was obtained using 48 time steps per period of oscillation and at each time step 8 subiterations were employed. The time needed to run one cycle of oscillation was less than 2 minutes on a Silicon Graphics Inc. (SGI) workstation with R8000/R8010 processors.

The adequacy of the present method for the current case is demonstrated further in figure 3.31 and in table 3.4 which illustrates the computational efficiency for

$\Delta\tau/\text{cycle}$	subiteration	$\partial Q/\partial\tau$	CPU time (min/cycle)
48	8	2nd order	1.74
24	8	2nd order	0.87
12	12	3rd order	0.64
8	12	3rd order	0.43

Table 3.4: CPU time comparison of running strategies shown in figure 3.31

several variations of the iteration strategy. The lift and moment coefficients show a very good agreement, even for an extremely low number of time steps per period

**UNSTEADY VISCOUS FLOW** Two cases are considered in this section. The first case pertains again to transonic flow conditions,  $M_\infty=0.754$ ,  $Re_\infty=5.7\times 10^6$ ,  $\alpha_{\text{mean}}=2.00$  deg,  $\alpha_{\text{amp}}=2.50$  deg and  $k=0.082$ . The experimental result is taken from Wood [177]. The transition was forced at 10% chord, both on the lower and on the upper surface. The calculation employs the Baldwin-Lomax turbulence model.

Figure 3.32 shows the comparison of the experimental and the calculated results. The inviscid flow results do not agree with the viscous flow results nor with the measurement. Concerning the viscous flow results, only during the upstroke **the lift and moment are reproduced relatively well. The discrepancy between the results starts near the maximum angle of attack and is most probably due to the inadequacy of the algebraic turbulence modeling to treat a strong shock-boundary layer interaction properly. During the downstroke only the second half of the stroke the lift coefficient is satisfactorily predicted.**

Another application of the present Navier-Stokes solver is shown in figure 3.33 for an AGARD standard test case of transonic viscous flow, case 3 of [97]. The flow conditions are  $M_\infty=0.60$ ,  $Re_\infty=4.8\times 10^6$ ,  $\alpha_{\text{mean}}=4.86$  deg and the flow is fully turbulent. The mode of vibration is a pitching oscillation about 0.25 chord with  $\alpha_{\text{amp}}=2.44$  deg and  $k=0.081$  based on semichord.



Figure 3.33 shows the results of the test case. Good agreement between both calculated results has been obtained for both the lift and moment coefficient. The agreement with the experimental data is also good as far as the lift coefficient is concerned, but less satisfactory for the moment coefficient. The present results were obtained using 400 steps per period of oscillation with 4 subiterations in each time step. The CPU time was 35 minutes on an SGI (R8000/R8010 processors) workstation. The maximum CFL number during the calculation was about 55,000. The adequacy of the present method for the current case is presented in figure 3.34 and in table 3.5 where the computational efficiency is demonstrated for several iteration strategies. The lift coefficient shows a very good agreement even for a very

$\Delta\tau/\text{cycle}$	subiteration	$\partial Q/\partial\tau$	CPU time (min/cycle)
400	4	2nd order	35.45
100	4	2nd order	8.83
24	12	3rd order	6.25
16	12	3rd order	4.46

Table 3.5: CPU time comparison of running strategies shown in figure 3.34

low number of steps per period. The moment coefficient is more sensitive to the choice of the time step and iteration strategy. Some differences are apparent, but the main features appear to be captured well enough by all strategies.

It is generally known that due to the accuracy in resolving the shear layer, an FDS method needs less mesh points to reach a certain accuracy compared to van Leer's FVS method which is more diffusive and therefore more robust. Therefore the results of Rumsey and Anderson [151] have been included in figure 3.33, which were obtained with a Thin-Layer Navier-Stokes method using van Leer's FVS to enable large time steps. The present result was obtained using FDS (with a coarser mesh) and moreover with a larger time step, thus requiring less CPU time compared to the method of [151].

**DYNAMIC STALL** Formally the TLNS flow model is not applicable to the case of dynamic stall, as the flow is massively separated and the concept of the thin-layer approximation is not valid anymore. For such cases the full Navier-Stokes equations (FNS) should be employed. Nevertheless, many authors still employ TLNS for this case. One reason for this is that when the flow is separated and vortices are formed, convective terms will become dominant, which reduces the role of viscosity. In other words: it reduces the improvement in applying FNS compared to TLNS. Another reason is that for FNS usually not enough points are used in the streamwise direction to resolve the flow separation, so that accurate FNS results would not be obtained.

The deep dynamic stall case considered by Ekaterinaris et al. [55] is used as a test case. An NACA 0015 airfoil is immersed in subsonic flow at a low Mach number of 0.30 and a Reynolds number of  $2 \times 10^6$ . In the experiment a turbulence trip was applied very close to the leading edge. This justifies the use of fully turbulent flow in the computation. The mean condition is beyond the stall condition at  $\alpha_{\text{mean}}=15$

deg. The airfoil was excited sinusoidally in a pitching oscillation about 0.25 chord with an amplitude of  $\alpha_{\text{amp}}=4.20$  deg and a reduced frequency of  $k=0.10$ . The employed mesh was  $160 \times 60$  with 140 points along the surface. The Spalart-Allmaras turbulence model was employed for the simulation. The steady mean flow was first calculated and then three periods of oscillation were carried out. The time step was set at 256 steps/period with 12 to 24 subiterations. The results of the second and third cycles showed negligible differences.

Figure 3.36 presents the instantaneous density contours at several times during the oscillation starting at  $\alpha(0) = \alpha_{\text{mean}}$ . In agreement with the experiment and the result of Ekaterinaris et al. [55], a vortex sheet is formed originating from the leading edge, and rolling up into the dynamic stall vortex at some distance above the trailing edge, before the maximum angle of attack is reached at  $t = 7T/32$ . The flow separation at the upper surface causes the reduction of lift and moment, see also figure 3.35. The stall vortex induces the formation of the so-called trailing edge vortex with a circulation of opposite sign. The figure at  $t = 8T/32$  shows this situation. Then the feeding of the vortex sheet diminishes. This and the interaction of two vortices result in the weakening of both vortices until they disperse and are transported downstream at about  $t = 11T/32$ . The interaction of the vortices causes the oscillation in lift and moment which can be seen in figure 3.35. After that the flow on the upper surface begins to reattach. These flow developments during the oscillation match with the experimental observation: massive flow separation before maximum angle of attack, shedding of leading edge vortex and forming of trailing edge vortex at the maximum angle of attack right before the down stroke begins.

The comparison of the lift and moment about 0.25 chord coefficients is presented in figure 3.35. Comparisons are provided by the computational and experimental results of Ekaterinaris et al. [55]. The computational result [55] was also obtained using a Thin-Layer Navier-Stokes flow method with the original Spalart-Allmaras one-equation turbulence model on a mesh of  $311 \times 91$  and with 16,000 time steps per period. Although the trends are well captured, the quantitative comparison is **not more than fairly good. Already at the mean condition the calculated lift of** both the present method and the computational result of [55] are too high. Moreover, the present result shows an oscillation in some part of the down stroke. A similar behavior was also obtained in [55] for the Johnson-King half-equation model, the Baldwin-Barth one-equation model and the  $k-\omega$  SST two-equation model. The recent paper by Ko and McCroskey [93] which employed also the Spalart-Allmaras turbulence model for this deep dynamic stall case showed also this oscillation. Considering the aeroelastic problems related to dynamic stall, e.g. for helicopter rotors and wind turbine blades, where the area of the loop is of main interest, the present results may be considered good compared to the experiment.

## 3.10.6 FIGURES

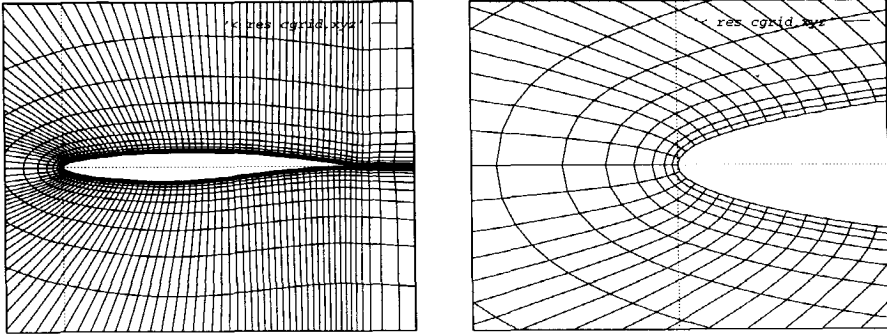


Figure 3.12: The initial  $160 \times 30$  mesh around RAE 2822 airfoil for the mesh deformation test

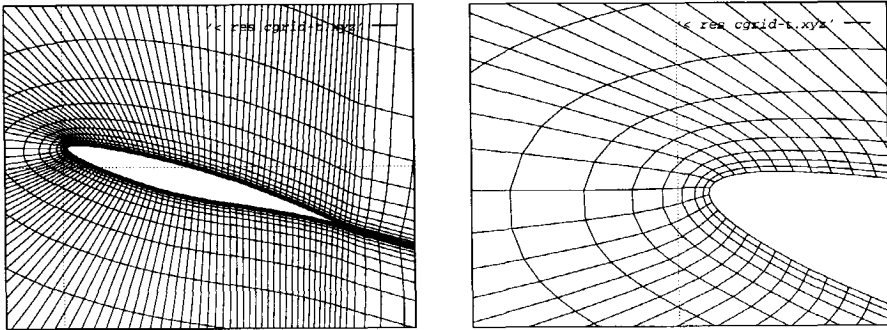


Figure 3.13: The deformed  $160 \times 30$  mesh around RAE 2822 airfoil using the elliptic method without surface forcing function

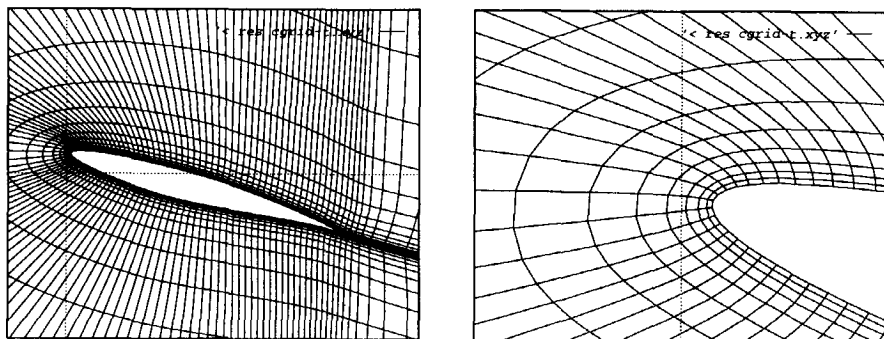


Figure 3.14: The deformed  $160 \times 30$  mesh around RAE 2822 airfoil using the elliptic method with surface forcing function to maintain orthogonality

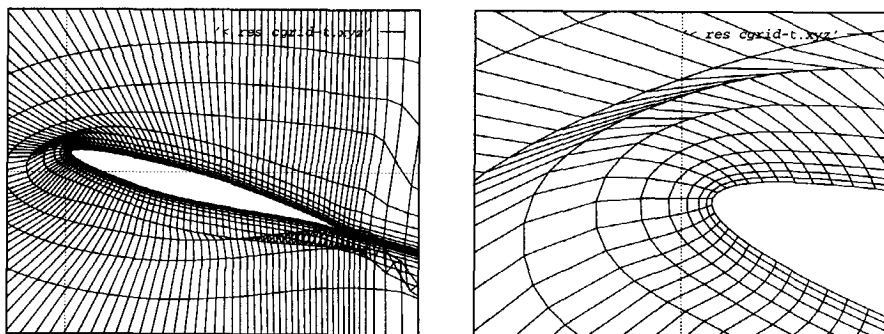


Figure 3.15: The deformed  $160 \times 30$  mesh around RAE2822 airfoil using the spring analogy with extrapolation predictor

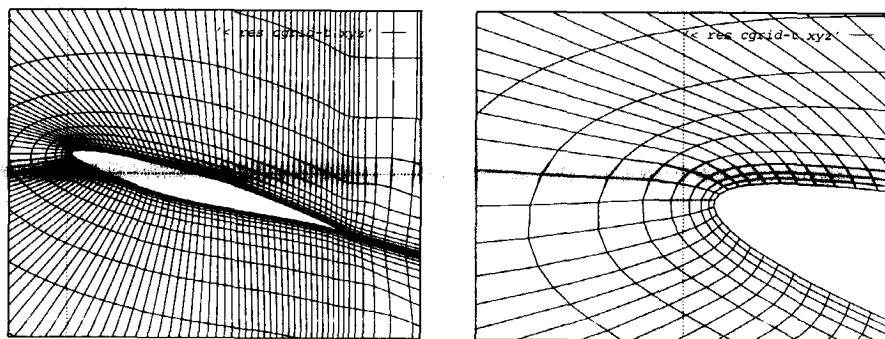


Figure 3.16: The deformed  $160 \times 30$  mesh around RAE2822 airfoil using the spring analogy with the new 'direct z-solve' predictor

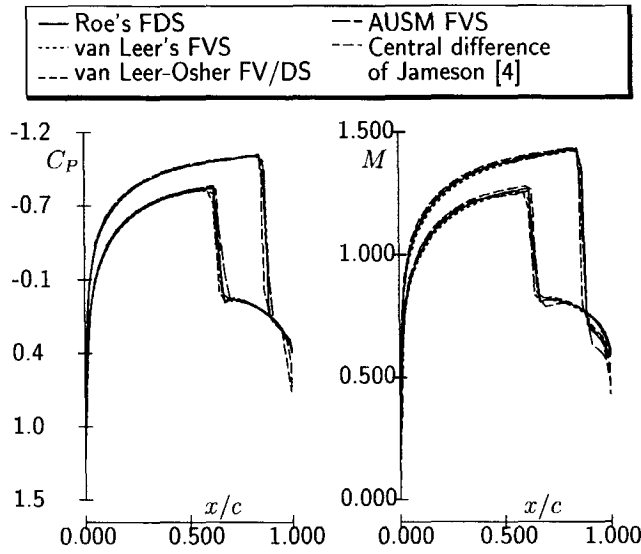


Figure 3.17: Comparison of pressure distributions and Mach number obtained with various inviscid flux methods for the inviscid flow test case. NACA 0012 airfoil at  $M_\infty=0.85$ ,  $\alpha=1.00$  deg,  $160\times60$  C-mesh

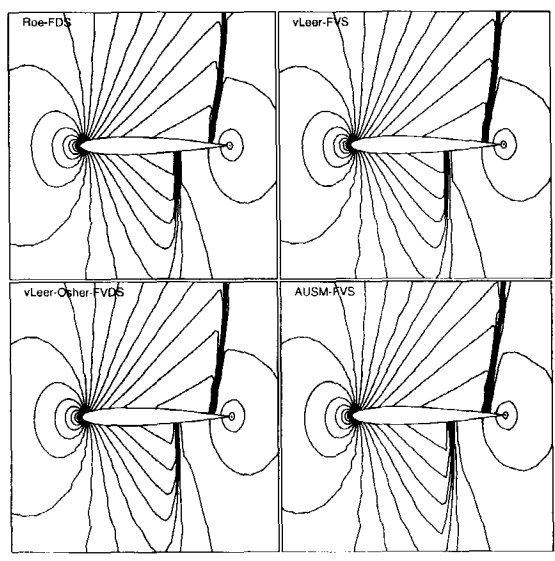


Figure 3.18: Comparison of isobars obtained with various inviscid flux methods for the inviscid flow test case. NACA 0012 airfoil at  $M_\infty=0.85$ ,  $\alpha=1.00$  deg,  $160\times60$  C-mesh

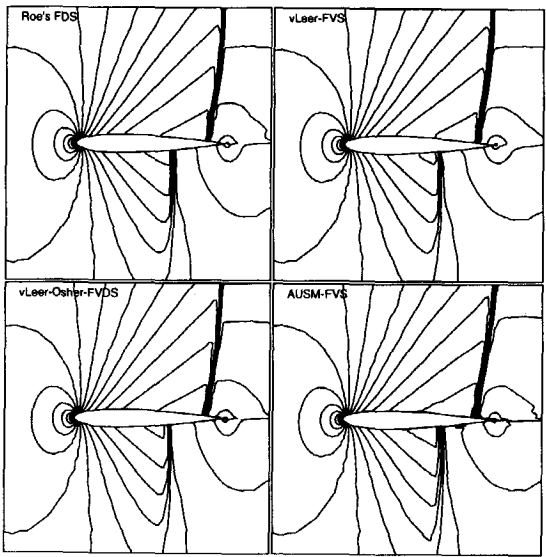


Figure 3.19: Comparison of isomach contours obtained from various inviscid flux methods for the inviscid flow test case. NACA 0012 airfoil at  $M_\infty=0.85$ ,  $\alpha=1.00$  deg,  $160\times60$  C-mesh

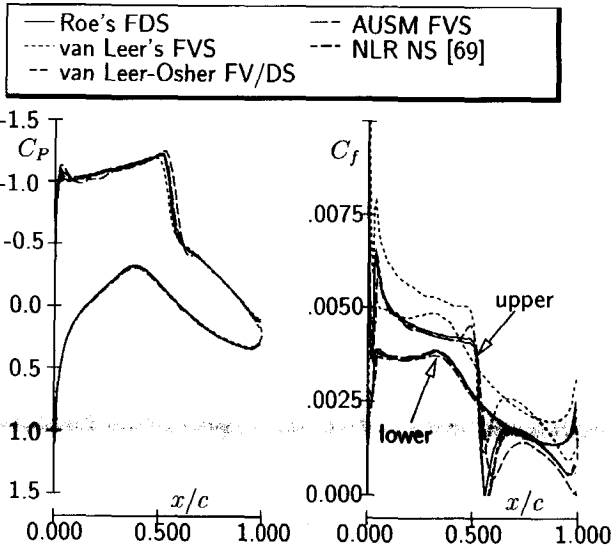


Figure 3.20: Comparison of pressure distributions and skin friction obtained from various inviscid flux methods for the viscous test case. RAE 2822 airfoil at  $M_\infty=0.729$ ,  $\alpha_{exp}=2.92$  deg and  $Re_\infty=6.5\times10^6$ ,  $160\times60$  C-mesh

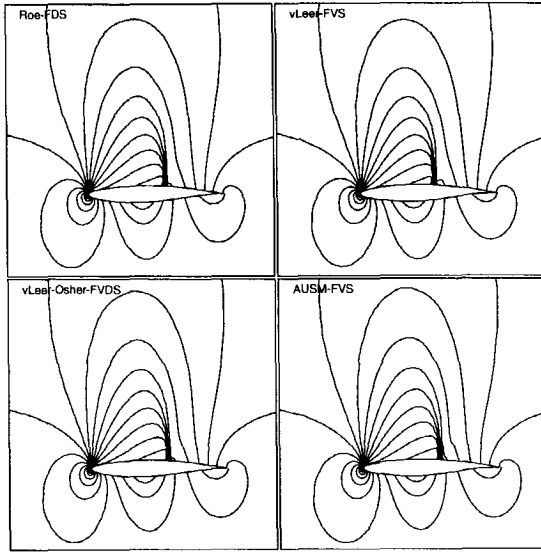


Figure 3.21: Comparison of isobars obtained from various inviscid flux methods for the viscous flow test case. RAE 2822 airfoil at  $M_\infty=0.729$ ,  $\alpha_{\text{exp}}=2.92$  deg and  $Re_\infty=6.5 \times 10^6$ ,  $160 \times 60$  C-mesh

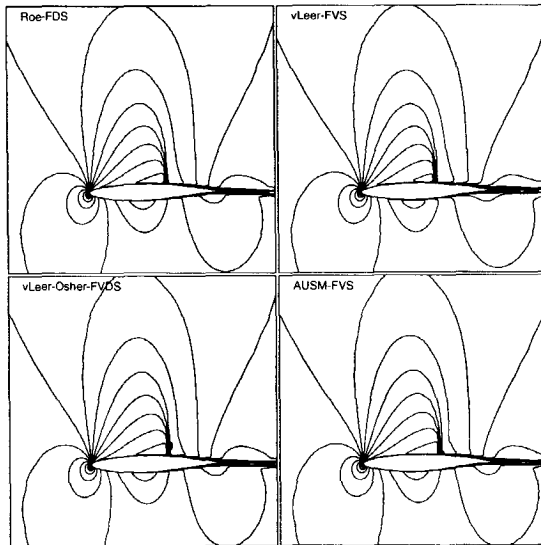


Figure 3.22: Comparison of isomach contours obtained from various inviscid flux methods for the viscous flow test case. RAE 2822 airfoil at  $M_\infty=0.729$ ,  $\alpha_{\text{exp}}=2.92$  deg and  $Re_\infty=6.5 \times 10^6$ ,  $160 \times 60$  C-mesh

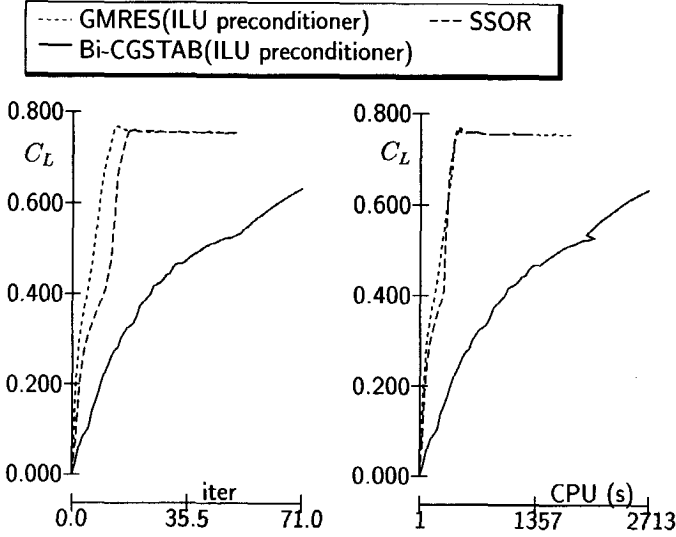


Figure 3.23: Convergence rates of the lift coefficient against the iteration number and CPU time for various relaxation methods. RAE 2822 airfoil at  $M_\infty=0.729$ ,  $Re_\infty=6.5 \times 10^6$  and  $\alpha_{corr}=2.31$  deg,  $160 \times 60$  C-mesh

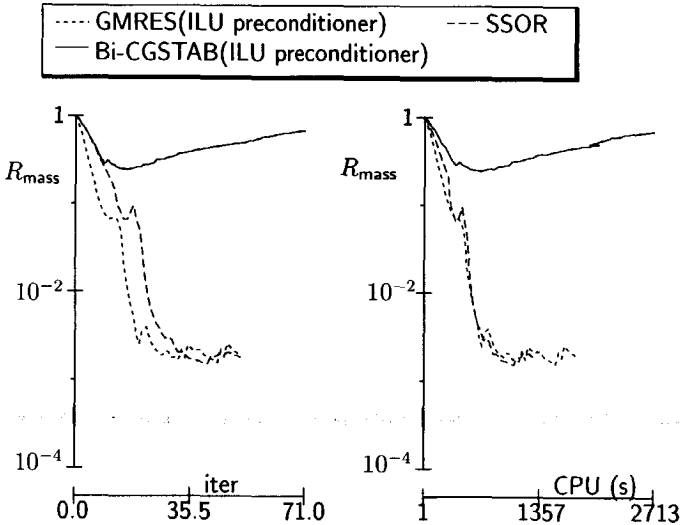


Figure 3.24: Convergence rates of the residual of the mass conservation equation against the iteration number and CPU time for various relaxation methods. RAE 2822 airfoil at  $M_\infty=0.729$ ,  $Re_\infty=6.5 \times 10^6$  and  $\alpha_{corr}=2.31$  deg,  $160 \times 60$  C-mesh



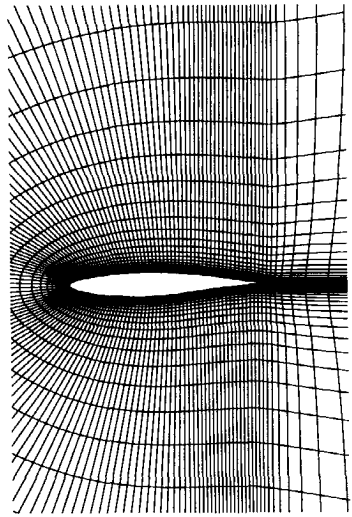


Figure 3.25: The mesh for the viscous flow calculation. RAE 2822 airfoil, 189×60 C-mesh

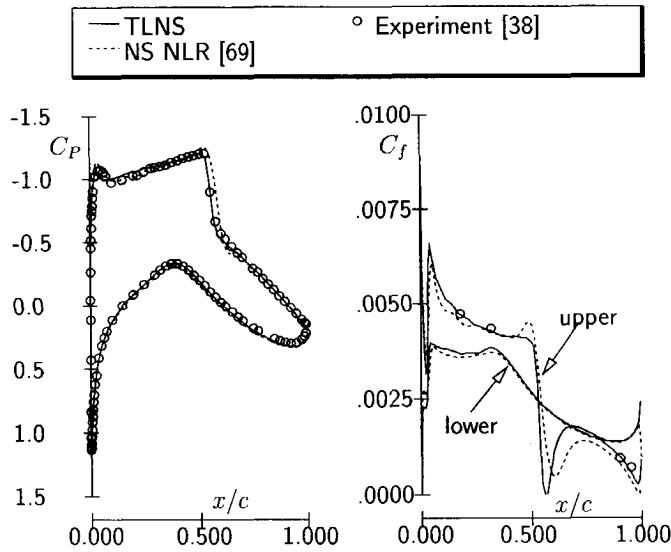


Figure 3.26: Comparison of calculated and measured distributions of pressure and skin friction coefficients for RAE 2822 airfoil at  $M_\infty=0.729$ ,  $\alpha_{\text{exp}}=2.92$  deg,  $\alpha_{\text{corr}}=2.31$  deg and  $Re_\infty=6.5 \times 10^6$ , 189×60 C-mesh

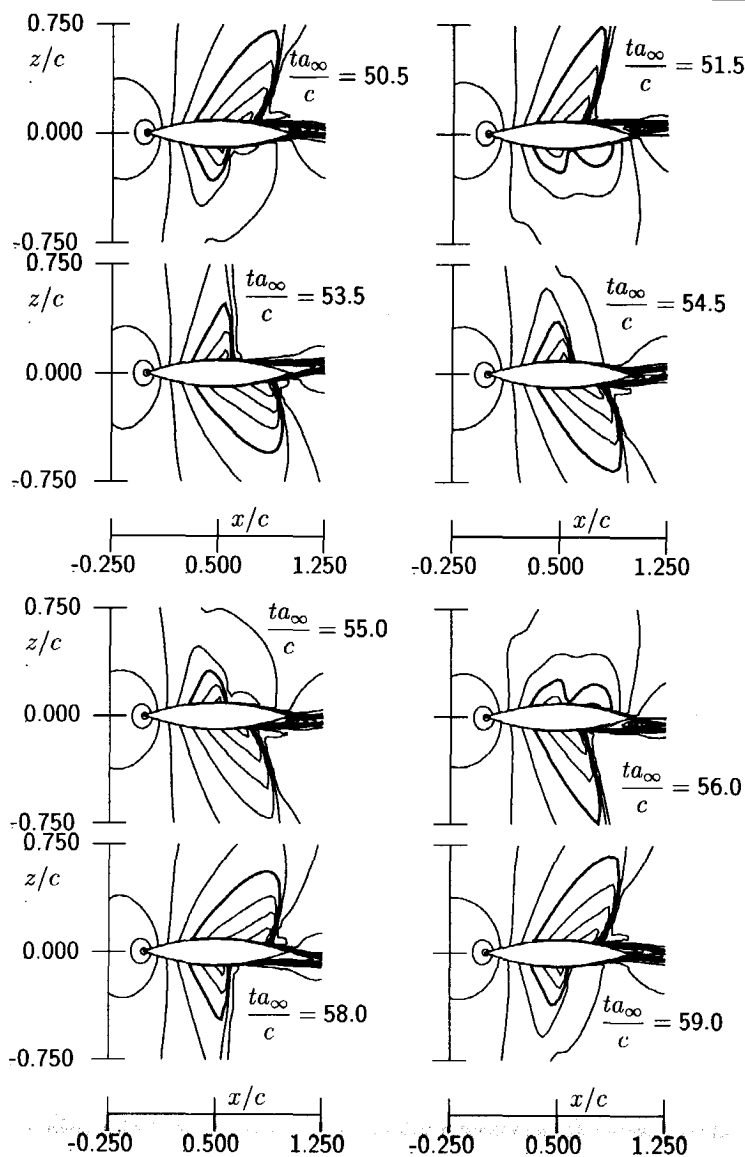


Figure 3.27: Instantaneous Mach contours at four time levels ( $\Delta M = 0.10$ ) of 18% circular arc airfoil at  $M_\infty = 0.76$  and  $Re_\infty = 11 \times 10^6$ , the time is relative to  $t_0 a_\infty / c = 50$ ,  $140 \times 60$  C-mesh

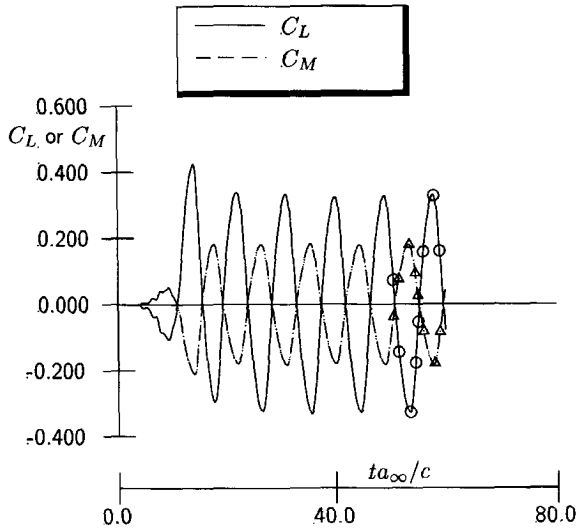


Figure 3.28: Time history of lift coefficient and moment coefficient about 0.25 chord of 18% circular arc airfoil at  $M_\infty=0.76$  and  $Re_\infty=11 \times 10^6$ ,  $140 \times 60$  C-mesh

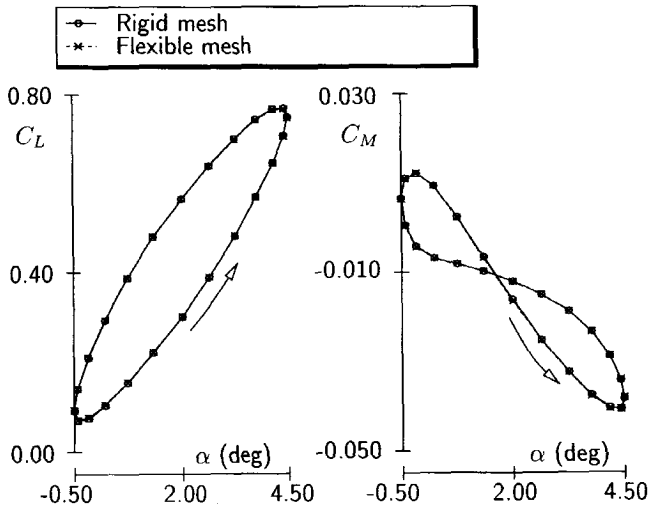


Figure 3.29: Comparison of  $C_L$  and  $C_{M,0.25}$  of NACA 0012 airfoil pitching about 0.25 chord at  $M_\infty=0.754$ ,  $\alpha_{\text{mean}}=2.00$ ,  $\alpha_{\text{amp}}=2.50$  and  $k=0.082$ , using rigid and dynamic mesh modeling,  $140 \times 30$  C-mesh

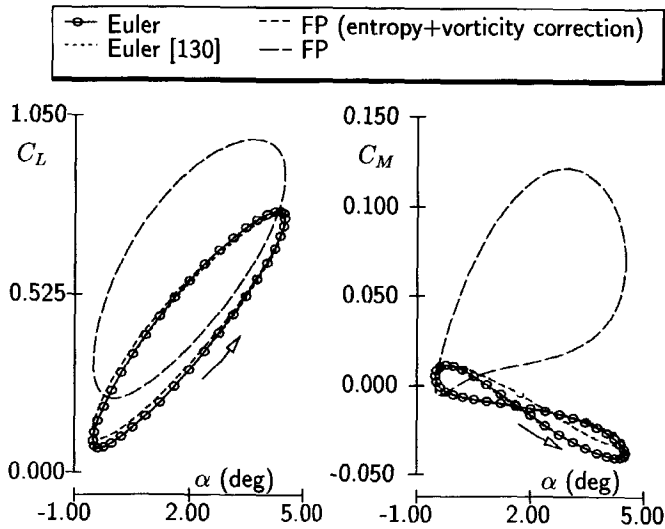


Figure 3.30: Comparison of calculated  $C_L$  and  $C_{M,0.25}$  of NACA 0012 airfoil pitching about 0.25 chord at  $M_\infty=0.754$ ,  $\alpha_{\text{mean}}=2.00$  deg,  $\alpha_{\text{amp}}=2.50$  deg and  $k=0.082$ , using different inviscid flow methods,  $140 \times 30$  C-mesh

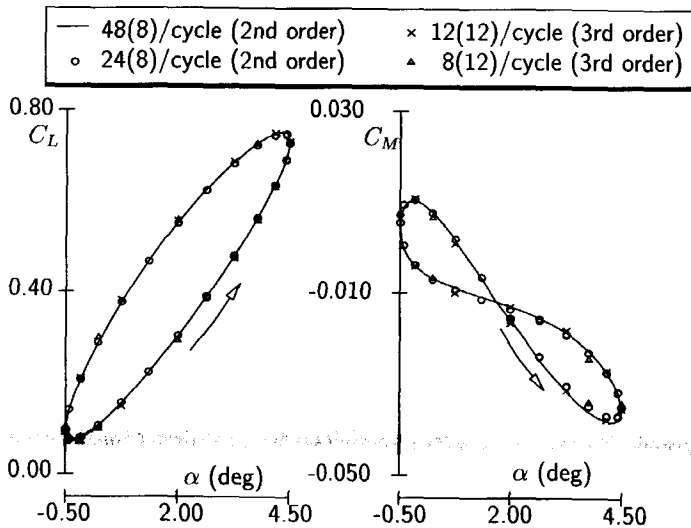


Figure 3.31: Comparison of calculated  $C_L$  and  $C_{M,0.25}$  of NACA 0012 airfoil pitching about 0.25 chord at  $M_\infty=0.754$ ,  $\alpha_{\text{mean}}=2.00$  deg,  $\alpha_{\text{amp}}=2.50$  deg and  $k=0.082$ , using various iteration strategies,  $140 \times 30$  C-mesh

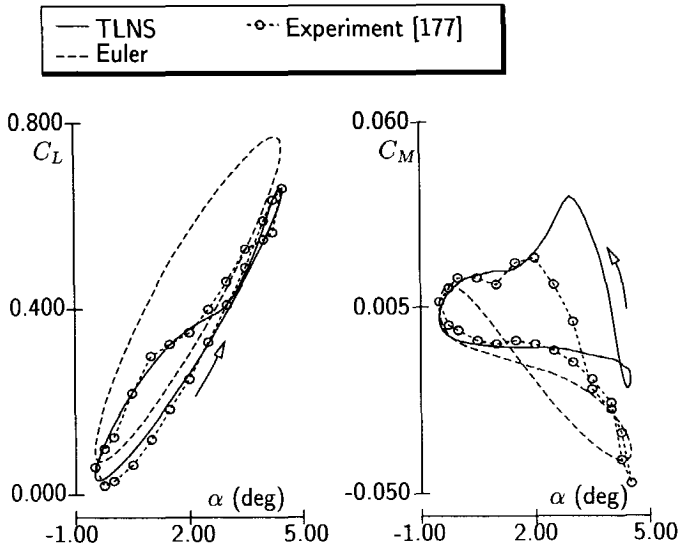


Figure 3.32: Comparison of calculated and experimental  $C_L$  and  $C_{M,0.25}$  of NACA 0012 airfoil pitching about 0.25 chord at  $M_\infty=0.754$ ,  $\alpha_{\text{mean}}=2.00$  deg,  $\alpha_{\text{amp}}=2.50$  deg,  $k=0.082$  and  $Re_\infty=5.7 \times 10^6$ ,  $140 \times 60$  C-mesh

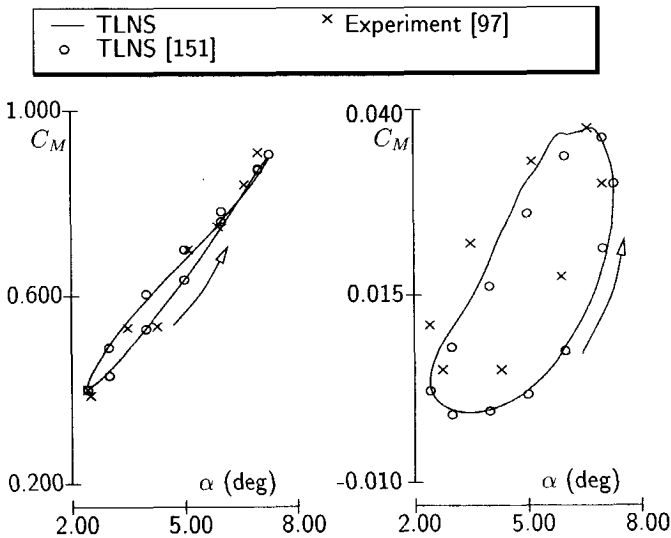


Figure 3.33: Comparison of calculated and experimental  $C_L$  and  $C_{M,0.25}$  of NACA 0012 airfoil pitching about 0.25 chord at  $M_\infty=0.60$ ,  $\alpha_{\text{mean}}=4.86$  deg,  $\alpha_{\text{amp}}=2.44$  deg,  $k=0.081$  and  $Re_\infty=4.8 \times 10^6$ ,  $140 \times 60$  C-mesh

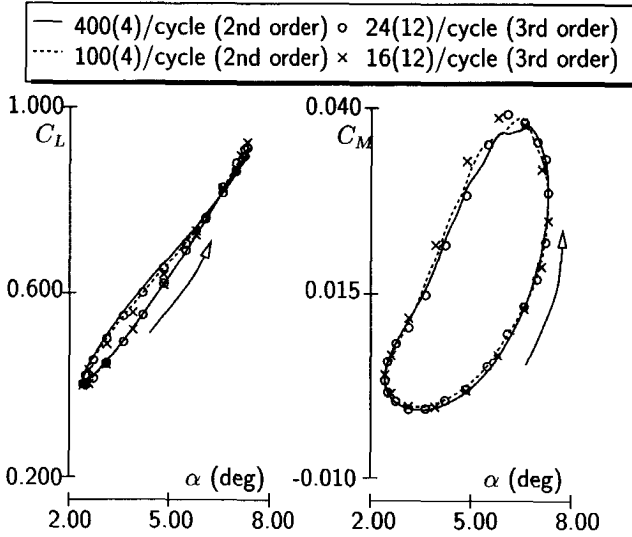


Figure 3.34: Comparison of calculated  $C_L$  and  $C_{M,0.25}$  of NACA 0012 airfoil pitching about 0.25 chord at  $M_\infty=0.60$ ,  $\alpha_{\text{mean}}=4.86$  deg,  $\alpha_{\text{amp}}=2.44$  deg,  $k=0.081$  and  $Re_\infty=4.8 \times 10^6$ , using various iteration strategies,  $140 \times 60$  C-mesh

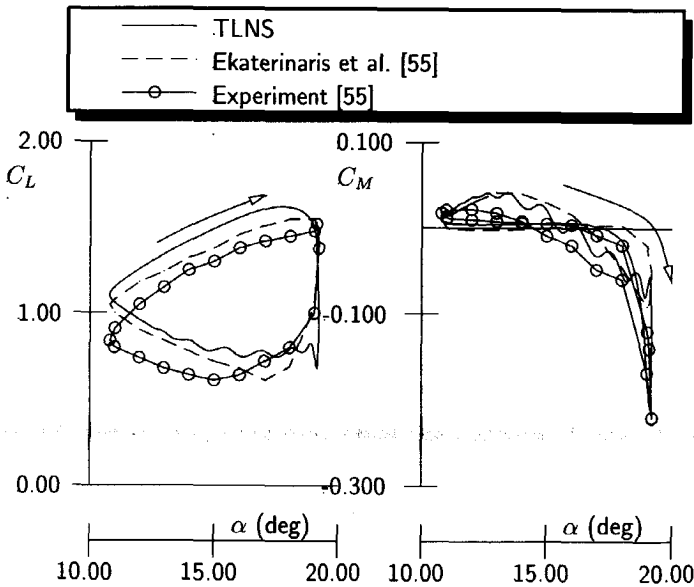


Figure 3.35: Comparison of calculated  $C_L$  and  $C_M$  of NACA 0015 airfoil pitching about 0.25 chord at  $M_\infty=0.30$ ,  $\alpha_{\text{mean}}=15$  deg,  $\alpha_{\text{amp}}=4.20$  deg,  $k=0.10$  and  $Re_\infty=2 \times 10^6$ ,  $160 \times 60$  C-mesh

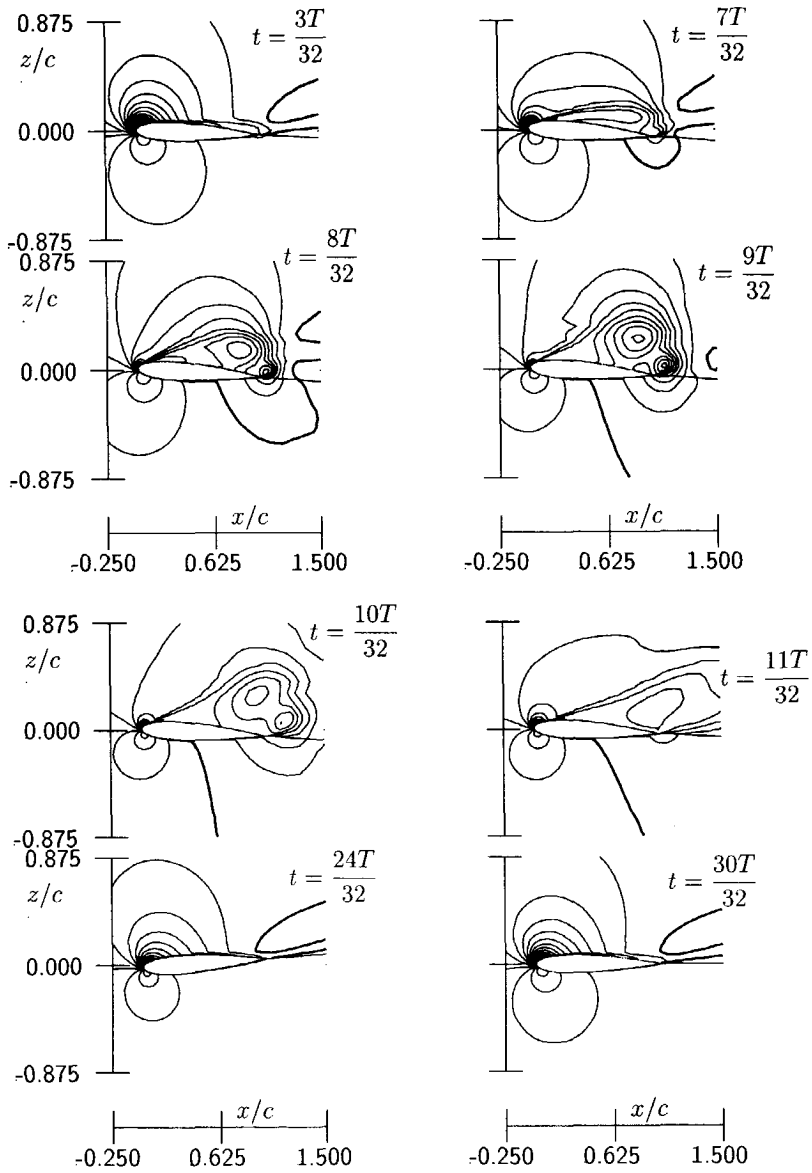


Figure 3.36: Instantaneous density contours at eight time steps of NACA 0012 airfoil pitching about 0.25 chord at  $M_\infty=0.30$ ,  $\alpha_{\text{mean}}=15^\circ$ ,  $\alpha_{\text{amp}}=4.20^\circ$ ,  $k=0.10$  and  $Re_\infty=1.93 \times 10^6$ ,  $160 \times 60$  C-mesh. The thickened contour is freestream density ( $\rho=1$ ) and  $\Delta\rho=0.05$

### 3.11 CONCLUSIONS CONCERNING THE TWO-DIMENSIONAL CUA METHOD

A method to solve the Thin-Layer Navier-Stokes/Euler equations for two-dimensional unsteady flow applications has been described. The method employs large time steps,  $\mathcal{O}(10)$  per cycle of oscillation, while maintaining accuracy by solving the unsteady nonlinear equations using subiterations. From the results of test cases the following conclusions may be drawn:

- From the test case for the dynamic mesh algorithm, it follows that the chosen quality parameters for both the elliptic method (i.e. forcing functions  $P(\xi, \zeta)$  and  $Q(\xi, \zeta)$ ) and the spring analogy method (i.e. the spring stiffnesses) preserve the mesh distribution effectively. The proposed surface forcing function for the elliptic method shows a similar performance in preserving the surface orthogonality.
- From the comparison of results obtained for the various inviscid flux methods, namely: van Leer's FVS, AUSM FVS, Roe's FDS and van Leer-Osher FV/DS, the following conclusions are drawn:
  - For inviscid flow, all methods show a good performance in capturing the shock waves. The chordwise surface pressure distributions do not differ significantly. However, the Mach number distributions show some discrepancies. The field isomach contours from the AUSM FVS even shows some wiggles close to the surface.
  - For viscous flow, all but van Leer's FVS method show a good result. The shock strength using van Leer's FVS is a bit weaker than those obtained with the other methods and the shock position is slightly more upstream. The most significant difference is in the friction coefficient which is much higher compared to those obtained with the other methods.
  - The AUSM method performs well in the viscous flow test case, but not as good in the inviscid flow test case. The wiggles in the Mach number distribution close to the surface suggest a lack of numerical dissipation. The method is also less robust than the one with van Leer's FVS.
  - The hybrid van Leer-Osher scheme performs well for all test cases. The inclusion of an 'anti-diffusive' flux from Osher's scheme into van Leer's FVS appears to dramatically improve van Leer's FVS. The drawback is the complexity of the Jacobian of the flux which allows only an approximate Jacobian to be employed.
  - The comparison of the CPU time of all methods reveals minor differences. The simplicity of the FVS seems to be overshadowed by the complexity of calculating the Jacobian of the flux. On the other hand, it is quite easy to construct an approximate Jacobian for Roe's FDS which leads to a good performance. Thus for an implicit method, where the Jacobian of the flux is required, the FVS is not better than Roe's FDS in terms of efficiency.



- As far as the CPU time is concerned the mixed van Leer-Osher scheme is the most expensive method and AUSM is the cheapest.

It can be concluded that the best method, which is the simplest and most straightforward one, is thus Roe's FDS.

- From the comparison of the results of the relaxation methods, nonlinear relaxation employing a simple SSOR sweep shows a good performance compared to a more complex non-stationary iteration method such as GMRES.
- The present method has been applied to an airfoil in a flow under various conditions: steady flow, unsteady flow about a stationary airfoil section, forced vibrations with a moving mesh in transonic flow and dynamic stall. The results demonstrate in each case an adequate quality.
- The computational efficiency of the method admits two-dimensional simulations to be performed on a routine basis. This efficiency, primarily expressed in terms of computation time, is obtained mainly due to the freedom of taking large time steps during the time-accurate simulations, while maintaining a satisfactory accuracy. Typical results shown have been obtained with 8 time steps per cycle with 12 subiterations for inviscid flow and 16 time steps with 12 subiterations for viscous flow.



## CHAPTER 4

# SIMULATION OF UNSTEADY FLOW PHENOMENA AROUND AIRFOILS

In this chapter the method to solve the Navier-Stokes equations developed in the previous chapter is further employed to study unsteady flow phenomena around airfoils. The applications discussed here are mostly dominated by viscous effects.

It is known, and has also been shown for the test case of the stationary circular arc airfoil in section 3.10.5, that under certain flow conditions the shock-induced separated flows exhibits time-dependent phenomena. At these conditions a distinct frequency appears which can be associated with a natural aerodynamic mode of the flow. Zwaan [184] showed that in case of a harmonically pitching airfoil the unsteady flow could be compared with a forced mass-spring-damper system, being brought into resonance. The present chapter presents numerical simulations and discussions about this type of flow.

Since the flows considered here always involve significant shock motions, the method is first validated with the experiment of Tijdeman [167] concerning the phase lag of the shock motion with respect to the motion of the airfoil, and the underlying physical phenomenon hypothesized by Tijdeman. Subsequently the behavior of the shock motions in separated flow is considered by reproducing experimental results of Davis and Malcolm [42]. The discussion will lead to the confirmation of the existence of a natural mode of the flow. Finally the flow at buffet onset of an NACA 0012 airfoil is calculated of which the results are compared with experimental data of McDevitt and Okuno [109]. Prior to the discussions about unsteady flow phenomena, an introductory section will explain how the results will be presented.

### 4.1 PRESENTATION OF THE RESULTS

In this chapter two types of unsteady flow are discussed: the unsteady flow due to *sinusoidal motion of the airfoil* and the *inherently unsteady flow* about a stationary airfoil. The most common form of representation of an unsteady flow quantity due to a sinusoidal displacement is its Fourier series. For an unsteady flow quantity, say  $C_P(t)$ , generated by the sinusoidal motion at a frequency  $\omega$ , the Fourier series is:

$$C_P(t) = C_{P0} + \sum_{n=1}^{\infty} (C'_{Pn} \cos \omega n t + C''_{Pn} \sin \omega n t), \quad (4.1)$$

with

$$\begin{aligned} C_{P0} &= \frac{1}{T} \int_0^T C_P(t) dt \\ C'_{Pn} &= \frac{2}{T} \int_0^T C_P(t) \cos n\omega t dt \\ C''_{Pn} &= \frac{2}{T} \int_0^T C_P(t) \sin n\omega t dt, \end{aligned} \quad (4.2)$$

where  $C_{P0}$  is simply the average of  $C_P$  over the period of  $T = 2\pi/\omega$ . In a linear case  $n=1$  is enough to completely express  $C_P(t)$ . According to common practice  $C_P(t)$  is supposed to be generated by an airfoil motion that is represented by a cosine function. This implies that at  $t=0$  the airfoil is in one of its extremal positions, and that at  $t=T/4$  the airfoil passes its mean position on its way to the other extremal position.  $C'_{Pn}$  is usually called the real (or in-phase) part and  $C''_{Pn}$  the imaginary (or out-of-phase) part of  $C_{Pn}$ . This designation is connected to the theory of linear unsteady aerodynamics, where  $C_P$  can be represented in the Argand plane as a rotating vector, with in-phase and out-of-phase (i.e. real and imaginary) components with the rotating vector representing the airfoil displacement. The integrations in equation (4.2) are carried out using the trapezoidal rule during the simulation. Commonly  $C'_{Pn}$  and  $C''_{Pn}$  are normalized with respect to the amplitude of the harmonic airfoil motion. In the cases to follow only the components for  $n=1$  are presented. In practice the simulation of the flow due to a cosine displacement function is rather difficult, since one has to start from maximum displacement. In the present simulations a sinusoidal displacement function was always used.

In the case of an inherently unsteady flow, the airfoil is stationary while the flow exhibits a time-dependent character. Usually more than one frequency exist in the flow. A similar Fourier decomposition as equation (4.1) can also be made in this case by choosing a reference frequency. Or if one would like to see the frequency spectra of a time-dependent data, a discrete Fourier transform is applied to the time signal as:

$$f_n = \sum_{k=0}^{N-1} f(k) e^{-i2\pi nk/N}, \quad n = 0, 1, 2, \dots, N-1$$

provided that there are  $N$  discrete points in the time signal. Another method of presentation, as shown by Roos [147], is by **correlation of the data**. The **normalized autocorrelation function** of an unsteady flow quantity  $f(t)$  at some spatial location is defined as:

$$R(f, \tau) = \frac{1}{\psi_f^2} \lim_{T \rightarrow \infty} \frac{1}{T} \int_0^T f(t)f(t+\tau) dt, \quad (4.3)$$

where the root-mean-square  $\psi_f$  is defined as:

$$\psi_f = \left[ \lim_{T \rightarrow \infty} \frac{1}{T} \int_0^T f(t)^2 dt \right]^{\frac{1}{2}}. \quad (4.4)$$

The autocorrelation function represents the correlation of an unsteady time signal at a certain time  $t$  with the same signal at time  $t + \tau$ . The normalized cross-correlation function of unsteady flow data  $f(t)$  at one location with unsteady flow data  $g(t)$  at another location is defined as:

$$R(f, g, \tau) = \frac{1}{\psi_f \psi_g} \lim_{T \rightarrow \infty} \frac{1}{T} \int_0^T f(t)g(t + \tau) dt. \quad (4.5)$$

The cross-correlation function shows whether data at a certain location is correlated to the data at another location at an earlier or later time. The cross-correlation functions of data at many locations would show the direction of the flow of information/disturbance. The normalized correlation functions are calculated using a standard routine employing discrete Fourier transforms.

#### 4.2 TRANSONIC FLOW ABOUT PITCHING NLR 7301 AIRFOIL

The proper simulation of a shock wave motion is a very important characteristic in testing the computational method. Tijdeman [167] categorized the shock motion in case of attached flow into three types: A, B and C. Type A involves an almost sinusoidal shock wave motion which indicates the existence of the shock during the whole period of oscillation. This type of shock wave motion usually occurs at a high subsonic speed with a well-developed shock wave. Type B shock wave motion occurs at a somewhat lower Mach number in which during the downstream motion of the shock the dynamic (weakening) effect is dominant causing the shock to disappear momentarily. Type C shock wave motion is characterized by the dominating dynamic (strengthening) effect during the forward motion of the shock which causes the shock to pass the sonic point and to leave the airfoil in upstream direction as a free shock wave.

The test case of the harmonically pitching NLR 7301 airfoil presented by Tijdeman for type A shock motion is discussed here. The main purpose is to confirm Tijdeman's phenomenological model concerning the flow mechanism which causes a phase lag between the shock motion and the airfoil motion. The model postulated that the phase angle between the shock motion and the motion of the airfoil is the time required by a pressure signal generated at the trailing edge to arrive at the shock:

$$\Delta t = - \int_{x=c}^{x_s} \frac{dx}{u_{loc} - a_{loc}} = - \int_{x=c}^{x_s} \frac{dx}{(1 - M_{loc})a_{loc}}, \quad (4.6)$$

where  $M_{loc}$  is calculated by taking into account the gradient of the Mach number normal to the surface as:

$$M_{loc} = R[M_{loc, \text{ at the surface }} - M_{\infty}] + M_{\infty}. \quad (4.7)$$

$R$  is a relaxation factor. The local Mach number at the surface should be understood as the one at the edge of the boundary layer. Waves which propagate from the trailing edge moving upstream are usually called Kutta waves. They may be explained

as follows. When the circulation at the airfoil changes (e.g. due to the change in the angle of attack) the wake will adapt itself to the new situation, resulting in a change of the angle at which the wake leaves the airfoil. This change involves a pressure disturbance at the trailing edge, which will expand as a Kutta wave.

For the numerical simulation, a  $160 \times 60$  mesh with 120 mesh points at the airfoil surface is used. The outer boundary is set at 100 chords away from the airfoil. The flow conditions are  $M_\infty=0.70$ ,  $\alpha_{\text{calc}}=2.00$  deg,  $\alpha_{\text{exp}}=3.00$  deg and  $Re_\infty=2.1 \times 10^6$ . The corrected angle of attack is the one suggested by Tijdeman [3, 167]. During the experiment a transition strip was placed at 0.30 chord. Two calculations were made, one for a fully turbulent flow and one with a turbulent flow starting at 0.30 chord, to see the effect of the transition strip. Figure 4.1 shows the comparison of the calculated steady pressure distribution with the measured results. Excellent agreement with the experimental result is obtained for the calculation with transition strip which shows the importance of applying the transition strip for this case. Thus this transition strip is used for further calculation of the unsteady flow. The skin friction coefficient is positive everywhere along the airfoil surface, confirming that the flow is indeed attached.

The unsteady flow case is a pitching oscillation about 0.40 chord with an amplitude of 0.50 deg. The reduced frequency based on semichord ranges from  $k=0.023$  up to  $k=0.192$ . Figures 4.2 and 4.3 show the normalized (by the amplitude of the oscillation) unsteady pressure distribution expressed in real and imaginary components and in magnitude and phase angle, respectively. In general the agreement is satisfactory. The differences between the calculated and the measured data may at least partly be attributed to wind tunnel wall effects which were not eliminated in reducing the measured data. The results of the computation using 96 time steps per cycle and those using 48 time steps per cycle show only slight differences in the phase angle close to the trailing edge, where the magnitude of the unsteady pressure is very small.

Further, figure 4.4 shows the history of the shock position during the oscillation for the reduced frequencies  $k=0.023, 0.072, 0.144$  and  $0.192$ . The phase lag between the shock wave and the airfoil motion is calculated by fitting a quadratic function centered on the peak in the shock trajectory at  $\phi_s \approx 450$  deg. The phase lag of the shock with respect to the airfoil motion is then  $\phi_s - 450$ .

$k$	experiment	computation	formula 4.6
0.023	~5 deg	9.65 deg	5.80 deg
<b>0.072</b>	<b>~20 deg</b>	<b>22.21 deg</b>	<b>18.25 deg</b>
0.144	~35 deg	38.41 deg	36.51 deg
0.192	~50 deg	50.11 deg	48.68 deg

Table 4.1: Comparison of calculated and measured phase angles of the shock motion lagging the airfoil motion

Table 4.1 presents the comparison of the computed and measured phase lag of the shock motion with respect to the airfoil motion, also included data obtained using equation (4.6) with  $R=0.70$ . It should be noted that the local Mach number

at the surface has been calculated from the pressure data of the steady flow calculation using the isentropic relation. This is done in order to be consistent with the procedure followed in post-processing the data from the experiment. Calculation using the true Mach number at the edge of the boundary layer gives almost the same result.

From the comparison of the results shown in table 4.1, it may be concluded that an adequate accuracy of the numerical simulation is obtained using the present method. The validity of Tijdeman's formula has also been assessed.

#### 4.2.1 FIGURES

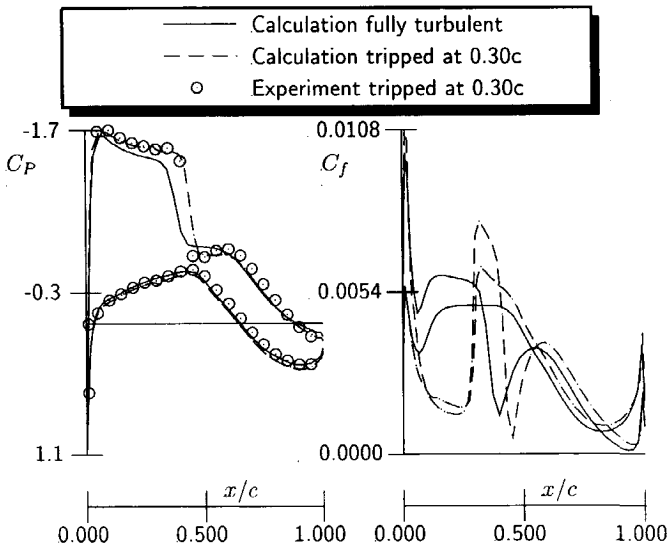


Figure 4.1: Comparison of calculated and measured pressure distributions of an NLR 7301 airfoil at  $M_\infty=0.70$ ,  $\alpha_{\text{calc}}=2.00$  deg,  $\alpha_{\text{exp}}=3.00$  deg, and  $Re_\infty=2.1 \times 10^6$  using  $160 \times 60$  C-mesh

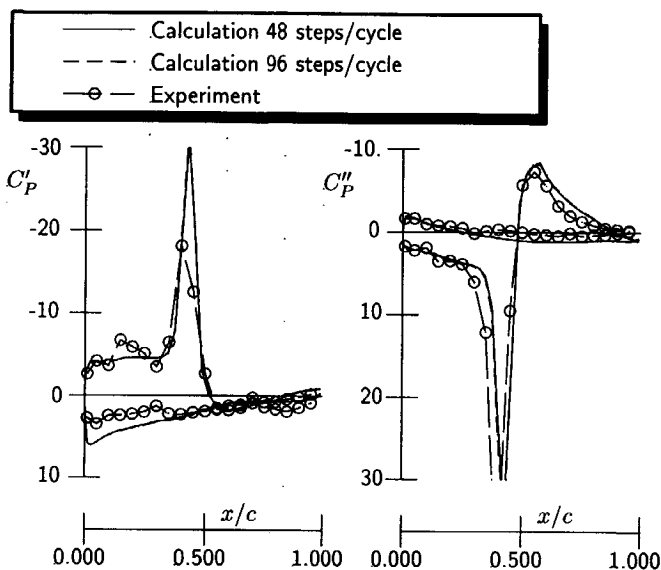


Figure 4.2: Comparison of calculated and measured pressure distributions of an NLR 7301 airfoil pitching about 0.40 chord at  $M_\infty=0.70$ ,  $\alpha_{\text{mean}}=2.00$  deg,  $\alpha_{\text{amp}}=0.50$  deg,  $k=0.192$  and  $Re_\infty=2.1 \times 10^6$  with transition strip at 0.30 chord, using two strategies using  $160 \times 60$  C-mesh

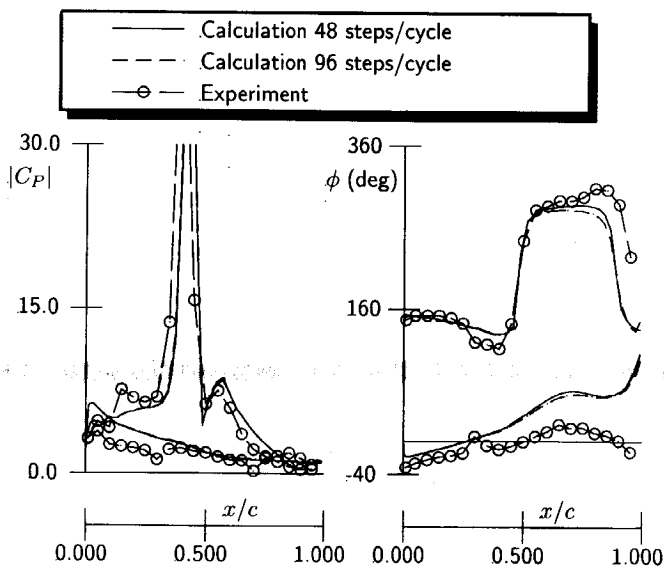


Figure 4.3: Similar as figure 4.2 but expressed in magnitude  $|C_P|$  and phase angle,  $\phi$



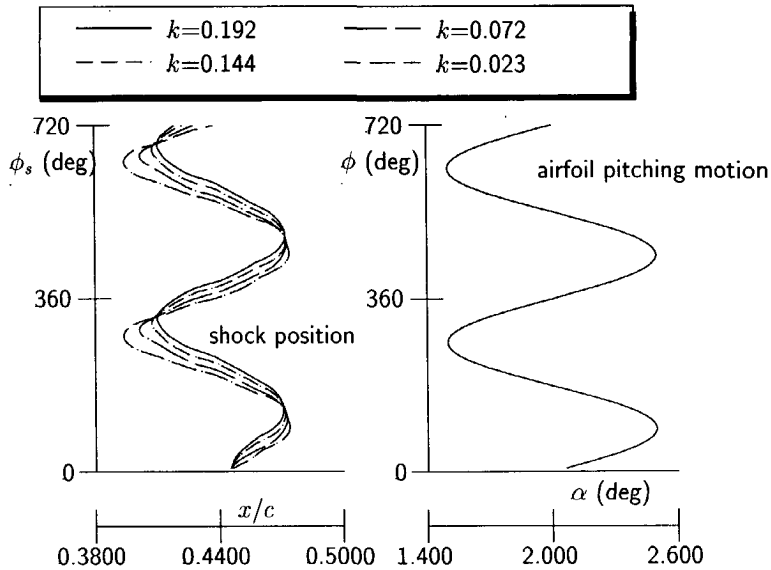


Figure 4.4: History of shock position for various excitation frequencies. NLR 7301 airfoil pitching about 0.40 chord at  $M_\infty=0.70$ ,  $\alpha_{\text{mean}}=2.00$  deg,  $\alpha_{\text{amp}}=0.50$  deg,  $k=0.023, 0.072, 0.144$  and  $0.192$  and  $Re_\infty=2.1 \times 10^6$  with transition strip at 0.30 chord

#### 4.3 SHOCK WAVE MOTIONS IN SEPARATED FLOW ABOUT NACA 64A010

NASA Ames has carried out extensive research, both experimentally and computationally, on unsteady transonic aerodynamics, including separated flow conditions. The experimental results presented by Davis and Malcolm [42] show the characteristics of the unsteady aerodynamic loads on an NACA 64A010A (the last A means Ames version) airfoil in transonic attached and shock-induced separated flow conditions. In the attached flow condition, in response to the airfoil motion, the shock wave behaved like the one observed by Tijdeman [167], see the previous section. This behavior will be called the normal shock response. In the case of shock-induced separated flow some interesting phenomena were observed. When the static angle of attack increased, the shock wave moved upstream rather than downstream. In the sequel this type of shock wave response will be called the reverse shock response. The reverse shock motion phenomenon has a direct influence on the unsteady aerodynamic loads, which will be discussed later in this section.

In this section simulations are discussed which were made with the aim to reproduce some experimental results of NASA Ames [42]. A C-mesh of  $160 \times 60$  is used with 120 points on the surface of the airfoil. The standard airfoil coordinate from [1] (NACA 64A010) are used instead of the Ames version. The standard NACA 64A010 coordinates are only slightly different from the Ames coordinates. The case at flow condition  $M_\infty=0.789$ ,  $\alpha_{\text{mean}}=4$  deg and  $Re_\infty=12 \times 10^6$  is selected. In the

experiment a transition strip was not applied and in general the transition point is not known. From a limited transition study at  $M_\infty=0.80$  and  $Re_\infty=12\times 10^6$  [42] it may be concluded that the transition point must have been located at 0.05 chord. In the calculation the flow was assumed to be fully turbulent. This case is called the shock stall case because flow separation induced by the shock wave occurs at the upper surface.

The comparison of the calculated and measured pressure distribution for steady flow is shown in figure 4.5. The pressure distribution on the lower side and the one on the upper side in front of the shock wave are in excellent agreement with the measured values. However, the shock wave is predicted too aft compared to the experiment, which might be attributed to the inadequacy of the turbulence model or to tunnel wall influence. From the skin friction coefficient, see the right plot of figure 4.5, the simulation predicts extensive flow separation behind the shock wave. This is in agreement with the observation in the experiment [42]. Therefore, despite of the inaccuracy in predicting the shock position, it may be concluded that the computational result is in qualitative agreement with the experimental result.

The unsteady flow case considered in this section is a pitching oscillation about 0.25 chord. The amplitude of oscillation is  $\alpha_{\text{amp}}=1.01$  deg. A wide range of reduced frequencies, from a low frequency  $k=0.051$  up to a relatively high frequency  $k=0.204$  based on semichord, is considered. The unsteady aerodynamic responses to the excitation at these frequencies were reported in [42] showing significant changes in behavior.

Figure 4.6 shows the comparison of the real and imaginary parts of the first Fourier component of the unsteady pressure distribution at  $k=0.051$ . The experimental data from [42] were digitized because they are not available as numerical data. Although the shock position and the pressure level are only in a fair agreement, all the trends are well captured. At this low frequency the unsteady pressure at the upper surface shows a peak with increased pressure in the real part. This peak is associated with the reverse motion of the shock, like the one observed in figure 12 of [42] for the so-called the quasi-steady condition, i.e.  $k=0$ .

Figure 4.7 shows the comparison of the real and imaginary parts of the first Fourier component of the unsteady pressure distribution at  $k=0.204$ . The experimental data were obtained from [41]. As in the case of low reduced frequency only a fair quantitative agreement is obtained but the trends are well captured. Now in the real part of the unsteady pressure distribution at the upper surface there is a peak **with decreased pressure. This seems to suggest that at this high reduced frequency** excitation, the shock motion returns to the normal one, like in an attached flow case. However, comparing figure 4.7 with a typical attached flow unsteady pressure distribution of figure 4.2, there are still characteristic differences. To further investigate this type of shock motion some more flow simulations at various reduced frequencies were carried out. Figure 4.8 shows the comparison of the instantaneous shock position during one cycle of the pitching oscillation at reduced frequency excitations of  $k=0.051$ , 0.102, 0.150 and  $k=0.204$ . Although the shock trajectories for the excitation at  $k=0.051$  and  $k=0.204$  clearly show a different direction of motion, the change in shock motion from low to high frequency case looks quite continuous.

Thus it can be concluded that the 'normal' shock motion at high frequency is caused by the *large* phase lag between the motion of the airfoil and the motion of the shock.

The same behavior of the shock motion at low and high frequency was observed by den Boer and Houwink [44] in the unsteady pressure measurement of the NLR 7301 airfoil. Moreover, Zwaan [184] noticed that at certain combinations of Mach number and angle of attack the unsteady flow behavior could be compared with a mass-spring-damper system with a natural frequency lying in the range of excitation frequencies, so that by varying the excitation frequency an aerodynamic resonance condition could be realized. Thus at shock-induced separated conditions, the flow may contain a natural frequency. In the case of the NLR experiments the natural mode was damped.

The existence of the natural frequency of the flow can be seen in figure 4.9 which shows the history of  $C_L$  and  $C_M$  and the magnitude of the Fourier components of  $C_L$  for the case of low reduced frequency excitation ( $k=0.051$ ). The first peak represents the response to the excitation. Although there are several more peaks corresponding to the 3rd harmonic, 5th harmonic, etc., the distinct peak at about  $k=0.17$  shows that the forced vibration has excited the natural mode of the flow. At a slightly higher angle of attack, i.e.  $\alpha=4.50$  deg, a self-sustained shock-induced oscillation occurs without exciting the airfoil, i.e. without oscillating the airfoil. Figure 4.10 shows the history of  $C_L$  and  $C_M$  and the magnitude of the Fourier components of  $C_L$ . A peak is observed in the magnitude of the Fourier components at about  $k=0.185$ , indicating a natural mode of the flow. This value is slightly higher than the natural frequency of the flow obtained at  $\alpha=4.00$  deg, presented in figure 4.9.

From the simulation of unsteady flows about the NACA 64A010 airfoil presented in this section some conclusions can be drawn: The present method has been successfully applied to simulate unsteady shock motions for shock-induced separated flow conditions. There exists a natural frequency of the flow which appears to be related to the mechanism of shock-induced flow separation. At a certain condition a self-sustained shock-induced oscillation occurs in the flow about the stationary airfoil, at a reduced frequency of the natural frequency of the flow.

4.3.1 FIGURES

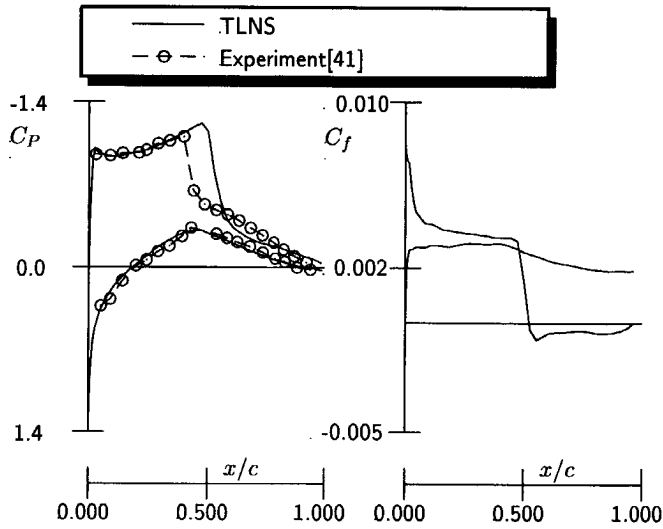


Figure 4.5: Comparison of calculated and measured pressure distributions. NACA 64A010 airfoil at  $M_\infty=0.80$ ,  $\alpha=4.00$  deg, and  $Re_\infty=12 \times 10^6$  using  $160 \times 60$  C-mesh

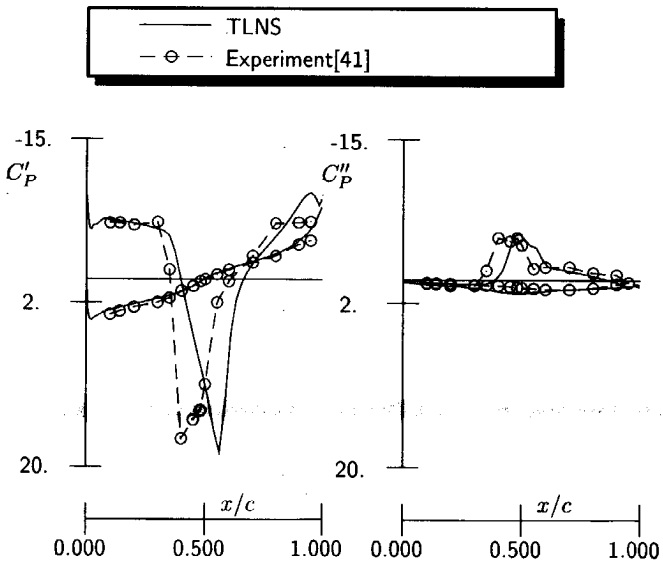


Figure 4.6: Comparison of calculated and measured pressure distributions. NACA 64A010 airfoil pitching about 0.25 chord at  $M_\infty=0.80$ ,  $\alpha_{mean}=4.00$  deg,  $\alpha_{amp}=1.01$  deg,  $k=0.051$  and  $Re_\infty=12 \times 10^6$  using  $160 \times 60$  C-mesh

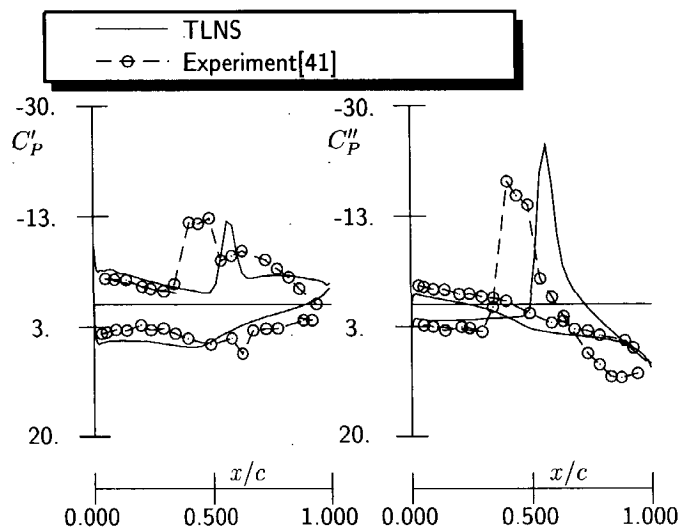


Figure 4.7: Comparison of calculated and measured pressure distributions. NACA 64A010 airfoil pitching about 0.25 chord at  $M_\infty=0.80$ ,  $\alpha_{\text{mean}}=4.00$  deg,  $\alpha_{\text{amp}}=1.01$  deg,  $k=0.204$  and  $Re_\infty=12 \times 10^6$  using  $160 \times 60$  C-mesh

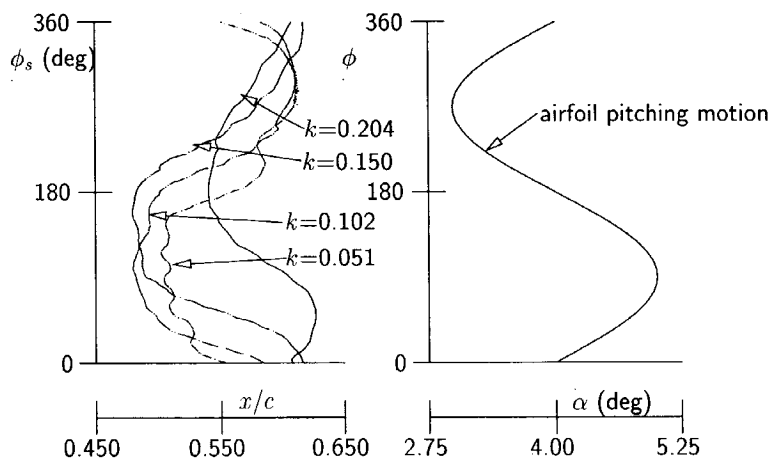


Figure 4.8: Comparison of calculated positions of the shock wave. NACA 64A010 airfoil pitching about 0.25 chord at  $M_\infty=0.80$ ,  $\alpha_{\text{mean}}=4.00$  deg,  $\alpha_{\text{amp}}=1.01$  deg,  $k=0.204$  and 0.051 and  $Re_\infty=12 \times 10^6$  using  $160 \times 60$  C-mesh

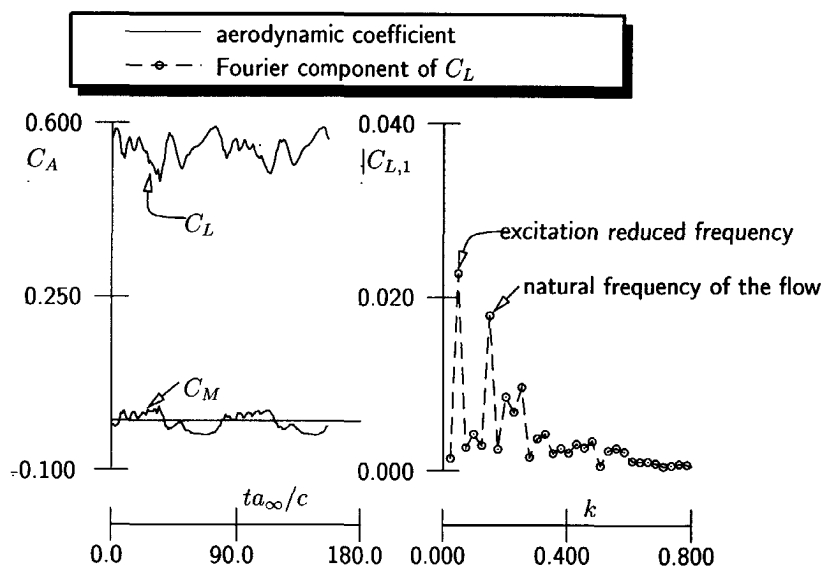


Figure 4.9: History of  $C_L$  and  $C_M$  and magnitude of the Fourier components of  $C_L$ . NACA 64A010 airfoil pitching about 0.25 chord at  $M_\infty=0.80$ ,  $\alpha_{\text{mean}}=4.00$  deg,  $\alpha_{\text{amp}}=1.01$  deg,  $k=0.051$  and  $Re_\infty=12 \times 10^6$

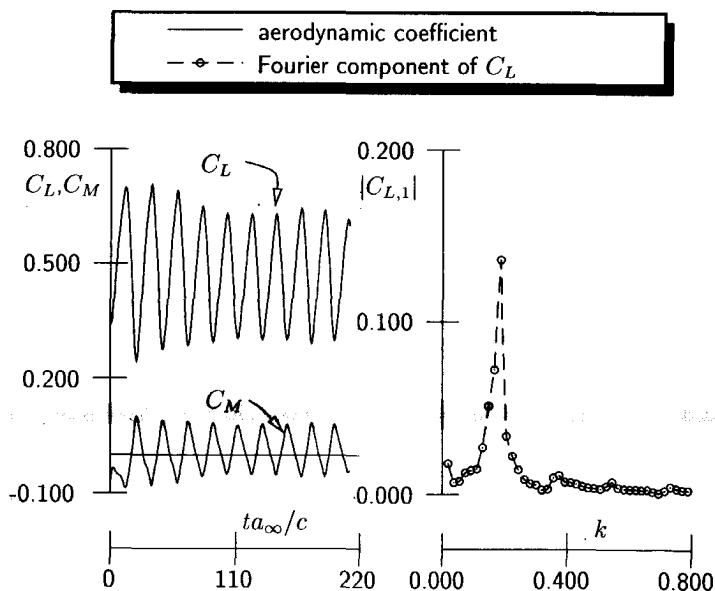


Figure 4.10: History of  $C_L$  and  $C_M$  and magnitude of the Fourier components of  $C_L$ . NACA 64A010 airfoil in a buffet condition at  $M_\infty=0.80$ ,  $\alpha=4.50$  deg and  $Re_\infty=12 \times 10^6$

#### 4.4 TRANSONIC BUFFET OF NACA 0012 AIRFOIL

The case of transonic buffet of the NACA 0012 airfoil, as occurs in the experiment of NASA Ames [109], is another example of shock-induced oscillation, besides the well-known circular arc airfoil in transonic flow. Now also nonzero angles of attack are involved. The case of 18% circular-arc airfoil, for which the present method gives very satisfactory results, see section 3.10.5, is more popular as an unsteady flow test case than the buffet of NACA 0012 airfoil. The effort to reproduce the complete buffet boundary using numerical simulation was done so far using a viscous-inviscid interaction method by Edwards [51] and Girodroux-Lavigne and LeBalleur [63]. To the author's knowledge, confirmed by a very recent paper of Bennett and Edwards [32], only little success has been reported for methods involving the Navier-Stokes equations. Recently, Raghunathan et al. [140] reproduced the buffet of NACA 0012 using TLNS at a particular Mach number and angle of attack. In this section the present method is employed to reproduce the buffet boundary and to study the unsteady flow phenomenon.

The experiment carried out at NASA Ames for an NACA 0012 airfoil by McDevitt and Okuno [109] included both static and dynamic measurements. A clear buffet boundary separating the steady and unsteady responses of a stationary NACA 0012 was obtained. The tests were carried out at Mach numbers ranging from 0.70 to approximately 0.80 and angles of attack up to 6 deg, sufficient to penetrate buffet onset. Beyond the buffet onset shock-induced oscillations occurred in the flow. The Reynolds number during the test ranged from 1 to 14 million, based on the chord. To minimize the wall interference the upper and lower tunnel walls were flexible and boundary layer suction was utilized.

Following the calculation of [63] and [51], a Reynolds number of 10 million was used here throughout the simulation. In all calculations, unless otherwise noted, the Baldwin-Lomax (BL) algebraic turbulence model was used. In the numerical experimentations the main reduced frequency of the response was found, like in the case of circular arc airfoil, to depend on the extent of the outer boundary where the freestream condition was imposed. However, the buffet boundary was hardly influenced. For the present calculations a  $160 \times 60$  mesh, with 120 points at the airfoil surface was employed. A distance of the outer boundary comparable to the one in the calculations of [63] and [51], i.e. 20 chords away, was applied. At this distance the reduced frequency is mildly dependent on changing this distance. The simulations were started from freestream condition. To avoid nonphysical results due to numerical transients, the first time step employed a small underrelaxation factor and many subiterations. Subsequently 12 to 20 subiterations were used depending on the convergence of the unsteady residual at each time step.

At each Mach number, i.e.  $M_\infty = 0.725, 0.750, 0.775$  and  $0.800$ , a sequence of simulations with an increasing angle of attack were carried out until an unsteady flow response was obtained. The increase of the angle of attack between subsequent simulations was  $0.50$  deg. For example, figure 4.11 shows the history of  $C_L$  and  $C_M$  for  $M_\infty = 0.775$  at three angles of attack,  $\alpha = 2.50, 3.00$  and  $4.00$  deg. The first unsteady response due to shock-induced separation is obtained at  $\alpha = 3.00$  deg. The

case of  $\alpha=4.00$  deg represents a heavy buffet condition.

Figure 4.12 shows the instantaneous Mach contours at four time levels for  $M_\infty=0.775$  and  $\alpha=4.00$  deg. It is more convenient to refer also to figure 4.13 which shows the corresponding isobars and contours of constant skin friction plotted in space and time. The first two plots of figure 4.12 show the strengthening and downstream motion of the shock wave. This strong shock wave causes the flow separation to extend further downstream and coalesce with the trailing edge separation, see figure 4.13. The growth of the separation bubble takes place in a rapid manner, being in agreement with the observation of Piercey [43]. After the flow behind the shock has become fully separated, indicated by the shedding of a vortex which formed due to the rapid change of the circulation around the airfoil, see the last plot of figure 4.12, the shock wave starts to move upstream and a strong disturbance, originating from the shock foot, is transported downstream. This disturbance is caused by a rapid change of the circulation around the airfoil due to the flow separation. On moving upstream the shock wave arrives at the slower supersonic region which weakens the shock wave, and reduces the pressure gradient to the level that causes flow reattachment. The flow reattachment causes the increase of the circulation around the airfoil which shifts the shock wave downstream and enlarges the supersonic region. The cycle then starts over again.

For the calculation at zero angle of attack, the sequence of simulations was calculated for increasing Mach numbers. The difference between subsequent simulations is  $M_\infty=0.05$ . Figure 4.14 shows the history of  $C_L$  and  $C_M$  at three difference Mach numbers:  $M_\infty=0.830$ ,  $0.840$  and  $0.845$ . The flow at  $M_\infty=0.845$  shows the first occurrence of an unsteady shock-induced oscillation. Figure 4.15 shows the instantaneous Mach contour at four time levels at  $M_\infty=0.845$  and  $\alpha=0.00$  deg. The phenomenon is similar to the nonzero incidence case of figure 4.12, only this time both sides experience shock-induced oscillations with 180 degree phase difference. Notice the similarity with the transonic buffet of the circular arc airfoil, figure 3.27.

The complete buffet boundary is presented in figure 4.16. Comparisons are provided by the experimental results of NASA Ames [109] and the computational results of [51, 63] employing a viscous-inviscid interaction method of TSP and a boundary layer method. In [63] a semi-implicit viscous-inviscid coupling was applied in a time-consistent manner, while in [51] an unsteady viscous-inviscid coupling method was introduced in which the coupling between viscous and inviscid flow contained active control elements in order to minimize the coupling error. This coupling, called **interactive boundary layer coupling, was designed to enable modeling of flows with shock-induced oscillations**. At each condition in figure 4.16 two symbols have been plotted, in the case of nonzero angle of attack the symbol at the lower incidence represents the last steady flow condition and the other symbol represents the first unsteady shock-induced oscillation condition. For the zero angle of attack case the two symbols represent subsequent Mach numbers at which a steady flow and an unsteady flow solution have been obtained, respectively. In general, good agreement between the calculated and the experimental results has been obtained. The buffet boundary predicted by the present method is slightly higher at high Mach numbers. The buffet boundary lies between those of [51] and [63]. The comparison of the



dominant reduced frequency during the buffet process is shown in figure 4.17. Although the buffet onset predicted by the present method is different from the results of [51], the trend of the dominant reduced frequency with the increase of the angle of attack is similar. At  $\alpha=4.00$  deg the present result is close to the result of [63] and is somewhat lower than the experimental result. This is probably due to the time consistent character of the method of Girodroux-Lavigne and LeBalleur [63] which is closer to a Navier-Stokes simulation. The result of [51] is slightly higher than the experiment.

Up to this point the calculations have been focused on the comparison to allow a further study of the aerodynamic mechanism in the unsteady flow. To study the unsteady flow phenomena further, inspection of the results of simulations for the nonzero ( $M_\infty=0.775$ ,  $\alpha=4.00$  deg) and zero ( $M_\infty=0.845$ ,  $\alpha=0.00$  deg) angle of attack conditions were carried out.

Figure 4.13 shows the space-time plot of the isobars and contours of constant skin friction. The following observations can be made: The shock moves downstream and near the most downstream shock position,  $x_s/c \approx 0.45$ , flow separation starts at the shock foot at  $(t - t_0)a_\infty/c \approx 3$ . The separation bubble spreads downstream towards the trailing edge and merges with the trailing edge separation at  $(t - t_0)a_\infty/c \approx 15$ . During this time the shock position remains almost constant. At  $(t - t_0)a_\infty/c \approx 13$  the shock starts to move upstream and a large disturbance is shed from the shock foot towards the trailing edge. On arriving at the trailing edge at  $(t - t_0)a_\infty/c \approx 15$  the flow on the lower surface becomes also influenced, probably primarily because the direction of the wake starts to rotate upwards (decambering of the airfoil), see also figure 4.12. The disturbances propagate upstream along the airfoil lower side with a speed lower than the convection speed in the separated region at the upper side. At  $(t - t_0)a_\infty/c \approx 22$  the flow at the upper surface starts to reattach at 0.70 chord. At this time the shock position is most forward. The reattachment region spreads rapidly both upstream and downstream. When the flow is fully attached the downstream motion of the shock sets in. Meanwhile the disturbances traveling along the lower side arrive at the leading edge at  $(t - t_0)a_\infty/c \approx 24$  and appear to change the local angle of attack (a change in oncoming flow direction, see figure 4.12). This variation of local angle of attack changes the pressure upstream of and in the supersonic flow region only slightly.

The propagation of pressure disturbances from the shock foot to the trailing edge for a heavy buffet condition found in the simulation was also observed by Roos [147] in a wind tunnel experiment. Roos [147] showed this feature by cross-correlating the pressures at the upper surface of a Whitcomb supercritical airfoil for a heavy buffet condition, see figure 4.18. The reference point of the cross-correlation was at 0.90 chord. The peaks, at positive value of  $\tau$ , in the cross-correlation of the pressure at the reference point and the pressures at a number of points upstream of the reference point show that the pressure at the reference point is correlated with the pressure upstream at an earlier time. This means that pressure disturbances propagate downstream. Here, similar cross-correlations have been calculated for the heavy buffet condition at  $M_\infty=0.775$  and  $\alpha=4.00$  deg. The results are presented in figure 4.19. Similar to the results of Roos, the pressure at the trailing edge is

correlated with the pressure upstream at an earlier time which means that the pressure disturbances propagate downstream. Thus the present method is in a qualitative agreement with the finding of Roos [147].

The physical explanation of this type of self-sustained unsteady flow has actually been attempted for quite a long time. Here, only the representative models, i.e. Lee's model [100] and Stanewsky and Basler's model [159], will be discussed.

Lee's model is shown in figure 4.20. The model hypothesizes a closed loop in which the pressure disturbance propagates in the separated flow region from the foot of the oscillating shock to the trailing edge, which then disturbs the wake. Subsequently, due to the disturbance the wake produces upstream propagating waves outside the boundary layer region to arrive at the shock and cause the shock motion of Tijdeman's type A. Lee tested his hypothesis using a computational method employing the TSP equation. A pulse disturbance was introduced explicitly at the trailing edge and the time required to close the loop, i.e. the period of oscillation, was calculated. Reduced frequencies of the same order of magnitude as the ones observed in the experiment were obtained. In his computational model, Lee assumed that waves are generated at the trailing edge and propagate upstream. However, in the present buffet simulation upstream propagating waves have not been observed. This will be demonstrated as follows. A similar cross-correlation as in figure 4.19 was computed in the flow region outside the separated flow which according to the hypothesis of Lee should contain upstream propagating waves. The result is presented in figure 4.22. Contrary to the model of Lee, a similar situation as in the separated flow region is observed, i.e. the waves propagate downstream. To further clarify this finding  $\tau$  at the peaks in the correlation diagram were calculated for all pressure data behind the shock wave. The reference point is located at  $x/c=1.055$ . The results have been plotted in figure 4.23. Each contour in figure 4.23 represents the location at which the peak in the correlation diagram occurs at the same value of  $\tau$ . These contours may also be interpreted as contours of constant phase lag with respect to the reference. Figure 4.23 shows a source of disturbances at the shock foot. The waves propagate mainly downstream and partly upstream to the upper part of the shock. Thus, two objections may be formulated for Lee's model: the upstream propagating waves have not been observed and the shock motion is not of type A, as postulated.

The other representative model of self-sustained shock-induced oscillation is due to Stanewsky and Basler [159], sketched in figure 4.21. The idea of their model is **similar to Lee's, but the pressure disturbances are now traveling mainly upstream** along the lower side of the airfoil and control the oncoming flow. The objection to this model is that although the upstream propagating waves were indeed observed in the calculation, their influence on the flow in front of and in the supersonic flow region at the upper side is very limited, see figure 4.13.

The application of the Spalart-Allmaras (SA) turbulence model for this case is not as successful as the BL model. Figure 4.24 shows the history of  $C_L$  and the magnitude of the Fourier components for the case at  $M_\infty=0.775$  and  $\alpha=4.00$  deg calculated with the BL and SA turbulence model, and the zero angle of attack case at  $M_\infty=0.845$  calculated with the BL model. Although the calculation with the SA

model predicts a similar shock-induced flow separation, the shock-induced oscillation is obviously damped. Very recently a similar calculation was carried out at NASA Langley by Bartels [21] which resulted also in damped responses. It should be noted that actually the natural frequency of the flow is still there, indicated by the presence of a peak at about  $k=0.19$  in the Fourier components of the lift coefficient.

To confirm the existence of a natural frequency in the flow in case of a calculation using the SA turbulence model, the airfoil was excited in pitching oscillation about the 0.25 chord. Figure 4.25 shows the history of  $C_L$  and the magnitude of the Fourier components of  $C_L$  for the excitation frequencies  $k=0.10$ , 0.19 and 0.40. It is clear that the response at  $k=0.19$  is always excited by the forced oscillations at all three frequencies. Moreover excitation at  $k=0.19$  produces a significant amplitude of  $C_L$  in the same order as the buffet condition calculated using the BL turbulence model. This result suggests that the natural mode of the flow is related to the shock-induced separated flow, whereas the self-sustained oscillation is determined by another mechanism.

From the simulation of transonic buffet of the NACA 0012 airfoil several conclusions are obtained: The present method has been successfully applied to simulate buffet flow for NACA 0012. Comparison of the buffet onset with the experimental results and other computational results employing viscous-inviscid interaction is satisfactory. The hypothesis of Lee [100] is not supported by the results of the simulation. Confirming the previous results obtained by others, the Spalart-Allmaras turbulence model does not give satisfactory results in modeling the buffet flow.

## 4.4.1 FIGURES

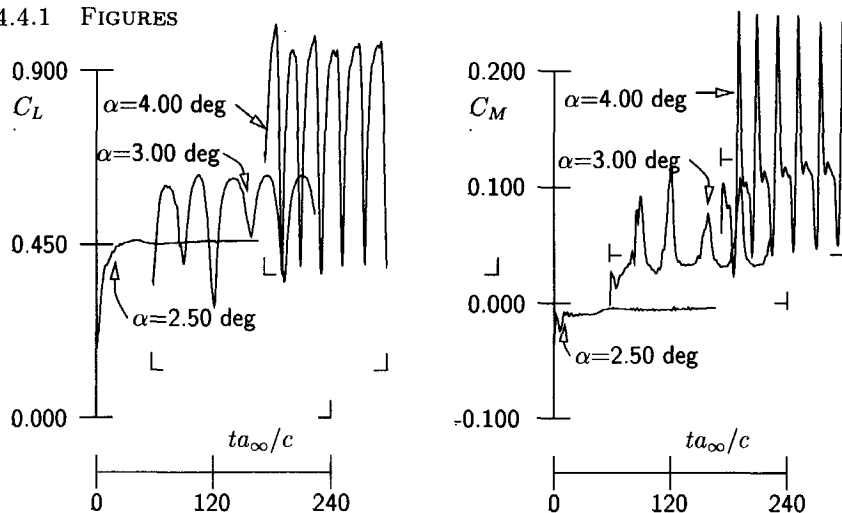


Figure 4.11: History of  $C_L$  and  $C_M$  of a NACA 0012 airfoil at  $M_\infty=0.775$ ,  $\alpha=2.50$  deg (last steady solution),  $\alpha=3.00$  deg (first unsteady solution),  $\alpha=4.00$  deg (deep buffeting condition) and  $Re_\infty=10^7$  using  $160 \times 60$  C-mesh

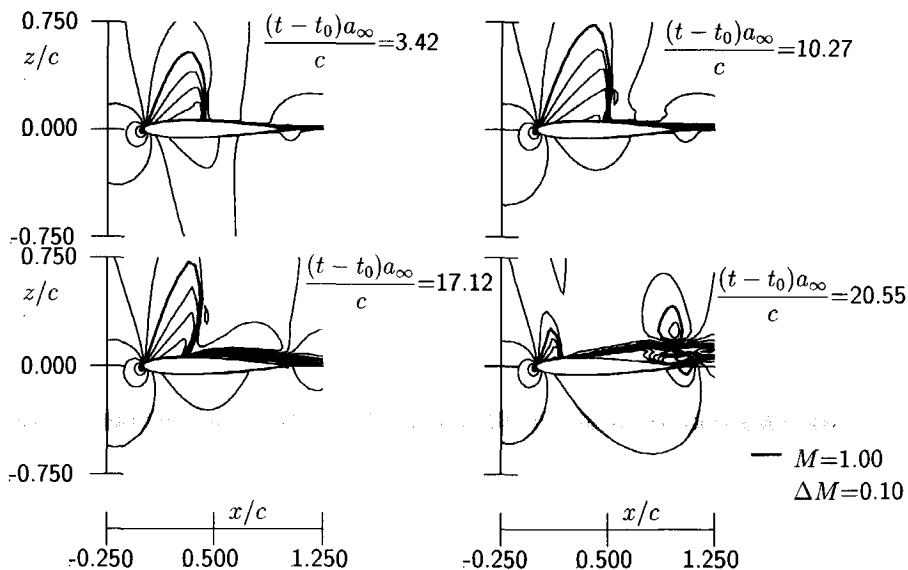


Figure 4.12: Instantaneous Mach contours at four time levels of an NACA 0012 airfoil at  $M_\infty=0.775$ ,  $\alpha=4.00$  and  $Re_\infty=10^7$ , using  $160 \times 60$  C-mesh. Time is relative to  $t_0 a_\infty/c=124.83$

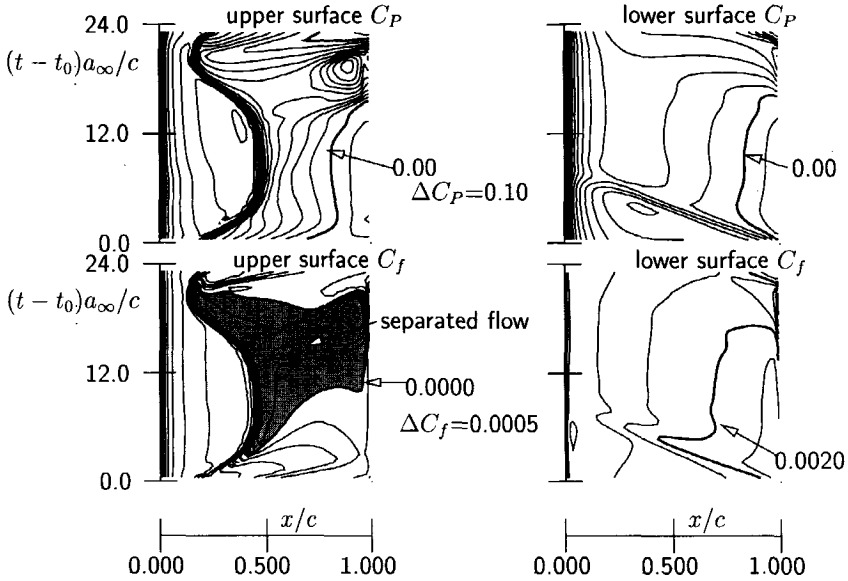


Figure 4.13: Contours of pressure and skin friction plotted in space-time of an NACA 0012 airfoil at  $M_\infty=0.775$ ,  $\alpha=4.00$  deg and  $Re_\infty=10^7$  using  $160 \times 60$  C-mesh

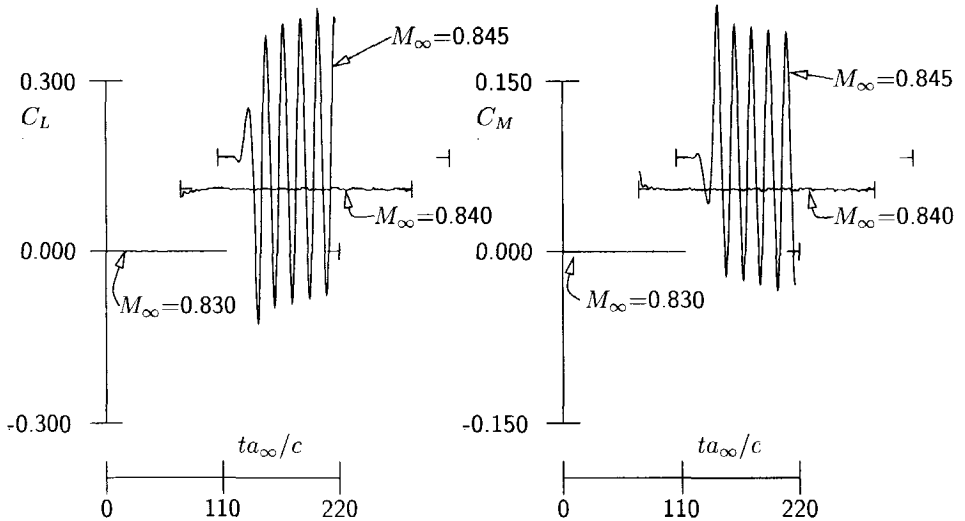


Figure 4.14: History of  $C_L$  and  $C_M$  of an NACA 0012 airfoil at  $\alpha=0.00$  deg,  $M_\infty=0.830$  (last steady solution),  $M_\infty=0.840$  (small fluctuation unsteady solution),  $M_\infty=0.845$  (unsteady solution) and  $Re_\infty=10^7$  using  $160 \times 60$  C-mesh

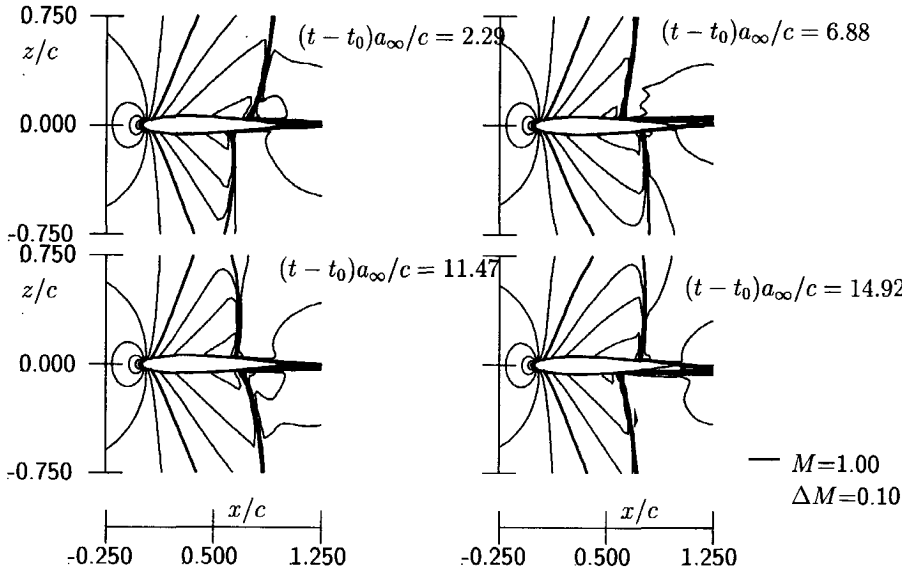


Figure 4.15: Instantaneous Mach contours at four time levels of an NACA 0012 airfoil at  $M_\infty=0.845$ ,  $\alpha=0.00$  deg and  $Re_\infty=10^7$  using  $160\times60$  C-mesh. Time is relative to  $t_0a_\infty/c=111.54$

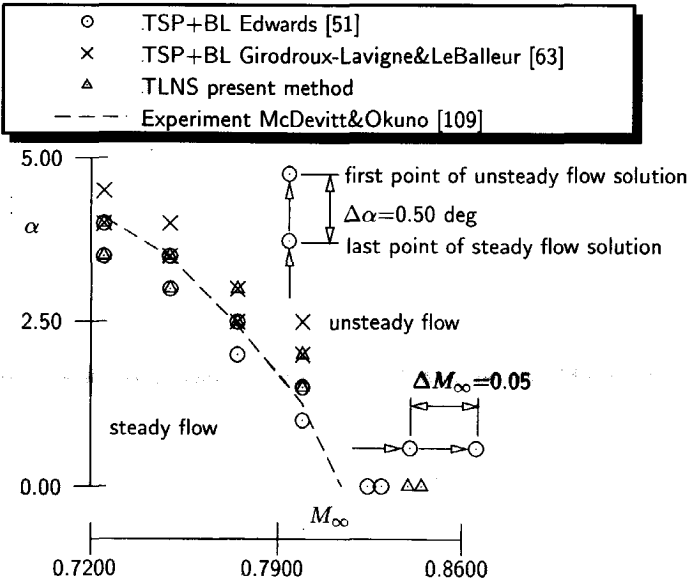


Figure 4.16: Comparison of calculated and measured buffet boundaries of an NACA 0012 airfoil at  $M_\infty=0.725\sim0.845$  and  $Re_\infty=10^7$

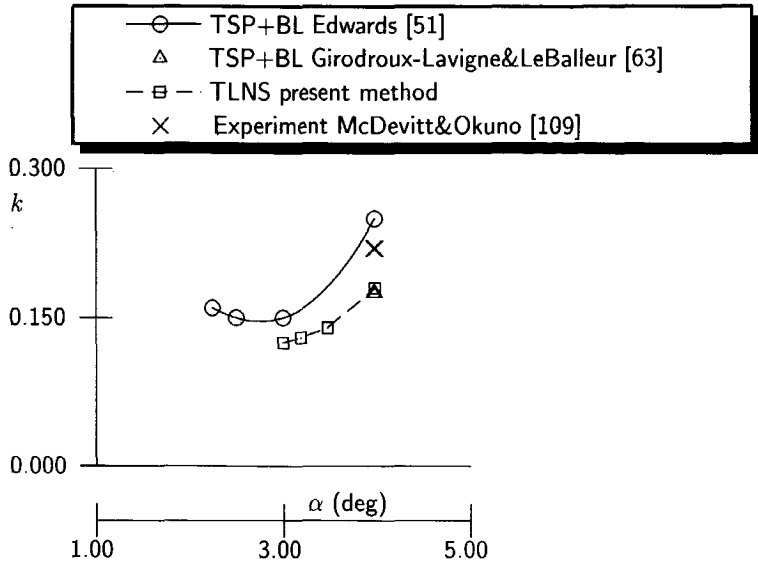


Figure 4.17: Comparison of calculated and measured dominant buffet reduced frequency of an NACA 0012 airfoil at  $M_\infty=0.775$ ,  $\alpha=2.00$  to  $4.00$  deg and  $Re_\infty=10^7$

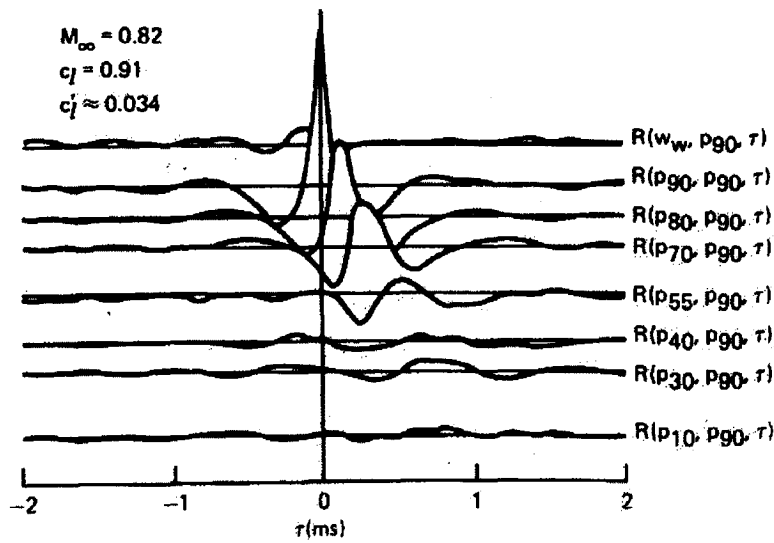


Figure 4.18: Cross-correlation function of pressures on the surface of a Whitcomb supercritical airfoil showing the propagation of disturbances during heavy buffet, taken from the experiment of Roos [147]

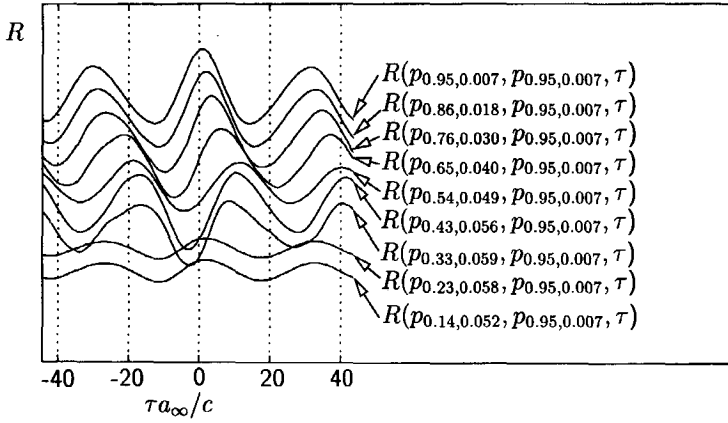


Figure 4.19: Cross-correlations of pressures on the surface of an NACA 0012 airfoil at a heavy buffet condition of  $M_\infty=0.775$ ,  $\alpha=4.00$  deg and  $Re_\infty=10^7$  using  $160 \times 60$  C-mesh

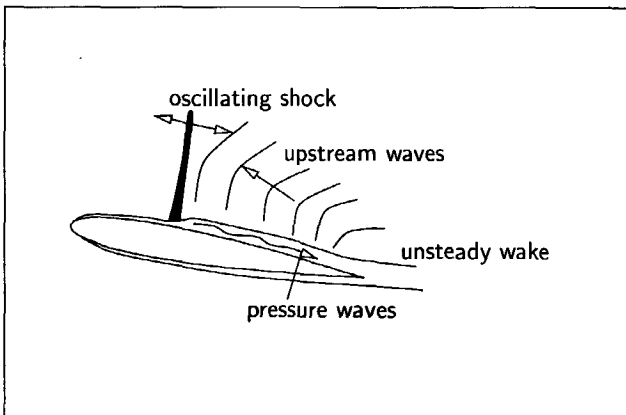


Figure 4.20: Self-sustained shock oscillation model of Lee [100]



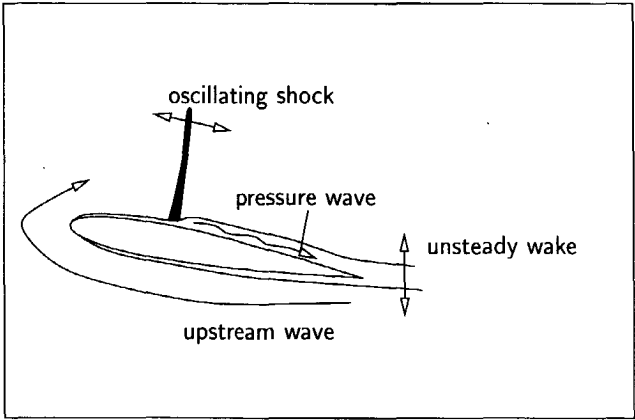


Figure 4.21: Self-sustained shock oscillation model of Stanewsky and Basler [159]

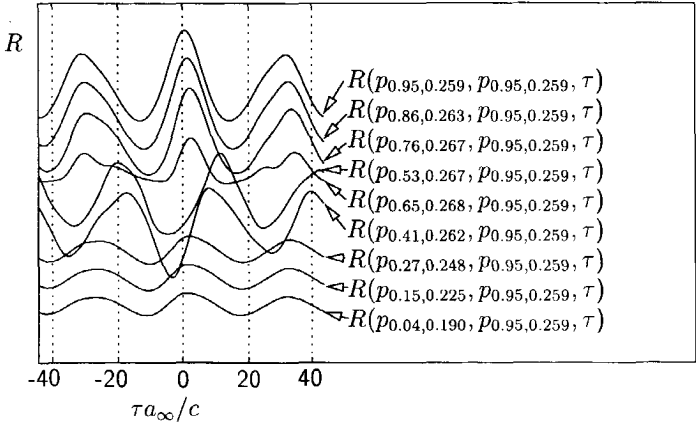


Figure 4.22: Cross-correlations of pressures outside the separated region of an NACA 0012 airfoil at a heavy buffet condition of  $M_\infty=0.775$ ,  $\alpha=4.00$  deg and  $Re_\infty=10^7$  using  $160 \times 60$  C-mesh

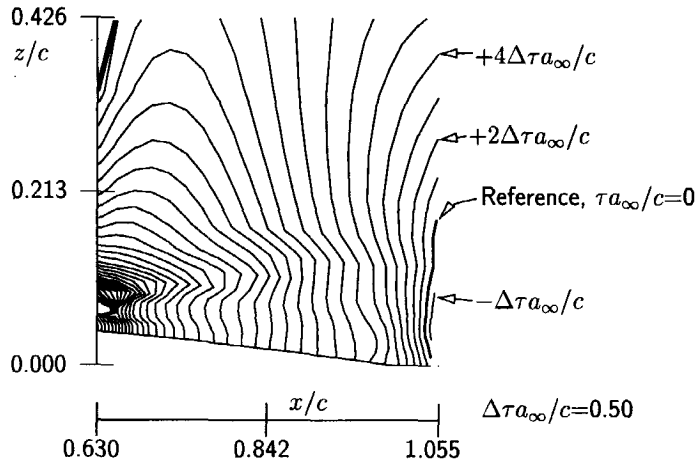


Figure 4.23: Contours of constant time lag, obtained from applying cross-correlation, of pressures behind the shock wave of an NACA 0012 airfoil at a heavy buffet condition of  $M_\infty=0.775$ ,  $\alpha=4.00$  deg and  $Re_\infty=10^7$  using  $160\times 60$  C-mesh

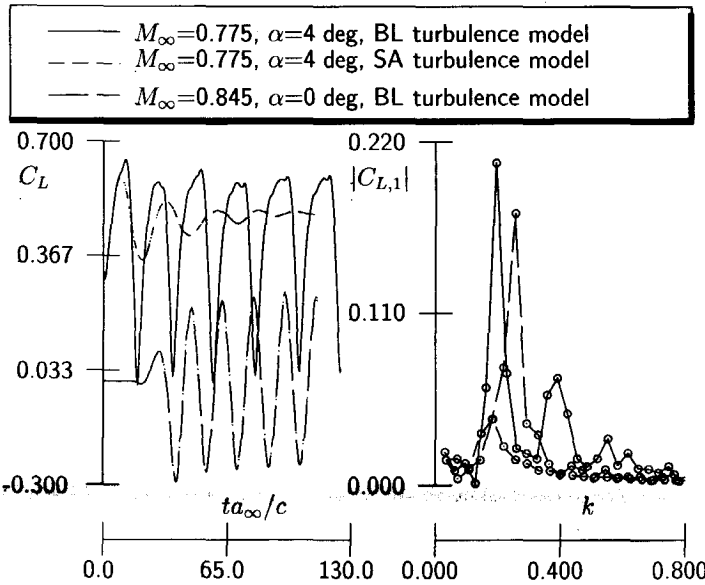


Figure 4.24: History of  $C_L$  and the magnitude of the Fourier components of  $C_L$  for three cases of a stationary NACA 0012:  $M_\infty=0.775$ ,  $\alpha=4.00$  deg using Baldwin-Lomax turbulence model and Spalart-Allmaras turbulence model and  $M_\infty=0.845$ ,  $\alpha=0.00$  deg using Baldwin-Lomax turbulence model, all at  $Re_\infty=10^7$

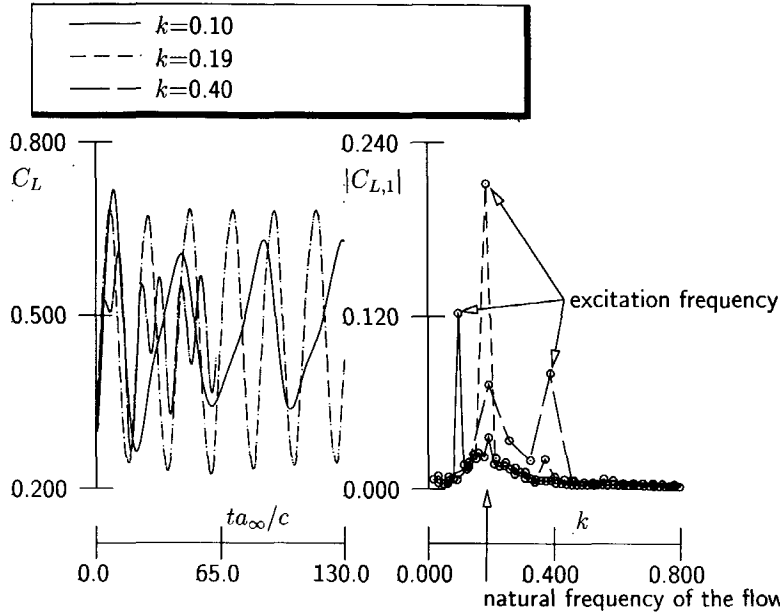


Figure 4.25: History of  $C_L$  and the magnitude of the Fourier components of  $C_L$  for the forced pitching oscillation about 0.25 chord of an NACA 0012 at  $M_\infty=0.775$ ,  $\alpha=4.00$  deg,  $k=0.10$ , 0.18, 0.40, calculated using Spalart-Allmaras turbulence model

#### 4.5 CONCLUSIONS CONCERNING THE SIMULATION OF UNSTEADY FLOW PHENOMENA AROUND AIRFOILS

The present method has been further validated by numerically simulating flows with significant viscous effects. From the cases considered in this chapter the following conclusions can be drawn:

1. Harmonically oscillating airfoil:

- The present method produces adequate accuracy in predicting shock motion for attached flow cases. Tijdeman's hypothesis concerning the phase lag of a type A shock motion has been reproduced.
- For flows with a large extent of separation, qualitatively correct results are also obtained. The behavior of the shock motion at low frequency and high frequency excitation are well predicted, i.e. the shock moves in a direction opposite to the one observed in the attached flow case, with a phase lag between shock and airfoil motion which increases with the excitation frequency.
- The occurrence of an aerodynamic resonance because of the presence of an aerodynamic natural mode of the flow can also be predicted.

2. Buffet:

- The buffet onset of the NACA 0012 airfoil for zero and nonzero angle of attack conditions is in a good agreement with experimental results.
- The finding of Roos [147] that in a heavy buffet condition the pressure disturbances propagate downstream behind the shock has been confirmed.
- The hypothesis of Lee [100] for the buffet/shock-induced oscillation mechanism has not been confirmed. There is no evidence of upstream propagating pressure waves generated at the trailing edge, which interfere with the shock wave. Instead, pressure waves have been observed to be generated at the shock foot and propagate downstream.

3. Turbulence modeling:

- The Spalart-Allmaras turbulence model appears to be less successful for **simulation of buffet flow. Despite the evidence of the existence of a natural frequency in the flow calculated using this turbulence model, no self-sustained oscillations have been obtained.**
  - Both Baldwin-Lomax and Spalart-Allmaras turbulence model predict similar shock-induced separated flow conditions. This seems to suggest that the presence of a natural frequency in the flow is more likely to be the consequence of a shock boundary layer interaction. There are other mechanisms which ensure the self-sustained oscillation to take place. More research is needed to determine these mechanisms.
-

## CHAPTER 5

# AEROLEASTIC SIMULATIONS USING CUA METHODS

According to the general directives for the development of a CAS method, section 2.3.3, the aerodynamic and the structural part should be loosely coupled. The aim of this chapter is to discuss in more detail the loose aero-structural coupling strategy to integrate both parts which were discussed in the previous chapter.

The following subjects are discussed in this chapter: introduction of the loose aero-structural coupling methods, the structural model used for the present two-dimensional CAS method, the temporal integration method for the structural part, the aero-structural coupling method based on aerodynamic and structural extrapolation, the analysis of the results and an example of a two-degree-of-freedom airfoil in transonic flow.

### 5.1 INTRODUCTION

In most of the methods found in the literature the time step of the unsteady aerodynamic method dictates the time step for the aeroelastic simulation. This has been the main drive to investigate an efficient CUA method for CAS applications, which was presented in chapter 3. It was concluded there that the present unsteady aerodynamic method can be used with large time steps while still maintaining sufficient accuracy. The choice of the time step is determined by the physical accuracy requirement rather than by the numerical stability limit.

In the beginning of the study the commonly used simple aerodynamic extrapolation method of Edwards et al. [52] was applied. It was shown by Prananta and Hounjet [132] that by using the present unsteady aerodynamic method, the time step of the aeroelastic simulation is determined by the accuracy of the aero-structural coupling procedure. This conclusion was drawn from the observation that although a large time step can be used for both the aerodynamic and the structural part to produce results with adequate accuracy, coupled simulations require a relatively small time step. Therefore, improvement of the coupling method is necessary to benefit from the large time step allowed by the current aerodynamic methods. Two coupling methods have been studied: an improved aerodynamic extrapolation method and a structural extrapolation method.

The methods discussed in this chapter will be applied also for three-dimensional

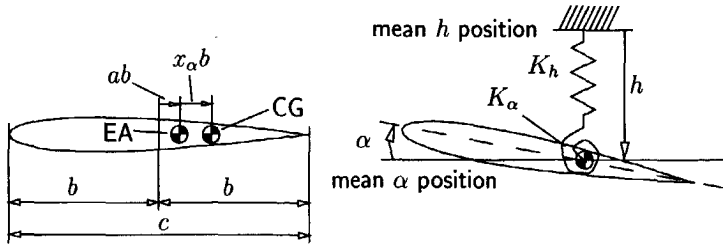


Figure 5.1: Typical section of a wing, CG is the center of gravity, EA is the elastic axis,  $K_h$  is the translational stiffness,  $K_\alpha$  is rotational stiffness

configurations, which will be presented in the next chapter.

## 5.2 STRUCTURAL MODEL

The assumption that the structural deformations are relatively small leads to linear models for the equation of motion of the structural part. For the purpose of the present discussion, a two-dimensional model of a wing is considered, which is rigid along its chord. The aeroelastic properties of this model, called typical section wing, is usually made to fit the properties at 70–75% of the actual wing semi-span. The motion of the typical section can be fully described by the translational and rotational displacements  $h$  and  $\alpha$ , respectively, representing typical bending and torsional displacements of the actual wing. Figure 5.1 shows the schematic picture of the typical section. The vibrational characteristics of the typical section are determined by the location of the center of gravity, CG, and the elastic axis, EA. The elastic axis marks the point where a vertical force will result in a translational displacement only and a moment about that point will result in a rotational displacement only.

As only these two degrees of freedom are involved, modal decomposition is not applied.

### 5.2.1 EQUATIONS OF MOTION

The equations of motion of the typical section wing may be derived by balancing the forces at and moments about EA. It should be noted that in deriving the equations of motion it is always assumed that  $\sin \alpha \approx \alpha$  and  $\cos \alpha \approx 1$ . The balance of forces then is:

$$m(\ddot{h} + x_{\alpha} b \ddot{\alpha}) + K_h \bar{h} + L = 0 \quad (5.1)$$

and the balance moment about EA is:

$$m \bar{h} x_{\alpha} b + I_{\alpha} \ddot{\alpha} + K_{\alpha} \alpha - M_{EA} = 0, \quad (5.2)$$

where  $\bar{h}$  is the translational displacement, positive downward,  $m$  is the mass of the typical wing section and  $I_{\alpha}$  is the mass moment of inertia with respect to EA, both

per unit wing span.  $L = q_\infty 2bC_L$  is the aerodynamic lift force, defined as positive upward, and  $M_{EA} = q_\infty 4b^2C_M$  is the aerodynamic moment about EA, defined as positive nose up, both quantities again per unit of wing span. After some simplifications equations (5.1) and (5.2) become:

$$\ddot{h} + x_\alpha \ddot{\alpha} + \omega_h^2 h = -2q_\infty C_L/m, \quad (5.3)$$

$$x_\alpha \ddot{h} + r_\alpha^2 \ddot{\alpha} + r_\alpha^2 \omega_\alpha^2 \alpha = 4q_\infty C_M/m, \quad (5.4)$$

where  $x_\alpha$  is the dimensionless distance of CG behind EA,  $r_\alpha = \sqrt{I_\alpha/(mb^2)}$  is the dimensionless radius of gyration with respect to EA,  $\omega_h = \sqrt{K_h/m}$  is the natural frequency of the uncoupled translation,  $\omega_\alpha = \sqrt{K_\alpha/I_\alpha}$  is the natural frequency of the uncoupled rotation and  $h = \bar{h}/b$  the dimensionless translational displacement.

Since both the equations of motion and the aerodynamic quantities  $C_L$  and  $C_M$  will be integrated simultaneously, their dimensionless time steps have to match. The nondimensionalization time parameter for the aerodynamic part,  $c/a_\infty$ , is used for the whole set of equations, to arrive at the following representation in a matrix form:

$$M\ddot{x}(t) + Kx(t) = B'U(x, t), \quad (5.5)$$

with:

$$M = \begin{bmatrix} 1 & x_\alpha \\ x_\alpha & r_\alpha^2 \end{bmatrix}, \quad K = \varphi^2 \begin{bmatrix} \omega_h^2/\omega_\alpha^2 & 0 \\ 0 & r_\alpha^2 \end{bmatrix},$$

$$B' = \frac{M_\infty^2}{\mu\pi} \begin{bmatrix} -4 & 0 \\ 0 & 8 \end{bmatrix},$$

where  $\varphi = 2M_\infty/\bar{U}$  is defined as the time scaling factor for a reason which will be explained later,  $\bar{U} = U_\infty/(\omega_\alpha b)$  is the reduced velocity,  $\mu = m/(\pi\rho b^2)$  is the mass ratio and the variables are  $x = [h, \alpha]^T$  and  $U = [C_L, C_M]^T$ . In case the accuracy of the structural part defines the time step for the whole set of aeroelastic equations one might adopt the structural time,  $t_s = t\omega_\alpha$ . The scaling factor between aerodynamic and structural time steps is then:  $\Delta t_s = \varphi\Delta t$ , for which  $\varphi$  is called the time scaling factor.

The consequence of defining  $h$  and  $\alpha$  with respect to EA, becomes clear by examining equation (5.5). The stiffness matrix  $K$  is diagonal, whereas the mass matrix  $M$  has off-diagonal elements.  $h$  and  $\alpha$ , are said to be inertially coupled, besides of course the aerodynamic coupling originating from  $U$ .

Equation (5.5) can be brought into a standard state space representation, i.e. a system of ordinary differential equations of order one as:

$$\dot{X} = AX + BU(X, t), \quad (5.6)$$

where:

$$A = \begin{bmatrix} 0 & I \\ -M^{-1}K & 0 \end{bmatrix}, \quad B = \begin{bmatrix} 0 \\ M^{-1}B' \end{bmatrix}$$

where the state variable is now  $X = [x, \dot{x}]^T$ . The state space form, which has been common in the study of aircraft flight dynamics for long, has also been adopted in structural dynamics because of its versatility in describing time-dependent processes. In equation (5.6), various similarity parameters are included: structural similarity parameters (offset of EA downstream of CG  $x_\alpha$ , radius of gyration  $r_\alpha$  and frequency ratio  $\omega_h/\omega_\alpha$ ), aerodynamic similarity parameter (Mach number  $M_\infty$ ) and the aero-structural coupling parameters (reduced velocity  $\bar{U}$  and mass ratio  $\mu$ ).

### 5.2.2 TEMPORAL INTEGRATION METHODS FOR STRUCTURAL DYNAMICS

In the study of structural dynamics, usually the forcing function does not depend on the state of the structure. The commonly applied temporal integration methods in structural dynamics are the Houbolt method, the Newmark- $\beta$  method and the Wilson- $\theta$  method. They are all implicit methods. The Houbolt method is applied directly to the second-order form of the equations of motion, equation (5.5), where  $\ddot{x}$  is approximated by a second-order backward difference formula and the resulting algebraic equation is solved for  $x^{n+1}$ . The Newmark- $\beta$  and the Wilson- $\theta$  method belong to the class of linear acceleration methods in which a linear variation of the acceleration from time  $t^n$  to  $t^n + \theta\Delta t$  is assumed. The reader should consult Bathe [23] for an excellent discussion of these methods. In addition, for nonlinear structural dynamic problems linear multistep methods are reported to be suitable, see Park [127].

In the present study only the Newmark- $\beta$  scheme with parameters resembling the trapezoidal scheme (average acceleration) will be considered. This method is known to be unconditionally stable and very accurate in resolving the amplitude of oscillation Gear [62]. Applying the trapezoidal scheme to the first-order equation, i.e. equation (5.6), results in:

$$\frac{X^{n+1} - X^n}{\Delta t} = A \frac{X^{n+1} + X^n}{2} + BU^{n+\frac{1}{2}}, \quad (5.7)$$

where  $U^{n+\frac{1}{2}}$  is a representative value of  $U$  between time level ( $n$ ) and ( $n+1$ ). Equation (5.7) can be easily solved for  $X^{n+1}$  which is the state of the structure at the next time level.

Considering a system represented by equation (5.6) where  $A$  is time-invariant, an exact solution can be derived if  $U$  does not depend on  $X$ . Similar to a scalar **ordinary differential equation**, the solution of equation (5.6) when  $U = U(t)$ , can be written as:

$$X^{n+1} = e^{At^{n+1}} X^0 + \int_0^{t^{n+1}} e^{A(t^{n+1} - \tau)} BU(\tau) d\tau. \quad (5.8)$$

The first part is the homogeneous solution and the second part is the particular solution. In some cases  $e^{At^{n+1}}$  can be calculated in an exact manner, but sometimes this is not done due to reasons of efficiency or convenience in the numerical implementation. Moreover, an exact integration of the particular part is usually



parameter	value	remark
airfoil	NACA 64A010	taken from [1]
$a$	-2.00	elastic axis in front of the airfoil
$x_\alpha$	1.80	
$r_\alpha^2$	3.48	
$\omega_h/\omega_\alpha$	1.00	ratio of uncoupled frequencies
$\mu$	60.00	

Table 5.1: Aeroelastic parameters of a typical section (Isogai's case A) used for the example of structural temporal integration methods

difficult. Therefore an approximate method is applied here. The method is called the transition matrix method; some notes on this method are presented in appendix D. The state at the next time level is obtained using the recursive relation:

$$X^{n+1} = \Phi X^n + \Theta U^{n+\frac{1}{2}}, \quad (5.9)$$

where a constant aerodynamic force  $U^{n+\frac{1}{2}}$  is assumed between time level ( $n$ ) and time level ( $n+1$ ). The methods for calculating  $\Phi$  and  $\Theta$  are presented in appendix D. For practical reasons it is more convenient to express the Newmark- $\beta$  method, viz. equation (5.7), in the form similar to equation (5.9). In this case  $\Phi$  and  $\Theta$  are:

$$\begin{aligned} \Phi &= [I - \frac{\Delta t}{2}A]^{-1}[I + \frac{\Delta t}{2}A], \\ \Theta &= [I - \frac{\Delta t}{2}A]^{-1}\Delta t B. \end{aligned} \quad (5.10)$$

The effectivity of the Newmark- $\beta$  and the transition matrix method has been tested using Isogai's case A [87]. The parameters are listed in table 5.1. This test case was originally proposed by Isogai [86] to investigate the transonic dip phenomenon of a swept back wing. Therefore the aeroelastic parameters of the typical section, shown in table 5.1, were designed to mimic the behavior of a swept wing: EA in front of the leading edge and a relatively high frequency ratio between the first bending and the first torsional modes. The natural frequencies of the free vibration can be easily calculated by considering the homogeneous part of equation (5.5):

$$\begin{bmatrix} 1 & x_\alpha \\ x_\alpha & r_\alpha^2 \end{bmatrix} \begin{Bmatrix} \ddot{h} \\ \ddot{\alpha} \end{Bmatrix} + \varphi^2 \begin{bmatrix} \omega_h^2/\omega_\alpha^2 & 0 \\ 0 & r_\alpha^2 \end{bmatrix} \begin{Bmatrix} h \\ \alpha \end{Bmatrix} = 0. \quad (5.11)$$

Substitution of  $[h, \alpha]^T = [\hat{h}, \hat{\alpha}]^T e^{i\omega t}$  into equation (5.11) results in an eigenvalue problem:

$$\begin{vmatrix} \omega_h^2/\omega_\alpha^2 \varphi^2 - \omega^2 & -x_\alpha \omega^2 \\ -x_\alpha \omega^2 & r_\alpha^2(\varphi^2 - \omega^2) \end{vmatrix} = 0, \quad (5.12)$$

which can be solved for  $\omega^2$ :

$$\omega^2 = \frac{r_\alpha^2 \varphi^2 (1 + \omega_h^2/\omega_\alpha^2)}{2(r_\alpha^2 - x_\alpha^2)} \pm \sqrt{\frac{r_\alpha^4 \varphi^4 (1 + \omega_h^2/\omega_\alpha^2)^2 - 4(r_\alpha^2 - x_\alpha^2) \omega_h^2/\omega_\alpha^2 r_\alpha^2 \varphi^4}{4(r_\alpha^2 - x_\alpha^2)^2}}. \quad (5.13)$$

Inserting the aeroleastic parameters of Isogai's test case A into equation (5.13) one obtains two eigenvalues,  $\omega_1=0.7134\varphi$  and  $\omega_2=5.3380\varphi$  (or using structural time  $\omega_1=0.7134\omega_\alpha$  and  $\omega_2=5.3380\omega_\alpha$ ). The pivot point of the vibration modes can be calculated with the help of the first equation of equation (5.12):

$$\begin{aligned} x_{pv} &= a - \dot{h}/\dot{\alpha} \\ &= a - \frac{x_\alpha \omega^2}{\omega_h^2/\omega_\alpha^2 \varphi^2 - \omega^2}, \end{aligned} \quad (5.14)$$

to arrive at:  $x_{pv}=-3.866$  for the first mode and  $x_{pv}=-0.134$  for the second mode, both are measured in  $b$  from the center of the airfoil. The wind-off mode shapes of

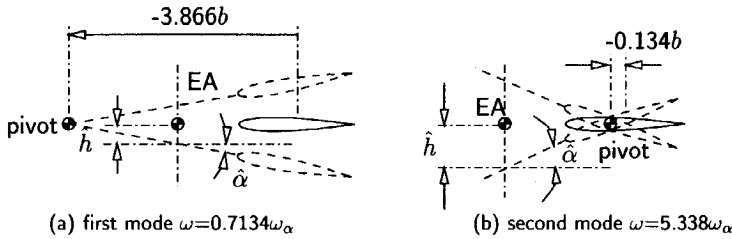


Figure 5.2: Vibration modes of Isogai's typical section

Isogai's typical section are sketched in figure 5.2, where the node of the first mode is in front of the leading edge and the node of the second mode is at the airfoil from the leading edge.

The simulation proceeds from an initial velocity for the pitching motion,  $\dot{\alpha}(0) = 0.01a_\infty/c$ . This initial condition will excite both modes. The number of time steps per cycle is set based on the highest frequency, i.e. the natural frequency of the second mode. The results for a small time step of 96 per cycle are shown in figure 5.3. The time traces show clearly the presence of two vibration modes with periods of oscillation of  $2\pi/(0.7134\omega_\alpha)=8.804/\omega_\alpha$  and  $2\pi/(5.338\omega_\alpha)=1.177/\omega_\alpha$ . It should be noted that the time along the horizontal axis of figure 5.3 has been nondimensionalized using the structural parameter because a nondimensionalization using the flow parameters would require the data of  $M_\infty$  and  $\bar{U}$ , which are not relevant in this case. The results of the transition matrix method are practically the same as those of the **Newmark- $\beta$  method**. **This test case also cross-checks the implementation of the two methods which turn out to be consistent.**

The results for a large time step of 8 steps per cycle are shown in figure 5.4. The reference is provided by the result of the transition matrix method using small time step presented in figure 5.3. The results of the transition matrix method do hardly differ from the reference, which suggests that the transition matrix  $\Phi$  has been accurately calculated. Meanwhile the results of the Newmark- $\beta$  method reveal an inaccuracy in resolving the high frequency component. The period of the high frequency component is clearly different from the reference. But it seems that the neutrally stable character of the Newmark- $\beta$  scheme, implying zero numerical

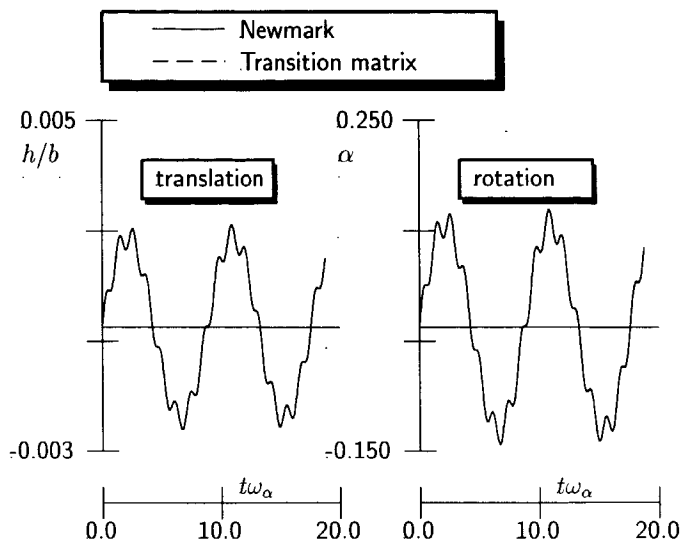


Figure 5.3: Comparison of the results between the matrix transition method, equation (5.9), and the Newmark- $\beta$  method, equation (5.7), for small time step

damping, ensures that the amplitude of the oscillation is in general correct. This neutrally stable character is further tested by executing the simulation up to 20 periods of the lower frequency modes. If there were inaccuracies in resolving the amplitude of oscillation this long simulation should reveal them. The results are presented in figure 5.5 which show that the amplitude is correctly reproduced, i.e. constant up to a very long simulation time.

### 5.3 LOOSE AERO-STRUCTURAL COUPLING METHODS

In the classical, linear aeroelastic approach the aerodynamic forces are divided into motion-dependent and motion-independent contributions (due to flow separation, wake, gust, etc.). The calculated responses to initial displacements and velocities and to motion-independent forces are superimposed afterwards. Since in nonlinear cases this superposition principle can not be applied, equation (5.5) treats all aerodynamic forces as one single term,  $U(x, t)$ . Moreover, since in general an explicit relation between  $U$  and  $x$  can not be obtained in a simple manner, the aerodynamic forces will be treated as an excitation of the structural system, thus  $U = U(t)$ . The coupling of the two equations of motion is effectuated via the (nonlinear) dependency of  $U(t) = [C_L(t), C_M(t)]^T$  on  $x = [h, \alpha]^T$ .

#### 5.3.1 COMMONLY USED METHOD

The commonly used loose aero-structural coupling method was introduced by Edwards et al. [52] and applied in [102, 141, 143]. In this method an approximation

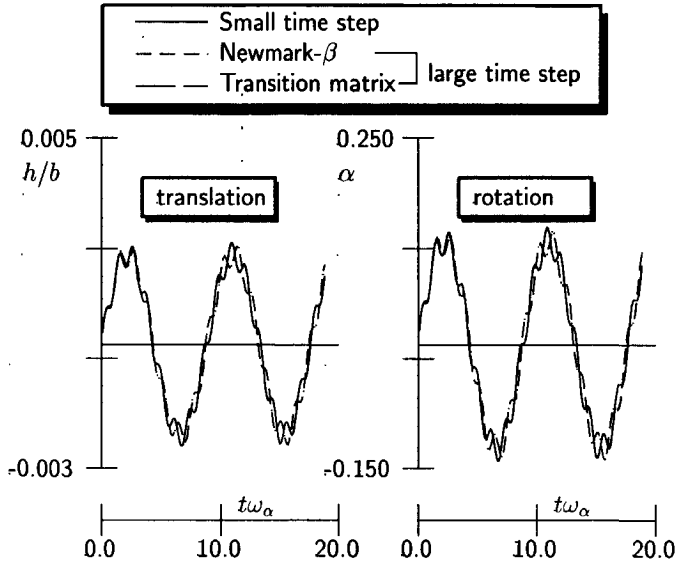


Figure 5.4: Comparison of the results between the matrix transition method, equation (5.9), and the Newmark- $\beta$  method, equation (5.7), for large time step

of the aerodynamic force is constructed and used to evaluate the nonhomogeneous part of equation (5.9). At the end of time level ( $n$ ) the structural equations need the aerodynamic loads at time level ( $n+1$ ) in order to solve the structural equations for the new position and velocity of the fluid/structure interface. These aerodynamic data are approximated using a simple extrapolation as:

$$\tilde{U}^{n+1} \approx 2U^n - U^{n-1}, \quad (5.15)$$

where  $\tilde{U}^{n+1}$  is the approximation of the aerodynamic force at time level ( $n+1$ ),  $U^n$  and  $U^{n-1}$  are the aerodynamic forces at time level ( $n$ ) and ( $n-1$ ), respectively. The integral of the particular part of equation (5.9) is then carried out by assuming a constant aerodynamic force of the form:

$$\begin{aligned} U^{n+\frac{1}{2}} &= \frac{1}{2}(\tilde{U}^{n+1} + U^n) \\ &= \frac{3}{2}U^n - \frac{1}{2}U^{n-1}. \end{aligned} \quad (5.16)$$

Solving equation (5.9) using the aerodynamic load defined by equation (5.16) results in an approximate position and velocity of the fluid/structure interface which are used to enforce boundary conditions to the flow solver, including the mesh deformation, to obtain the aerodynamic data,  $U^{n+1}$ . Rausch et al. [141] applied a corrector step in which the last aerodynamic data are used to solve the structural equations once more and subsequently update the mesh.

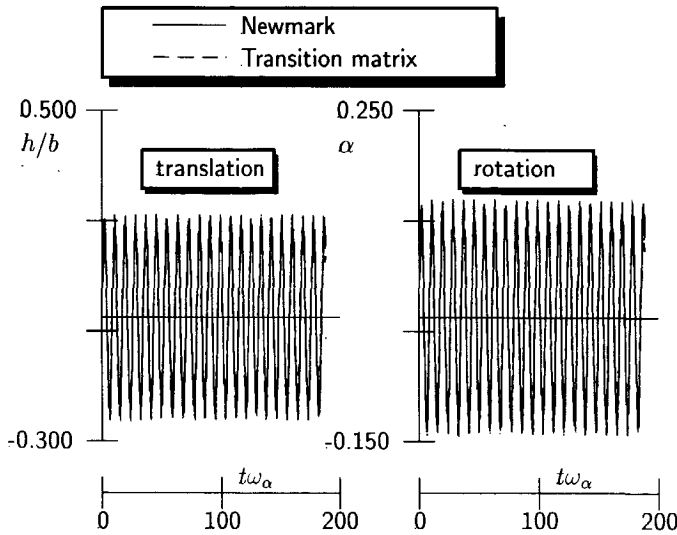


Figure 5.5: Comparison of the results between the transition matrix method, equation (5.9), and the Newmark- $\beta$  method, equation (5.7), for large time step and very long simulation time

It has already been shown by Prananta and Hounjet [133] that this method fails to give good results for aeroelastic simulations with large time steps. Two methods are considered to improve the commonly used loose aero-structural coupling procedure: an improved aerodynamic extrapolation method and a structural extrapolation method.

### 5.3.2 AERODYNAMIC EXTRAPOLATION

The most straightforward improvement of the commonly applied aerodynamic extrapolation method is by simply taking into account more data from the past, i.e. to apply a higher-order extrapolation.

To set up an extrapolation method, the aerodynamic force is expressed as a function of the flow variable  $Q$  and the state variable  $X$  as  $U = U(Q, X)$ . The extrapolation of  $U$  from the data up to time level  $(n)$  to time level  $(n + \frac{1}{2})$ , neglecting higher order terms, is:

$$U^{n+\frac{1}{2}} \approx U^n + \left( \frac{\partial U}{\partial Q} \frac{\partial Q}{\partial t} + \frac{\partial U}{\partial X} \frac{\partial X}{\partial t} \right) \frac{\Delta t}{2}. \quad (5.17)$$

The first term takes into account the change in the flow and the second term the change in the geometry. The  $\partial Q/\partial t$  and  $\partial X/\partial t$  are readily available data or can be calculated easily, while  $\partial U/\partial Q$  and  $\partial U/\partial X$  have to be calculated.

To calculate  $\partial U/\partial Q$  and  $\partial U/\partial X$  the aerodynamic forces are expressed explicitly as function of  $Q$ ,  $h$  and  $\alpha$ . Note that the  $h$  direction is parallel to the  $z$  direction

and pointing downward, the aerodynamic force coefficients are calculated as:

$$\begin{aligned} C_L(t) &= -\frac{2}{M_\infty^2} \sum_i p_i(t) \hat{\zeta}_{z,i}(t), \\ C_M(t) &= -\frac{2}{M_\infty^2} \sum_i p_i(t) [(z(t) - z_{EA}) \hat{\zeta}_x(t) - (x(t) - x_{EA}) \hat{\zeta}_z(t)]_i, \end{aligned}$$

where  $p(t)$  is the surface pressure nondimensionalized by  $\rho_\infty a_\infty^2$  and  $[\hat{\zeta}_x, \hat{\zeta}_z]^T$  denotes the normal vector of the surface, nondimensionalized by the chord length  $c$ , as defined in equation (3.7). The coordinates of the fluid/structure interface are written explicitly as functions of  $h$  and  $\alpha$  as:

$$\begin{aligned} x(t) &= x_{EA} + (x(0) - x_{EA}) \cos \alpha(t) + (z(0) - z_{EA}) \sin \alpha(t) \\ z(t) &= z_{EA} - (x(0) - x_{EA}) \sin \alpha(t) + (z(0) - z_{EA}) \cos \alpha(t) - h(t)/2, \end{aligned}$$

where  $[x(0), z(0)]^T$  is the coordinate of the interface at its mean steady position. The change of the lift coefficient due to the change in flow variable, i.e. the first term of equation (5.17), is:

$$\frac{\partial C_L}{\partial p} \frac{\partial p}{\partial t} = \frac{\partial C_L}{\partial t} \Big|_{h,\alpha} = -\frac{2}{M_\infty^2} \sum_i \frac{\partial p_i}{\partial t} \hat{\zeta}_{z,i}, \quad (5.18)$$

where the pressure  $p$  is used instead of  $Q$ . The gradients of the lift coefficient with respect to the state variables are:

$$\begin{aligned} \frac{\partial C_L}{\partial \alpha} &= -\frac{2}{M_\infty^2} \sum_i p_i (-\hat{\zeta}_z(0) \sin \alpha(t) - \hat{\zeta}_x(0) \cos \alpha(t))_i, \\ \frac{\partial C_L}{\partial h} &= \frac{\partial C_L}{\partial h} = \frac{\partial C_L}{\partial \dot{\alpha}} = 0. \end{aligned}$$

The change of the moment coefficient about the elastic axis EA due to the change in flow variable is:

$$\frac{\partial C_M}{\partial p} \frac{\partial p}{\partial t} = \frac{\partial C_M}{\partial t} \Big|_{h,\alpha} = -\frac{2}{M_\infty^2} \sum_i \frac{\partial p_i}{\partial t} [(z - z_{EA}) \hat{\zeta}_x - (x - x_{EA}) \hat{\zeta}_z]_i. \quad (5.19)$$

The gradients of the moment  $C_M$  with respect to the state variables are calculated in a similar manner:

$$\begin{aligned} \frac{\partial C_M}{\partial \alpha} &= -\frac{2}{M_\infty^2} \sum_i p_i(t) [(z(t) - z_{EA}) \frac{\partial \hat{\zeta}_x}{\partial \alpha} + \frac{\partial z}{\partial \alpha} \hat{\zeta}_x(t) - (x(t) - x_{EA}) \frac{\partial \hat{\zeta}_z}{\partial \alpha} - \frac{\partial x}{\partial \alpha} \hat{\zeta}_z(t)]_i, \\ \frac{\partial C_M}{\partial h} &= \frac{\partial C_M}{\partial h} = \frac{\partial C_M}{\partial \dot{\alpha}} = 0, \end{aligned}$$

where  $\partial \hat{\zeta}_x / \partial \alpha$ ,  $\partial \hat{\zeta}_z / \partial \alpha$ ,  $\partial x / \partial \alpha$  and  $\partial z / \partial \alpha$  can be easily calculated from equation

(5.18) as:

$$\begin{aligned}\frac{\partial \hat{\zeta}_x}{\partial \alpha} &= \hat{\zeta}_z(0) \cos \alpha(t) - \hat{\zeta}_x(0) \sin \alpha(t) \\ \frac{\partial \hat{\zeta}_z}{\partial \alpha} &= -\hat{\zeta}_z(0) \sin \alpha(t) - \hat{\zeta}_x(0) \cos \alpha(t) \\ \frac{\partial x}{\partial \alpha} &= -(x(0) - x_{EA}) \sin \alpha(t) + (z(0) - z_{EA}) \cos \alpha(t) \\ \frac{\partial z}{\partial \alpha} &= -(x(0) - x_{EA}) \cos \alpha(t) - (z(0) - z_{EA}) \sin \alpha(t).\end{aligned}$$

Inserting these expressions in equation (5.17) the aerodynamic forces at time level  $(n + \frac{1}{2})$  can then be predicted using  $X$  and  $\partial p / \partial t$  data at time level  $(n)$ .

### 5.3.3 STRUCTURAL EXTRAPOLATION

The structural part behaves like a filter to the aerodynamic signal. This results in structural motions which are smoother functions of time than the aerodynamic forces. Thus it may be expected that extrapolating the structural state yields a better result than extrapolating the aerodynamics data.

To obtain the aerodynamic force at time level  $(n + \frac{1}{2})$ , the position of the interface is first approximated as:

$$\begin{aligned}h^{n+\frac{1}{2}} &\approx h^n + \frac{\partial h^n}{\partial t} \frac{\Delta t}{2} \\ \alpha^{n+\frac{1}{2}} &\approx \alpha^n + \frac{\partial \alpha^n}{\partial t} \frac{\Delta t}{2}.\end{aligned}\tag{5.20}$$

The quantities  $\partial h / \partial t = \dot{h}$  and  $\partial \alpha / \partial t = \dot{\alpha}$  are readily available. Using these data, the mesh can be generated at time level  $(n + \frac{1}{2})$ . Actually a similar method was introduced by Farhat and Lesoinne [58] for a different reason, namely to satisfy the GCL on the fluid/structure interface.

For the velocity a linear extrapolation is applied:

$$\dot{h}^{n+\frac{1}{2}} \approx \frac{3}{2} \dot{h}^n + \frac{1}{2} \dot{h}^{n-1}\tag{5.21}$$

$$\dot{\alpha}^{n+\frac{1}{2}} \approx \frac{3}{2} \dot{\alpha}^n + \frac{1}{2} \dot{\alpha}^{n-1}.\tag{5.22}$$

Using these data the velocity of the interface can be calculated and used to impose the boundary condition on the flow equations. It was concluded in [58] that the surface velocity at time level  $(n)$  has to be used to impose boundary condition at time level  $(n + \frac{1}{2})$ , otherwise high frequency oscillations would occur due to the violation of the GCL. In the present study, although the velocity is assumed to be linear, no high frequency oscillations have been experienced so far. This may be explained by the fact that the GCL is satisfied by the CUA method, see chapter 3 and Prananta and Hounjet [132].

In this method the aerodynamic part marches at a time level between the structural states. This method is more efficient than the first one since all quantities needed for extrapolation are readily available or otherwise can be easily calculated.

### 5.3.4 RESULTS

In this section some results for the coupling procedures discussed in the previous section are presented. The same case as in section 5.2.2 is considered, i.e. Isogai's case A [86]. The aeroelastic parameters are given in table 5.1. Only results employing the Euler equations are considered, since for reasons of accuracy these allow the largest time steps to be taken. The flutter boundaries of this case using the present method will be compared to results of some other methods and discussed at the end of this chapter. The result presented here will concentrate on the large time step aspect of the method.

A mesh consisting of  $140 \times 32$  points was used. The steady flow was first calculated at the mean condition. The aeroelastic simulation was subsequently started from this steady condition by setting an initial velocity  $\dot{x}(0)$ . The small time step simulation used 32 time steps/period of the uncoupled mode while the large time step simulation applies 8 time steps/period. Two cases are considered, the first one is a supercritical, i.e. slightly unstable, condition at  $M_\infty = 0.775$  with speed index  $V^* = U_\infty / (\omega_\alpha b \sqrt{\mu}) = 1.00$  and the second one is a subcritical condition at  $M_\infty = 0.85$  with  $V^* = 0.53$ .

Applying the small time step for the supercritical case, the common aerodynamic extrapolation of [52], the present aerodynamic extrapolation and the present structural extrapolation methods produce the same results, see figure 5.6.

The comparison of simulation results obtained using small and large time steps for the supercritical case are presented in figures 5.7 to 5.9. Figure 5.7 reveals clearly the inadequacy of the commonly used method for large time step simulations. On the other hand, the results of the present aerodynamic extrapolation method, depicted in figure 5.8, show a good agreement between results of large time step and small time step simulations. Figure 5.9 shows that a similar good agreement is obtained using the structural extrapolation method.

To obtain the damping of the response a fitting method, which will be discussed in section 5.4, is applied. The fitting method is based on the work presented by Hounjet et al. [81]. After the analysis a quantitative comparison can be made:

method	$\sigma$	CPU(min/simulation)
small $\Delta t$	0.00616	46
large $\Delta t$ , aerodynamic extrapolation	0.00617	15
large $\Delta t$ , structural extrapolation	0.00679	15
<b>large <math>\Delta t</math>, simple extrapolation [52]</b>	<b>0.01270</b>	<b>15</b>

where  $\sigma$  is the damping decay coefficient. It can be seen that the present extrapolation methods give more accurate  $\sigma$  values compared to the commonly used method of [52] for the same cost in terms of CPU time.

The simulations using the small time step needed 46 minutes of CPU time on an SGI R8000 workstation, while large time step simulations needed 15 minutes, which is a significant saving of turn-around time. It should be noted that although the time step is four times larger, the speed-up of the large time step simulation is less than four because more subiterations are required per time step.



These damping coefficients are for a particular speed index. To obtain the flutter speed index at this Mach number  $M_\infty=0.775$  some more simulations at different speed indices have to be carried out usually at least three. The corresponding damping coefficients are then interpolated to zero value. After running more simulations the flutter speed index obtained using each of the methods is:

method	$V_F^*$
small $\Delta t$	0.942
large $\Delta t$ , aerodynamic extrapolation	0.942
large $\Delta t$ , structural extrapolation	0.938
large $\Delta t$ , simple extrapolation [52]	0.911

Edwards' [52] simple extrapolation method eventually produces a flutter speed which is about 5% lower than the rest.

A similar study has been performed for the subcritical case where a strong shock wave is present. The results are shown in figures 5.10 to 5.13. Similar observations can be made as for the supercritical example. At the small time step the method of [52], the present aerodynamic extrapolation method and the present structural extrapolation method produce practically the same result. At the large time step the current methods are superior to the common aerodynamic extrapolation method of [52]. A more detailed comparison after analysis of the time responses is:

method	$\sigma$	CPU (min/simulation)
small $\Delta t$	-0.00167	46
large $\Delta t$ , aerodynamic extrapolation	-0.00167	15
large $\Delta t$ , structural extrapolation	-0.00146	15
large $\Delta t$ , simple extrapolation [52]	+0.00172	15

Note that the simple method produces an unstable result, contrary to the other methods. After running more simulations the flutter speed indices are obtained:

method	$V_F^*$
small $\Delta t$	0.541
large $\Delta t$ , aerodynamic extrapolation	0.541
large $\Delta t$ , structural extrapolation	0.540
large $\Delta t$ , simple extrapolation [52]	0.528

From the presented test cases it may be concluded that the present aero-structural coupling methods maintain adequate accuracy for simulations using large time steps. This possibility to carry out the aeroelastic simulation using large time steps leads to a CPU time reduction of about 60% compared to the one for simulation using small time steps.

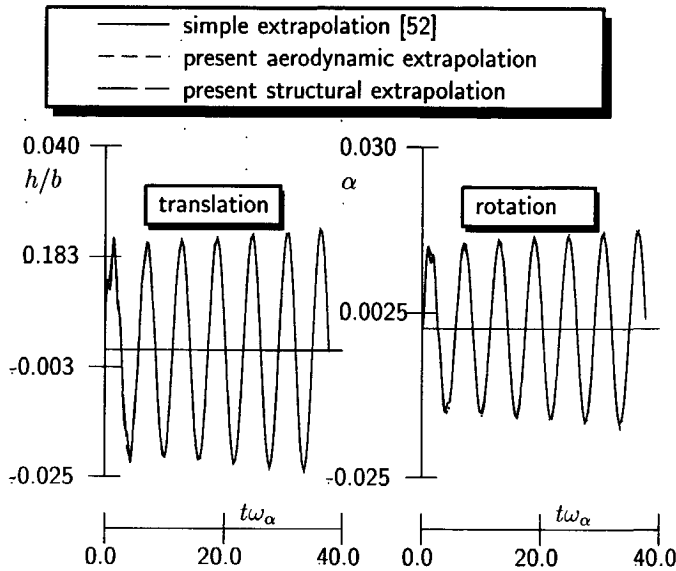


Figure 5.6: Comparison of time response of  $h$  and  $\alpha$  for small time step simulations of Isogai's case A at  $M_\infty=0.85$

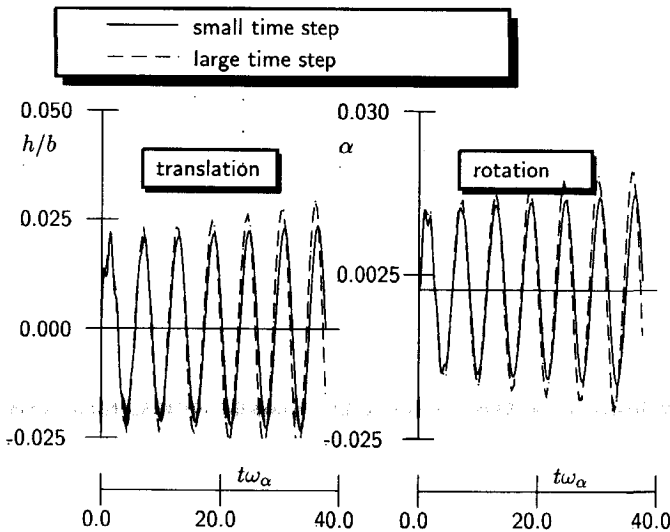


Figure 5.7: Comparison of time responses between small and large time step simulations for extrapolation method of [52], Isogai's case A at  $M_\infty=0.775$

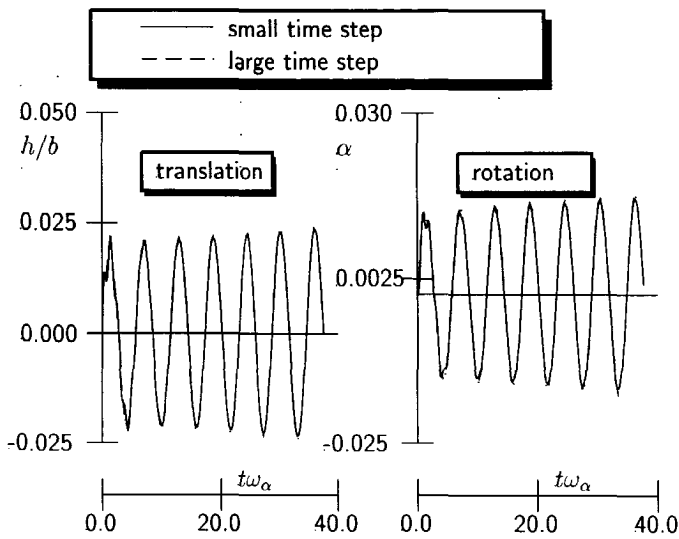


Figure 5.8: Comparison of time responses between small and large time step simulations for the present aerodynamic extrapolation method, Isogai's case A at  $M_\infty=0.775$

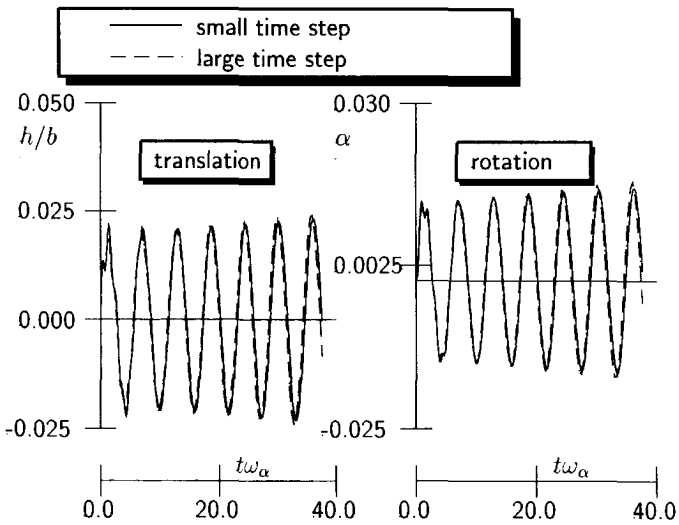


Figure 5.9: Comparison of time responses between small and large time step simulations for the present structural extrapolation method, Isogai's case A at  $M_\infty=0.775$

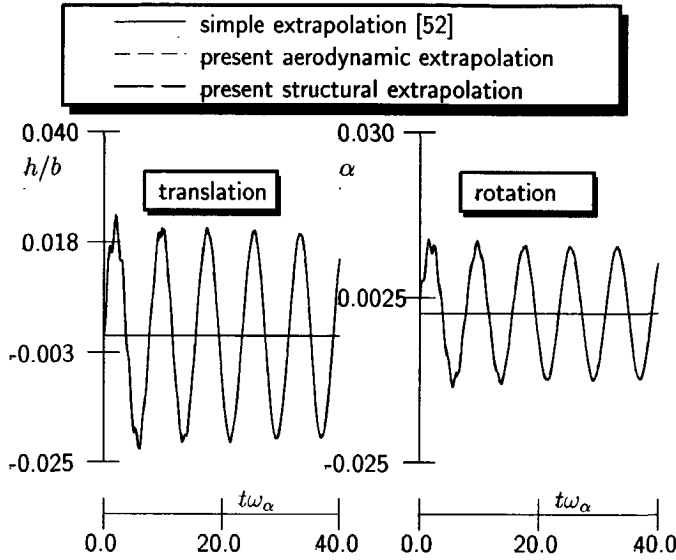


Figure 5.10: Comparison of time response of  $h$  and  $\alpha$  for small time step simulations of Isogai's case A at  $M_\infty=0.85$

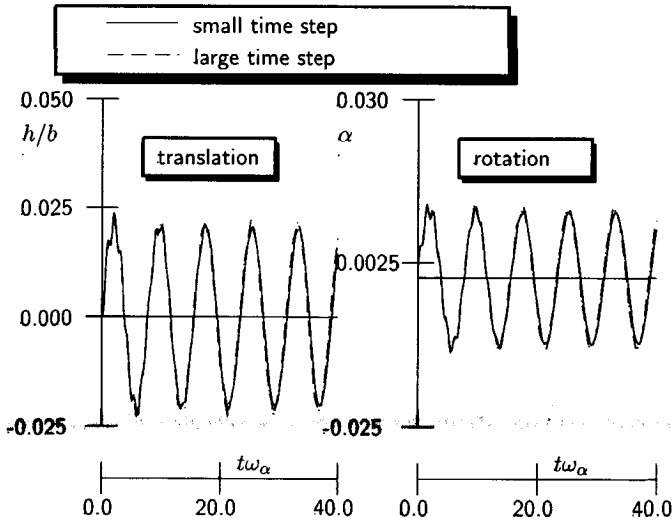


Figure 5.11: Comparison of time responses between small and large time step simulations for aerodynamic extrapolation method of [52], Isogai's case A at  $M_\infty=0.85$

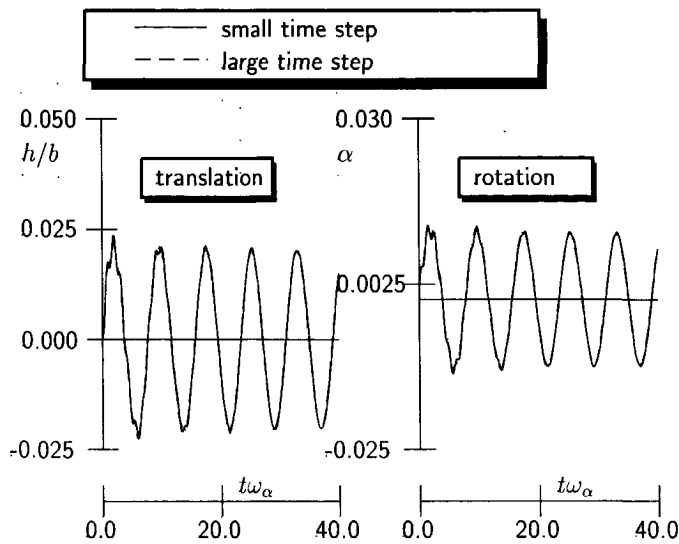


Figure 5.12: Comparison of time responses between small and large time step simulations for the present aerodynamic extrapolation method, Isogai's case A at  $M_\infty=0.85$

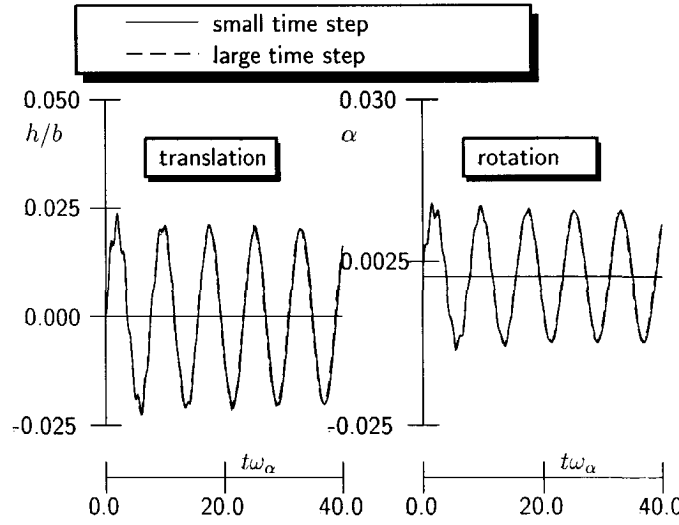


Figure 5.13: Comparison of time responses between small and large time step simulations for the present structural extrapolation method, Isogai's case A at  $M_\infty=0.85$

## 5.4 ANALYSIS OF THE RESPONSE

The purpose of the analysis of the time responses is to obtain the damping and the frequency of the oscillatory components involved. The response signals are approximated by the following function:

$$x(t) = a_0 + a_1 e^{\sigma_1 t} \cos(\omega_1 t + \phi_1) + a_2 e^{\sigma_2 t} \cos(\omega_2 t + \phi_2) + \dots, \quad (5.23)$$

where  $\sigma_i$ ,  $\omega_i$  and  $\phi_i$  is the damping, frequency and phase lag of mode  $i$ , respectively. Each component is generally known as a damped cosine function or exponential cosine function and has been used in Bennett and Desmarais [31], Hounjet et al. [81]. The maximum number of oscillating components which is selected depends on the number of vibration modes involved in the simulation.

The approximation function, equation (5.23), assumes linearity in the response signals. This assumption limits the application to small amplitude vibrations. For example, at a certain condition, in the beginning of a simulation a growing response is observed, but after the amplitude has increased sufficiently large it stabilizes at a certain amplitude. Such a response is known as a limit cycle oscillation (LCO). In this case only the signal at the beginning of the response, where the amplitude of oscillation is still sufficiently small, is fitted to equation (5.23). The concept of stability in this sense is known as asymptotic stability, Hagedorn [71], Meirovitch [112], where, starting from an equilibrium condition, a response to a disturbance is called stable if it returns to the equilibrium condition as  $t \rightarrow \infty$ . This is the most common concept applied in practice<sup>1</sup>. Although the present method can be applied in the conditions beyond the asymptotic stability boundary, for example to find the amplitude of LCO, the term *flutter boundary* which separates the stable and unstable responses should be interpreted here in the sense of asymptotic stability.

The fitting procedure proceeds by an iteration containing two steps: the linear step and the nonlinear step. The linear step is a simple least-squares fitting method to calculate the  $a_i$  with assumed values of  $\sigma_i$ ,  $\omega_i$  and  $\phi_i$  (or values calculated at the previous iteration). The nonlinear step is a minimization procedure for the  $\sigma_i$ ,  $\omega_i$  and  $\phi_i$  with constant  $a_i$ . The iteration is stopped after the cost function reaches a certain tolerance. For example, assume a set of  $N$  sample points which will be used to fit a response with two damped cosine functions. In both steps the cost function is defined as:

$$I = \sum_{i=1}^N [a_0 + a_1 e^{\sigma_1 t_i} \cos(\omega_1 t_i + \phi_1) + a_2 e^{\sigma_2 t_i} \cos(\omega_2 t_i + \phi_2) - x_i]^2. \quad (5.24)$$

First an initial guess for  $\sigma_i$ ,  $\omega_i$  and  $\phi_i$  is made. The coefficients  $a_i$  are then calculated using three equations obtained from  $\partial I / \partial a_i = 0$ . Applying these coefficients in the second step,  $I$  is minimized using the downhill simplex method with respect to  $\sigma_i$ ,  $\omega_i$  and  $\phi_i$ . After obtaining a better approximation of  $\sigma_i$ ,  $\omega_i$  and  $\phi_i$ , a least-square fitting is carried out to determine new values for  $a_i$ . This loop is stopped after  $I$  has reached a certain tolerance, see [31, 81] for a detailed description of the method.

<sup>1</sup>According to airworthiness requirements the damping of the system must have a prescribed minimum value.

### 5.5 APPLICATIONS FOR TWO-DEGREE-OF-FREEDOM AIRFOIL

In this section some results of the two-dimensional CAS method are presented. The aims are to validate the present approach and to produce new results. The Isogai case A [87] is again considered. This case is selected for validation because many results can be found in the literature.

#### 5.5.1 ATTACHED FLOW CASE

The angle of attack of the oncoming flow is zero. The Mach number ranges from 0.75 to 0.95. Well-known inviscid flow results of Isogai [87] are used to validate the present CAS method. Also the interesting features of multiple flutter points at a certain Mach number and LCO found by Bendiksen and Kousen [29] will be reproduced. Furthermore, new results using a viscous flow modeling will be presented. In this viscous flow case the Reynolds number is  $Re_\infty = 6 \times 10^6$ .

The analysis proceeds by first calculating the steady-state condition at a certain Mach number. The airfoil is then excited sinusoidally in a rotational mode about the elastic axis at the frequency  $\omega_\alpha$  with an amplitude of 1.00 deg. After 2 periods of forced oscillation the airfoil is released for another 4 to 5 periods to obtain the response.

The dimensions of the C-type mesh are  $140 \times 32$  for the inviscid flow and  $140 \times 60$  for the viscous flow. For these simulations the present aerodynamic extrapolation method is employed. The time needed for one simulation run is about 15 minutes for an inviscid flow computation and about 45 minutes for a viscous flow computation on a SUN SPARC 20 workstation. The viscous flow case takes much longer CPU time since it needs a smaller time step and also a finer grid.

Figures 5.14 and 5.15 show typical time responses close to the lowest flutter boundary at various Mach numbers for inviscid and viscous flow, respectively. The vibration mode depicted by translational and rotational displacements at almost the same phase is mostly bending with the node in front of the elastic axis, see the sketch of figure 5.2(a). In both inviscid and viscous cases the position of the node,  $a - h/\alpha$ , moves towards the airfoil as the Mach number increases, i.e. the ratio  $h/\alpha$  increases. An exception is for the inviscid flow response at  $M_\infty = 0.90$ , where the vibration mode is mostly rotation, i.e.  $h/\alpha \approx -1$ , see the sketch of figure 5.2(b).

The flutter mode in which the node resides in front of the airfoil is the classical bending-torsion flutter where the aerodynamic forces generated by the torsion mode amplify the motion of the bending mode. In the case of a swept wing the first bending mode has the elastic axis in front of the airfoil which is very similar to a bending-torsion mode of a straight wing. Therefore Isogai [86] concluded that this type of flutter mode of a swept wing may be called a one-mode flutter. The other flutter mode, the torsion mode, is typical for transonic flow conditions. The motion is strongly related to the motion of the shock wave [29, 87].

Figure 5.16 compares the flutter speed indices and the associated nondimensional flutter frequencies obtained using the present inviscid flow method with inviscid flow results obtained by Isogai [86] using a TSP method and by Bendiksen and Kousen

[29] using an Euler method. As a reference, results using linear thin-airfoil theory are also presented. The flutter speed indices were calculated starting from  $M_\infty=0.75$  to  $M_\infty=0.95$  with an increment of 0.025. The present inviscid flow results agree fairly well with the other results. The bottom of the dip is predicted at  $V^*=0.53$  which is close to the TSP result. Until  $M_\infty=0.875$  the lowest flutter is primarily due to the first mode which is mainly bending with a frequency close to the first coupled wind-off frequency. Thereafter a bulge occurs causing multiple flutter points. At  $M_\infty=0.90$  the flutter is now primarily due to the second mode, which is mainly rotation. This situation can be noticed in the time response of figure 5.14.

Figure 5.16 shows that the rotational mode flutter starts at  $M_\infty=0.85$  and at a speed index higher than the first mode flutter. It should be noted that the flutter point at  $M_\infty=0.90$  and the adjacent one at  $M_\infty=0.9125$  have a very different character, the first representing primarily the second mode and the latter primarily the first mode. This difference can not be seen in the plot of flutter speed indices but is indicated clearly in the plot of the flutter frequencies, i.e. the right plot of figure 5.16. The second mode flutter does not occur at  $M_\infty=0.9125$  since at this condition the shock has reached the trailing edge which restrains its motion. These two types of flutter mode have also been found by Ehlers and Weatherhill [54] using a TSP equation.

Figure 5.17 shows the comparison between the viscous and inviscid flow results. The viscosity apparently reduces the dip, fills up the bulge and passes the higher frequency flutter mode found in inviscid flow. To display the different behavior of the viscous and inviscid flow results at  $M_\infty=0.85$  the time responses at various speed indices are shown in figures 5.18 and 5.19. For the inviscid flow case, at a speed index higher than the lowest flutter speed index, a stable solution has been found and at an even higher speed index flutter occurs again at a different flutter mode. One can see from figure 5.18 that solutions of LCO type have been obtained at a speed index beyond the uppermost flutter boundary. For the viscous flow case, although at speed indices higher than the flutter speed index low damping responses were encountered, no stable solution and no high frequency rotational flutter mode was found. As a final remark, to the author's knowledge no bulges have ever been found in wind tunnel tests with a flutter model, which seems to confirm the present result for viscous flow.



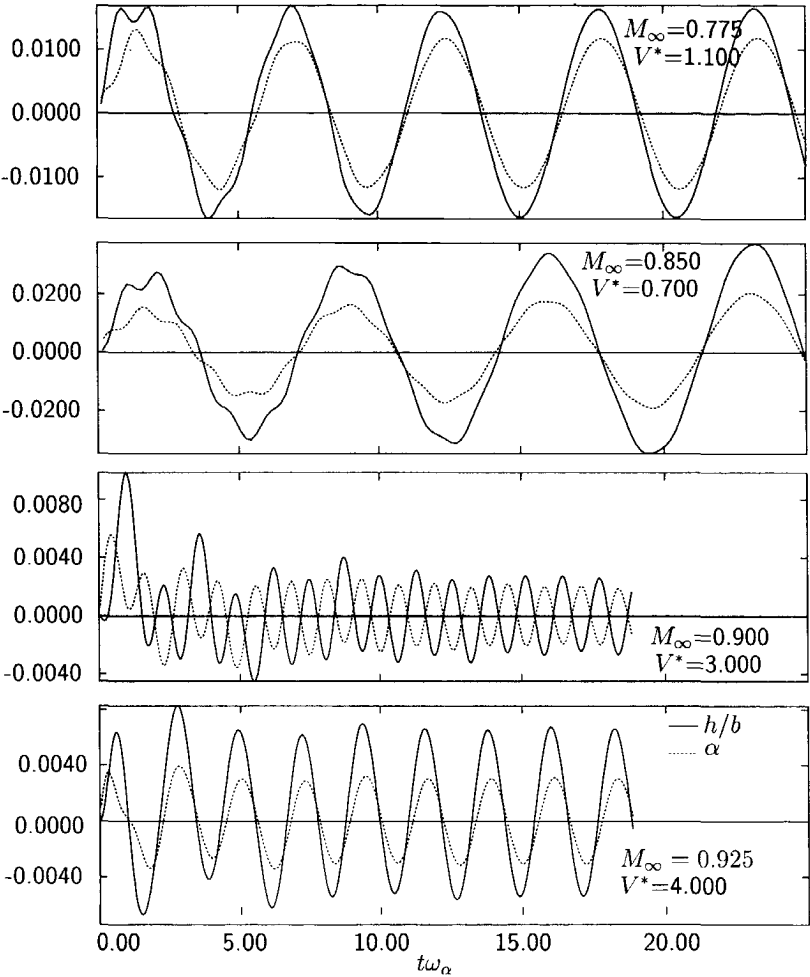


Figure 5.14: Time responses close to the flutter boundary for inviscid flow case. Isogai's case A

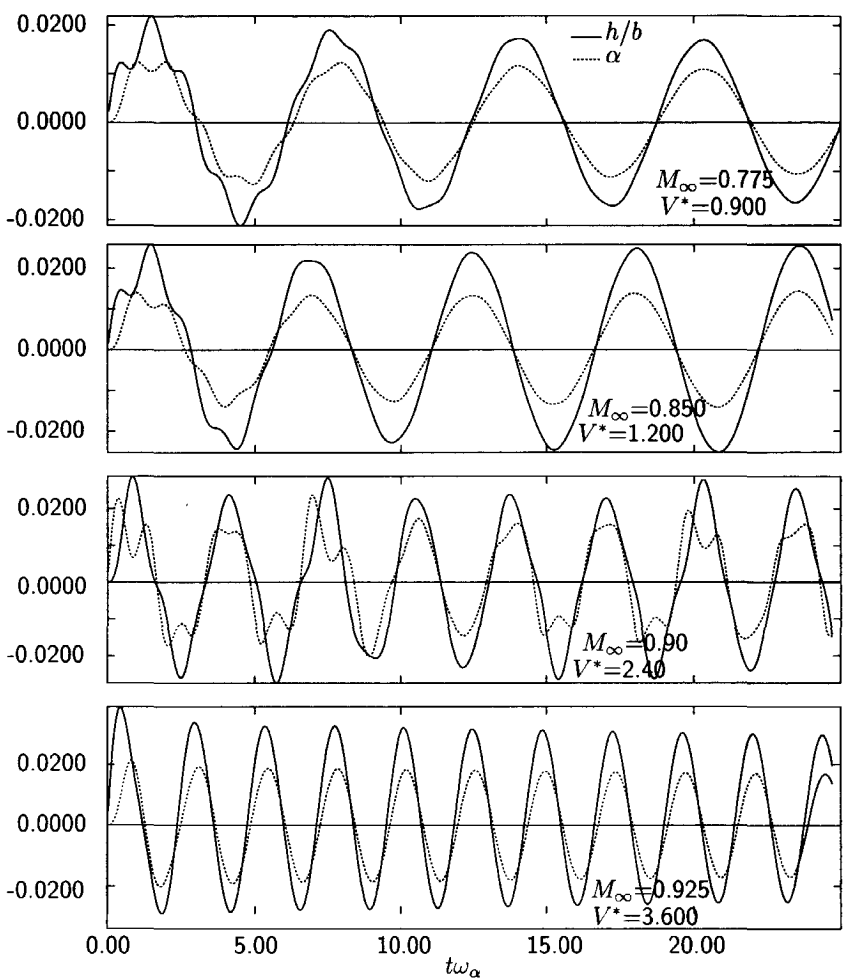


Figure 5.15: Time responses close to the flutter boundary for the viscous flow case. Isogai's case A

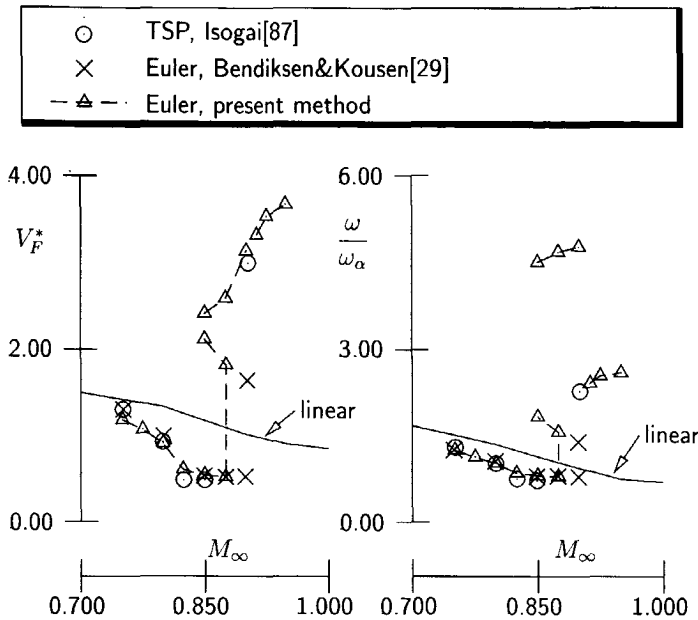


Figure 5.16: Comparison of calculated speed indices and nondimensional frequency at the flutter boundaries for inviscid flow cases. Isogai's case A

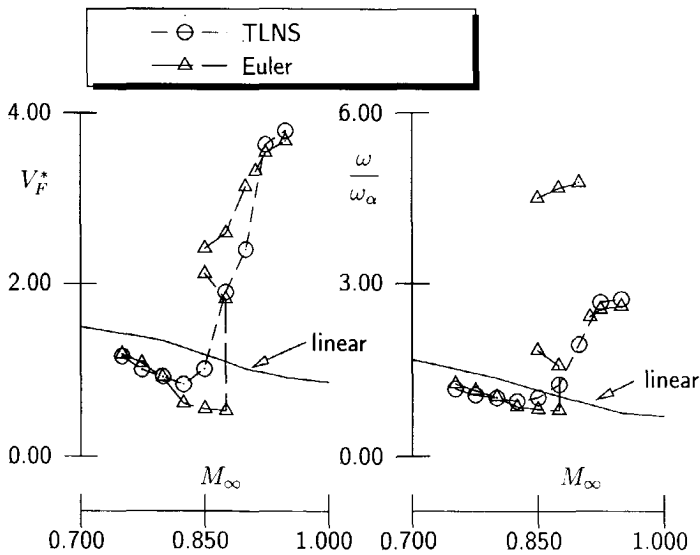


Figure 5.17: Comparison of calculated speed indices and nondimensional frequency at the flutter boundaries of the viscous and inviscid flow cases. Isogai's case A

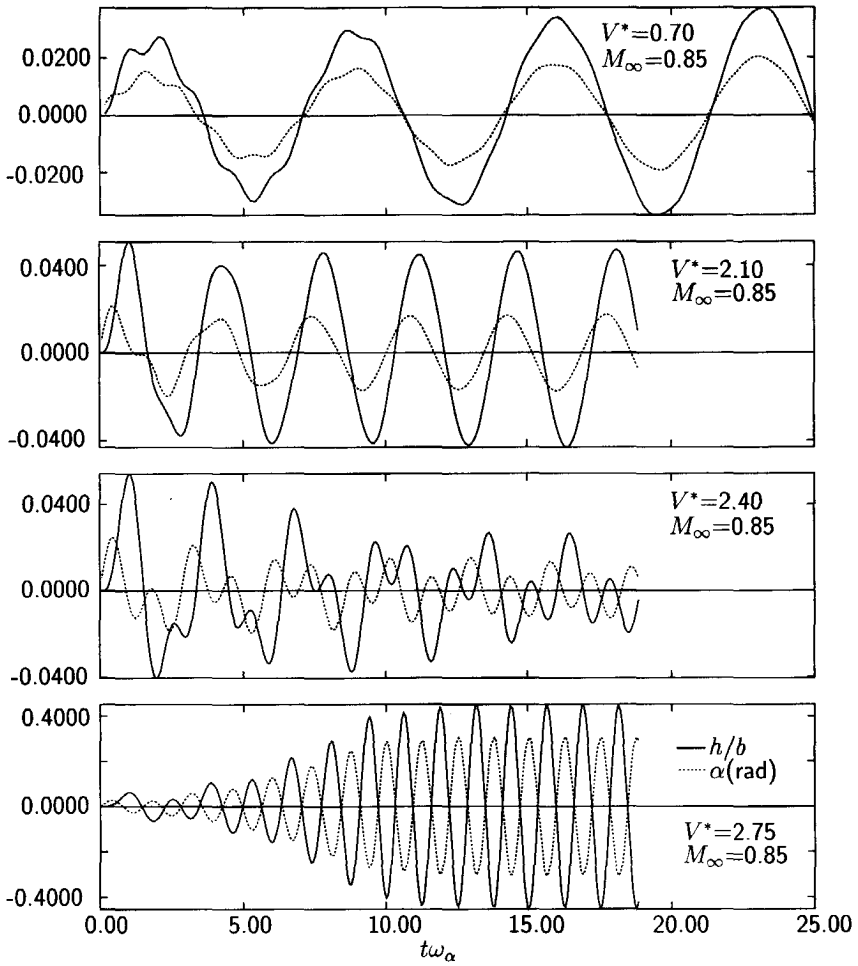


Figure 5.18: Time responses at  $M_\infty = 0.85$  for increasing speed indices for inviscid flow case. Isogai's case A

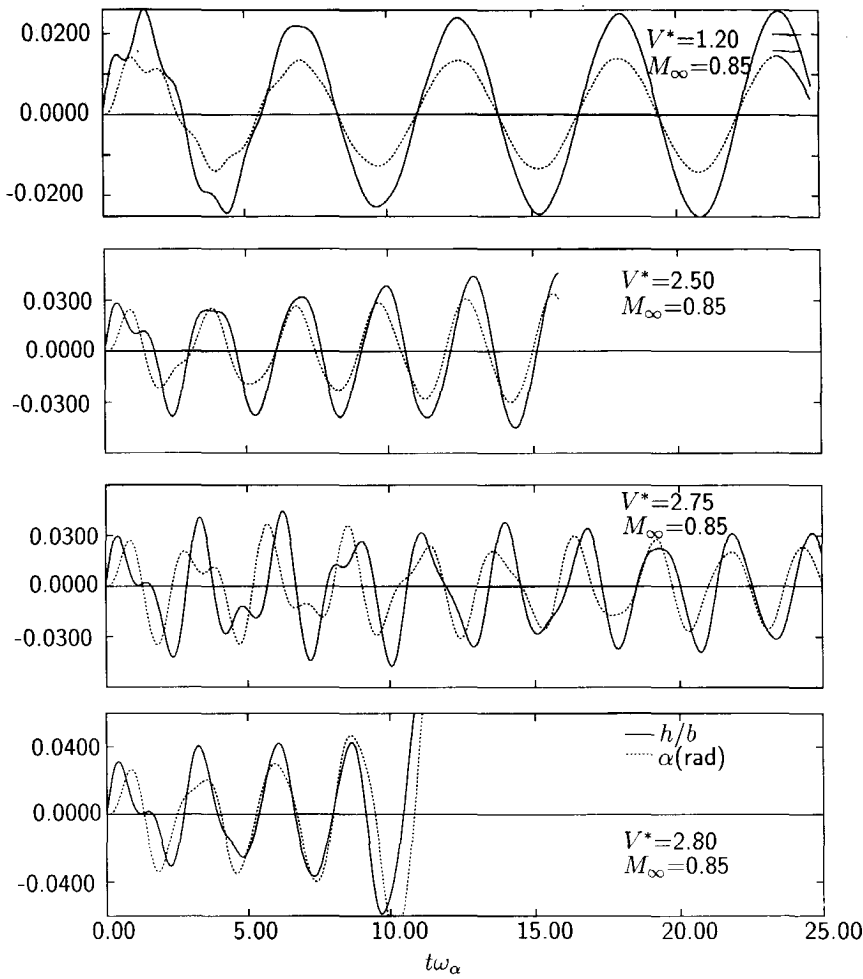


Figure 5.19: Time responses at  $M_\infty=0.85$  for increasing speed indices for the viscous flow case. Isogai's case A

### 5.5.2 SEPARATED FLOW

In this section an exploratory test case is presented. A high angle of attack case is considered with the aeroelastic parameters of the Isogai case A. Flutter calculations were presented in many papers, e.g. [29, 52, 54, 87, 135], for flow conditions in which viscous effects are not dominant. Here an aeroelastic simulation is presented at  $M_\infty=0.650\text{--}0.825$ ,  $Re_\infty=12\times 10^6$  and  $\alpha_{\text{mean}}=4$  deg, where the viscous effects are expected to be significant.

The angle of attack is included in the aeroelastic simulation by prescribing the direction of the oncoming flow, i.e. not by prescribing an initial  $\alpha$ , see figure 5.20. The steady situation is always assumed to be in equilibrium. In the calculation

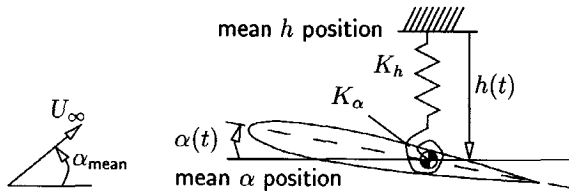


Figure 5.20: Typical section of a wing with nonzero mean angle of attack

this is assured simply by subtracting the steady flow aerodynamic forces from their instantaneous values during the simulation.

Flow simulations using the present method for viscosity dominated flows about an NACA 64A010 airfoil have already been presented in section 4.3. The simulation of steady flow at  $M_\infty=0.80$  showed a good qualitative agreement (figure 4.5). Most importantly, the simulations of the unsteady flow due to forced vibrations showed a correct behavior at high and low frequency, as compared to the experiment. At low frequency the shock moves forward with the increase of the angle of attack (figure 4.6), whereas at high frequency the shock motion lags the airfoil motion so much (figure 4.7) that it resembles the attached flow case where the shock moves backward by the increase of the angle of attack, see also figure 4.8. These results justify the application of the present method for the aeroelastic simulation at this separated flow condition.

Aeroelastic simulations are performed starting from the steady flow condition at  $\alpha_{\text{mean}}=4.00$  deg. An initial condition of  $\dot{\alpha}(0)$  is used. The time responses of the translational and rotational motion about the elastic axis at  $M_\infty=0.70$ , 0.80 and 0.825 for various speed indices are presented in figures 5.21 to 5.23. At  $M_\infty=0.70$  where the flow is fully attached the time responses for various speed indices, shown in figure 5.21, is dominated by the first mode, see also figure 5.2. Figure 5.22 shows the time responses at  $M_\infty=0.80$ , where the flow behind the shock wave is separated, for various speed indices. The time responses at this Mach number are mostly second mode and as can be seen from figure 5.22 the flutter boundary is difficult to determine. At  $M_\infty=0.825$  the first mode responses are obtained again, presented in figure 5.23.

The flutter speed indices at various Mach numbers are presented in figure 5.24. Isomach contours at some Mach numbers have also been plotted. These plots refer to the corresponding steady flow conditions. The flutter speed indices show a dip at  $M_\infty=0.70$ . After the dip the flutter speed index increases with the increase of Mach number. However, at  $M_\infty=0.775$  and  $0.80$  the flutter boundary becomes unclear. The time responses are lowly damped at low speed indices and become an LCO at high speed indices. The responses at these Mach numbers are dominated by the second mode. Considering an LCO response as an unstable response, in the sense of asymptotic stability, this means that the flutter speed index decreases again. A similar characteristic to the one observed in the SKV-5 test program (figure 1.2) for the highest angle of attack case where flow separation occurred at the second dip and the flutter mode became mostly torsional. When the flutter speed index increases again after the second dip, at  $M_\infty=0.825$ , the first mode flutter returns. This is different from the result of the SKV-5 test, where second mode flutter remained dominating.

The other known problem associated with flow separation is the so-called buffeting. Buffeting is defined as the structural response due to buffet excitation. In the previous chapter, the buffet boundary of a stationary NACA 0012 airfoil was calculated. At  $M_\infty=0.775$ ,  $Re_\infty=\times 10^7$  and angle of attack  $4.00$  deg, i.e. a condition beyond buffet boundary for this Mach number, the  $C_L(t)$  history shows a sustained oscillation with a distinct reduced frequency, see figure 4.11. Aeroelastic simulation at this flow condition has been carried out using the structural data of Isogai's case A at  $V^*=0.40$  and  $V^*=0.50$ . The airfoil was released from the beginning of the simulation without initial conditions of  $\dot{h}/b(0)$  nor  $\dot{\alpha}(0)$ . The history of  $C_L$  and  $h/b$  and the corresponding spectrum (expressed in terms of the period of oscillation  $T\omega_\alpha$ ) are shown in Figure 5.25. The  $C_L$  history for this freely-moving airfoil looks quite similar to the one for a stationary airfoil, i.e. figure 4.11. The spectrum of  $C_L$  for each simulation shows a high peak which corresponds to a peak in the spectrum of  $h/b$  response. The second mode (with  $T\omega_\alpha=1.177$  at wind-off condition, see section 5.2.2) seems to be excited but the response due the buffet is more dominant.

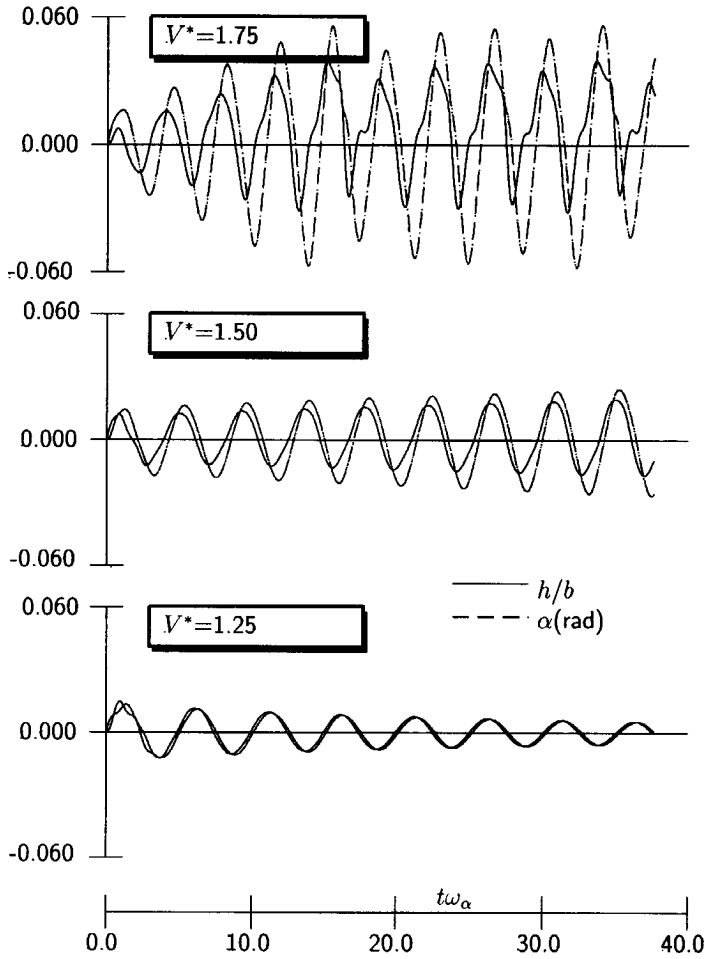


Figure 5.21: History of translational and rotational displacement about the elastic axis at various speed indices for Isogai case A of NACA 64A010,  $M_\infty=0.70$ ,  $\alpha=4$  deg,  $Re_\infty=12\times 10^6$



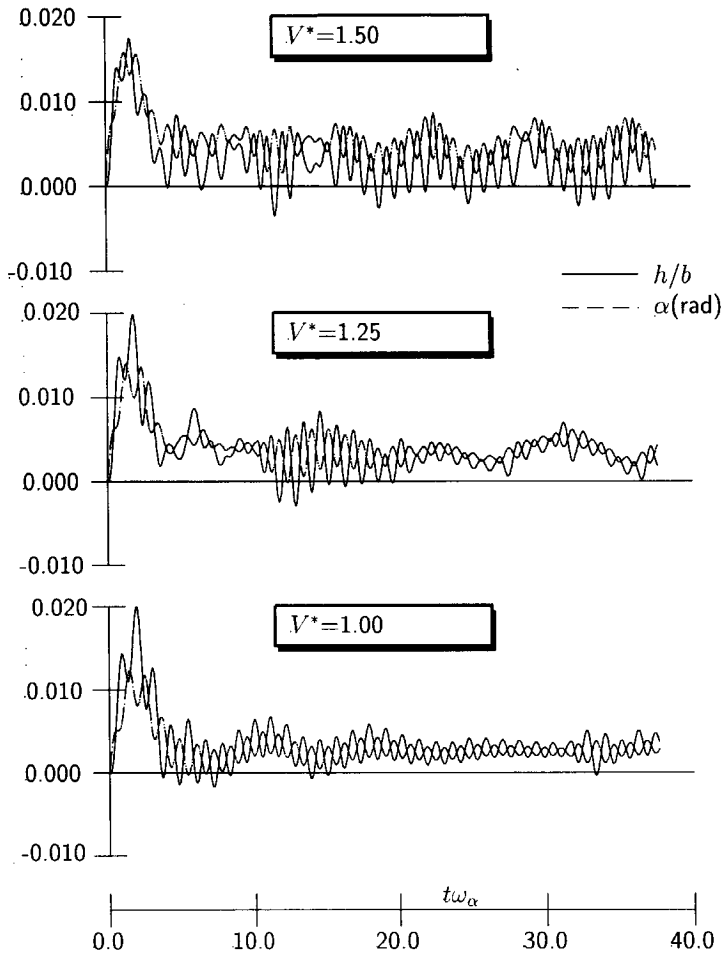


Figure 5.22: History of translational and rotational displacement about the elastic axis at various speed indices for Isogai case A of NACA 64A010,  $M_\infty=0.80$ ,  $\alpha=4$  deg,  $Re_\infty=12\times 10^6$

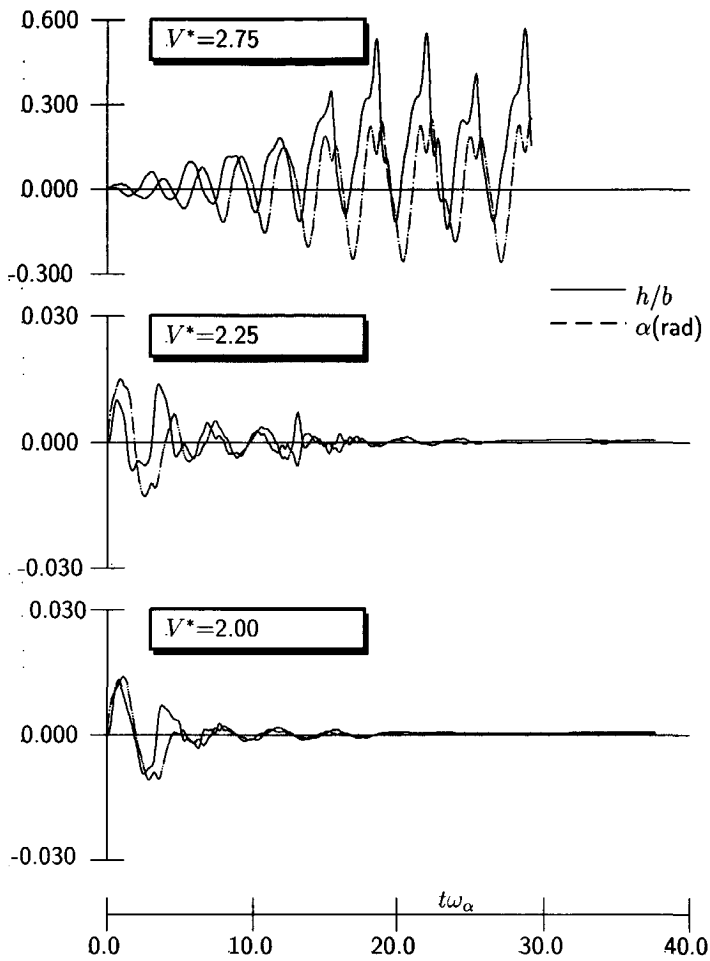


Figure 5.23: History of translational and rotational displacement about the elastic axis at various speed indices for Isogai case A of NACA 64A010,  $M_\infty=0.825$ ,  $\alpha=4^\circ$ ,  $Re_\infty=12\times 10^6$

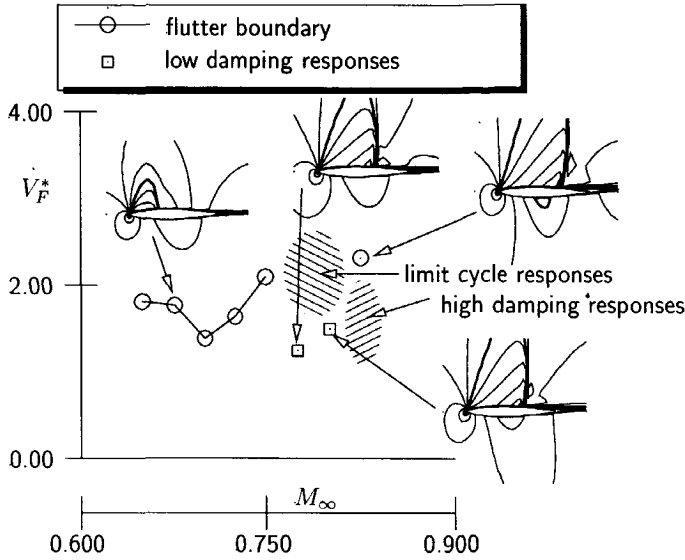


Figure 5.24: Results of aeroelastic simulations for Isogai case A of NACA 64A010,  $M_\infty=0.650$ – $0.825$ ,  $\alpha=4$  deg,  $Re_\infty=12\times 10^6$ . The isomach contours are at steady flow conditions,  $\Delta M=0.10$  and the thickened contour is  $M=1$

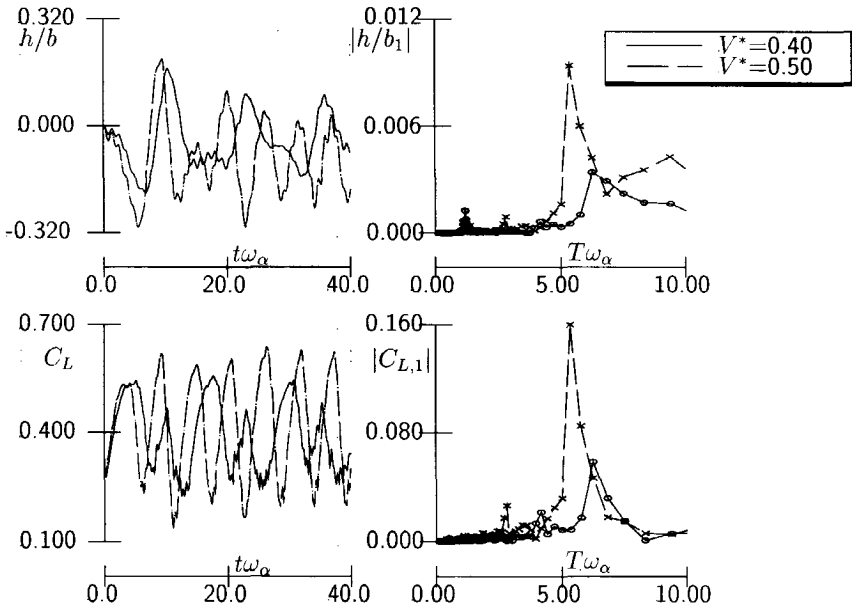


Figure 5.25: Buffeting of NACA 0012 at  $M_\infty=0.775$ ,  $\alpha=4.0$  deg,  $Re_\infty=10\times 10^6$

## 5.6 CONCLUSIONS CONCERNING THE TWO-DIMENSIONAL CAS METHOD

A two-dimensional CAS method employing the Thin-Layer Navier-Stokes/Euler equations has been developed.

Attention has been given to simple and fast aero-structural coupling procedures. They are based on the extrapolation of the aerodynamic state or the structural state using gradient information from the equations and from the previous time steps.

Results of test cases have been presented with the aim of validating the present aero-structural coupling method and producing new test cases for the Navier-Stokes equations. The results of the test cases presented in this chapter have led to the following conclusions:

- The aero-structural coupling methods improved the simple aerodynamic extrapolation method of [52].
  - Accurate results can be obtained with time steps corresponding to 8 steps/period of the highest frequency mode.
  - Two-dimensional flutter boundaries can be obtained in acceptable turnaround times on a moderate type workstation.
  - Flutter boundaries, calculated for the Isogai case A using the inviscid flow method agree fairly well with data provided by other methods.
  - A significant computer cost reduction of more than 60% is obtained by the implementation of the current extrapolation schemes allowing large time steps.
-

## CHAPTER 6

# COMPUTATIONAL AEROELASTIC SIMULATION METHOD FOR THREE-DIMENSIONAL FLOW

This chapter discusses the extension of the CUA/CAS methods for two-dimensional flow presented in the previous chapters to the flow about three-dimensional configurations. The objective is to obtain a three-dimensional CAS method capable of analyzing isolated wings and simple wing-body configurations, retaining the acceptable turnaround times of the simulations which were achieved for two-dimensional flow applications. A necessary step towards this objective is the application of parallel computing to the CUA method. Due to the adoption of the modal decomposition approach in which a limited number of degrees of freedom is defined, parallelization of the structural part is not worthwhile as the computing time of the structural part is negligible compared to that of the aerodynamic part.

The requirement concerning the geometrical modeling for three-dimensional aeroelastic applications should reflect the general requirements presented in section 2.5.1. For example, the fuselage/body should be taken into account only when its flexibility can not be neglected which may cause aeroelastic problems, or otherwise when its aerodynamic interference with the lifting surfaces (where aeroelastic phenomena are usually decisive) is significant. The aeroelastic simulations of a T-tail configuration presented by Eussen et al. [57] and a blended wing-body with low aspect ratio wing reported by Guruswamy [67] are examples of aeroelastic cases requiring the modeling of the fuselage. In many cases the inclusion of a fuselage or bodies in the aeroelastic analysis is to investigate their effect on the aerodynamic characteristics of the wing and thus may not be of primary concern for the aeroelastic analyses.

Most developments of the two-dimensional CAS method can be directly extended to the three-dimensional CAS method. The main difference is of course the treatment of the geometry in the aerodynamic as well as in the structural parts.

In the following the method for three-dimensional flows will be discussed and a number of results will be given. Next, the structural model and the solution of the aeroelastic simulation method are presented. Finally an example of the aeroelastic simulation will be shown.

## 6.1 AERODYNAMIC MODEL

The aerodynamic part employs a time-accurate three-dimensional Euler/Navier-Stokes method with a deforming mesh capability. In this section some aspects of the method are presented: the mesh topology, the spatial discretization and the temporal integration. Subsequently some results are presented.

### 6.1.1 MESH TOPOLOGY

Defining the proper mesh topology for a three-dimensional flow case is more difficult than for a two-dimensional flow case. The difficulty stems from the existence of many more features, both in the geometry and in the flow. Features in the geometry are those related to the effort in generating the mesh around three-dimensional configurations, while features in the flow are those related to the effort to represent the physics properly. The difficulty in accommodating the multitude of features is the main reason for the application of a multi-block approach for structured meshes. In a multi-block method the domain is split into blocks which are constructed to capture the features conveniently and/or accurately. A multi-block structured mesh method is considered as the state of the art for steady flow problems in obtaining accurate aerodynamic forces for aircraft performance analysis, e.g. see Oskam and Slooff [125]. The main disadvantage of a multi-block structured mesh method is the significant effort to generate a mesh with adequate quality for which in most cases an expert in mesh generation is needed.

On the other hand, a mono-block mesh approach offers less flexibility in capturing the geometrical and flow features of the problem and one is restricted to concentrate on certain features. Therefore, the precise definition of a mesh topology in a mono-block approach is more important than that in a multi-block approach. In return, generating a mono-block mesh is a much less strenuous task than generating a multi-block mesh. As mentioned previously, the primary concern in geometrical modeling are the lifting surfaces for which important aero-structural interaction is expected to occur. Inaccuracies in modeling the fuselage are usually acceptable which makes it possible to use a simple block for the wing. For this reason, in the present study a mono-block approach has been taken. Most of the meshes employed in the present study were generated using the FOLDIT-BLOWUP mono-block mesh generator described in [80], which is based on a hyperbolic method and has a very **flexible surface mesh handling**.

For an isolated wing the most straightforward extension of the two-dimensional method is to apply a CH-topology (C in  $\xi$ -direction and H in  $\eta$ -direction). The geometrical transformation from the Cartesian physical domain to a curvilinear computational domain is depicted in figure 6.1. Using this topology a good mesh resolutions can be obtained near the leading edge and near the trailing edge. On the other hand, a good resolution near the wing tip is in most cases more difficult to realize. This topology can be considered as a series of two-dimensional sections in  $\eta$ -direction with C-topology. Another possibility is an O-topology in the  $\eta$ -direction; an example will be shown in the next paragraph. As can be seen in figure 6.1, on

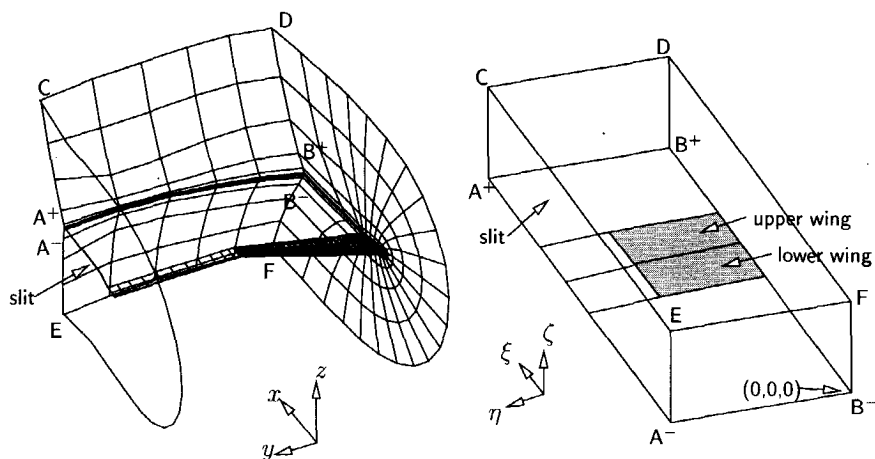


Figure 6.1: Geometrical transformation from Cartesian physical domain to computational domain with CH-topology for isolated wing configurations

the plane of  $\zeta = 0$  two types of boundary conditions have to be satisfied: the solid surface boundary and the continuity condition. This is another disadvantage of a mono-block approach, i.e. the complexity in applying various boundary conditions in the same boundary plane.

A further extension which enables the method to handle also a fuselage is by letting a part of the boundary plane  $\eta = 0$  represent a solid surface, namely that of the fuselage. An example of the geometrical transformation of a mesh around a wing-body configuration is shown in figure 6.2, taken from Haase et al. [70]. The mesh has an O-topology in  $\eta$ -direction, which improves the resolution near the wing tip.

Another way to wrap a wing-body configuration is by employing a mesh with an HO-topology. An example of the geometrical transformation of a mesh around a fighter-type wing-body-tail configuration is shown in figure 6.3. One can see that the solid surface resides only in one plane, i.e. plane  $\zeta = 0$ . In general, keeping the solid surface to reside only in one plane means that the clustering for capturing the boundary layer will occur only in one direction ( $\zeta$ -direction). To achieve the same goal, the mesh with CO-topology shown in figure 6.2 needs clustering in two directions, i.e. the  $\zeta$ -direction, to capture the boundary layer of the wing, and the  $\eta$ -direction, to capture the boundary layer of the fuselage.

### 6.1.2 DYNAMIC MESH ALGORITHM

In the three-dimensional CUA method, only the spring analogy method is applied. It has been shown in section 3.10.1 that the method is robust and efficient. In this method the mesh points are connected by a spring system which reacts to the displacements of the solid surface.

The same implicit predictor as the one applied in the two-dimensional CUA

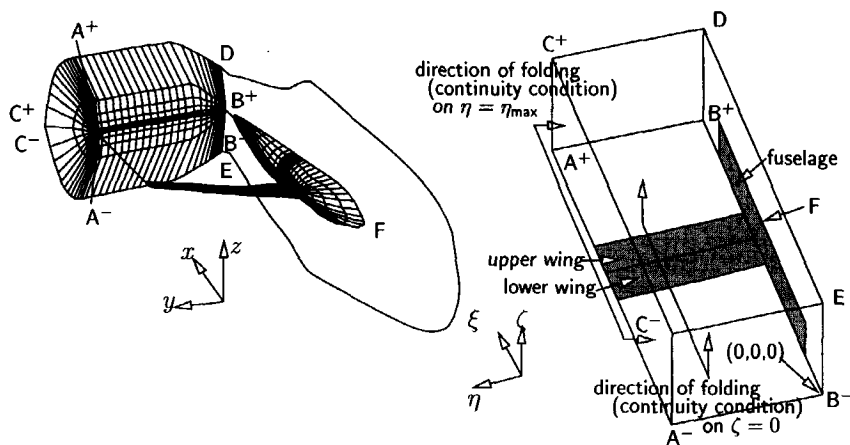


Figure 6.2: Geometrical transformation from Cartesian physical domain to computational domain with CO-topology for wing-body configurations

method is employed because it has shown to retain its robustness for three-dimensional flow applications. An example of the mesh deformation using the spring analogy method is shown in figure 6.4. The deformation was artificially introduced by twisting the wing at its tip (distributed linearly in the spanwise direction,  $\theta(y) = y/s \theta(y_{\text{tip}})$ ,  $s$  is the half span of the wing). A large deformation which was carried out in two steps with each step  $\theta(y_{\text{tip}}) = 25$  deg, was applied to show the robustness of the method. In each twisting step the implicit predictor and 4 PGS iterations were employed to solve the static balance equations. The resulting mesh, shown in figure 6.4, does not have mesh folding and/or negative cell volumes, as required for the flow solver.

### 6.1.3 GOVERNING EQUATIONS

The Thin-Layer Navier-Stokes equations in the computational domain are obtained through a coordinate transformation from the Cartesian physical domain:

$$\begin{aligned} \xi &= \xi(x, y, z, t), & \eta &= \eta(x, y, z, t), \\ \zeta &= \zeta(x, y, z, t), & \tau &= t. \end{aligned} \quad (6.1)$$

The conservation form of the Thin-Layer Navier-Stokes equations in a curvilinear coordinate system  $[\xi, \eta, \zeta]$  reads:

$$\frac{\partial \hat{Q}}{\partial \tau} + \frac{\partial \hat{F}_\xi^I}{\partial \xi} + \frac{\partial \hat{F}_\eta^I}{\partial \eta} + \frac{\partial \hat{F}_\zeta^I}{\partial \zeta} = \frac{\partial \hat{F}_\zeta^V}{\partial \zeta}, \quad (6.2)$$



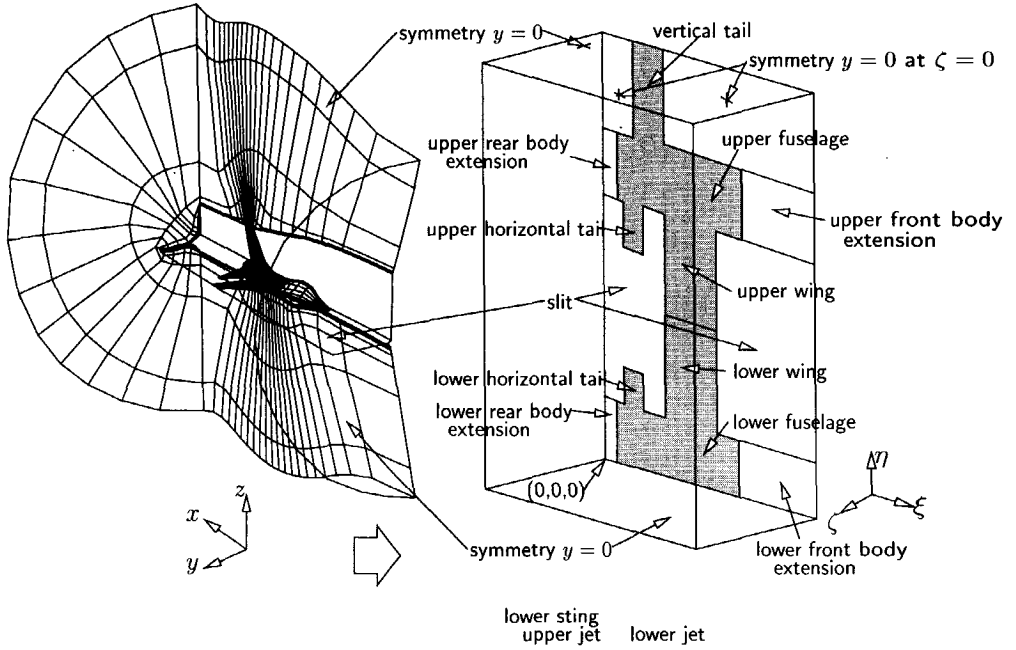


Figure 6.3: Geometrical transformation from Cartesian physical domain to computational domain with HO-topology

where the conservative variable is  $\hat{Q} = hQ$  and  $Q = [\rho, \rho u, \rho v, \rho w, \rho E]^T$ , the inviscid flux vector are:

$$\hat{F}_\xi^I = \begin{bmatrix} \rho \hat{U} \\ \rho u \hat{U} + \hat{\xi}_x p \\ \rho v \hat{U} + \hat{\xi}_y p \\ \rho w \hat{U} + \hat{\xi}_z p \\ \rho E \hat{U} + \hat{U} p \end{bmatrix}, \quad \hat{F}_\eta^I = \begin{bmatrix} \rho \hat{V} \\ \rho u \hat{V} + \hat{\eta}_x p \\ \rho v \hat{V} + \hat{\eta}_y p \\ \rho w \hat{V} + \hat{\eta}_z p \\ \rho E \hat{V} + \hat{V} p \end{bmatrix}, \quad \hat{F}_\zeta^I = \begin{bmatrix} \rho \hat{W} \\ \rho u \hat{W} + \hat{\zeta}_x p \\ \rho v \hat{W} + \hat{\zeta}_y p \\ \rho w \hat{W} + \hat{\zeta}_z p \\ \rho E \hat{W} + \hat{W} p \end{bmatrix},$$

where the contravariant velocities are:

$$U = \xi_t + \xi_x u + \xi_y v + \xi_z w$$

$$V = \eta_t + \eta_x u + \eta_y v + \eta_z w$$

$$W = \zeta_t + \zeta_x u + \zeta_y v + \zeta_z w,$$

and  $U' = U - \xi_t$ ,  $V' = V - \eta_t$  and  $W' = W - \zeta_t$ . Similar to the form of the thin-layer viscous terms in the two-dimensional flow case one gets for the three-dimensional

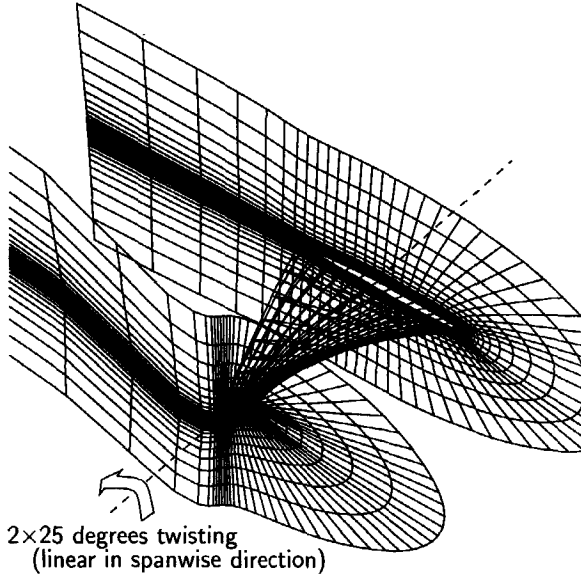


Figure 6.4: A deformed mesh for viscous flow calculations around an isolated wing, the mesh follows the deformation of the wing using the spring analogy method with the implicit predictor

case:

$$\hat{F}_{\zeta}^V = \frac{\mu}{Re} \begin{bmatrix} 0 \\ m_{11}u_{\zeta} + m_{12}v_{\zeta} + m_{13}w_{\zeta} \\ m_{12}u_{\zeta} + m_{22}v_{\zeta} + m_{23}w_{\zeta} \\ m_{13}u_{\zeta} + m_{23}v_{\zeta} + m_{33}w_{\zeta} \\ \hat{F}_{\zeta}^{V5} \end{bmatrix}, \quad (6.3)$$

where:

$$\hat{F}_{\zeta}^{V5} = \frac{m_{11}}{2}(u^2)_{\zeta} + \frac{m_{22}}{2}(v^2)_{\zeta} + \frac{m_{33}}{2}(w^2)_{\zeta} + m_{12}(uv)_{\zeta} + m_{23}(vw)_{\zeta} + m_{13}(wu)_{\zeta} + m_4 \frac{\gamma}{Pr} e_{\zeta}. \quad (6.4)$$

The metrics functions  $m$  are:

$$\begin{aligned} m_{11} &= h \left( \frac{4}{3} \zeta_x^2 + \zeta_y^2 + \zeta_z^2 \right), & m_{12} &= \frac{h}{3} \zeta_x \zeta_y, \\ m_{22} &= h \left( \zeta_x^2 + \frac{4}{3} \zeta_y^2 + \zeta_z^2 \right), & m_{23} &= \frac{h}{3} \zeta_y \zeta_z, \\ m_{33} &= h \left( \zeta_x^2 + \zeta_y^2 + \frac{4}{3} \zeta_z^2 \right), & m_{31} &= \frac{h}{3} \zeta_z \zeta_x, \\ m_4 &= h (\zeta_x^2 + \zeta_y^2 + \zeta_z^2). \end{aligned}$$

The metrics of transformation are obtained in a similar manner as in the two-dimensional case:

$$\begin{aligned}\xi_x &= J(y_\eta z_\zeta - y_\zeta z_\eta), & \eta_x &= J(y_\zeta z_\xi - y_\xi z_\zeta), & \zeta_x &= J(y_\xi z_\eta - y_\eta z_\xi), \\ \xi_y &= J(z_\eta x_\zeta - z_\zeta x_\eta), & \eta_y &= J(z_\zeta x_\xi - z_\xi x_\zeta), & \zeta_y &= J(z_\xi x_\eta - z_\eta x_\xi), \\ \xi_z &= J(x_\eta y_\zeta - x_\zeta y_\eta), & \eta_z &= J(x_\zeta y_\xi - x_\xi y_\zeta), & \zeta_z &= J(x_\xi y_\eta - x_\eta y_\xi).\end{aligned}\quad (6.5)$$

The Jacobian of the mesh transformation,  $J = \partial(\xi, \eta, \zeta)/\partial(x, y, z)$ , can be calculated from  $J = h^{-1}$ , where  $h$  is the determinant of  $\partial\mathbf{x}/\partial\boldsymbol{\xi}$ :

$$h = \begin{vmatrix} x_\xi & x_\eta & x_\zeta \\ y_\xi & y_\eta & y_\zeta \\ z_\xi & z_\eta & z_\zeta \end{vmatrix} = x_\xi(y_\eta z_\zeta - y_\zeta z_\eta) - y_\xi(x_\eta z_\zeta - x_\zeta z_\eta) + z_\xi(x_\eta y_\zeta - x_\zeta y_\eta), \quad (6.6)$$

in which a cofactor expansion of the first column has been carried out,  $h$  represents the ratio of the volume in the physical domain and the corresponding element in the computational domain. The metrics,  $[\xi_x, \xi_y, \xi_z]^T$ ,  $[\eta_x, \eta_y, \eta_z]^T$ ,  $[\zeta_x, \zeta_y, \zeta_z]^T$ , are the normal vectors (the contravariant directions) of the cell face of constant  $\xi, \eta, \zeta$ , respectively.

#### GEOMETRIC CONSERVATION LAW

As in the two-dimensional case, the transformation of the conservation form of the governing equations in the Cartesian coordinate system, equation (2.33), into another conservation set of equations in a curvilinear coordinate system, i.e. equation (6.2), assumes that the transformation invariants are satisfied. The first transformation invariant, related to fixed mesh problems, is expressed here as:

$$\frac{\partial}{\partial \xi} \begin{bmatrix} \hat{\xi}_x \\ \hat{\xi}_y \\ \hat{\xi}_z \end{bmatrix} + \frac{\partial}{\partial \eta} \begin{bmatrix} \hat{\eta}_x \\ \hat{\eta}_y \\ \hat{\eta}_z \end{bmatrix} + \frac{\partial}{\partial \zeta} \begin{bmatrix} \hat{\zeta}_x \\ \hat{\zeta}_y \\ \hat{\zeta}_z \end{bmatrix} = 0. \quad (6.7)$$

This equation ensures that a cell volume is defined without ambiguity (e.g. matching faces, no overlap, no gaps). If the mesh deforms when proceeding in time, the following invariant has to be satisfied in addition to equation (6.7):

$$\frac{\partial h}{\partial \tau} + \frac{\partial \hat{\xi}_t}{\partial \xi} + \frac{\partial \hat{\eta}_t}{\partial \eta} + \frac{\partial \hat{\zeta}_t}{\partial \zeta} = 0, \quad (6.8)$$

which ensures that a closed cell at a certain time level remains closed at the next time level. Equation (6.8) is the statement of the GCL in the differential form for three-dimensional meshes.

#### BOUNDARY CONDITIONS

At solid surfaces the normal velocities vanish in inviscid and viscous flow cases, while in the latter case the tangential velocity components vanish as well. The

application of the velocity boundary condition is carried out in the same way as for the two-dimensional case, using equations (3.52) and (3.53).

The extrapolation of the pressures from the computational domain to a solid surface is carried out using the component of the momentum equation normal to the solid surface. For three-dimensional configurations this results in a two-dimensional set of equations. Instead of solving these equations, an explicit extrapolation is carried out as:

$$\begin{aligned}
 (\nabla \hat{\zeta} \cdot \nabla \hat{\zeta}) \frac{\partial p}{\partial \zeta} = & -(\nabla \hat{\zeta} \cdot \nabla \hat{\xi}) \frac{\partial p}{\partial \xi} - (\nabla \hat{\zeta} \cdot \nabla \hat{\eta}) \frac{\partial p}{\partial \eta} + \\
 & \rho h |\nabla \hat{\zeta}| \left( \frac{\partial \tilde{\zeta}_t}{\partial \tau} + u \frac{\partial \tilde{\zeta}_x}{\partial \tau} + v \frac{\partial \tilde{\zeta}_y}{\partial \tau} + w \frac{\partial \tilde{\zeta}_z}{\partial \tau} \right) + \\
 & \rho \hat{U} |\nabla \hat{\zeta}| \left( \frac{\partial \tilde{\zeta}_t}{\partial \xi} + u \frac{\partial \tilde{\zeta}_x}{\partial \xi} + v \frac{\partial \tilde{\zeta}_y}{\partial \xi} + w \frac{\partial \tilde{\zeta}_z}{\partial \xi} \right) + \\
 & \rho \hat{V} |\nabla \hat{\zeta}| \left( \frac{\partial \tilde{\zeta}_t}{\partial \eta} + u \frac{\partial \tilde{\zeta}_x}{\partial \eta} + v \frac{\partial \tilde{\zeta}_y}{\partial \eta} + w \frac{\partial \tilde{\zeta}_z}{\partial \eta} \right), \quad (6.9)
 \end{aligned}$$

where the geometrical data are evaluated using the solid surface data and the flow data at the right hand side are evaluated using the data at the first layer above the solid surface. It should be noted that equation (6.9) is valid for inviscid flow cases where the condition  $\hat{W} = 0$  has been imposed. For viscous flow cases, imposing also  $\hat{U} = \hat{V} = 0$ , a simpler form is obtained as:

$$(\nabla \hat{\zeta} \cdot \nabla \hat{\zeta}) \frac{\partial p}{\partial \zeta} = -(\nabla \hat{\zeta} \cdot \nabla \hat{\xi}) \frac{\partial p}{\partial \xi} - (\nabla \hat{\zeta} \cdot \nabla \hat{\eta}) \frac{\partial p}{\partial \eta} + \rho h |\nabla \hat{\zeta}| \frac{\partial \tilde{\zeta}_t}{\partial \tau}, \quad (6.10)$$

where the viscous stresses have been neglected.

The treatment of the far-field boundary condition follows the one for two-dimensional configurations employing the locally one-dimensional boundary conditions based on Riemann invariants.

For the present study where the side slip angle  $\beta$  is always assumed to be zero, so that the condition at the symmetry plane,  $y = 0$ , becomes simply:

$$\frac{\partial Q}{\partial y} = 0. \quad (6.11)$$

The application of this boundary condition, using ghost cells, is very simple, i.e. **setting the value at the ghost cell equal to its mirror value, with respect to the plane  $y=0$ , in the field.** Two ghost cells are defined for second-order accuracy and also for ease of application of the MUSCL scheme.

### 6.1.4 DISCRETIZATION

Equation (6.2) is spatially discretized, like in the two-dimensional case, using a cell-centered finite-volume method:

$$\int_v h \frac{\partial Q}{\partial \tau} d\xi d\eta d\zeta + \int_v Q \frac{\partial h}{\partial \tau} d\xi d\eta d\zeta + \int_{\partial v} \hat{\mathbf{F}} \cdot [d\xi, d\eta, d\zeta]^T = 0. \quad (6.12)$$

At time level  $(n + 1)$  the semi-discretized equations of equation (6.12) in a uniform computational domain reads:

$$\frac{\partial Q}{\partial \tau} h^{n+1} + \frac{\partial h}{\partial \tau} Q^n + \hat{F}_{\xi, i+\frac{1}{2}, j, k}^{I, n+1} - \hat{F}_{\xi, i-\frac{1}{2}, j, k}^{I, n+1} + \hat{F}_{\eta, i, j+\frac{1}{2}, k}^{I, n+1} - \hat{F}_{\eta, i, j-\frac{1}{2}, k}^{I, n+1} + (\hat{F}_{\zeta}^I - \hat{F}_{\zeta}^V)_{i, j, k+\frac{1}{2}}^{n+1} - (\hat{F}_{\zeta}^I - \hat{F}_{\zeta}^V)_{i, j, k-\frac{1}{2}}^{n+1} = 0, \quad (6.13)$$

where,  $\hat{F}_{\xi}$ ,  $\hat{F}_{\eta}$ ,  $\hat{F}_{\zeta}$ , are the fluxes normal to the cell face at constant  $\xi$ ,  $\eta$  and  $\zeta$ , respectively.

#### CALCULATION OF METRICS

To conform to the transformation invariants defined by equation (6.7) the metrics are calculated at the cell face at which they are needed. For example,  $\nabla \hat{\xi}$  is needed at cell face  $(i \pm \frac{1}{2}, j, k)$  and calculated as  $\nabla \hat{\xi} = \mathbf{x}_{\eta} \times \mathbf{x}_{\zeta}$ , where:

$$\mathbf{x}_{\eta, i \pm \frac{1}{2}, j, k} = \frac{1}{2} (\mathbf{x}_{i \pm \frac{1}{2}, j+\frac{1}{2}, k+\frac{1}{2}} + \mathbf{x}_{i \pm \frac{1}{2}, j+\frac{1}{2}, k-\frac{1}{2}} - \mathbf{x}_{i \pm \frac{1}{2}, j-\frac{1}{2}, k+\frac{1}{2}} - \mathbf{x}_{i \pm \frac{1}{2}, j-\frac{1}{2}, k-\frac{1}{2}}),$$

$$\mathbf{x}_{\zeta, i \pm \frac{1}{2}, j, k} = \frac{1}{2} (\mathbf{x}_{i \pm \frac{1}{2}, j+\frac{1}{2}, k+\frac{1}{2}} + \mathbf{x}_{i \pm \frac{1}{2}, j-\frac{1}{2}, k+\frac{1}{2}} - \mathbf{x}_{i \pm \frac{1}{2}, j+\frac{1}{2}, k-\frac{1}{2}} - \mathbf{x}_{i \pm \frac{1}{2}, j-\frac{1}{2}, k-\frac{1}{2}}),$$

see figure 6.5. The rate of change of the cell volume,  $\partial h / \partial \tau$ , is calculated from the

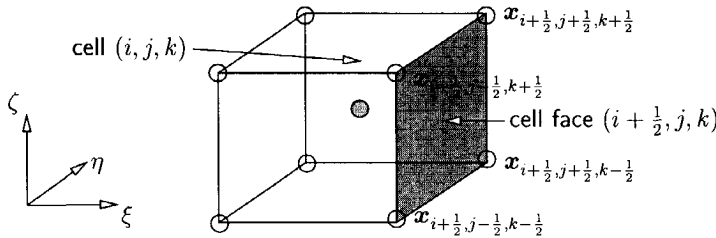


Figure 6.5: A three-dimensional volume cell

contravariant grid speed using equation (6.8) as:

$$\frac{\partial h}{\partial \tau} = -\frac{\partial \hat{\xi}_t}{\partial \xi} - \frac{\partial \hat{\eta}_t}{\partial \eta} - \frac{\partial \hat{\zeta}_t}{\partial \zeta}, \quad (6.14)$$

which ensures that the GCL is always satisfied. The calculation of the contravariant grid speed is carried out in the volume swept by the cell face when moving from time level  $(n)$  to time level  $(n + 1)$ .

#### CALCULATION OF INVISCID FLUX

As has been concluded in developing the two-dimensional method, section 3.10.2, Roe's FDS is the most suitable among the upwind methods for the problems considered in the present study. Therefore, only Roe's FDS is applied in the three-dimensional CAS method. Roe's FDS for three-dimensional flow problems is not

fundamentally different from the one for two-dimensional flow because the method is quasi one-dimensional. The only difference is the set of left and right eigenvectors, and the corresponding eigenvalues, used for splitting the flux difference.

The eigenvectors and the corresponding eigenvalues for the three-dimensional Euler equations are presented in appendix B.

#### TURBULENCE MODELING

As a logical extension, the algebraic turbulence model of Baldwin-Lomax [18] (BL) is also implemented in the three-dimensional flow method. The implementation is carried out in a stripwise manner in the spanwise direction. For the mesh with CH-topology the turbulent eddy viscosity at the wing tip is extrapolated using a prescribed damped exponential function from the wing tip to the far field in order to have a smooth transition away from the solid surface. In general, the algebraic turbulence model is difficult to apply in a three-dimensional configuration due to several reasons: the various topologies, the possible existence of staggering solid surfaces and moreover since the Baldwin-Lomax turbulence model is not 'local' it may not be suitable for domain decomposition.

Therefore the one-equation turbulence model of Spalart-Allmaras [157] (SA) is also applied in this study. The SA one-equation model solves a transport equation for working variable  $\tilde{\nu}$ , from which the turbulent eddy viscosity can be calculated, see equation (C.10). The only configuration-related geometrical data is the distance from each cell to the closest wall, which is required to be accurate only for cells close to a solid surface. For three-dimensional configurations this data can be easily calculated, even for a relatively complex configuration. Since the governing equation for the Spalart-Allmaras turbulence model is to a certain extent similar to the flow equations, a similar method can be employed to solve the SA equation. Consequently, in a multi-domain environment the dependence between the solutions in neighboring domains will resemble that of the flow equations. This convenience in implementation for three-dimensional configurations was the primary reason to apply SA turbulence model.

A more detailed description of the BL turbulence model and the SA one-equation turbulence model can be found in appendix C.

#### TEMPORAL INTEGRATION METHOD

**Following the two-dimensional method, the linear multi-step method is applied.** In each time step the residual for the unsteady equations is constructed, i.e. equation (6.13) with a suitable backward time differencing of  $\partial Q/\partial \tau$  from table 3.1, and with the expression of  $\partial h/\partial \tau$  using equation (6.14). The resulting nonlinear set of algebraic equations is subsequently solved using a relaxation scheme. Several subiterations are employed in each time step to reduce the error to the required level of accuracy. Thus at the end of each time step the nonlinear unsteady equations are satisfied to a certain tolerance.

The left-hand side involved in the subiteration is constructed in a similar way as in the two-dimensional method, see section 3.7.3. In the two-dimensional method a

line relaxation is applied with an update of  $Q$  after each sweep or after several sweeps. The sweeping is in  $\xi$ -direction while the equations along  $\zeta$ -lines are solved directly. The direct inversion of the equations along  $\zeta$ -lines should resolve the stiffness due to the mesh stretching and implicitly treats the viscous terms which have an elliptic behavior. In the three-dimensional version the line relaxation with a direct inversion of equations along  $\zeta$ -lines is retained which leaves some possibilities for the sweep direction:

- Forward-backward sweep in the planes of constant  $\xi$  or  $\eta$ , see figure 6.6. For

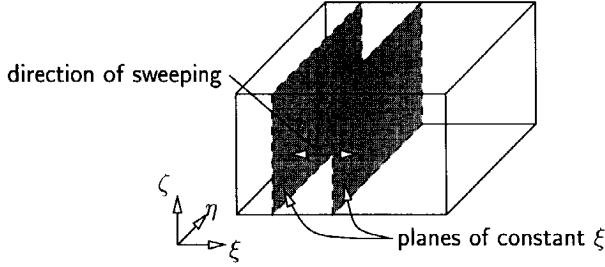


Figure 6.6: Relaxation sweep along the planes of constant  $\xi$

example, for sweeping in the  $\xi$ -direction the equation for the forward sweep reads:

$$[P_i]\Delta\bar{Q}_i^{p+1} = -R(Q^p, Q^n, Q^{n-1}) - [P_i^-]\Delta\bar{Q}_{i-1}^{p+1} - \omega_l[P_i^+]\Delta Q_{i+1}^p, \quad (6.15)$$

which results in an intermediate correction,  $\Delta\bar{Q}$ , followed by a backward sweep:

$$[P_i]\Delta Q_i^{p+1} = -R(Q^p, Q^n, Q^{n-1}) - \omega_l[P_i^+]\Delta Q_{i+1}^{p+1} - [P_i^-]\Delta\bar{Q}_{i-1}^{p+1}. \quad (6.16)$$

The  $[P]$ 's represent the entry of a plane of constant  $\xi$ :

$$[P_i^-]\Delta Q_{i-1} = -[A_{\xi, i-\frac{1}{2}, j, k}^+]\Delta Q_{i-1, j, k} \quad (6.17)$$

$$[P_i]\Delta Q_i = -[A_{\eta, i, j-\frac{1}{2}, k}^+]\Delta Q_{i, j-1, k} + [L_{\zeta, i, j}]\Delta Q_{i, j} + [A_{\eta, i, j+\frac{1}{2}, k}^-]\Delta Q_{i, j+1, k} \quad (6.18)$$

$$[P_i^+]\Delta Q_{i+1} = [A_{\xi, i+\frac{1}{2}, j, k}^-]\Delta Q_{i+1, j, k}, \quad (6.19)$$

where the entry along a  $\zeta$ -line,  $[L_{\zeta, i, j}]\Delta Q_{i, j}$ , is:

$$[L_{\zeta, i, j}]\Delta Q_{i, j} = -[A_{\zeta, i, j, k-\frac{1}{2}}^+]\Delta Q_{i, j, k-1} + [D_{i, j, k}]\Delta Q_{i, j, k} + [A_{\zeta, i, j, k+\frac{1}{2}}^-]\Delta Q_{i, j, k+1},$$

and the entry of the diagonal,  $[D_{i, j, k}]$ , is:

$$\begin{aligned} [D_{i, j, k}] = & [c_0 \frac{h^{n+1}}{\Delta\tau} + A_{\xi, i+\frac{1}{2}, j, k}^+ - A_{\xi, i-\frac{1}{2}, j, k}^- + A_{\eta, i, j+\frac{1}{2}, k}^+ - A_{\eta, i, j-\frac{1}{2}, k}^- \\ & + A_{\zeta, i, j, k+\frac{1}{2}}^+ - A_{\zeta, i, j, k-\frac{1}{2}}^-], \end{aligned} \quad (6.20)$$

in which  $c_0$  can be found in table 3.1. The entry of plane  $[P_i]$ , equation (6.18), has the same form as the left-hand side of the two-dimensional relaxation, equations (3.65–3.67), for which application of a direct inversion is too expensive. Several approximate inversion schemes in each plane are applied: the two-dimensional method, i.e. SSOR, ILU decomposition, zebra relaxation or a PGS relaxation with red-black (RB) ordering. The last two methods are applied to take advantage of the implementation in a vector computer. Similar to the two-dimensional relaxation method,  $Q$  can be updated after several linear iterations or in each sweep using the intermediate correction,  $\Delta\bar{Q}$ . The latter may be seen as a nonlinear relaxation scheme.

- Forward-backward sweep along the planes of constant  $(\xi + \eta)$ , see figure 6.7. The equation for the forward sweep reads:

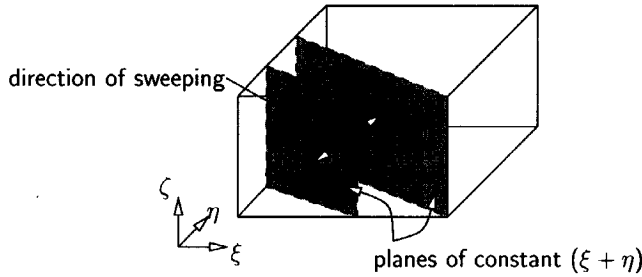


Figure 6.7: Relaxation sweep along the planes of constant  $(\xi + \eta)$

$$\begin{aligned}
 [L_{\zeta i,j}] \Delta\bar{Q}_{i,j}^{p+1} = & -R(Q^p, Q^n, Q^{n-1}) - [A_{\xi i+\frac{1}{2},j,k}^-] \Delta\bar{Q}_{i+1,j,k}^{p+1} \\
 & - [A_{\eta i,j+\frac{1}{2},k}^-] \Delta\bar{Q}_{i,j+1,k}^{p+1} + \omega_l [A_{\xi i-\frac{1}{2},j,k}^+] \Delta Q_{i-1,j,k}^p + \omega_l [A_{\eta i,j-\frac{1}{2},k}^+] \Delta Q_{i,j-1,k}^p,
 \end{aligned} \quad (6.21)$$

which results in an intermediate correction,  $\Delta\bar{Q}$ , followed by a backward sweep:

$$\begin{aligned}
 [L_{\zeta i,j}] \Delta Q_{i,j}^{p+1} = & -R(Q^p, Q^n, Q^{n-1}) - \omega_l [A_{\xi i+\frac{1}{2},j,k}^-] \Delta\bar{Q}_{i+1,j,k}^{p+1} \\
 & - \omega_l [A_{\eta i,j+\frac{1}{2},k}^-] \Delta\bar{Q}_{i,j+1,k}^{p+1} + [A_{\xi i-\frac{1}{2},j,k}^+] \Delta Q_{i-1,j,k}^{p+1} + [A_{\eta i,j-\frac{1}{2},k}^+] \Delta Q_{i,j-1,k}^{p+1},
 \end{aligned} \quad (6.22)$$

where the equation along a  $\zeta$ -line,  $[L_{\zeta i,j}] \Delta Q_{i,j}$ , and  $[D_{i,j,k}]$  are defined by equation (6.20). This scheme is called here Line LU-SGS, since equations along the  $\zeta$ -lines are directly inverted. The original LU-SGS scheme of Yoon and Jameson [181] sweeps along the planes of constant  $(\xi + \eta + \zeta)$  and only a block-diagonal matrix is inverted in each plane, see figure 6.8.

Another method is using a PGS relaxation, either with natural ordering or with red-black ordering. Red and black are used to call computational cells with  $(\xi + \eta + \zeta)$  odd and even, respectively. During the first relaxation sweep only the flow variables



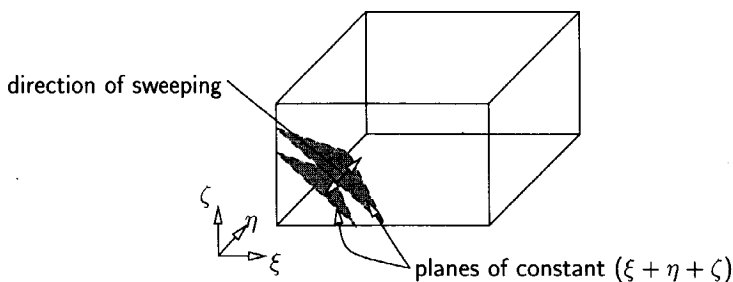


Figure 6.8: Relaxation sweep along the planes of constant  $(\xi + \eta + \zeta)$

with red color are updated and during the second sweep only the flow variables with black color are updated. The set of linear equations with red color depends only on the data with black color. Consequently, the update of the flow variables with the same color does not depend on each other and can be done concurrently. The equation for a PGS relaxation is:

$$\begin{aligned}
 [D_{i,j,k}] \Delta Q_{i,j}^{p+1} = & -R(Q^p, Q^n, Q^{n-1}) - [A_{\xi i+\frac{1}{2},j,k}^-] \Delta Q_{i+1,j,k}^p + [A_{\xi i-\frac{1}{2},j,k}^+] \Delta Q_{i-1,j,k}^p \\
 & - [A_{\eta i,j+\frac{1}{2},k}^-] \Delta Q_{i,j+1,k}^p + [A_{\eta i,j-\frac{1}{2},k}^+] \Delta Q_{i,j-1,k}^p \\
 & - [A_{\zeta i,j,k+\frac{1}{2}}^-] \Delta Q_{i,j,k+1}^p + [A_{\zeta i,j,k-\frac{1}{2}}^+] \Delta Q_{i,j,k-1}^p,
 \end{aligned} \tag{6.23}$$

where  $[D_{i,j,k}]$  is defined by equation (6.20).

## 6.2 PARALLELIZATION STRATEGY

The solution methods for the flow equations including the turbulence model and the spring analogy equation have been parallelized using a domain decomposition approach. The equations for the structure are not parallelized because the number of degrees of freedom is too small to justify the additional overhead cost of parallelization. The adoption of a domain decomposition strategy, instead of data parallelization, was dictated by the portability requirement. Data parallelization usually leads to a fine grain parallelization which is not suitable for networked computers. Moreover, it needs a special compiler (HPF). The current implementation has been ported to a variety of computers, from PCs up to MPP and PVP supercomputers.

To execute the relaxation in each subdomain in parallel the dependency among the subdomains has to be frozen. This means that some boundary values are treated explicitly. Consequently, in contrast with a parallel domain-decomposed explicit method, the convergence will decrease as the number of subdomains increases.

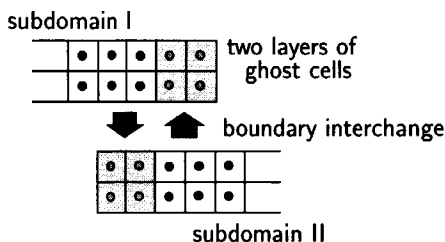


Figure 6.9: Artificial boundary condition between two subdomains using ghost cells

### 6.2.1 DOMAIN DECOMPOSITION

The computational domain is divided into subdomains, where each subdomain is assigned to a processor<sup>1</sup>. The subdomains are created by dividing the mesh in  $\xi$ - and  $\eta$ -directions only, i.e. not in the direction of body surface normals. From numerical experimentation it turned out, as was expected, that dividing the mesh in  $\zeta$ -direction results in a significant penalty in convergence. This probably can be explained from the usually high stretching of the mesh in  $\zeta$ -direction, while also the viscous terms behave in an elliptic manner. Thus the  $\zeta$ -lines are not split up but kept as a whole.

The decomposition is carried out statically prior to executing the code. The difference in boundary conditions between the subdomains usually does not contribute significantly to the computing time. Thus e.g. for a set equal of processors the mesh is divided equally among the nodes. For a set of unequal processors the mesh is divided according to the speed of the different nodes.

### 6.2.2 EXPLICIT SUBDOMAIN COUPLING

At the boundary of each subdomain the ghost cells have two possible conditions: a physical boundary condition, like a solid surface, freestream, etc., or an artificial boundary condition, i.e. the flow variables of its neighboring domain. For maintaining second-order spatial accuracy two layers of ghost cells are needed for the artificial boundary, see figure 6.9. The flow state at the ghost cells of the artificial boundary is transferred from the neighboring subdomain using inter-process communication routines. In this manner the subdomain coupling is conservative.

For the flow equations the possible coupling variables between the subdomains is either  $Q$  or  $\Delta Q$ . In the first case the interchange takes place after the  $Q$  has been updated (using Newton's method), so that the linear step works completely locally in a subdomain. In the latter case the interchange already takes place during the linear step. Concerning the convergence, the transfer of  $\Delta Q$  would certainly have a positive effect. Even for the RB point-relaxation there is no penalty at all if after each linear step a transfer of  $\Delta Q$  is carried out. But certainly this costs some communication time. As will be shown, the convergence penalty for a moderate

<sup>1</sup>In the parallel programming term a processor or a computer participating in parallel computing is also called a node, or a processing element (PE) in case of an MPP machine

number of processors (up to 64) is not really significant. Therefore, in most cases, except when it is mentioned otherwise, the results in this study have been obtained using the transfer of  $Q$ . The solution method for the one-equation turbulence model is along exactly the same lines as for the flow equations.

For the spring analogy equations the mesh position is transferred to the neighboring subdomains. A slight difference exists compared to the decomposition of flow and turbulence model. The unknown for the spring equation is at the vertex, which means that there is an overlap region which is shared by two subdomains. This overlap region is updated following the update in the field and the transfer to the neighboring subdomains. In this manner the neighboring subdomains will share a unique value of the mesh position in the overlap region.

### 6.2.3 IMPLEMENTATIONS

The implementation of the subdomain coupling method can be carried out conveniently using a communication library, e.g. Parallel Virtual Machine (PVM), Message Passing Interface (MPI), Bulk Synchronized Parallel (BSP), CRAY SHMEM, etc.. There are two possibilities in communicating the interface values between two subdomains: using message passing (MP) (a pair of send-receive routines) or direct remote memory access (DRMA). The first method already has some sort of synchronization mechanism, whereas the latter needs a user-specified synchronization.

Transferring a message from processor 1 to processor 2 using the MP method needs `send` and `receive` routines. For example, in PVM the transfer of  $Q$  looks like:

```
proc 1: call PVM_Send(Q(1,n,j,k),5,proc_2)
proc 2: call PVM_Recv(Q(1,0,j,k),5,proc_1).
```

The `receive` routine will block the program in processor 2 while waiting for the data to arrive from processor 1. Thus it is ensured that the program in processor 2 will get the proper data for further processing.

In the DRMA method the memory of the data which will be transferred has to be *symmetric*. This means that the addresses of the memory in two computers (or processing elements in case of an MPP machine) are the same. The transfer proceeds simply as: processor 1 writes to the memory of processor 2. For example, using the CRAY SHMEM library the transfer of  $Q$  looks like:

```
proc 1: call SHMEM_put(Q(1,n,j,k),proc_1,
    & Q(1,0,k,k),proc_2,5)
    call SHMEM_barrier()
proc 2: call SHMEM_barrier().
```

It should be noted that processor 2 does not know whether processor 1 has already written the data to its memory or not. Therefore both processors have to call the so-called `barrier` routine which blocks the programs until both processors have called it.

In the present method the PVM communication library is employed since it is available on most of today computers. The PVM library employs the message passing method. In the CRAY computers the native communication library, the SHMEM library, transfers data much faster than the PVM library. Therefore, in the implementation on the CRAY computer (MPP T3E and PVP J910) the most critical part of the communication routine, i.e. the interchange of the boundary data, is applied using the CRAY native communication library SHMEM which uses the DRMA method.

While waiting for completing the transfer of the data between the processors, some other tasks can be carried out. For example, since the transfer is only in the  $\eta$ - and  $\xi$ -direction, the flux in the  $\zeta$ -direction can readily be calculated without waiting for the neighbors. This technique reduces the portion of communication time in the whole computation.

### 6.3 RESULTS OF CUA METHOD FOR THREE-DIMENSIONAL FLOW

In this section a number of applications of the CUA method to three-dimensional flow is presented. Some standard test cases are considered to establish the validity of the method. First the results of the parallelization of the method will be discussed.

#### 6.3.1 RESULTS OF PARALLELIZATION

The purpose of the test cases presented in this section is to validate the decomposition method and to investigate its scalability. Scalability is a measure of the efficiency of a parallel computing method when more nodes are employed. Scalability of a parallel method can be quantified using the speed-up. Speed-up of a simulation using  $p$  processors with respect to a simulation using  $n$  processors is defined here as:

$$S_p^n = \frac{T_n n}{T_p p}, \quad (6.24)$$

where  $T_n$  is the wall-clock time of the simulation using  $n$  processors and  $T_p$  is the wall-clock time of the simulation using  $p$  processors. A perfectly scalable method will have a linear speed-up.

The speed-up is determined by various aspects: the ratio of the computing time to the communication time, the imbalance between the programs running on different processors and the efficiency of the solution method. The higher the ratio of computing time to the communication time the better the speed-up. By the increase of the number of processors the communication time between the sub-domains, for imposing the artificial boundary conditions, changes slightly and the communication time for the global coordination increases depending on the type of the computer. Meanwhile the computing time will reduce strongly by the increase of the number of processors. Therefore, when the size of the problem (the number of mesh points) is fixed, the so-called fixed mesh problem<sup>1</sup>, the speed-up will certainly decrease with the increase of the number of processors.

---

<sup>1</sup>Fixed mesh problem should not be confused with stationary mesh (non moving mesh) problem

Another measure of the speed-up is the so-called proportional mesh speed-up where the number of mesh points per processor is kept constant. Thus the total mesh size is proportional to the number of processors. The latter will produce a better measure of the speed-up since the ratio of computing time to the communication time changes only slightly. Thus the speed-up of a fixed mesh case may be considered as conservative.

To measure the speed-up for the proportional mesh, a series of meshes is needed. In general, generating a series of meshes is difficult for a realistic configuration. Many authors presented the test case of the flow over a flat plate. In this section only a fixed mesh case is presented with a reasonable number of mesh points. For this purpose the CT5 case of the standard AGARD LANN wing test case is used [34]. This case concerns the transonic flow about a supercritical transport type wing at  $M_\infty=0.82$ ,  $\alpha=0.60$  deg, oscillating about an axis parallel to the  $y$ -axis located at  $x/c_r=0.621$  with a reduced frequency  $k=0.102$  based on the root semi-chord and an amplitude of 0.25 deg. For this calculation the DLR mesh [118] is employed. The mesh, shown in figure 6.10, has a CH topology and dimensions of  $161 \times 33 \times 41$ . The same mesh was used by Heinrich et al. [74] for a similar study using an implicit dual time stepping method.

The calculations were carried out on the SUN MP 1000 machine (8 processors) of the Chair Aerospace Structures and Computational Mechanics of the DUT Faculty of Aerospace Engineering and on the CRAY T3E of the DUT Center for High Performance Applied Computing (HP $\alpha$ C) with 72 processing elements (PE). The SUN MP is a shared memory system with 1 GB of RAM (4 byte words), while the CRAY T3E is a distributed memory system with 128 MB of RAM (8 byte words) in each PE.

The calculations were carried out with all variables in core. On the CRAY T3E at least 8 PEs had to be employed for memory and load balancing. Thus the comparison for 1 to 8 processors was done on the SUN MP and 8 to 64 processors on the CRAY T3E. The speed-up with the CRAY T3E has been calculated relative to the 8-processor performance.

#### STEADY FLOW

The results of the steady flow calculations are presented in figures 6.11 to 6.13. Figure 6.11 shows the comparison between the results using 8 processors, the results using 64 processors and the experiment. A more comprehensive comparison of the results of the present method with experimental data will be presented in the next section. It can be concluded that the parallelization does not change the quality of the solution. Figure 6.12 presents the convergence history of the simulations using different numbers of processors. The convergence penalty caused by the explicit treatment of the artificial boundary increases with the number of processors. It can be seen from the L2 norm of the residual of the mass conservation equation that this penalty is not severe, even for a large number of processors. In line with this, the history of the lift coefficient is hardly influenced by the parallelization. The speed-up of running on more processors is shown in figure 6.13. This speed-up was

---

calculated based on the wall-clock time required to converge using the criterion of the L2 norm of the residual of the mass conservation equation. The execution using 64 processors took less than 4 minutes.

### UNSTEADY FLOW

The calculations for the forced vibration case were carried out using 24 time steps per cycle, with a number of subiterations between 12 and 20 with the convergence of the simulated lift coefficient as the criterion. The left part of figure 6.14 shows the comparison of the history of the lift coefficient using 8 processors and 64 processors. It can again be concluded that the parallelization does not alter the solutions. For the simulations using 32 and 64 processors, on average one additional subiteration is required in each time step to achieve the same convergence level as the 8 and 16 processors runs. The speed-up is shown in the right part of figure 6.14. The simulation using 64 processors took about 3 minutes per cycle of oscillation. The speed-up of the unsteady flow simulation is better than for the steady flow simulation. This can be explained by the convergence criterion of the lift coefficient used in stopping the subiteration. Figure 6.12 has shown already that the lift coefficient seems to be insensitive to the parallelization.

The speed-up obtained here for both steady and unsteady flow simulation is comparable to the result of Heinrich et al. [74]. Therefore, the present method can be concluded to be satisfactory, since the implicit temporal integration method of [74] employs explicit subiterations, which does not have a convergence penalty when increasing the number of processors.

### 6.3.2 RESULTS OF FLOW SIMULATIONS

The results of the flow simulations are presented in this section. The cases range from a simple isolated wing case up to wing-body configurations of a transport aircraft and a fighter type configuration. The purpose of these test cases is to validate the flow modeling and temporal integration method for three-dimensional applications. Some results have been produced using a single workstation and some others using a cluster of workstations or an MPP machine.

#### ONERA-M6 WING

**The ONERA-M6 wing was selected to verify the current method for three-dimensional** steady flow applications. Results have been obtained for  $M_\infty=0.84$  and  $Re_\infty=14.6 \times 10^6$ , based on the root chord, with  $\alpha=3.06$  deg and  $\alpha=5.06$  deg. The first test case represents an attached flow condition and the second one has a flow separation bubble just behind the shock over a part of the wing span. The dimension of the grid is  $128 \times 23 \times 25$  for the inviscid flow case and  $128 \times 23 \times 48$  for the viscous flow case. The mesh for the viscous flow calculation, shown in figure 6.15, has been obtained by redistributing the mesh points in the  $\zeta$ -direction so that sufficient resolution was obtained near the wing surface. The experimental results for comparison were obtained from Schmitt and Charpin [155]. For the first case calculations were also

performed by Hounjet and Eussen [80] with a FP method (AESIM) on the same grid.

Figure 6.16 shows a comparison of the pressure distributions calculated with the present method and the FP method at several span stations of  $y/s=0.20, 0.44, 0.80$  and  $0.90$ . The presence of two shock waves at the inner wing and one shock wave at the tip region suggests the presence of a lambda shock at the upper side of the wing. The overall comparison is fairly good. Near the root section the results agree very well, except in the trailing edge zone which might be caused by the onset of shock generated entropy and vorticity which are not modeled in the FP method. The other possible explanation is that the Kutta condition is explicitly satisfied by the FP method, while for the Euler method the flow at the trailing edge is captured as a contact discontinuity. An attempt was made to reduce the differences by redistributing the grid in the trailing edge zone which had however only a limited effect. In comparison to the FP method the second shock has been predicted a bit further aft by the Euler method. At the wing tip the differences are slightly larger.

Figure 6.17 shows a comparison of the calculated pressure distribution with experimental data. Near the root section there are two shock waves which are well predicted, except for the peak value of the first one. The second shock wave is a bit too far downstream which is only slightly improved by the viscous flow method. The pressure distributions on the lower side agree well. Near the wing tip the Navier-Stokes method performs not as good as the inviscid flow methods. This is probably due to an insufficient resolution of the mesh in the spanwise direction near the tip and the inadequacy of the algebraic turbulence model. These results are similar to the Navier-Stokes results presented in the literature for this configuration.

Figure 6.18 shows a comparison of the calculated surface pressure coefficient with the experimental data at several span stations of  $y/s=0.20, 0.65, 0.80$  and  $0.90$ , at the higher incidence of  $\alpha=5.06$  deg. Starting at the root section there are two shock waves which are well predicted, including the peak value of the first one. Again the second shock wave is situated a bit too far downstream which is fairly well improved by the viscous method. Also the pressure distributions on the lower side agree well. The measured pressure distributions at  $y/s=0.80$  and  $0.90$  show the presence of a separation bubble at the foot of the shock. Although the calculated pressure distributions close to the trailing edge agree reasonably well compared to the experiment, the separation bubble could not be captured properly. A calculation employing the Spalart-Allmaras turbulence model has not improved this deficiency. Similar results for methods using the Baldwin-Lomax and Spalart-Allmaras turbulence model were obtained by Radespiel et al. [139]. They also showed that the Johnson-King turbulence model could model this separation bubble well.

The CPU time of the viscous flow calculation ( $\approx 1000$  relaxation sweeps) was a factor 3 higher than that of the inviscid flow calculations ( $\approx 500$  relaxation sweeps) for obtaining a 4 digit accuracy of the lift coefficient. The calculations were carried out on a SGI workstation with R8000/R8010 processors. It took about 10 hours for the Navier-Stokes calculation.

## NLR F-5 WING

The applicability of the present CUA method is validated using the NLR F-5 fighter type isolated wing. Geometrical and experimental data of NLR wind tunnel tests are described by Tijdeman et al. [169] for the clean wing. In this case the viscous effects are weak to mild.

The vibration mode is a rigid pitching oscillation with an amplitude of 0.25 deg about the root midchord. The axis of rotation is perpendicular to the root plane. The frequency is 40 Hz, corresponding to  $k=0.274$ , based on the root semi-chord. The flow condition is  $M_\infty=0.90$ ,  $Re_\infty=12\times 10^6$ , based on the root chord, and  $\alpha=0$  deg. The steady flow calculations were performed with the Navier-Stokes equations and the Euler equations on a coarse mesh of  $128\times 22\times 36$  and  $128\times 22\times 24$  points, respectively. Similar dimensions of the mesh were also used by Guruswamy [68] for this case.

Figure 6.19 compares the steady pressure distributions at the span stations  $y/s=0.20, 0.50, 0.70$  and  $0.85$ . Only slight differences are noticed between the Euler and the Navier-Stokes results. Therefore only the Euler method was applied further for the unsteady flow case. The unsteady flow calculations were performed using 24 time steps and 48 time steps per cycle with 12 to 20 subiterations.

The unsteady first harmonic pressure coefficients are compared in figures 6.20 and 6.21. Except for peak values a fairly good agreement is shown. The differences close to the leading edge may be caused by the insufficient mesh resolution around the nose. Inspection of the time signals revealed the existence of a moving shock close to the leading edge which can not be found in the experimental results. Most probably the relatively widely spaced distribution of pressure orifices did not allow a precise recording of the shock wave motion, especially for the small amplitude of the pitching motion. The differences due to the applied number of time steps are so small that in conclusion 24 time steps per cycle were sufficient for the calculation. The CPU time for the inviscid calculation using 24 time steps per cycle was about 1.5 hours per cycle using a SUN workstation with ULTRA SPARC 1 processor. It may be concluded that the present method gives satisfactory results for the steady and unsteady flows around NLR F-5 fighter type wing.

## LANN WING

The LANN wing is considered again. An extensive comparison of calculated results **was already performed in 1984 by Hounjet and Meijer [82] using the measured wing geometry**, the static deformation, the measured vibration modes and an angle of attack correction for matching with the steady flow pressure distribution, in validating the time-linearized inviscid FTRAN3 method. In the present calculations design contours were applied, no account was taken for the static deformation, the angle of attack correction and the vibration mode correction. The LANN wing geometry was taken from Bland [34]. Experimental data were obtained from Zwaan [183].

Calculations and comparisons were made for pitching about 0.621 root chord at  $M_\infty=0.822$ ,  $\alpha=0.6$  deg and  $Re_\infty=7.3\times 10^6$  based on root chord. The amplitude



of oscillation was 0.25 deg with a reduced frequency of  $k = 0.102$  based on root semi-chord. The same mesh as employed in the parallelization test cases was used. This case has moderate viscous and transonic effects.

A comparison of the steady pressure distributions is shown in figure 6.22 at the span stations of  $y/s=0.20, 0.47, 0.65$  and  $0.82$ . The Euler results show a substantial deviation from the experimental data, even for the lower side. The calculated data using the Navier-Stokes equations are in fairly good agreement with the experimental data for the whole wing at both sides, for both shock positions at the inner wing and peak suction levels at the leading edge.

Unsteady first harmonic pressure distributions are compared in figures 6.23 and 6.24. The Euler results were generated with 24 time steps per cycle and the Navier-Stokes results were obtained using 48 time steps per cycle. It is immediately clear that the agreement of the experimental data with the Navier-Stokes results is better than with the Euler results, although both sets of calculated results are qualitatively correct. The results using the Euler equations are similar to those presented by Brenneis and Eberle [35] which were also validated for the case of  $k=0.076$ . Part of the differences between the computational and the experimental results should be attributed to the presence of additional vibration modes of the wing model observed during the wind tunnel tests, which were partly not in complete phase or counterphase with the excitation force, see [82].

The CPU time for the inviscid flow case was about 2.5 hours per cycle of oscillation on an SGI workstation with R8000/R8010 processors. The CPU time of the unsteady viscous flow calculation (48 time steps  $\times$  16 relaxation sweeps) was a factor 3 higher than that of the inviscid flow calculations (24 time steps  $\times$  12 relaxation sweeps) for one cycle. It should be noted that unsteady flow results of the aforementioned FP method required about 5 times less computing time than the present Euler method.

The application of the present method for the transport type wing suggests the importance of viscous flow modeling for flow about a relatively thick wing. The computing time for the viscous flow case which was about 7.5 hours required an overnight run on a workstation. This was one of the reasons to apply a parallel computing method to reduce the wall-clock time. Finally it may be concluded that the present method gives also satisfactory results for a transport type wing.

#### DLR-F4 WING-BODY CONFIGURATION

Recently, many European research institutes have carried out a common project to validate CFD methods and assess turbulence models, see Haase et al. [70] for a complete report on the project. One of the configurations considered in the project was the DLR-F4 transport wing-body configuration. This case is perhaps the best test case for validation since the mesh and the results of many well-known institutes in Europe are available on a CD-ROM. Steady transonic flow experiments were conducted in the high speed wind tunnel (HST) of the NLR, Amsterdam.

The case considered is the transonic flow at  $M_\infty=0.75$ ,  $\alpha=0.93$  deg and  $Re_\infty=12.49 \times 10^6$  based on the semi-span of the wing model. The mesh had a CO topol-

ogy, with solid surfaces on both  $\eta=0$  and  $\zeta=0$ , see figure 6.2. The dimensions of the mesh were  $257 \times 89 \times 49$  which in total amounts to about 1.1 million mesh points.

The calculation with the present method was carried out on 32 processors of the CRAY T3E computer. The convergence of the lift coefficient and the L2 norm of the residual of the mass and energy conservation equations is shown in figure 6.25. The work unit along the horizontal axis is the wall-clock time required to evaluate the residual. Thus it represents more or less the time required to perform one explicit step. The iterations were stopped after the lift coefficient reached 4 digits of accuracy. By this time the residual had dropped about 3 orders of magnitude. Similar figures were also presented in [70]. The calculation time was about 90 minutes.

The comparison of the computed and measured pressure distributions on the surface of the wing is shown in figure 6.26. Comparisons are provided by the experimental data and also two other computational results, namely of Daimler-Benz Aerospace (DA) using a Thin-Layer Navier-Stokes method with the Baldwin-Lomax algebraic turbulence model, and British Aerospace (BA) using also a Thin-Layer Navier-Stokes method but with the  $k-\tau$  two-equation turbulence model. Both computational methods apply central difference schemes for the inviscid fluxes, where the method of DA is of Jameson type and the method of BA is of Lax-Wendroff type. It is repeated here that the present method employs an upwind method of Roe's FDS with the Spalart-Allmaras one-equation turbulence model. The results of the present method are in good agreement with the other computational results and the experimental data, except for the shock position which resides between the result of BA and DA.

It may be concluded that satisfactory steady flow results have also been obtained using the present method for this wing-body configuration of transport type.

#### FIGHTER TYPE WING-BODY-TAIL CONFIGURATION

The most complicated configuration considered in the present study is a wing-body-tail fighter type configuration. Unsteady flow experiments were conducted in the HST of the NLR, Amsterdam for a semi-span model of this configuration. The wing was excited sinusoidally in a pitching motion. Figure 6.27 shows a mesh with about 200,000 points. The inlet of the engine was smoothed over. The case considered is a transonic flow case at  $M_\infty=0.92$  and  $\alpha_{\text{mean}}=6.00$  deg. All results were obtained **using the Euler mode.**

The comparison of the calculated pressure distributions on the wing upper surface and the experimental data is presented in figure 6.28. The overall agreement is good, except for the shock which is too strong and located too much downstream. The differences near the wing tip may be explained by the experimental result being obtained with a wind tunnel model having a missile tip-launcher, whereas the present calculation was carried out with a clean wing. The shock strength and location may be improved by using the Navier-Stokes method.

In the unsteady flow case the pitching oscillation had an amplitude of  $\alpha_{\text{amp}}=0.50$  deg. Figures 6.29 and 6.30 show the real and imaginary part of the pressure dis-

tributions on the upper surface of the wing compared to the experimental results. Two simulations were performed employing small and large time steps on a SUN MP using 6 processors out of a maximum of 8. The small time step was 64/cycle requiring 3 hours/cycle of wall-clock time and the large time step was 8/cycle requiring 25 minutes/cycle of wall-clock time. Large and small time step results are very similar. Their differences are almost negligible when the results are compared with the experimental data. In view of the complicated configuration and the differences in geometrical modeling, the agreement is reasonable for the inboard part of the wing, but diminishes towards the tip. The differences at the outboard part of the wing may be caused by the flow separation which was observed during the experiment.

In general the results for this relatively complex configuration are satisfactory. The low number of time steps per cycle required to obtain adequate unsteady flow results with a computing time less than half an hour justifies the present approach. The results presented in this section validate the application of the present method for a complex configuration.

#### FIGURES

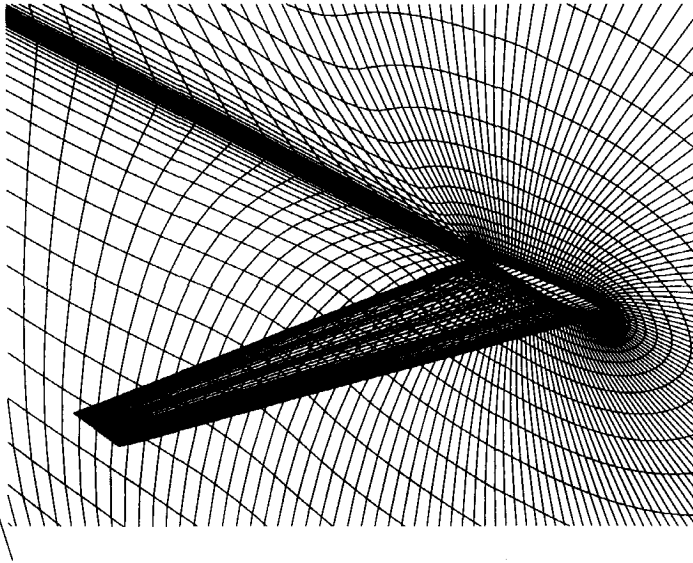


Figure 6.10: Mesh around LANN wing with CH topology, number of mesh points  $\approx 220,000$

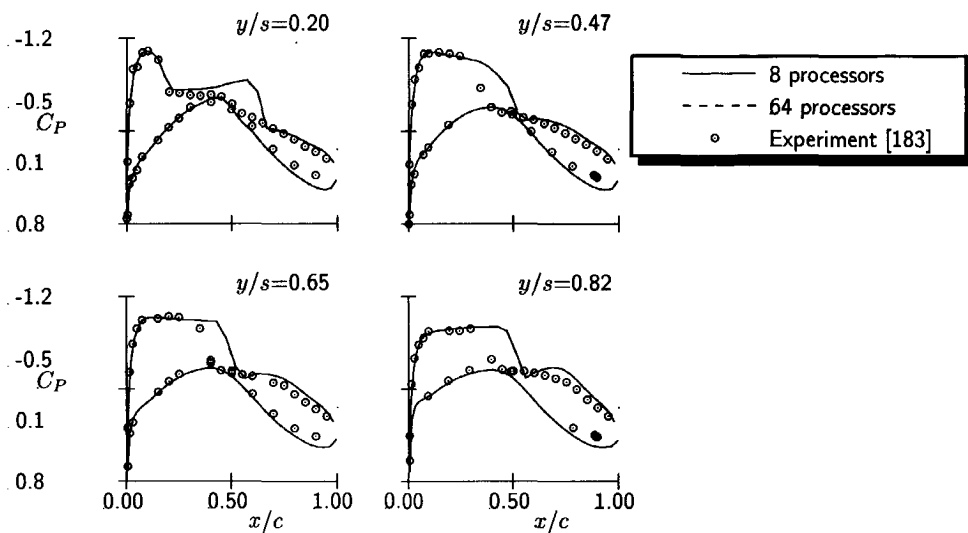


Figure 6.11: Steady pressure distributions on LANN wing, case CT5

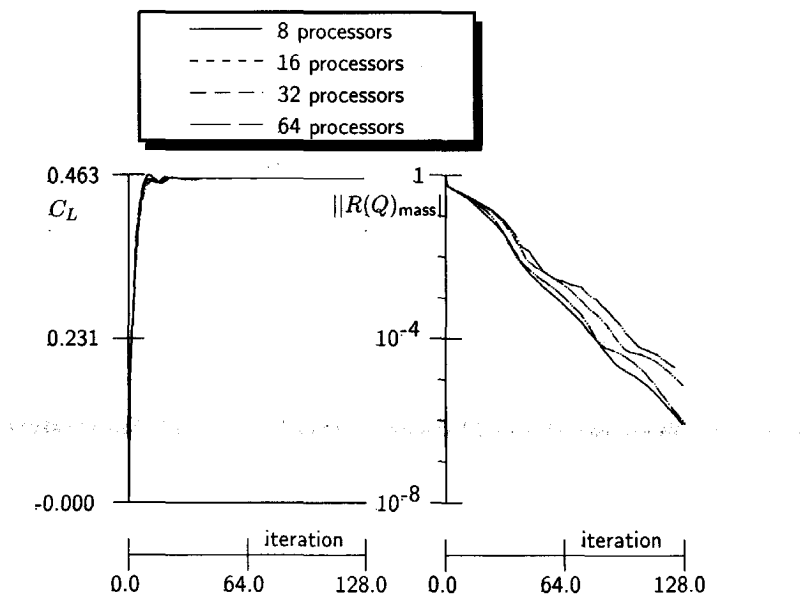


Figure 6.12: Convergence of lift coefficient and residual in mass conservation equation

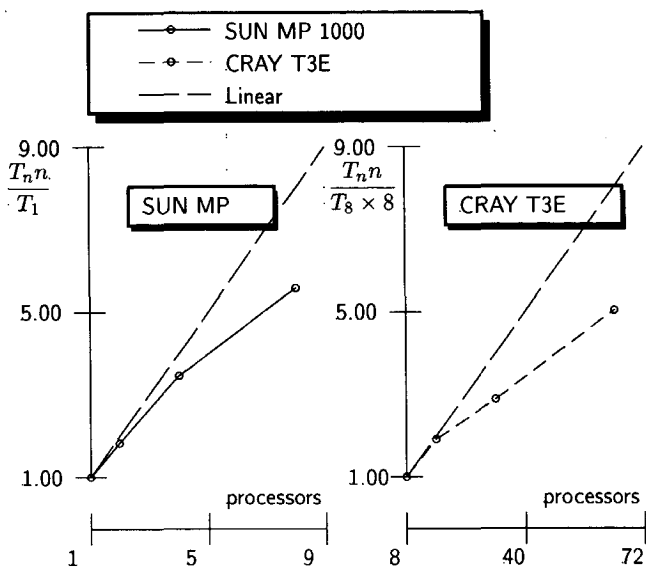


Figure 6.13: Speed-up of parallelization of steady flow calculation for LANN wing, case CT5, fixed mesh problem

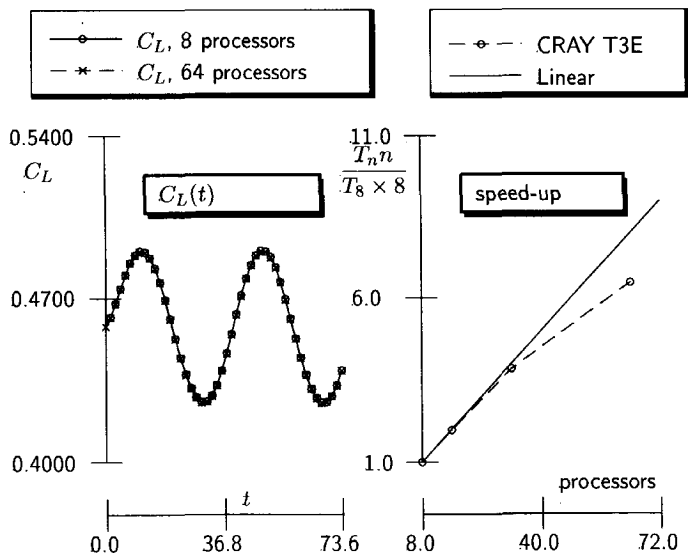


Figure 6.14: Performance of parallelization of unsteady flow calculation for LANN wing, case CT5, fixed mesh problem

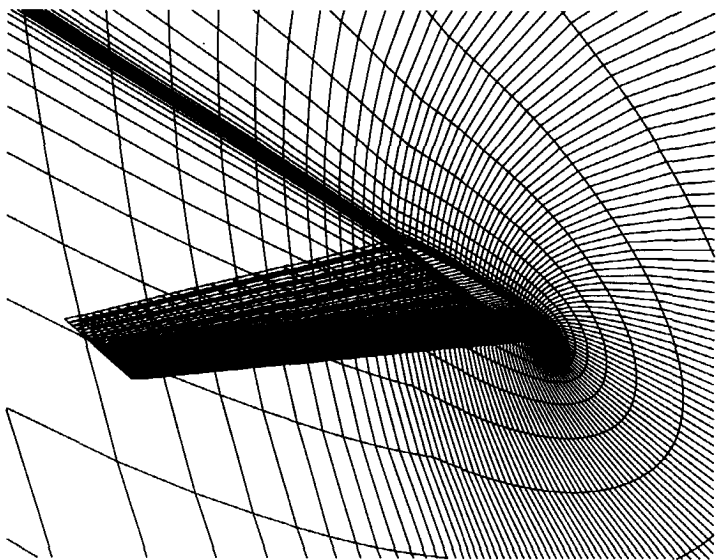


Figure 6.15: Mesh around ONERA M6 wing with CH topology for calculations involving the Navier-Stokes equations

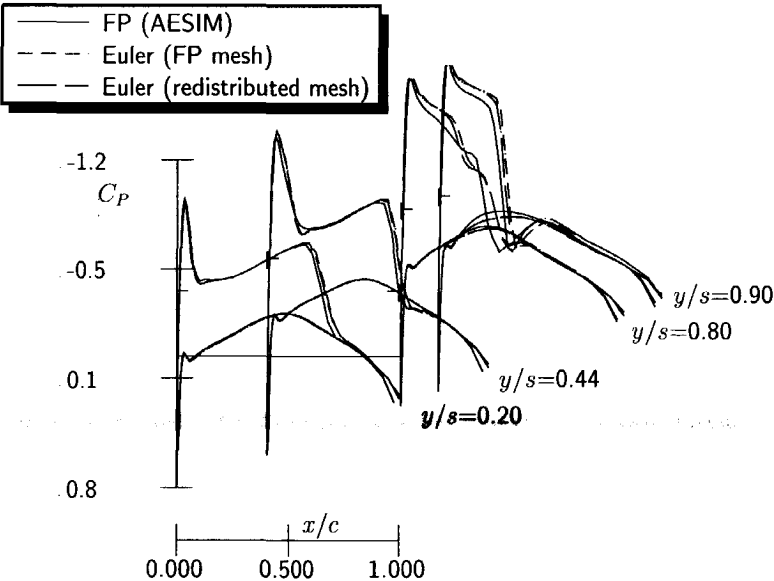


Figure 6.16: Comparison of steady pressure distribution on ONERA-M6 wing calculated with FP and Euler methods at  $M_\infty = 0.84$ ,  $\alpha = 3.06$  deg

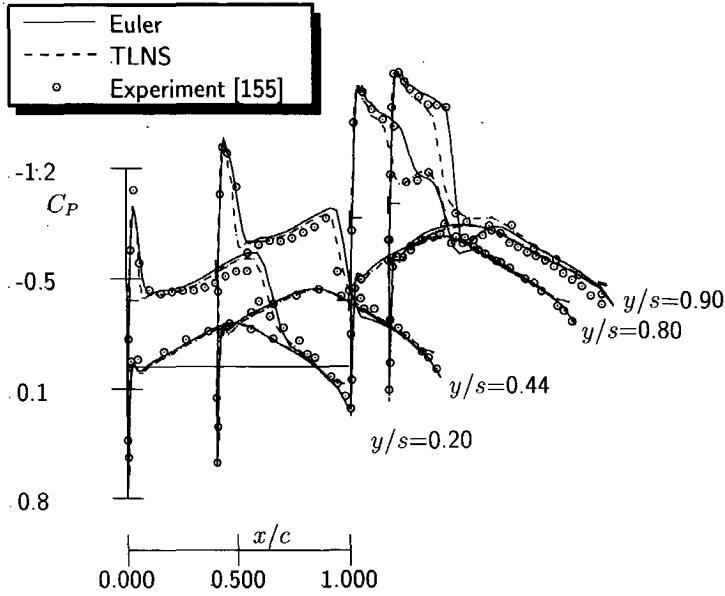


Figure 6.17: Comparison of experimental and calculated steady pressure distributions for ONERA-M6 wing at  $M_\infty=0.84$ ,  $\alpha=3.06$  deg and  $Re_\infty=14.6 \times 10^6$

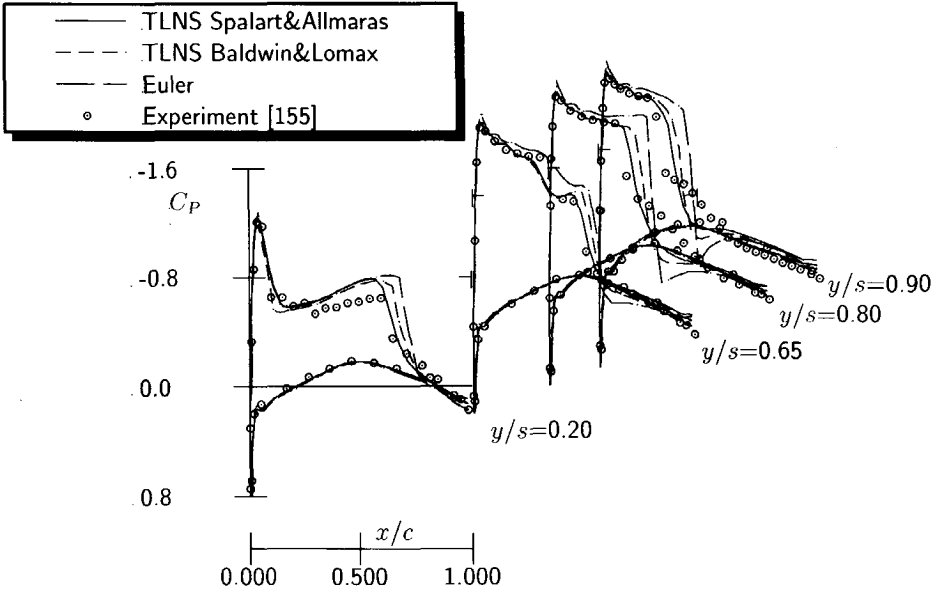


Figure 6.18: Comparison of experimental and calculated steady pressure distributions for ONERA-M6 wing at  $M_\infty=0.84$ ,  $\alpha=5.06$  deg and  $Re_\infty=14.6 \times 10^6$

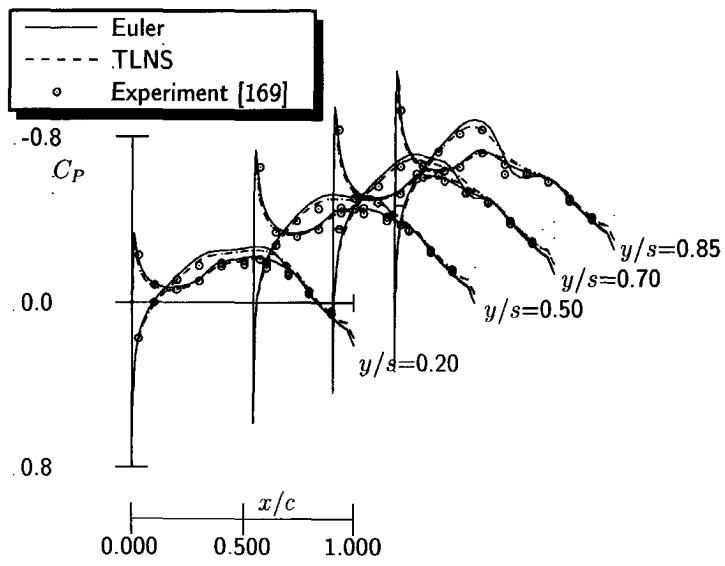


Figure 6.19: Comparison of experimental and calculated steady pressure distributions for fighter type wing at  $M_\infty=0.90$ ,  $\alpha=0$  deg and  $Re_\infty=12 \times 10^6$

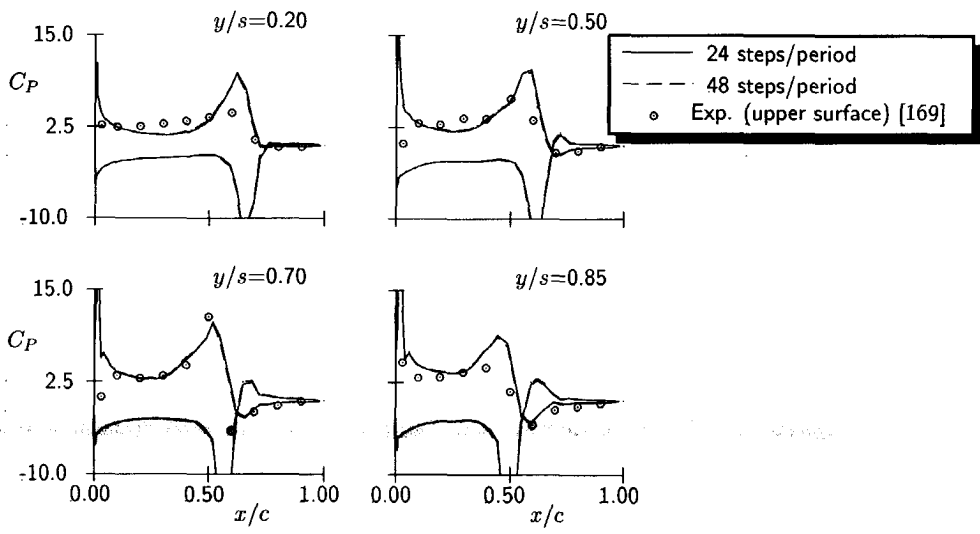


Figure 6.20: Comparison of real part of experimental and calculated (Euler) first harmonic pressure distributions for fighter type wing at  $M_\infty=0.90$ ,  $\alpha_{amp}=0.25$  deg and  $k=0.274$



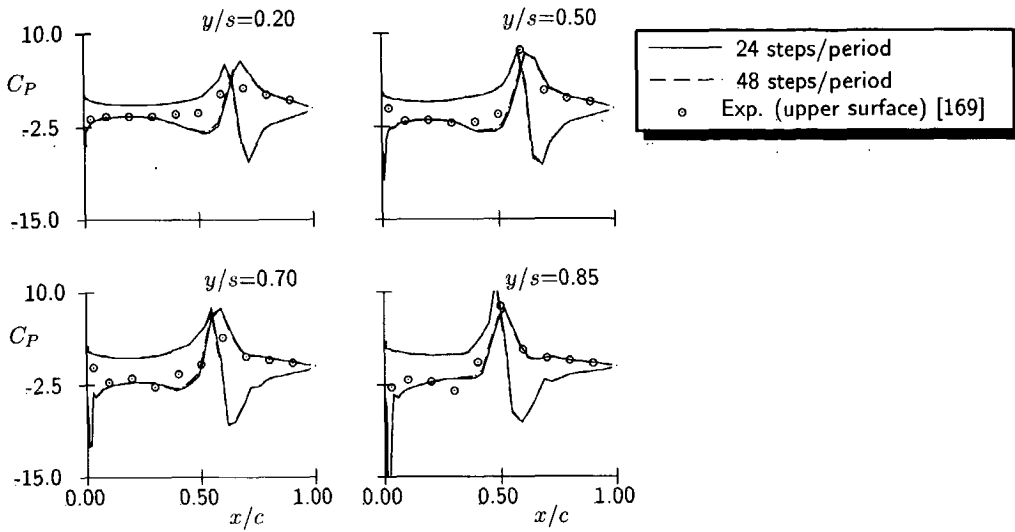


Figure 6.21: Comparison of imaginary part of experimental and calculated (Euler) first harmonic pressure distributions for fighter type wing at  $M_\infty=0.90$ ,  $\alpha_{amp}=0.25$  deg and  $k=0.274$

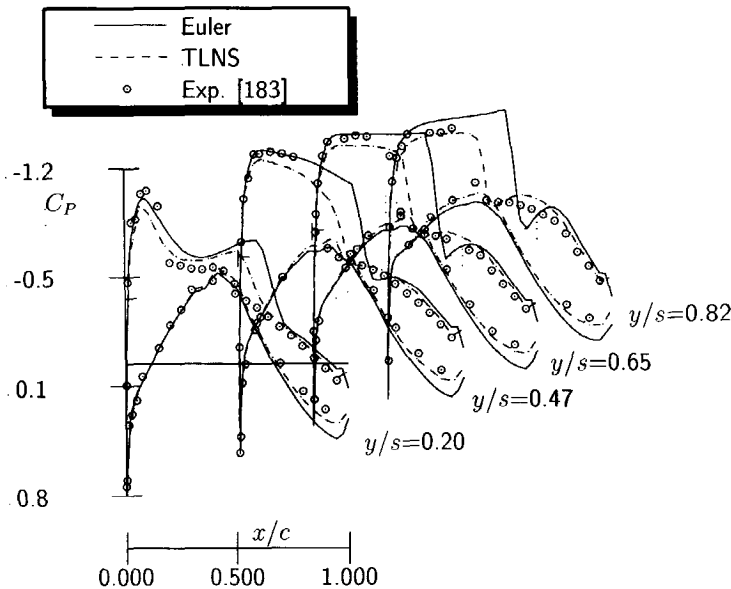


Figure 6.22: Comparison of experimental and calculated steady pressure distributions on LANN wing at  $M_\infty=0.82$ ,  $\alpha=0.6$  deg and  $Re_\infty=7.3 \times 10^6$

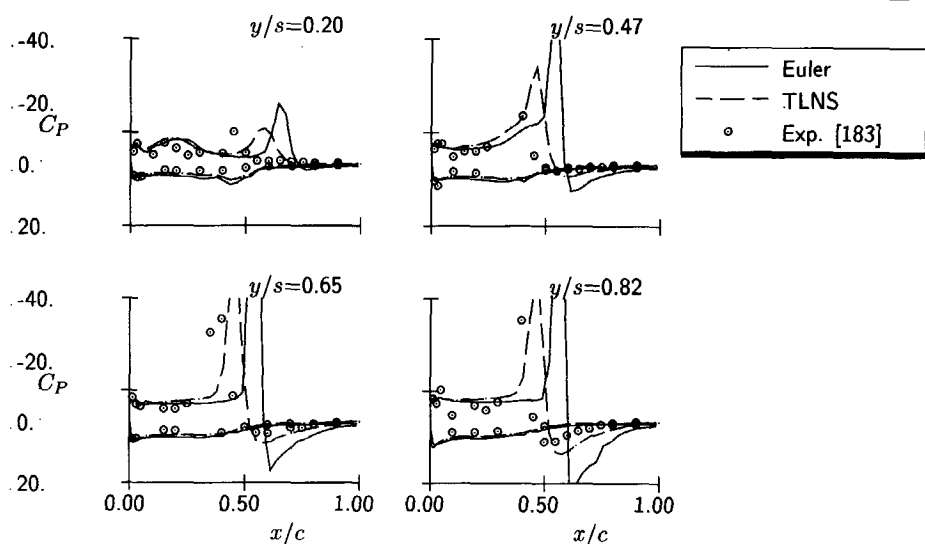


Figure 6.23: Comparison of real part of experimental and calculated first-harmonic pressure distributions on LANN wing at  $M_\infty=0.82$ ,  $\alpha_{\text{mean}}=0.6$  deg,  $\alpha_{\text{amp}}=0.25$  deg and  $k=0.102$

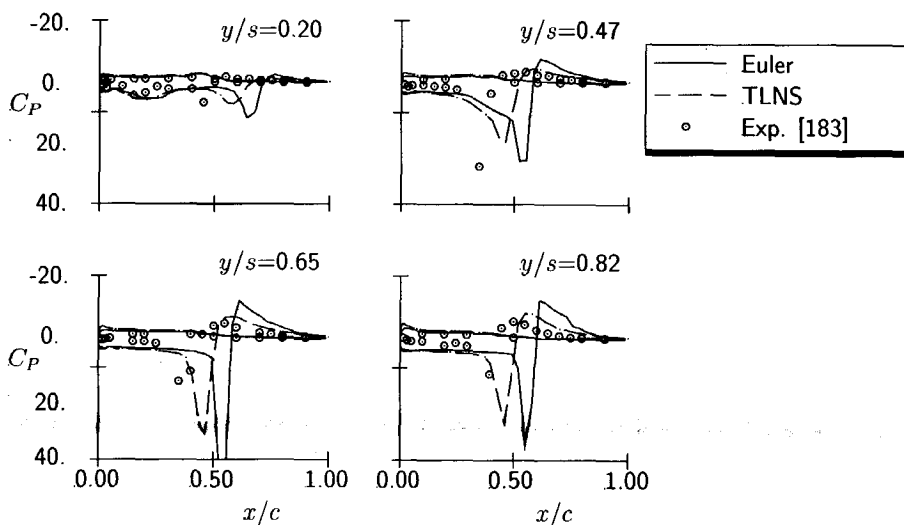


Figure 6.24: Comparison of imaginary part of experimental and calculated first harmonic pressure distributions on LANN wing at  $M_\infty=0.82$ ,  $\alpha_{\text{mean}}=0.6$  deg,  $\alpha_{\text{amp}}=0.25$  deg and  $k=0.102$

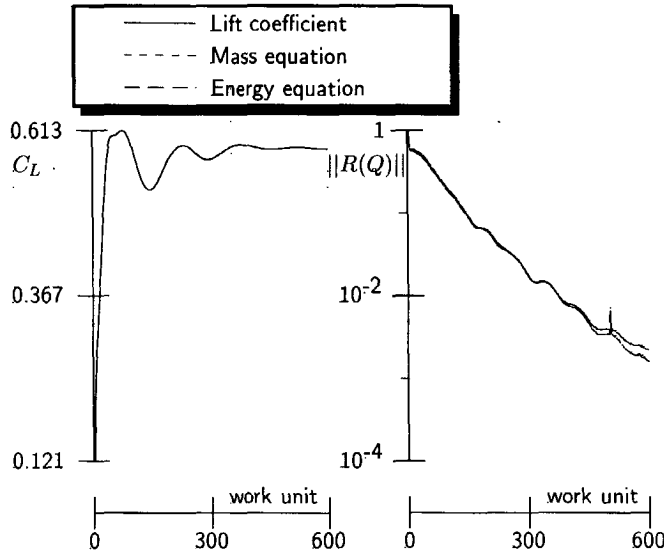


Figure 6.25: Convergence history of lift and residual for the DLR-F4 wing-body test case at  $M_\infty=0.75$ ,  $\alpha=0.93$  deg,  $Re_\infty=12.49 \times 10^6$

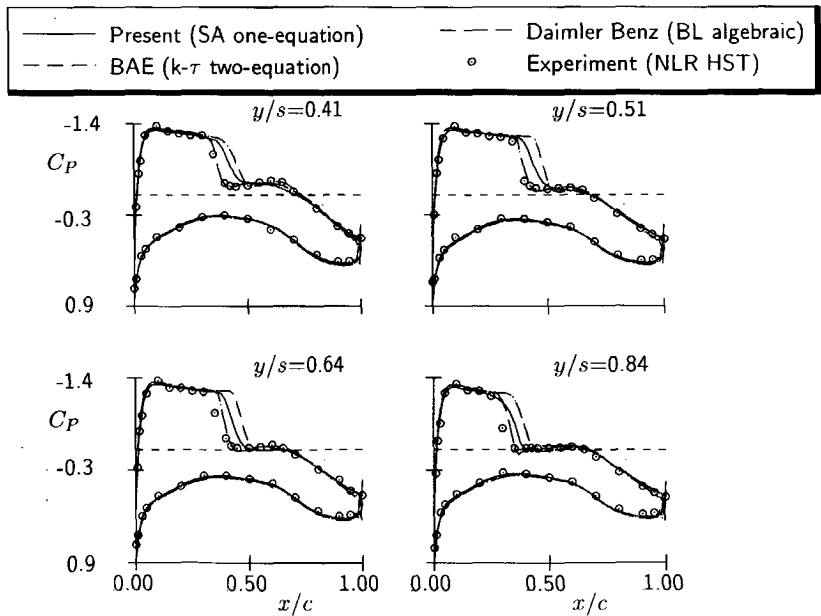


Figure 6.26: Comparison of experimental and calculated pressure distributions on the wing of DLR-F4 wing-body configuration at  $M_\infty=0.75$ ,  $\alpha=0.93$  deg

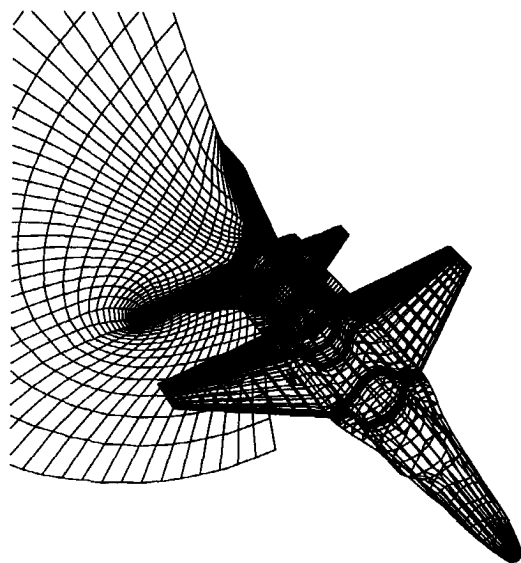


Figure 6.27: Mesh around wing-body-tail fighter type configuration with HO topology, number of mesh points  $\approx 200,000$ .

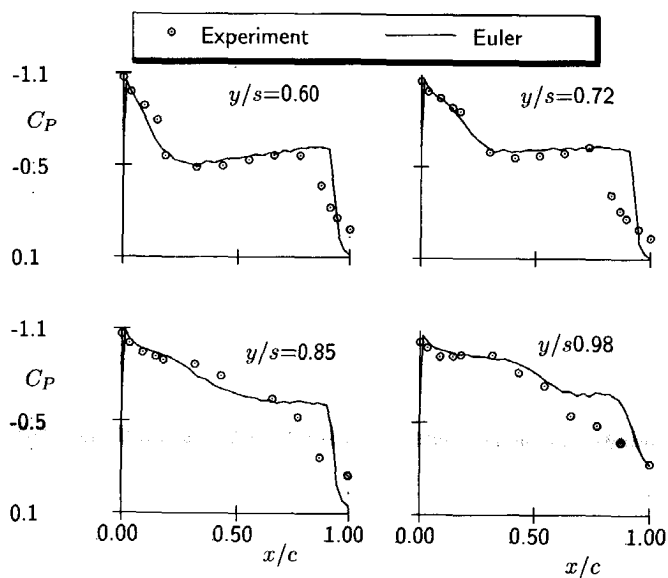


Figure 6.28: Comparison of experimental and calculated steady pressure distributions on the upper side of the wing of fighter type configuration at  $M_\infty = 0.92$ ,  $\alpha = 6.00$  deg,  $\alpha_{amp} = 0.50$  deg

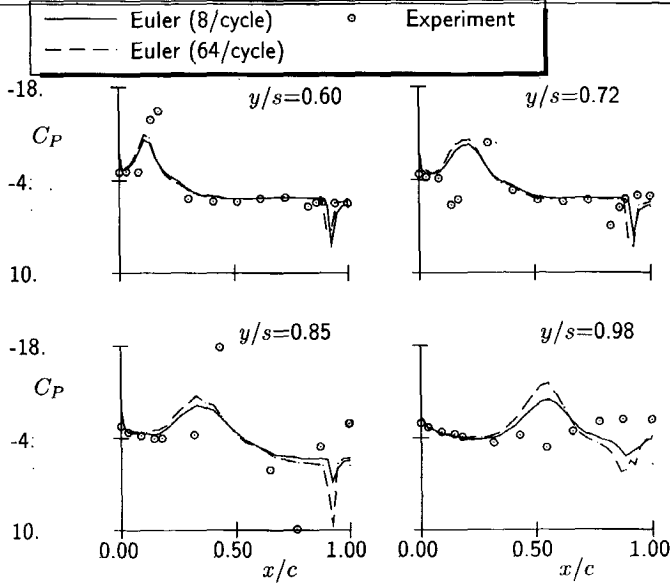


Figure 6.29: Comparison of the real part of experimental and calculated unsteady pressure distributions on the upper side of the wing of fighter type configuration at  $M_\infty = 0.92$ ,  $\alpha = 6.00$  deg,  $\alpha_{amp} = 0.50$  deg

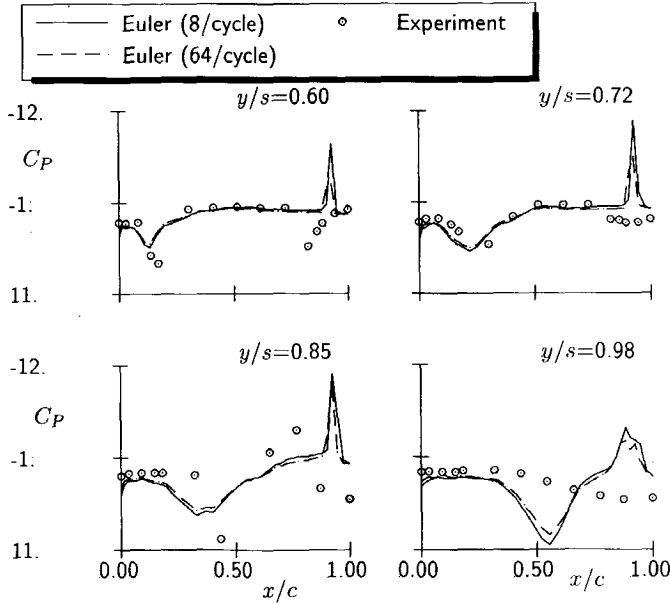


Figure 6.30: Comparison of the imaginary part of experimental and calculated unsteady pressure distributions on the upper side of the wing of fighter type configuration at  $M_\infty = 0.92$ ,  $\alpha = 6.00$  deg,  $\alpha_{amp} = 0.50$  deg

## 6.4 STRUCTURAL MODEL

In the two-dimensional case of a rigid airfoil, the motion is completely defined by the two variables  $[h, \alpha]$ , representing a two-degree-of-freedom system. For the three-dimensional case, a more general approach is applied in which  $N$  degrees of freedom can be employed in the analysis.

As has been introduced in section 2.4, the motion of the structural part is represented by a finite number of predefined mode shapes. These modes are obtained from solving the homogeneous equation for the motion of the structure, i.e. equation (2.2). Thus, the structural part in the present CAS method is represented by the mode shapes,  $\phi$ , which have been normalized by the mass matrix, see equation (2.3), and the corresponding natural frequencies of these mode shapes.

Since a loose aero-structural coupling is employed, the choice of the level of modeling of the structural part is quite flexible as long as the mode shapes can be defined at the nodes of the CUA mesh that are located on the solid surface. For example, a high aspect ratio wing structure can be modeled as a beam with the spanwise variation of the translation and the rotation as the variables, a thin low aspect ratio wing can be modeled as a flat plate, and so on. The most general method for modeling the structure is by a finite element method (FEM), see e.g. Bathe [23].

The determination of modal parameters of an aircraft structure by calculation or experiment is a theme in itself and lies outside the scope of the present study. The limited attention that is given here to this theme does not imply that it is less important than the CUA/CAS issue. Mass and stiffness forces are usually much larger than the unsteady aerodynamic forces, as it has been made clear in table 2.1, and the accuracy of the modal parameters is a matter of primary concern. Experience has learned that the natural frequencies can be determined quite accurately. Generalized masses and natural mode shapes data are generally less accurate, especially at higher natural frequencies. The mode shapes are constituent elements in the generalized aerodynamic forces besides the aerodynamic pressures. Moreover, the mode shapes are required to prescribe the boundary condition for the aerodynamic calculations.

The interfacing between the aerodynamic data and the structural data in the aeroelastic system will be the subject of the next sections.

## 6.5 AEROELASTIC EQUATIONS

As has been mentioned in chapter 1, and also shown by the examples in the previous section, in almost all cases of aeroelastic analysis an incompatibility exists between aerodynamic nodes and structural nodes at the fluid/structure interface. Figure 6.31 shows an example the FEM modeling of the structural part using flat plate elements and FVM modeling of the aerodynamic part. Figure 6.32 shows the situation near the nose of the AGARD 445.6 wing. It can be clearly seen that the aerodynamic surface control points (points on the surface where the solid-surface boundary condition is imposed and the pressure is calculated) and the structural

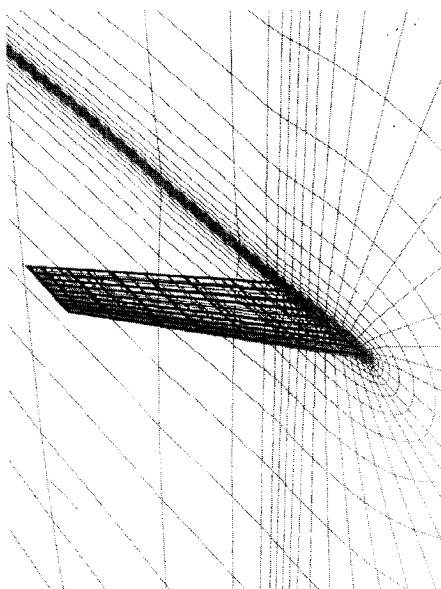


Figure 6.31: Different types of discretization and geometrical modeling of the aerodynamic (finite volume) and structural (finite element) part of AGARD wing 445.6

FEM nodes (points where the structural displacement, velocity and acceleration are calculated) do not coincide. In this case an interpolation method is required. In aeroelastic problems the aerodynamic mesh at the interface is usually denser than the structural mesh. Therefore, representing the aerodynamic data at the structural mesh may be called restriction, whereas representing the structural data at the aerodynamic mesh may be called prolongation.

The interpolation method to be adopted for the present three-dimensional CAS method is based on aeroelastic applications. Aeroelastic practice has shown that spline methods are effective interpolation methods. Such a method has also been applied in the present study. The most important requirement for the spline method is stated in section 2.1, i.e. that the work transfer should be conserved. The aerodynamic force restriction to the structural mesh can be written as:

$$f^s = [R] f^a, \quad (6.25)$$

where  $f^s$  are the aerodynamic forces at the structural nodes and  $f^a$  are the aerodynamic forces at the aerodynamic surface control points, whereas the prolongation of the structural displacements to the aerodynamic surface control points can be written as:

$$d^s = [P] d^a. \quad (6.26)$$

The requirement that the transfer of work is constant can be expressed as:

$$f^s d^s = f^a d^a, \quad (6.27)$$

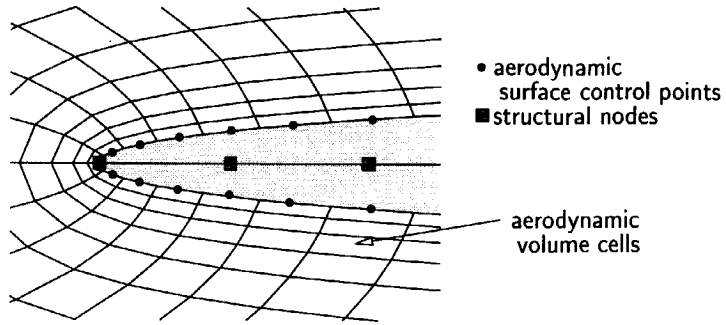


Figure 6.32: Control point incompatibility between the structural computational model and the aerodynamic computational model

which upon substitution of equation (6.25) and equation (6.26) results in the condition:

$$[R] = [P]^T. \quad (6.28)$$

In the present study the volume spline method of Hounjet and Meijer [83], which was developed primarily for the conservation of aeroelastic data transfer, is applied to determine the restriction and prolongation operators. The volume spline method employs a series of three-dimensional functions which are solutions of the Laplace equation. The interpolation also has to satisfy the requirements: applicable for smooth and non-smooth data, monotone and correct far-field behavior. A detailed description of the method was given in [83].

To solve equation (2.4) the GAFs have to be evaluated at those structural nodes which represent the solid boundaries. Assuming a conservative work transfer the GAFs can also be calculated by first prolongating the mode shape data to the aerodynamic control points on the solid surface. Therefore, prior to the aeroelastic simulation the mode shapes obtained from the structural dynamic calculation have to be prolonged to the aerodynamic mesh points on the solid surface. Figure 6.33 shows the first four mode shapes and the corresponding natural frequencies of the AGARD 445.6 wing after the prolongation to the aerodynamic surface control points using the volume spline method.

Following the determination of the mode shapes at the aerodynamic surface control points, the aeroelastic simulation proceeds by solving the aeroelastic equations. In a generalized coordinate system the structural equations, i.e. equation (2.4), are written here as:

$$\ddot{q}_i + 2\zeta_i\omega_i\dot{q}_i + \omega_i^2q_i = \hat{Q}_i, \quad i = 1..N, \quad (6.29)$$

where  $q_i$  is the generalized coordinate and  $\hat{Q}_i = q_\infty S Q_i$ , in which  $Q_i$  is the dimensionless generalized force, given by equation (2.5). As for the two-dimensional method, the set of second-order differential equations, equation (6.29) is brought into



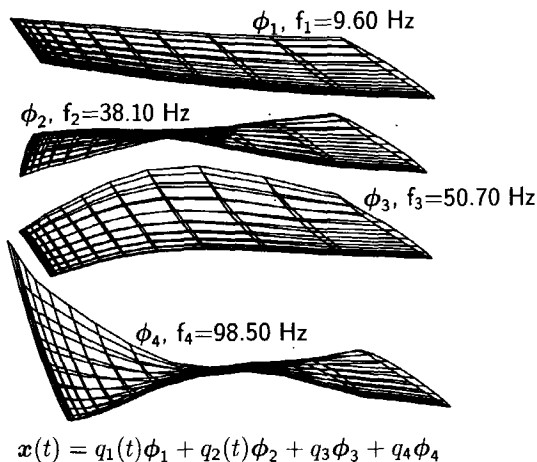


Figure 6.33: The first four mode shapes prolonged from the structural nodes to the aerodynamic surface control points of AGARD 445.6 wing. Note that for clarity not all mesh lines have been plotted

a standard state-space representation in a system of first-order differential equations:

$$\dot{X} = AX + BQ, \quad (6.30)$$

where:

$$A = \begin{bmatrix} 0 & 1 \\ -\omega^2 & -2\zeta\omega \end{bmatrix}, \quad B = \begin{bmatrix} 0 \\ 1 \end{bmatrix},$$

and the state variable is defined as  $X = [q, \dot{q}]^T$ . The solution of equation (6.30) follows the method presented in chapter 5 for two-dimensional aeroelastic simulations.

#### 6.5.1 CONFORMITY OF AERODYNAMIC AND STRUCTURAL PARAMETERS

The most serious and always returning problem faced by an aeroelastician in daily practice turns out to be the painstaking merging of the data supplied by the structural engineer and the data supplied by the aerodynamic engineer. In this section the approach which is taken in the current study is highlighted. This approach should be general enough to handle most of the practical problems.

Neglecting the structural damping parameter, the equations relating the structural data and aerodynamic data in the dimensional form can be expressed by the following equation:

$$m_i \ddot{q}_i + m_i \omega_i^2 q = Q_i, \quad (6.31)$$

where both sides have the dimension of a force.  $Q$  is the generalized aerodynamic force defined as:

$$Q_i = \frac{1}{2} \rho_\infty U_\infty^2 \iint_{S_{str}} C_P \phi_{i,str}^T \cdot \mathbf{n} dS_{str}, \quad (6.32)$$

where the subscript *str* means that the data are based on the structural data. The mode shapes  $\phi_i$  are taken to be dimensionless, thus  $q_i$  has the dimension of a length.

In the computation of structural data with e.g. a finite element model, usually the original measures of the structure are employed, whereas in the aerodynamic calculation normalized measures of the mesh are preferred, e.g. by using a unit root chord or a unit semi-span, etc. To harmonize the structural and aerodynamic data one common reference length is used here for both data sets, but this length should be expressed relative to the separate definitions of nondimensionalization. Accordingly, when the root chord is selected as the reference length of the structural data,  $c_{r,s}$ , the aerodynamic data has to use also the root chord, but now expressed as the reference length  $c_{r,a}$ .

Equation (6.31) is nondimensionalized using the following parameters: the aerodynamic dimensionless quantities: length using  $c_{r,a}$ , time using  $c_{r,a}/a_\infty$ , density using  $\rho_\infty$ ; and the structural dimensionless quantities: mass using the reference mass  $m_r$ , frequency using the reference frequency  $\omega_r$ . The resulting equation becomes:

$$\bar{m}_i \ddot{\bar{q}}_i + \frac{M_\infty^2}{\bar{U}^2} \bar{m}_i \bar{\omega}_i^2 \bar{q} = \frac{M_\infty^2}{2\mu} \bar{Q}, \quad (6.33)$$

where the variables with a bar denote dimensionless variables,  $\bar{U} = U_\infty/(\omega_r c_{r,a})$  is the reduced velocity and  $\bar{Q}$  is the dimensionless generalized aerodynamic force defined on the aerodynamic mesh as:

$$\bar{Q}_i = \frac{1}{\bar{c}_{r,a}^2} \iint_{S_{aer}} C_P \phi_{i,aer}^T \cdot \mathbf{n} dS_{aer}. \quad (6.34)$$

The mode shapes  $\phi_i$  and the surface area defined on the aerodynamic mesh are simply:

$$\phi_{i,aer} = \frac{c_{r,a}}{c_{r,s}} \phi_{i,str}, \quad (6.35)$$

$$S_{aer} = \frac{c_{r,a}^2}{c_{r,s}^2} S_{str}, \quad (6.36)$$

and the mass ratio  $\mu$  is defined as:

$$\mu = \frac{m_r}{\rho_\infty c_{r,s}^3}. \quad (6.37)$$

**The aeroelastic equation has now, like the two-dimensional version, two aero-structural coupling parameters, namely the reduced velocity  $\bar{U}$  and the mass ratio  $\mu$ .** For each problem a proper scaling factor is calculated for the reduced velocity and mass ratio according to the present definition. An example will be given in the next chapter for the AGARD standard test case of the 445.6 wing.

### 6.5.2 RESULTS OF CAS METHOD FOR THREE-DIMENSIONAL FLOW

The well-known AGARD 445.6 wing is considered, a three-dimensional AGARD standard aeroelastic configuration which is described in [179]. The configuration

for dynamic response, i.e. the weakened model number 3, was selected. The mesh applied for this calculation consists of  $121 \times 29 \times 24$  mesh points. First the case for  $M_\infty=0.96$  and  $\mu = 225.820$  is considered. It should be noted that this value of  $\mu$  is only consistent at the experimental flutter point which was obtained at  $V^*=0.3076$ . In the present calculation it is used also for all other speeds.

The data given in [179] are: mass of the model  $m_A=0.12764$  slugs<sup>1</sup>, reference volume  $v_A=4.595$  ft<sup>3</sup>, density  $\rho_\infty=0.000193$  slugs/ft<sup>3</sup>, root chord  $c_{r,s}=1.833$  ft and generalized mass  $m_i=1$  lbf s<sup>2</sup>/in=0.0833 slugs. The speed index is defined in [179] as  $V^* = U_\infty / (\omega_2 b_{r,s} \sqrt{\mu_A})$ , where the mass ratio is defined as  $\mu_A = m_A / (\rho_\infty v_A)$  and  $\omega_2$  is the frequency of the second mode (first torsion mode, see figure 6.33).

To use the present aero-structural coupling parameters, the reduced velocity is defined as  $\bar{U}_A = 2U_\infty / (c_{r,s} \omega_2)$ . The scaling parameters for the reduced velocity and mass ratio are calculated as follows. First define the reference length as  $c_{r,a}=1$  ft. The reference mass is the mass of the wing model  $m_r=0.12764$  slugs. The reduced velocity and the mass ratio for the simulation are calculated as:

$$\bar{U} = \bar{U}_A U_{scal} \quad (6.38)$$

$$\mu = \mu_A \mu_{scal}, \quad (6.39)$$

where the scaling factors are:

$$U_{scal} = \frac{c_{r,s}}{2c_{r,a}} = 0.9165 \quad (6.40)$$

$$\mu_{scal} = \frac{v_A}{c_{r,s}^3} = 0.7461. \quad (6.41)$$

The factor 2 in the denominator of equation (6.40) arises from the reference length being the semi-chord in the definition of speed index according to AGARD [179].

To show the applicability of the present aerodynamic method for large time step simulations a forced vibration case is first considered. The second mode of the 445.6 wing was excited in a sinusoidal motion with a reduced frequency of  $k=0.10$ , based on root semi-chord, and an amplitude of  $0.005c_{r,a}$ . Figure 6.34 shows the generalized aerodynamic forces  $\bar{Q}_1$  and  $\bar{Q}_2$  associated with the first two vibration modes using a small time step (48 steps/period) and a large time step (10 steps/period). No significant differences were found. The CPU time for the small time step simulation was about 120 minutes/period using one processor of the CRAY J90, or 20 minutes/period using a cluster of 4 SUN ULTRA SPARC workstations. The large time step simulation on the CRAY and the SUN takes about 60 and 12.5 minutes/period, respectively.

Next the validation of the structural extrapolation method is presented. For this purpose only the first two vibration modes were used, namely the first bending and first torsion mode. These modes are primarily involved in the flutter mechanism, see Lee-Rausch and Batina [101]. The simulations proceeded by first calculating the steady flow around the mean condition. Subsequently all modes involved in the simulation were excited by giving an initial speed of  $\dot{q}_i=0.01$ .

---

<sup>1</sup> 1 slug=1 lbf s<sup>2</sup>/ft=32.2 lbm

To cross-check the methods, simulations with the simple aerodynamic extrapolation method of Edwards et al. [52] and the present structural extrapolation method were made using a small time step (48 steps/period of the second mode). The results are presented in figure 6.35. Both methods showed an excellent agreement.

For the large time step simulation 8 steps/period of the second mode were applied. The comparison of the results for the simple aerodynamic extrapolation method of [52] is shown in figure 6.36. As already noted for the two-dimensional case this method is not adequate for large time step simulations. The results in figure 6.37, obtained using the current structural extrapolation method at large time steps, show in general a good agreement with those obtained with small time steps. The comparison of the value of the damping decay coefficients is:

method	$\sigma$	CPU (min/simulation)
small $\Delta\tau$	0.0040	40
large $\Delta\tau$ , structural extrapolation	0.0042	25
large $\Delta\tau$ , simple extrapolation [52]	0.0102	25

Finally the present structural extrapolation method is employed for a simulation involving all four vibration modes. The time step is set at 8 steps/period of the highest modes. Three simulations were made at  $V^*=0.253$ ,  $V^*=0.266$  and  $V^*=0.293$  using the same initial condition as in the previous simulations. The time responses of the first two modes are depicted in figure 6.38. The flutter speed index was calculated from the quadratic interpolation of damping data. The comparison with data available from other references is shown in the table below:

Method	$V_F^*$
AESIM (full-potential) [80]	0.303
CFL3D (Euler) [101]	0.256
CFL3D (Navier-Stokes) [101]	0.287
Experiment [179]	0.3076
Present (Euler)	0.279

It should be noted that the results of CFL3D were estimated from [101]. The CPU time for each simulation was about 48 minutes/simulation on a cluster of 6 SUN ULTRA SPARC workstations or about 18 minutes/simulation using 8 processing elements of CRAY T3E.

The comparison of the flutter speed indices at various Mach numbers with the results of Hounjet and Eussen [80], C. Farhat and M. Lesoinne [37] and the experiment of NASA Langley, is shown in figure 6.39. In general a good agreement is obtained between the results of all methods in predicting the transonic dip.

FIGURES

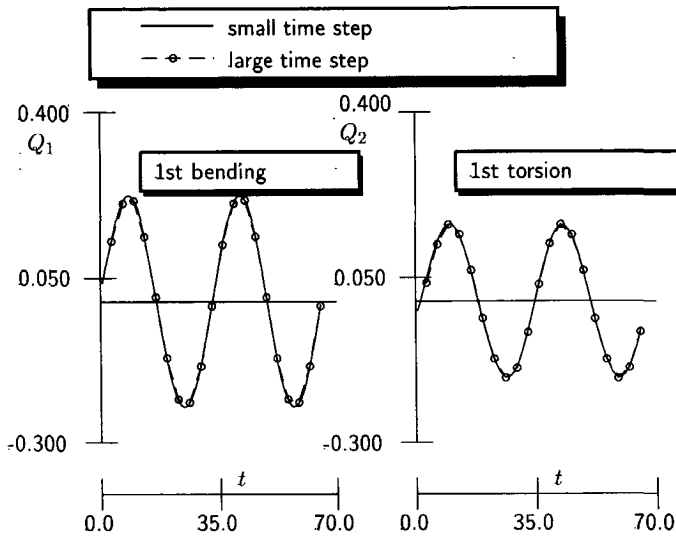


Figure 6.34: Comparison of forced vibration case of 445.6 wing at  $M_\infty=0.96$  between small 48/period and large 10/period time steps runs

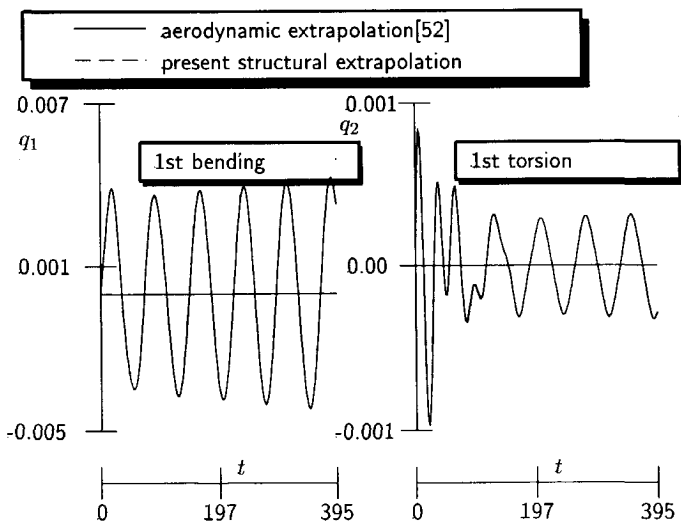


Figure 6.35: Comparison of time responses between the aerodynamic extrapolation method of [52] and the present structural extrapolation method for small 48/period time steps, 445.6 wing at  $M_\infty=0.96$

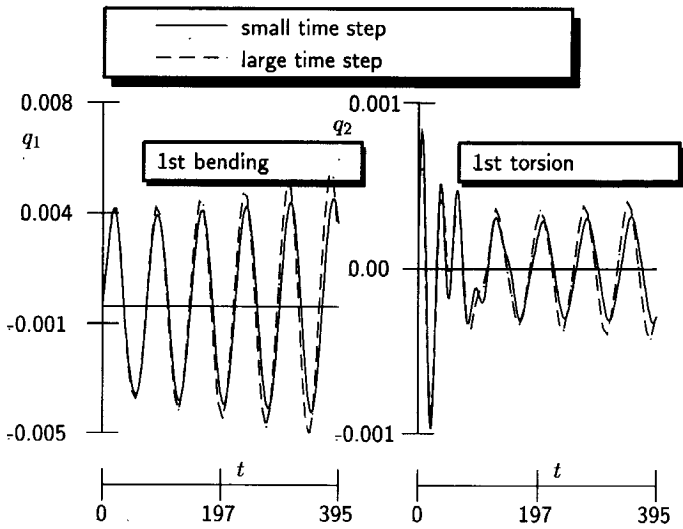


Figure 6.36: Comparison of time responses between small 48/period and large 8/period time steps simulation for aerodynamic extrapolation method of [52], 445.6 wing at  $M_\infty=0.96$

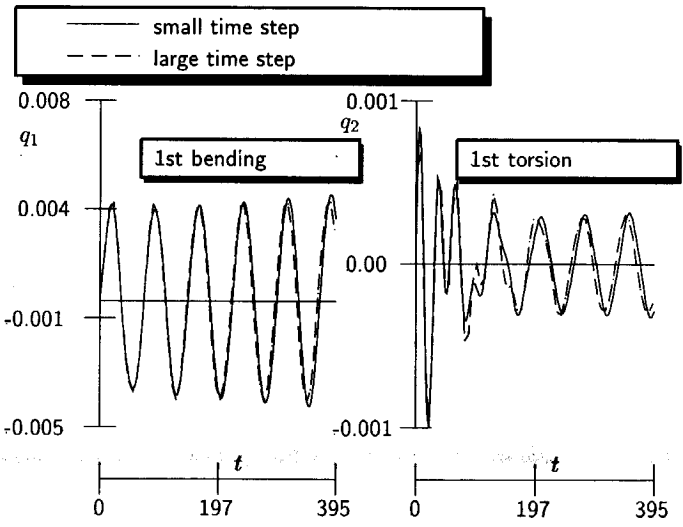


Figure 6.37: Comparison of time responses between small 48/period and large 8/period time steps simulation for the present structural extrapolation method, 445.6 wing at  $M_\infty=0.96$

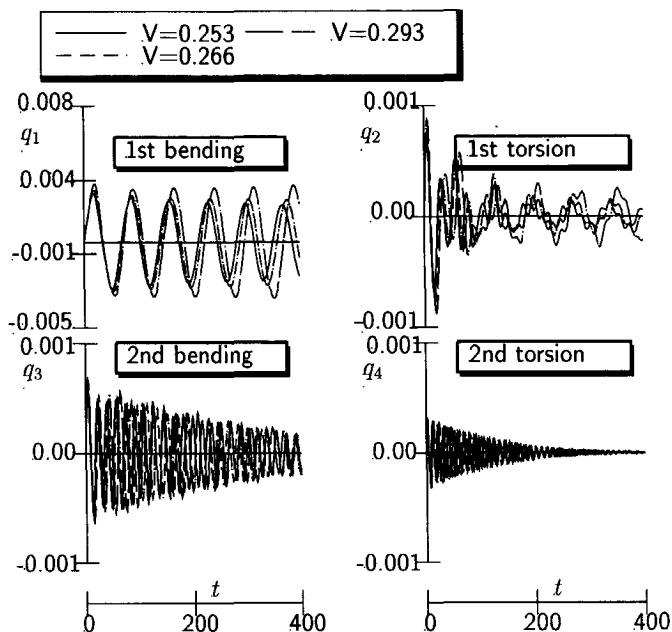


Figure 6.38: Time responses of the first four modes of 445.6 wing at  $M_\infty=0.96$  for three speed indices

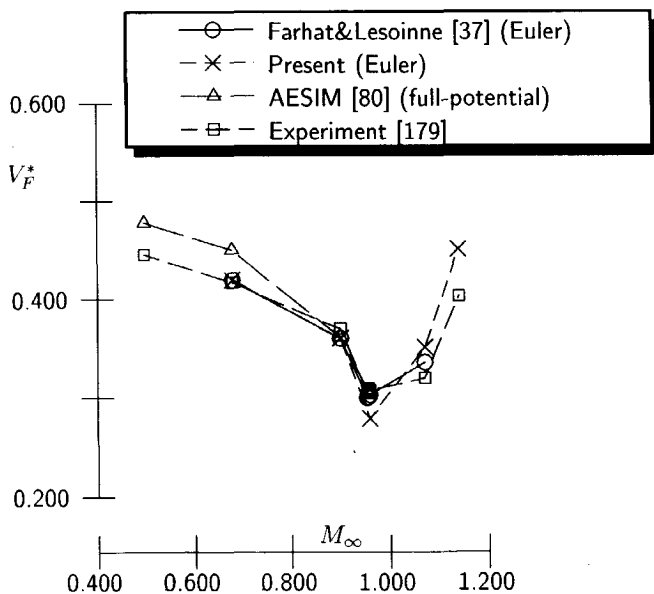


Figure 6.39: Flutter boundaries of AGARD I-wing 445.6

## 6.6 CONCLUSIONS OF THREE-DIMENSIONAL CUA AND CAS METHODS

The extension of the two-dimensional CUA/CAS method to a method for three-dimensional configurations has been carried out. Only the methods which were concluded in chapter 3 to be suitable for three-dimensional configurations have been applied: Roe's FDS for the inviscid fluxes and the spring analogy method for the dynamic mesh deformation.

Attention has been given to retaining an acceptable computing time by applying a parallel computing method based on domain decomposition.

Test cases have been presented with the aim of validating the present parallel computing, flow simulation and aeroelastic simulation methods. The test cases presented in this chapter lead to the following conclusions:

- Most of the parts of the two-dimensional method can be extended straightforwardly for application to three-dimensional configuration straightforwardly. The relaxation and the spring analogy method retain their robustness.
- The scalability of the parallel method is satisfactory. The penalty in convergence due to the explicit treatment of the artificial boundary between sub-domains turned out to be mild up to 64 processors. The scalability of the unsteady flow test case was better than that of the steady flow case.
- The flow simulation results show that the temporal integration performance of the two-dimensional method is retained to a large extent. A time step in the  $\mathcal{O}(10)$  per cycle can be employed for the simulation of forced vibration cases which leads to an acceptable turnaround time for unsteady flow simulation.
- Satisfactory results have also been obtained for a geometrically more complicated wing-body transport type configuration and a wing-body-tail fighter type aircraft.
- The present aero-structural coupling method developed in chapter 5 for two-dimensional configurations has been successfully applied in three-dimensional aeroelastic simulations.
- Aeroelastic simulations can be carried out in an acceptable turnaround time provided that a sufficient number of computers or processors is employed. This is made possible by both the present aero-structural coupling procedure and the parallel computing capability. For the AGARD standard aeroelastic test case, the employment of the present aero-structural coupling procedure reduces the running time to almost a half. Each simulation can be run as fast as 18 minutes using 8 processors of the CRAY T3E.



## CHAPTER 7

# CONCLUSIONS AND PROSPECTS OF CAS FOR APPLICATIONS IN PRACTICE

In the previous chapters opportunities to include higher-level flow modeling (i.e. the Euler and Navier-Stokes equations) in CUA and CAS methods have been investigated, with the aim to make these methods more attractive for practical aeroelastic applications, especially in industry. This last chapter presents a summary of the results of the study, some concluding remarks and recommendations for further research in this field. Detailed conclusions of each part of the study have been given at the end of the corresponding chapter.

A new CUA/CAS method has been developed in which the results of the study have been incorporated. The features and capability of the method can be summarized as follows:

### 1. Governing equations:

- Flow: the Euler/Navier-Stokes equations on deforming mesh.
- Turbulence modeling: Baldwin-Lomax algebraic model and Spalart-Allmaras one-equation model.
- Structure: linearized equation of motions: two-degree-of-freedom airfoil, multiple-degree-of-freedom modal decomposition for three-dimensional configurations.

### 2. Discretization methods:

- Upwind spatial discretization of the inviscid fluxes: van Leer's FVS, AUSM FVS, Roe's FDS, van Leer's/Osher's FV/DS.
- Mesh topologies: mono-block C-mesh for two-dimensional flow; mono-block CH-, HO-, CO-meshes for three-dimensional flow.
- Central spatial discretization of the viscous terms, approximated using thin-layer assumption.
- Implicit temporal integration employing line relaxation schemes in each time step.

- Spring analogy mesh deformation method with implicit predictor.
- Parallel domain decomposition for the solution of the flow equations, Spalart-Allmaras transport equation and mesh deformation scheme, applied using PVM communication library.
- Loose aero-structural coupling method: aerodynamic extrapolation and structural extrapolation.
- Transition matrix method for the aeroelastic equations.

Several new approaches have been introduced: the implicit treatment of the spring analogy mesh deformation method to allow large structural deformation, the treatment of the GCL and the aero-structural coupling methods which allow large time step aeroelastic simulations.

3. The method has been validated using various test cases:

- Two-dimensional cases of steady flow, transonic buffet of a circular arc airfoil, unsteady flow forced vibration, dynamic stall and aeroelastic simulation of Isogai's case A.
- Three-dimensional cases of steady flow, unsteady flow at forced vibration and aeroelastic simulation.

4. In addition, several new cases have been considered:

- Analysis of two-dimensional flow field at transonic buffet to improve the understanding of the flow physics.
- Two-dimensional viscous flow modeling of Isogai's case A aeroelastic simulation at low as well as high angle of attack.
- Buffeting of an NACA 0012 airfoil using Isogai's case A structural data.
- Three-dimensional unsteady transonic flow about wing-body-tail fighter type configuration.

5. The cases considered in this study demonstrate the following characteristics of the present CUA/CAS method:

- **Robustness:** thanks to the application of upwind methods almost no parameter has to be tuned for a wide range of cases. The only important parameter is the underrelaxation factor. This robustness will be of great value to an aeroelastician in applying the CAS method.
  - **Versatility:** a wide variety of applications has been presented which shows the generality of the present approach. For attached flow conditions quantitative agreement has been generally obtained. Concerning flows with significant viscous effects the present method gives correct results, at least in a qualitative sense, which makes the present method a useful tool for studying flow physics.
-

- Reasonable computing time on moderate computer hardware, provided that a number of computers is available for parallel computation of three-dimensional cases. The time step can be determined based on the physics and is not limited by the numerical stability boundary. Typical applications: a two-dimensional aeroelastic simulation requires 15 minutes/simulation in the Euler mode or 45 minutes/simulation in the Navier-Stokes mode on a moderate workstation, while a three-dimensional aeroelastic simulation in the Euler mode requires 48 minutes/simulation on a cluster of 6 workstations or 18 minutes/simulation on a CRAY T3E using 8 processing elements.

These characteristics of the present approach should make application of the CUA/CAS method attractive for the design office.

In the course of the study some possible improvements have been indicated for further development of the present CUA/CAS method:

1. In striving for still increased efficiency, acceleration methods can be applied to improve the convergence of the relaxation scheme. Furthermore, optimizing the use of the mesh can be obtained by adapting the mesh to the solution, see e.g. Hagmeijer [72]. However, this adaptation may require a considerable effort.
2. The frequency content of the time response of an aeroelastic simulation usually changes during the simulation. In the beginning often many frequencies exist after which only the flutter mode, which is usually of low frequency, becomes dominant. In such cases the application of an adaptive time step size can reduce the simulation time by increasing the time step size as soon as high frequency content has been damped out.
3. If the flutter boundary in the asymptotic stability sense is sought, an analysis method which proceeds by identifying a linearized aerodynamic model will be more efficient than the method presented in section 5.4. A preliminary result of such a method has been presented by Hounjet et al. [81], where after one time domain simulation the flutter boundary can already be determined.



## BIBLIOGRAPHY

- [1] I.H. Abbott and A.E. von Doenhoff. *Theory of Wing Sections; Including a Summary of Airfoil Data*. Dover, New York, 1959.
- [2] *Unsteady Aerodynamics*, AGARD Conference Proceedings CP-227, Neuilly-sur-Seine, 1978.
- [3] *Compendium of Unsteady Aerodynamic Measurement*, AGARD Report R-702, Neuilly-sur-Seine, 1982.
- [4] *Test Cases for Inviscid Flow Field Methods*, AGARD Advisory Report AR-211, Neuilly-sur-Seine, 1985.
- [5] *Transonic Unsteady Aerodynamics and Its Aeroelastic Applications*, AGARD Conference Proceedings CP-374, Neuilly-sur-Seine, 1985.
- [6] *Transonic Unsteady Aerodynamics and Aeroelasticity*, AGARD Conference Proceedings CP-507, Neuilly-sur-Seine, 1992.
- [7] *Numerical unsteady aerodynamics and aeroelastic simulation*, AGARD Report R-822, 1998.
- [8] G.D. van Albada, B. van Leer, and W.W. Roberts, Jr. A comparative study of computational methods in cosmic gas dynamics. *Astronomy and Astrophysics*, 108:76-84, 1982.
- [9] E. Albano and W.P. Rodden. A doublet-lattice method for calculating the lift distributions on oscillating surfaces in subsonic flow. *AIAA Journal*, 7(2): 279-285, 1969.
- [10] J.J. Alonso and A. Jameson. A Fully-implicit time-marching aeroelastic solution. AIAA Paper 94-0056, AIAA, 1994.
- [11] J.J. Alonso, L. Martinelli, and A. Jameson. Multigrid Unsteady Navier-Stokes calculations with aeroelastic applications. AIAA Paper 95-0048, AIAA, 1995.
- [12] W.K. Anderson, J.L. Thomas, and C.L. Rumsey. Extension and applications of Flux Vector Splitting to unsteady calculations on dynamic meshes. AIAA Paper 87-1152, AIAA, 1987.

- [13] J.D. Anderson Jr. *Fundamentals of Aerodynamics*. McGraw-Hill, New York, 1991.
  - [14] A. Arnone, M.S. Liou, and A.L. Povinelli. Integration of Navier-Stokes equations using dual time stepping and a multigrid method. *AIAA Journal*, 33(6): 985-990, 1995.
  - [15] Associazione Italiana di Aeronautica ed Astronautica. *Proceedings of 1997 CEAS International Forum on Aeroelasticity and Structural Dynamics*, volume 3, Rome, 1997.
  - [16] E.H. Atzema and J. Huétink. Finite element analysis of forward/backward extrusion using ALE techniques. In S.F. Chen and P.R. Dawson, editors, *Simulation of Materials Processing. Theory, Methods and Applications*, Proceedings of the Fifth International Conference on Numerical Methods in Industrial Forming Process, June 18-21 1995, Ithaca, New York, USA, pages 681-685, Rotterdam, 1995. Balkema.
  - [17] M. L. Baker. CFD based correction for linear aerodynamic methods. In *Numerical Unsteady Aerodynamics and Aeroelastic Simulation*, AGARD Report R-822, pages 8-1~8-12, 1998.
  - [18] B.S. Baldwin and H. Lomax. Thin layer approximation and algebraic model for separated turbulent. AIAA Paper 78-0257, AIAA, 1978.
  - [19] W.F. Ballhaus and J.O. Bridgeman. Unsteady transonic flow calculations for realistic aircraft configurations. In , AGARD Report R-679, pages 12.1-12.13, 1971.
  - [20] R. Barret, M. Berry, T.F. Chan, J. Demmel, J. Donato, J. Dongarra, V. Eijkhout, R. Pozo, C. Romine, and H. van der Vorst. *Templates for the solution of linear system: building blocks for iterative methods*. SIAM, Philadelphia, PA, 1994.
  - [21] R.E. Bartels. Flow and turbulence modeling and computationa of shock buffet onset for conventional and supercritical airfoils. Technical Publication TP 206908, NASA, 1998.
  - [22] T.J. Barth. Analysis of implicit local linearization techniques for upwind and **TVD algorithm**. **AIAA Paper 87-0595, AIAA, 1987.**
  - [23] K.J. Bathe. *Finite Element Procedures in Engineering Analysis*. Prentice-Hall, Englewood Cliffs, 1982.
  - [24] J.T. Batina. Unsteady Euler algorithm with unstructured dynamic mesh for complex-aircraft aeroelastic analysis. AIAA Paper 89-1189, AIAA, 1989.
  - [25] J.T. Batina, D.A. Seidel, S.R. Bland, and R.M. Bennett. Unsteady transonic flow calculations for realistic aircraft configurations. *Journal of Aircraft*, 26 (2):131-139, 1989.
-

- [26] R.M. Beam and R.F. Warming. An implicit factored scheme for the compressible Navier-Stokes equations. *AIAA Journal*, 16:393-402, 1978.
  - [27] O.O. Bendiksen. A new approach to computational aeroelasticity. AIAA Paper 91-0939-CP, AIAA, 1991.
  - [28] O.O. Bendiksen and G.Y. Hwang. Nonlinear flutter calculations for transonic wings. In *Proceedings of 1997 CEAS International Forum on Aeroelasticity and Structural Dynamics*, volume 2, pages 105-114, Rome, 1997. Associazione Italiana di Aeronautica ed Astronautica.
  - [29] O.O. Bendiksen and K.A. Kousen. Transonic flutter analysis using the Euler equations. AIAA Paper 87-0911, AIAA, 1987.
  - [30] R.M. Bennett and J.T. Batina. Application of the CAP-TSD unsteady transonic small disturbance program to wing flutter. In *Proceedings European Forum on Aeroelasticity and Structural Dynamics 1989*, number 89-003 in DGLR Bericht, pages 25-34. DGLR, 1989.
  - [31] R.W. Bennett and R.N. Desmarais. Curve fitting of aeroelastic transient response data with exponential function. Report SP-415, NASA, 1982.
  - [32] R.W. Bennett and J.W. Edwards. An overview of recent developments in computational aeroelasticity. AIAA Paper 98-2421, AIAA, 1998.
  - [33] R.L. Bisplinghoff, H. Ashley, and R.L. Halfman. *Aeroelasticity*. Addison-Wesley, New York, 1955.
  - [34] S.R. Bland. AGARD Three dimensional aeroelastic configurations. AGARD Advisory Report AR-167, AGARD, Neuilly-sur-Seine, 1979.
  - [35] A. Brenneis and A. Eberle. Evaluation of an unsteady implicit Euler code against two and three dimensional standard configuration. In *Transonic Unsteady Aerodynamics and Aeroelasticity*, AGARD Conference Proceedings CP-507, pages 10-1~10-15, Neuilly-sur-Seine, 1992.
  - [36] M. Burt. The impact of computational unsteady aerodynamics in aerospace engineering - past, present and future. Recent Developemnts and Applications in Aeronautical CFD (paper 12), European Forum, 1993.
  - [37] C. Farhat and M. Lesoinne. Fast staggered algorithms for the solution of three-dimensional nonlinear aeroelastic problems. In *Numerical Unsteady Aerodynamics and Aeroelastic Simulation*, AGARD Report R-822, pages 7-1~7-11, 1998.
  - [38] P.H. Cook, M.A. Mc Donald, and M.C.P. Firmin. Aerofoil RAE 2822 Pressure distributions, boundary layer and wake measurements. Advisory Report AR-138, AGARD, Neuilly-sur-Seine, 1979.
-

- [39] F. Coquel and M.S. Liou. Field by field hybrid upwind splitting method. AIAA Paper 93-3302-CP, AIAA, 1993.
  - [40] M. Damodaran. Finite volume computation of unsteady inviscid rotational transonic flows past airfoil in rigid body motion. AIAA Paper 88-0006, AIAA, 1988.
  - [41] S. Davis. NACA64A010 (NASA Ames model). Oscillatory pitching. In *Compendium of Unsteady Aerodynamic Measurement*, AGARD Report R-702, Neuilly-sur-Seine, 1982.
  - [42] S.S. Davis and G.N. Malcolm. Transonic shock-wave/boundary-layer interactions on an oscillating airfoil. *AIAA Journal*, 18(11):1306-1312, 1980.
  - [43] J. Delery and J.G. Marvin. Shock-wave Boundary-layer Interactions. AGARDograph AG-280, AGARD, Neuilly-sur-Seine, 1986.
  - [44] R.G. den Boer and R. Houwink. Analysis of transonic aerodynamic characteristics for a supercritical airfoil oscillating in heave, pitch and with oscillating flap. In *Transonic Unsteady Aerodynamics and its Aeroelastic Applications*, AGARD Conference Proceedings CP-274, pages 4-1~4-15, Neuilly-sur-Seine, 1984.
  - [45] DGLR. *Proceedings of 1989 European Forum on Aeroelasticity and Structural Dynamics*, Aachen, 1989.
  - [46] E. Dick. Multigrid relaxation for steady Euler equations. In J. Mandel et al., editor, *Proceedings of Fourth Copper Mountain Conference on Multigrid Methods*, Copper Mountain, 1989.
  - [47] E.H. Dowell. *Nonlinear Studies on Aeroelasticity*. Sijthoff-Noordhoff, Berlin Heidelberg, 1986.
  - [48] J. Dugunji. *Nonlinear problems of aeroelasticity*. AIAA Publishing, Washington, 1992.
  - [49] A. Eberle. 3D Euler calculations using characteristic flux extrapolation. AIAA Paper 85-0119, AIAA, 1985.
  - [50] J.R. Edwards and S. Chandra. Comparison of eddy viscosity transport turbulence models for three-dimensional, shock separated flowfields. AIAA Paper 94-2275, AIAA, 1994.
  - [51] J.W. Edwards. Transonic shock oscillation and wing flutter calculated with an interactive boundary layer coupling method. In *Simulation of Fluid-Structure Interaction in Aeronautics*, EUROMECH Colloquium 349, Gottingen, 1996.
  - [52] J.W. Edwards, R.W. Bennett, W. Whitlow Jr, and D.A. Seidel. Time marching transonic flutter solutions including angle of attack effects. AIAA Paper 82-0685, AIAA, 1982.
-



- [53] J.W. Edwards and J.B. Malone. Current status of computational methods for transonic unsteady aerodynamics and aeroelastic applications. In *Transonic Unsteady Aerodynamics and Aeroelasticity*, AGARD Conference Proceedings CP-507, pages 1-1~1-24, Neuilly-sur-Seine, 1992.
  - [54] F.E. Ehlers and W.H. Weatherhill. A harmonic analysis method for unsteady transonic flow and its application to the flutter of airfoils. Report CR-3537, NASA, 1982.
  - [55] J.A. Ekaterinaris, G.R. Srinivasan, and W.J. McCroskey. Present capabilities of predicting two-dimensional dynamic stall. In *AGARD 75th Fluid Dynamics Panel Meeting and Symposium on Aerodynamics and Aeroacoustics of Rotorcraft*, AGARD Conference Proceedings CP-552, pages 2-1~2-23, Neuilly-sur-Seine, 1994.
  - [56] B. Engquist and S. Osher. Stable and entropy satisfying approximations for transonic flow calculations. *Mathematics of Computation*, 34:45-75, 1980.
  - [57] B.J.G. Eussen, M.H.L. Hounjet, and R.J. Zwaan. Experiences in Aeroelastic Simulations Practices. NLR Technical Publication TP 96591 L, NLR, 1996.
  - [58] C. Farhat and M. Lesoinne. On the accuracy, stability and performance of the solution of three-dimensional nonlinear transient aeroelastic problems by partitioned procedures. AIAA Paper 96-1388-CP, AIAA, 1996.
  - [59] H. Försting. Challenges and perspective in computational aeroelasticity. In *Proceedings of 1995 CEAS International Forum on Aeroelasticity and Structural Dynamics*, pages 1.1-1.7, London, 1995. Royal Aeronautical Society.
  - [60] B. Franzen, B. Nilsson, and B. Winzell. Experience with unsteady aerodynamics computation for SAAB aircraft. In *Numerical Unsteady Aerodynamics and Aeroelastic Simulation*, AGARD Report R-822, pages 15-1~15-10, 1998.
  - [61] A.L. Gaitonde and S.P. Fiddes. A Three-dimensional moving mesh method for the calculation of unsteady transonic flows. Report, University of Bristol, 1995.
  - [62] C.W. Gear. *Numerical Initial Value Problem in Ordinary Differential Equations*. Series in automatic computation. Prentice-Hall, Englewood Cliffs, 1971.
  - [63] P. Girodroux-Lavigne and J.C. LeBalleur. Time consistent computation of transonic buffet over airfoils. ICAS Paper 88-5.5.2, ICAS, 1988.
  - [64] J.P. Grisval, C. Sauvignet, and Z. Johan. Aeroelasticity calculations using a finite element method. In *Proceedings of 1997 CEAS International Forum on Aeroelasticity and Structural Dynamics*, volume 2, pages 343-349, Rome, 1997. Associazione Italiana di Aeronautica ed Astronautica.
-

- 
- [65] G.P. Guruswamy. Time accurate unsteady aerodynamics and aeroelastic calculations of wings using Euler equations. *AIAA Journal*, 28(3):641-649, 1990.
- [66] G.P. Guruswamy. Vortical flow computations on swept flexible wings using Navier-Stokes equations. *AIAA Journal*, 28(12):2077-2084, 1990.
- [67] G.P. Guruswamy. Vortical flow computations on a flexible blended wing-body configuration. AIAA Paper 91-1013, AIAA, 1991.
- [68] G.P. Guruswamy. Transonic aeroelastic computations on wings using Navier-Stokes equations. In *Transonic Unsteady Aerodynamics and Aeroelasticity*, AGARD Conference Proceedings CP-507, pages 22-1~22-22, Neuilly-sur-Seine, 1992.
- [69] W. Haase, F. Brandsma, and E. Elsholz. *EUROVAL: An European Initiative on Validation of CFD Codes*. Notes on Numerical Fluid Mechanics. Vieweg Verlag, Braunschweig, 1993.
- [70] W. Haase, E. Chaput, E. Elsholz, M. Leschziner, and U.R. Muller, editors. *ECARP - European Computational Aerodynamics Research Project: Validation of CFD Codes and Assessment of Turbulence Models*. Notes on Numerical Fluid Mechanics. Vieweg Verlag, Braunschweig, 1997.
- [71] P. Hagedorn. *Non-Linear Oscillations*. Oxford University Press, Oxford, 1988.
- [72] R. Hagmeijer. *Adaptation of Structured Grids based on Weighted Least Square Formulations*. Dissertation, Technische Universiteit Delft, Delft, 1997.
- [73] H.J. Hassig. An approximate true damping solution of the flutter equation by determinant iteration. *Journal of Aircraft*, 8(11):885-890, 1971.
- [74] R. Heinrich, K. Pahlke, and H. Bleecke. A three dimensional dual-time stepping method for the solution of the unsteady Navier-Stokes equations. In *Proceedings of 1996 Unsteady Aerodynamics Conference*, pages 5.1-5.12, London, 1996. Royal Aeronautical Society.
- [75] M.J. de C. Henshaw, D. McKeirnon, and C. Mairs. Flutter prediction for complex configurations. In *Numerical unsteady aerodynamics and aeroelastic simulation*, AGARD Report R-822, pages 12-1~12-8, 1998.
- [76] C. Hirsch. *Numerical Computation of Internal and External Flow*, volume I&II. John Wiley and Sons, Chichester, 1994.
- [77] M.H.L. Hounjet. A field panel/finite-difference method for potential unsteady transonic flow. *AIAA Journal*, 23(4):537-545, 1985.
- [78] M.H.L. Hounjet. Application of diverging motions to calculate loads for oscillating motions. *AIAA Journal*, 24(10):1723-1725, 1986.
-

- [79] M.H.L. Hounjet. FTRAN3S and FTRAN3: Methods to calculate steady and time linearized unsteady transonic flows about wings. Technical Report TR 87020 L, NLR, 1987.
  - [80] M.H.L. Hounjet and B.J.G. Eussen. Outline and application of the NLR aeroelastic simulation method. In *Proceedings of 19th Congress of ICAS*, pages 1418-1441, Anaheim, 1994. ICAS.
  - [81] M.H.L. Hounjet, B.J.G. Eussen, and M. Soijer. Analysis of aeroelastic simulations by fitting time signals. In *Proceedings of 1997 CEAS International Forum on Aeroelasticity and Structural Dynamics*, volume 3, pages 131-141, Rome, 1997. Associazione Italiana di Aeronautica ed Astronautica.
  - [82] M.H.L. Hounjet and J. J. Meijer. Application of time-linearized methods to oscillating wings in transonic flow and flutter. In *AGARD Conference Proceedings CP-374*, pages 11-1~11-16, Neuilly-sur-Seine, 1984.
  - [83] M.H.L. Hounjet and J.J. Meijer. Evaluation of Elastomechanical and Aerodynamic Data Transfer Methods for Non-planar Configurations in Computational Aeroelastic Analysis. In *Proceedings of 1995 CEAS International Forum on Aeroelasticity and Structural Dynamics*, pages 11.1-11.24, Manchester, 1995. Royal Aeronautical Society.
  - [84] M.Y. Hussaini, B. van Leer, and J. Van Rosendale, editors. *Upwind and High-Resolution Schemes*. Berlin, Springer, 1994.
  - [85] H. Ide and V.J. Shankar. Unsteady full potential aeroelastic computations for flexible configurations. AIAA Paper 87-1238, AIAA, 1987.
  - [86] K. Isogai. On the transonic dip mechanism of flutter of a sweptback wing. *AIAA Journal*, 17:793-795, 1979.
  - [87] K. Isogai. Transonic dip mechanism of flutter of sweptback wing : part II. *AIAA Journal*, 19:1240-1242, 1981.
  - [88] K. Isogai. The development of unsteady transonic 3-D full potential code and its aeroelastic applications. In *AGARD Conference Proceedings CP-374*, pages 17-1~17-25, Neuilly-sur-Seine, 1984.
  - [89] K. Isogai. Numerical simulation of shock-stall flutter of an airfoil using the Navier-Stokes equations. *Journal of Fluids and Structures*, 7:595-609, 1993.
  - [90] A. Jameson. Time Dependent Calculations Using Multigrid, with Applications to Unsteady Flows Past Airfoils and Wings. AIAA Paper 91-1596, AIAA, 1991.
  - [91] A. Jameson, W. Schmidt, and E. Turkel. Numerical simulation of the Euler equations by finite volume methods using Runge-Kutta time stepping schemes. AIAA Paper 81-1259, AIAA, 1981.
-

- 
- [92] M.J. Knott. Transonic aeroelastic calculations in both the time and frequency domain. In *Transonic unsteady aerodynamics and aeroelasticity*, AGARD Conference Proceedings CP-507, pages 15.1–15.8, 1992.
- [93] S. Ko and W.J. McCroskey. Computation of unsteady separating flows over an oscillating airfoil. AIAA Paper 95-0312, AIAA, 1995.
- [94] B. Koren. *Multigrid and Defect Correction for the Steady Navier-Stokes Equations Application to Aerodynamics*. Dissertation, Technische Universiteit Delft, Delft, 1989.
- [95] K.A. Kousen and O.O. Bendiksen. Nonlinear aspects of the transonic aeroelastic stability problem. AIAA Paper 88-2306, AIAA, 1988.
- [96] M. Lacabanne and R.J. Zwaan. Technical evaluation report on 1997 Specialist Meeting on Numerical Unsteady and Aeroelastic Simulation. In *Numerical Unsteady Aerodynamics and Aeroelastic Simulation*, AGARD Report R-822, pages T-1~T-6, 1998.
- [97] R. Landon. NACA 0012. Oscillatory and transient pitching. In *Compendium of Unsteady Aerodynamic Measurement*, AGARD Report R-702, Neuilly-sur-Seine, 1982.
- [98] B. Laschka. Zur Theorie der harmonisch schwingenden tragenden Fläche bei Unterschallanströmung. *ZFW Zeitschrift für Flugwissenschaften*, 11:265–265, 1963.
- [99] P.D. Lax. *Hyperbolic systems of conservation laws and the mathematical theory of shock waves*. SIAM Publication, Philadelphia, 1973.
- [100] B.H.K. Lee. Transonic buffet on a supercritical aerofoil. *Aeronautical Journal*, 22(5):143–152, 1990.
- [101] E.M. Lee-Rausch and J.T. Batina. Calculation of AGARD wing 445.6 flutter using Navier-Stokes aerodynamics. AIAA Paper 93-3476-CP, AIAA, 1993.
- [102] E.M. Lee-Rausch and J.T. Batina. Wing flutter boundary prediction using unsteady Euler method. AIAA Paper 93-1422-CP, AIAA, 1993.
- [103] B. van Leer. **Flux vector splitting for the Euler equations**. **ICASE Report 82-30**, ICASE, 1982.
- [104] H.W. Liepmann and A. Roshko. *Elements of Gas Dynamics*. John Wiley and Sons, New York, 1957.
- [105] M.S. Liou. A new flux splitting scheme. *Journal of Computational Physics*, 107:23–39, 1993.
- [106] M. Lesoinne and C. Farhat. A numerical method for solving aeroelastic eigen problems in all flight regimes. AIAA Paper 97-0467, AIAA, 1997.
-

- [107] R.W. MacCormack and A.J. Paulay. Computational efficiency achieved by time splitting of finite difference operator. AIAA Paper 72-154, AIAA, 1972.
  - [108] J.B. McDevitt, L.L. Levy Jr, and G.S. Deiwert. Transonic flow about a thick circular-arc airfoil. *AIAA Journal*, 14:606-613, 1976.
  - [109] J.B. McDevitt and A.F. Okuno. Static and dynamic measurements on a NACA 0012 airfoil in the Ames High Reynold Number facility. Report TP-2485, NASA, 1985.
  - [110] J.J. Meijer. Determination of transonic unsteady aerodynamics loads to predict the aeroelastic stability of fighter aircraft. In *Proceedings of 1997 CEAS International Forum on Aeroelasticity and Structural Dynamics*, volume 2, pages 373-382, Rome, 1997. Associazione Italiana di Aeronautica ed Astronautica.
  - [111] J.J. Meijer, M.H.L. Hounjet, B.J.G. Eussen, and B.B. Prananta. NLR-TUDelft experience in unsteady aerodynamics and aeroelastic simulation applications. In *Numerical Unsteady Aerodynamics and Aeroelastic Simulation*, AGARD Report R-822, pages 11-1~11-21, 1998.
  - [112] L. Meirovitch. *Elements of Vibration Analysis*. Berlin, Springer, 1994.
  - [113] J.H. Morrison. Flux-difference split scheme for turbulent transport equations. AIAA Paper 90-5251, AIAA, 1990.
  - [114] G.D. Mortchelewicz. Applications des equations d'Euler linearisees a la prevision du flottement. In *Numerical Unsteady Aerodynamics and Aeroelastic Simulation*, AGARD Report R-822, pages 5-1~5-7, 1998.
  - [115] K. Nakahashi and G.S. Deiwert. Self-adaptive-grid method with application to airfoil flow. *AIAA Journal*, 25:513-520, 1987.
  - [116] J. Nakamichi. Calculations of unsteady aerodynamics over oscillating wings. In *Proceedings of 1989 European Forum on Aeroelasticity and Structural Dynamics*, pages 123-131, Aachen, 1989. DGLR.
  - [117] J. Nakamichi, H. Keirandish, and Masahiro Fujita. Numerical simulation of viscous unsteady flow around a high speed aircraft. In *Proceedings of 1997 CEAS International Forum on Aeroelasticity and Structural Dynamics*, volume 2, pages 385-392, Rome, 1997. Associazione Italiana di Aeronautica ed Astronautica.
  - [118] D. Neisius. The importance of geometric modelling of elastically oscillating wings in unsteady transonic CFD calculations. In *Proceedings of 1995 CEAS International Forum on Aeroelasticity and Structural Dynamics*, pages 11.1-11.24, Manchester, 1995. Royal Aeronautical Society.
-

- 
- [119] D. Nixon. *Unsteady Transonic Aerodynamics*, volume 120 of *Progress in Astronautics and Aeronautics*. AIAA Publishing, Washington, 1989.
  - [120] J. Nordstrom. Accuracy of the time dependent Navier-Stokes equations using extrapolation procedures at outflow boundaries. AIAA Paper 91-1605, AIAA, 1991.
  - [121] S. Obayashi. Freestream capturing for moving coordinates in three dimensions. *AIAA Journal*, 30:1125-1128, 1992.
  - [122] S. Obayashi, G.P. Guruswamy, and P.M. Goorjian. Streamwise upwind algorithm for computing unsteady transonic flows past moving oscillating wing. *AIAA Journal*, 29:1668-1677, 1991.
  - [123] P.D. Orkwis. Comparison of Newton's and quasi-Newton's method solvers for the Navier-Stokes equations. *AIAA Journal*, 31:832-836, 1993.
  - [124] S. Osher and F. Solomon. Upwind difference schemes for hyperbolic systems of conservation law. *Mathematics of Computation*, 38:339-374, 1982.
  - [125] B. Oskam and J.W. Slooff. Recent advances in computational aerodynamics at NLR. AIAA Paper 98-0138, AIAA, 1998.
  - [126] H. Paillere, J.C. Carette, and H. Deconinck. *Multidimensional upwind and SUPG methods for the solution of the compressible flow equations on unstructured grids*. VKI Lecture Series. Von Kármán Institute, Rhode Saint Genèse, 1994.
  - [127] K.C. Park. An improved stiffly stable method for direct integration of nonlinear structural dynamic equations. *Journal of Applied Mechanics*, 19(5): 464-470, 1975.
  - [128] I. Parpia. Van Leer flux vector splitting in moving coordinates. *AIAA Journal*, 26:113-115, 1988.
  - [129] R. Peyret, H. Viviand, and J.J. Smolderen. Computation of viscous compressible flows based on the Navier-Stokes equations. AGARDograph AG-212, **AGARD, Neuilly-sur-Seine, 1975.**
  - [130] G. Polz. Current European rotorcraft research activities on development of advanced CFD methods for the design of rotor blades (BRITE/EURAM DACRO Project). In *Proceedings of 17th European Rotorcraft Forum*, pages 39.1-39.10, Berlin, 1991.
  - [131] B.B. Prananta. Some works on FTRANC: steady and unsteady time-linearized full potential solver. Memorandum M-655, Aerospace Engineering DUT, Delft, 1991.
-

- [132] B.B. Prananta and M.H.L. Hounjet. Aeroelastic Simulation with Advanced CFD Methods in 2-D and 3-D Transonic Flow. In *Proceedings of 1996 Unsteady Aerodynamics Conference*, pages 7.1–7.14, London, 1996. Royal Aeronautical Society.
  - [133] B.B. Prananta and M.H.L. Hounjet. Large time step aero-structural coupling procedures for aeroelastic simulation. In *Proceedings of 1997 CEAS International Forum on Aeroelasticity and Structural Dynamics*, volume 2, pages 63–71, Rome, 1997. Associazione Italiana di Aeronautica ed Astronautica.
  - [134] B.B. Prananta, M.H.L. Hounjet, and H.W.M. Hoeijmakers. Computational unsteady aerodynamics for aeroelastic applications. In *Proceedings of 21st Congress of ICAS*, ICAS 98-2.6.3, Melbourne, 1998. International Council of the Aeronautical Sciences, AIAA Electronic Publications.
  - [135] B.B. Prananta, M.H.L. Hounjet, and R.J. Zwaan. A Thin-Layer Navier Stokes solver and its applications for aeroelastic analysis of an airfoil in transonic flows. In *Proceedings of 1995 CEAS International Forum on Aeroelasticity and Structural Dynamics*, pages 15.1–15.15, Manchester, 1995. Royal Aeronautical Society.
  - [136] B.B. Prananta, M.H.L. Hounjet, and R.J. Zwaan. Two-dimensional transonic aeroelastic analysis using Thin-Layer Navier-Stokes method. *Journal of Fluids and Structures*, 12:655–676, 1998.
  - [137] T.H. Pulliam. Recent improvements in efficiency, accuracy, and convergence for implicit approximate factorization algorithms. AIAA Paper 85-0360, AIAA, 1985.
  - [138] T.H. Pulliam. Implicit method in CFD. In *Symposium Transonicum*, pages 117–136, 1991.
  - [139] R. Radespiel, C.C. Rossow, and R.C. Swanson. Efficient cell-vertex multigrid scheme for the three-dimensional Navier-Stokes equations. *AIAA Journal*, 28 (8):1464–1472, 1990.
  - [140] S. Raghunathan, R.D. Mitchell, and M.A. Gillan. Transonic shock oscillation on NACA0012 aerofoil. *Shock Waves*, 8:191–202, 1998.
  - [141] R.D. Rausch, J.T. Batina, and H.T.Y. Yang. Three-dimensional time marching aeroelastic analyses using an unstructured-grid Euler method. AIAA Paper 92-2506-CP, AIAA, 1992.
  - [142] A. Rizzi. Numerical implementation of solid body boundary conditions for the Euler equations. *ZAMM*, 58:301–304, 1978.
  - [143] B.A. Robinson, J.T. Batina, and H.T.Y. Yang. Aeroelastic analysis of wings using the Euler equations with a deforming mesh. *AIAA Journal*, 28:781–788, 1991.
-

- [144] W.P. Rodden, J.P. Giesing, and T.P. Kalman. New developments and applications of the subsonic doublet-lattice method for nonplanar configurations. In *Symposium on Unsteady Aerodynamics for Aeroelastic Analyses of Interfering Surfaces*, AGARD Conference Proceedings CP-80, pages 4.1-4.27, 1971.
  - [145] P.L. Roe. Approximate Riemann solver, parameter vector, and difference schemes. *Journal of Computational Physics*, 43:357-372, 1981.
  - [146] K.L. Roger. Aircraft math modeling method for active control design. In *Structural Aspects of Active Controls*, AGARD Conference Proceedings CP-228, pages 4-1~4-11, Neuilly-sur-Seine, 1977.
  - [147] F.W. Roos. Some features of the unsteady pressure field in transonic airfoil buffeting. *Journal of Aircraft*, 17(11):781-788, 1980.
  - [148] R. Roos, B. Bennekens, and R.J. Zwaan. A calculation method for unsteady flow about hamonically oscillating wing-body configurations. AIAA Paper 75-0864, AIAA, 1975.
  - [149] C.C. Rossow. Efficient cell-vertex upwind scheme for the two-dimensional Euler equations. *AIAA Journal*, 32(2):278-284, 1994.
  - [150] Royal Aeronautical Society. *Proceedings of 1995 CEAS International Forum on Aeroelasticity and Structural Dynamics*, London, 1995.
  - [151] C.L. Rumsey and W.K. Anderson. Some numerical and physical aspects of unsteady Navier-Stokes computations over airfoils using dynamic meshes. AIAA Paper 88-0329, AIAA, 1988.
  - [152] C.L. Rumsey, M.D. Sanetrik, R.T. Biedron, N.D. Melson, and E.B. Palette. Efficiency and accuracy of time-accurate turbulent Navier-Stokes computations. AIAA Paper 95-1835, AIAA, 1995.
  - [153] C.L. Rumsey and V.N. Vatsa. A comparison of the predictive capabilities of several turbulence models using upwind and central-difference computer codes. AIAA Paper 93-0192, AIAA, 1993.
  - [154] H. Schippers. TULIPS: A method to calculate transonic potential flow about oscillating airfoils. Report TR-88193, NLR, 1988.
  - [155] V. Schmitt and F. Charpin. Pressure distribution on the ONERA-M6-wing at transonic Mach numbers. In *Experimental Data Base for Computer Program Assesment*, AGARD Advisory Report AR-138, pages B1-1~B1-44, Neuilly-sur-Seine, 1979.
  - [156] H.L. Seegmiller, J.G. Marvin, and L.L. Levy Jr. Steady and unsteady transonic flow. *AIAA Journal*, 16(12):1262-1270, 1978.
  - [157] P.R. Spalart and S.R. Allmaras. A one-equation turbulence model for aerodynamic flows. AIAA Paper 92-0439, AIAA, 1992.
-



- [158] S.P. Spekreijse. *Multigrid Solution of the Steady Euler Equations*. Dissertation, Technische Universiteit Delft, Delft, 1987.
  - [159] E. Stanewsky and D. Basler. Experimental investigation of buffet onset and penetration of a supercritical airfoil at transonic speed. In *Aircraft Dynamic Loads due to Flow Separation*, AGARD Conference Proceedings CP-843, pages 4-1~4-11, Neuilly-sur-Seine, 1990.
  - [160] J.L. Steger and R.F. Warming. Implicit Finite-Difference Simulation of Flow about Arbitrary Two-Dimensional Geometries. *AIAA Journal*, 16(7):679-686, 1978.
  - [161] J.L. Steger and R.F. Warming. Flux Vector Splitting of the inviscid gas-dynamic equations with application to finite-difference methods. *Journal of Computational Physics*, 40:263-393, 1981.
  - [162] R. Struijs, H. Deconinck, P. de Palma, P.L. Roe, and K.G. Powell. Progress on multidimensional upwind Euler solvers for unstructured grids. *AIAA Paper* 91-1550, AIAA, 1991.
  - [163] R.C. Swanson and R. Radespiel. Cell centered and cell vertex multigrid schemes for the Navier-Stokes equations. *AIAA Journal*, 29(5):697-703, 1991.
  - [164] J.L. Thomas, B. van Leer, and R.W. Walters. Implicit flux-split scheme for the Euler equations. *AIAA Paper* 85-1680, AIAA, 1985.
  - [165] P.D. Thomas and C.K. Lombard. Geometric conservation law and its application to flow computations on moving grids. *AIAA Journal*, 17(10):1030-1037, 1979.
  - [166] J.F. Thompson. A general three-dimensional elliptic grid generation system on a composite block-structure. *Computer Methods in Applied Mechanics and Engineering*, 64:377-411, 1987.
  - [167] H. Tijdeman. *Investigations of the Transonic Flow Around Oscillating Airfoils*. Dissertation, Technische Hogeschool Delft, Delft, 1977.
  - [168] H. Tijdeman and R.J. Zwaan. Unsteady aerodynamics for wings with control surfaces. In *Symposium on Unsteady Aerodynamics for Aeroelastic Analyses of Interfering Surfaces*, AGARD Conference Proceedings CP-80, pages 12.1-12.13, 1971.
  - [169] H. Tijdeman et al. Transonic wind-tunnel tests on an oscillating wing with external store. *NLR Technical Report* TR 78106 U, NLR, 1978.
  - [170] K.J. Vanden and D.L. Whitfield. Direct and iterative algorithms for the three-dimensional Euler equations. *AIAA Journal*, 33:851-857, 1995.
  - [171] V. Venkatakrishnan. Newton solution of inviscid and viscous problem. *AIAA Paper* 88-0413, AIAA, 1988.
-

- 
- [172] S. Weeratunga and E. Pramono. Direct coupled aeroelastic analysis through concurrent implicit time integration on a parallel computer. AIAA Paper 94-1550-CP, AIAA, 1994.
- [173] J. Westland and M.H.L. Hounjet. Clebsch variable model for unsteady, inviscid, transonic flow with strong shock waves. AIAA Paper 93-3025, AIAA, 1993.
- [174] D.L. Whitfield and J.M. Janus. Three-dimensional unsteady Euler equations solution using flux vector splitting. AIAA Paper 84-1552, AIAA, 1984.
- [175] Wilcox. *Turbulence Model*. Addison-Wesley, New York, 1990.
- [176] Y.S. Wong, B.H.K. Lee, and H.S. Murty. A time-linearization approach for unsteady transonic flows. In *Transonic unsteady aerodynamics and aeroelasticity*, AGARD Conference Proceedings CP-507, pages 6-1~6-22, 1992.
- [177] M.E. Wood. Results of oscillatory pitch and ramp tests on the NACA0012 blade section. ARA Memo 220, Aircraft Research Associated Limited, 1979.
- [178] J.C. Wu, K.R.V. Kaza, and L.N. Sankar. Technique for the prediction of airfoil flutter characteristics in separated flow. *AIAA Journal*, 26(2):168-177, 1989.
- [179] E.C. Yates Jr. AGARD standard aeroelastic configurations for dynamic response, I-wing 445.6. Report R-765, AGARD, 1988.
- [180] J. Yff and R.J. Zwaan. T-tail aeroelastic analysis for Fokker F.28. In *Symposium of Unsteady Aerodynamics for Aeroelastic Analyses of Interfering Surfaces*, AGARD Conference Proceedings CP-80, pages 10-1~10-14, Neuilly-sur-Seine, 1971.
- [181] S. Yoon and A. Jameson. An LU-SSOR scheme for the Euler and Navier-Stokes equations. AIAA Paper 87-0600, AIAA, 1987.
- [182] X.D. Zhang, J.Y. Trépanier, M. Regio, A. Benmeddour, and R. Camarero. Grid influence on upwind schemes for the Euler and Navier-Stokes equations. *AIAA Journal*, 34(4):717-727, 1996.
- [183] R.J. Zwaan. LANN-wing in pitching oscillation. In *Compendium of Unsteady Aerodynamic Measurement*, AGARD Report R-702, pages 9-1~9-22, Neuilly-sur-Seine, 1982.
- [184] R.J. Zwaan. Verification of calculation method for unsteady airloads in the prediction of transonic flutter. *AIAA Journal*, 22(10):833-839, 1985.
- [185] R.J. Zwaan. Aeroelasticity of aircraft. Lecture Note D-44, Delft University of Technology, 1990.
- [186] R.J. Zwaan. Getting things to work, aeroelastic research in The Netherlands. Scientific Colloquium, dedicated to the 65th birthday of Prof. Dr.-Ing. habil. Hans Försching, DLR Institute of Aeroelasticity, Göttingen, 1996.
-

## APPENDIX A

# REYNOLDS-AVERAGED NAVIER-STOKES EQUATIONS

For a stationary turbulent flow, the Navier-Stokes equations are averaged in time. The set of partial differential equation for the time-averaged Navier-Stokes equations is obtained by defining for example the pressure as the sum of its average value and its fluctuation:

$$\begin{aligned} p(x, y, z, t) &= \bar{p}(x, y, z, t) + p' \\ \bar{p}(x, y, z, t) &= \lim_{T \rightarrow \infty} \frac{1}{T} \int_{-T/2}^{T/2} p(x, y, z, t + \tau) d\tau \\ p' &= p - \bar{p}. \end{aligned} \quad (\text{A.1})$$

In practice a finite value is taken for  $T$  and the time-averaging process is valid if the time scale of the simulated unsteady flow phenomena remains large compared to  $T$ . By definition, the time-average of the fluctuating part is zero,  $\bar{p}' = 0$ . The other flow variables are represented in the same manner. The desired set of equations is obtained by expressing the flow variables in the governing equations in a time-averaged value and its fluctuation and by subsequent time-averaging. The continuity equation becomes

$$\frac{\partial(\bar{\rho} + \rho')}{\partial t} + \frac{\partial(\bar{\rho} + \rho')(\bar{u} + u')}{\partial x} + \frac{\partial(\bar{\rho} + \rho')(\bar{v} + v')}{\partial y} + \frac{\partial(\bar{\rho} + \rho')(\bar{w} + w')}{\partial z} = 0. \quad (\text{A.2})$$

After expanding the multiplication, the whole equation is time-averaged to arrive at:

$$\begin{aligned} \frac{\partial \bar{\rho}}{\partial t} + \frac{\partial \bar{\rho}'}{\partial t} + \frac{\partial \bar{\rho} \bar{u}}{\partial x} + \frac{\partial \bar{\rho} u'}{\partial x} + \frac{\partial \bar{\rho}' \bar{u}}{\partial x} + \frac{\partial \bar{\rho}' u'}{\partial x} + \frac{\partial \bar{\rho} \bar{v}}{\partial y} + \frac{\partial \bar{\rho} v'}{\partial y} + \frac{\partial \bar{\rho}' \bar{v}}{\partial y} + \frac{\partial \bar{\rho}' v'}{\partial y} + \\ \frac{\partial \bar{\rho} \bar{w}}{\partial z} + \frac{\partial \bar{\rho} w'}{\partial z} + \frac{\partial \bar{\rho}' \bar{w}}{\partial z} + \frac{\partial \bar{\rho}' w'}{\partial z} = 0 \end{aligned}$$

With the help of a few relations in the averaging process, such as

$$\bar{\bar{p}} = \bar{p} \quad \bar{\bar{u}} = \bar{\rho} \bar{u} \quad \bar{\bar{\rho} u'} = \bar{\rho} u' = 0,$$

the remaining terms are

$$\frac{\partial \bar{\rho}}{\partial t} + \frac{\partial \bar{\rho} \bar{u}}{\partial x} + \frac{\partial \bar{\rho} \bar{v}}{\partial y} + \frac{\partial \bar{\rho} \bar{w}}{\partial z} + \frac{\partial \bar{\rho}' u'}{\partial x} + \frac{\partial \bar{\rho}' v'}{\partial y} + \frac{\partial \bar{\rho}' w'}{\partial z} = 0.$$

Comparing the last equation with the original continuity equation, new terms have appeared. The last three terms can be eliminated by introducing mass-averaging into velocity components, temperature, and energy according to Favre:

$$\bar{u} = \frac{\bar{\rho}u}{\bar{\rho}}, \quad \bar{v} = \frac{\bar{\rho}v}{\bar{\rho}}, \quad \bar{w} = \frac{\bar{\rho}w}{\bar{\rho}}, \quad \bar{E} = \frac{\bar{\rho}E}{\bar{\rho}}.$$

The pressure and density use the original time-averaging process. The velocity components and energy variables then become  $u = \bar{u} + u''$ , etc. With mass-averaged variables the continuity equation after dropping terms that become zero reads

$$\frac{\partial \bar{\rho}}{\partial t} + \frac{\partial \bar{\rho}\bar{u}}{\partial x} + \frac{\partial \bar{\rho}u''}{\partial x} + \frac{\partial \bar{\rho}'u''}{\partial x} + \frac{\partial \bar{\rho}\bar{v}}{\partial y} + \frac{\partial \bar{\rho}v''}{\partial y} + \frac{\partial \bar{\rho}'v''}{\partial y} + \frac{\partial \bar{\rho}\bar{w}}{\partial z} + \frac{\partial \bar{\rho}w''}{\partial z} + \frac{\partial \bar{\rho}'w''}{\partial z} = 0$$

The third and fourth term can be combined since  $\bar{\rho}u'' + \bar{\rho}'u'' = \bar{\rho}u''$ , which can be evaluated further with the help of the following manipulation:

$$\bar{\rho}u = \overline{\rho(\bar{u} + u'')} = \bar{\rho}\bar{u} + \bar{\rho}'\bar{u} + \bar{\rho}u'',$$

into

$$\bar{\rho}u'' = \bar{\rho}u - \bar{\rho}\bar{u},$$

which is zero according to the definition of a mass-averaged variable. Using this result, the mass-weighted time-averaged continuity equation can be brought into:

$$\frac{\partial \bar{\rho}}{\partial t} + \frac{\partial \bar{\rho}\bar{u}}{\partial x} + \frac{\partial \bar{\rho}\bar{v}}{\partial y} + \frac{\partial \bar{\rho}\bar{w}}{\partial z} = 0. \quad (\text{A.3})$$

This equation is more convenient to work with than the original time averaged one and will be used henceforth.

The time-averaged momentum equations are obtained using the same technique and the same manipulations. The fluctuation of the viscosity coefficient is usually small and therefore assumed negligible. For example, the momentum equation in the  $x$ -direction becomes

$$\frac{\partial \bar{\rho}\bar{u}}{\partial t} + \frac{\partial \bar{\rho}\bar{u}^2}{\partial x} + \frac{\partial \bar{\rho}\bar{u}\bar{v}}{\partial y} + \frac{\partial \bar{\rho}\bar{u}\bar{w}}{\partial z} = -\frac{\partial \bar{p}}{\partial x} + \frac{\partial(\bar{\tau}_{xx} + \tau_{xx}^T)}{\partial x} + \frac{\partial(\bar{\tau}_{xy} + \tau_{xy}^T)}{\partial y} + \frac{\partial(\bar{\tau}_{xz} + \tau_{xz}^T)}{\partial z}. \quad (\text{A.4})$$

The last equation shows that in turbulent flow the stresses like  $\tau_{xx}^T$ ,  $\tau_{xy}^T$  and  $\tau_{xz}^T$  have appeared in addition to the laminar stresses. They are called turbulent stresses. The turbulent stresses in the  $x$ -direction are

$$\begin{aligned} \tau_{xx}^T &= \frac{\mu}{Re} \left( 2 \frac{\partial u''}{\partial x} - \frac{2}{3} \nabla \cdot \mathbf{u}'' \right) - \overline{\rho u'' u''} \\ \tau_{xy}^T &= \frac{\mu}{Re} \left( \frac{\partial v''}{\partial x} + \frac{\partial u''}{\partial y} \right) - \overline{\rho u'' v''} \\ \tau_{xz}^T &= \frac{\mu}{Re} \left( \frac{\partial w''}{\partial x} + \frac{\partial u''}{\partial z} \right) - \overline{\rho u'' w''}. \end{aligned} \quad (\text{A.5})$$

The last terms in all three equations,  $-\overline{\rho u''u''}$ ,  $-\overline{\rho u''v''}$ , and  $-\overline{\rho u''w''}$ , are called the Reynolds stresses. The momentum equation in the other coordinate directions have a similar form.

The energy equation is more complicated since a new variable arises from the definition of total energy:

$$\begin{aligned}\bar{\rho}\tilde{E} &= \overline{\rho\left[e + \frac{1}{2}(u^2 + v^2 + w^2)\right]} \\ &= \bar{\rho}\tilde{e} + \bar{\rho}\tilde{k} + \bar{\rho}k,\end{aligned}\quad (\text{A.6})$$

where  $\tilde{k}$  is the kinetic energy of the mass-averaged mean flow,

$$\tilde{k} = \frac{1}{2}(\bar{u}^2 + \bar{v}^2 + \bar{w}^2), \quad (\text{A.7})$$

and  $k$  is the turbulent kinetic energy per unit mass,

$$\bar{\rho}k = \overline{\rho k''} = \frac{1}{2}\overline{\rho(u''^2 + v''^2 + w''^2)}. \quad (\text{A.8})$$

Thus  $k$  is defined as the Favre-average of the kinetic energy of the turbulent fluctuations. The relation of time-averaged pressure and other variables due to the perfect gas law becomes

$$(\bar{p} + p') = (\gamma - 1)(\bar{\rho} + \rho')(\tilde{e} + e'').$$

After time-averaging the time-averaged pressure is obtained:

$$\begin{aligned}\bar{p} &= (\gamma - 1)\bar{\rho}\tilde{e} + \overline{\rho'\tilde{e}} + \overline{\rho e''} \\ &= (\gamma - 1)\bar{\rho}\tilde{e}.\end{aligned}$$

The energy equation with these definitions becomes:

$$\begin{aligned}\frac{\partial \bar{\rho}\hat{E}}{\partial t} + \frac{\partial \bar{\rho}\hat{E}\tilde{u}}{\partial x} + \frac{\partial \bar{\rho}\hat{E}\tilde{v}}{\partial y} + \frac{\partial \bar{\rho}\hat{E}\tilde{w}}{\partial z} &= -\frac{\partial \bar{p}\tilde{u}}{\partial x} - \frac{\partial \bar{p}\tilde{v}}{\partial y} - \frac{\partial \bar{p}\tilde{w}}{\partial z} + \\ &\quad \frac{\partial(\tilde{u}\tau_{xx}^{L+T} + \tilde{v}\tau_{yx}^{L+T} + \tilde{w}\tau_{zx}^{L+T})}{\partial x} + \\ &\quad \frac{\partial(\tilde{u}\tau_{xy}^{L+T} + \tilde{v}\tau_{yy}^{L+T} + \tilde{w}\tau_{zy}^{L+T})}{\partial y} + \\ &\quad \frac{\partial(\tilde{u}\tau_{xz}^{L+T} + \tilde{v}\tau_{yz}^{L+T} + \tilde{w}\tau_{zz}^{L+T})}{\partial z} + \\ \nabla \cdot \mathbf{q} &= \frac{\partial \overline{\rho h''u''}}{\partial x} + \frac{\partial \overline{\rho h''v''}}{\partial y} + \frac{\partial \overline{\rho h''w''}}{\partial z},\end{aligned}$$

where superscript  $L + T$  means total stresses from the contribution of the averaged mean flow and the turbulent stresses. The total energy without turbulence kinetic energy was denoted by  $\hat{E}$ , thus  $\tilde{E} = \hat{E} - k$ . Similar to the stresses, the influence of

turbulence on the heat flux is shown by the appearance of additional terms in the balance of energy, called the turbulent heat flux:

$$-\frac{\overline{\partial \rho h'' u''}}{\partial x} - \frac{\overline{\partial \rho h'' v''}}{\partial y} - \frac{\overline{\partial \rho h'' w''}}{\partial z}.$$

Due to the appearance of turbulent stresses and turbulent heat fluxes, the set of time-averaged Navier-Stokes equations needs some more relations to form a closed set of equations. The simplest way to handle these terms is by following the concept of eddy viscosity, where the Reynolds stresses are assumed to depend also on the gradient of the mean flow like their laminar counterpart. According to Boussinesq the Reynolds stresses are assumed to be:

$$\begin{aligned} -\overline{\rho u'' u''} &= \tau_{xx}^R = \frac{\mu_E}{\hat{Re}} \left( \frac{4}{3} \frac{\partial \bar{u}}{\partial x} - \frac{2}{3} \frac{\partial \bar{w}}{\partial z} \right) - \frac{2}{3} \bar{\rho} k, \\ -\overline{\rho u'' v''} &= \tau_{xy}^R = \frac{\mu_E}{\hat{Re}} \left( \frac{\partial \bar{v}}{\partial x} + \frac{\partial \bar{u}}{\partial y} \right), \\ -\overline{\rho u'' w''} &= \tau_{xz}^R = \frac{\mu_E}{\hat{Re}} \left( \frac{\partial \bar{w}}{\partial x} + \frac{\partial \bar{u}}{\partial z} \right), \quad \text{etc.} \end{aligned} \quad (\text{A.9})$$

In the above expressions  $\mu_E$  is called turbulent eddy viscosity. In the same manner the heat flux vector is assumed to have a similar form as the laminar heat flux vector:

$$\mathbf{q}^T = -[ \overline{\rho h'' u''}, \overline{\rho h'' v''}, \overline{\rho h'' w''} ]^T = \frac{\gamma \mu_E}{Pr_T} \nabla \bar{e},$$

where the Prandtl number is taken to be constant,  $Pr_T = 0.90$ . Substitution of equation (A.9) into equation (A.5) results in the expression of stresses in the  $x$ -direction with the eddy viscosity concept:

$$\begin{aligned} \tau_{xx}^T &= \frac{\mu}{\hat{Re}} \left( 2 \frac{\partial \bar{u}''}{\partial x} - \frac{2}{3} \nabla \cdot \bar{\mathbf{u}}'' \right) + \frac{\mu_E}{\hat{Re}} \left( 2 \frac{\partial \bar{u}}{\partial x} - \frac{2}{3} \nabla \cdot \bar{\mathbf{u}} \right) - \frac{2}{3} \bar{\rho} k \\ \tau_{xy}^T &= \frac{\mu}{\hat{Re}} \left( \frac{\partial \bar{v}''}{\partial x} + \frac{\partial \bar{u}''}{\partial y} \right) + \frac{\mu_E}{\hat{Re}} \left( \frac{\partial \bar{v}}{\partial x} + \frac{\partial \bar{u}}{\partial y} \right) \\ \tau_{xz}^T &= \frac{\mu}{\hat{Re}} \left( \frac{\partial \bar{w}''}{\partial x} + \frac{\partial \bar{u}''}{\partial z} \right) + \frac{\mu_E}{\hat{Re}} \left( \frac{\partial \bar{w}}{\partial x} + \frac{\partial \bar{u}}{\partial z} \right). \end{aligned} \quad (\text{A.10})$$

A simplification of the turbulent stresses may be obtained by assuming that the gradients of the fluctuating variables are small and also that  $\mu$  is relatively very small compared to  $\mu_E$ . Hence, neglecting the first group will not degrade the accuracy.

In summing up, the Navier-Stokes equations for turbulent flow with eddy viscosity approximation in matrix form become:

$$\frac{\partial Q}{\partial t} + \frac{\partial F_x^I}{\partial x} + \frac{\partial F_y^I}{\partial z} + \frac{\partial F_z^I}{\partial z} = \frac{\partial F_x^V}{\partial x} + \frac{\partial F_y^V}{\partial z} + \frac{\partial F_z^V}{\partial z}, \quad (\text{A.11})$$

where the conservative variables and inviscid fluxes are:

$$Q = \begin{bmatrix} \bar{\rho} \\ \bar{\rho}\tilde{u} \\ \bar{\rho}\tilde{v} \\ \bar{\rho}\tilde{w} \\ \bar{\rho}\tilde{E} \end{bmatrix}, \quad F_x^I = \begin{bmatrix} \bar{\rho}\tilde{u} \\ \bar{\rho}\tilde{u}^2 + \bar{p} + \frac{2}{3}\bar{\rho}k \\ \bar{\rho}\tilde{u}\tilde{v} \\ \bar{\rho}\tilde{u}\tilde{w} \\ (\bar{\rho}\tilde{E} + \bar{p} + \frac{2}{3}\bar{\rho}k)\tilde{u} \end{bmatrix} \quad (\text{A.12})$$

$$F_y^I = \begin{bmatrix} \bar{\rho}\tilde{v} \\ \bar{\rho}\tilde{v}\tilde{u} \\ \bar{\rho}\tilde{v}^2 + \bar{p} + \frac{2}{3}\bar{\rho}k \\ \bar{\rho}\tilde{v}\tilde{w} \\ (\bar{\rho}\tilde{E} + \bar{p} + \frac{2}{3}\bar{\rho}k)\tilde{v} \end{bmatrix}, \quad F_z^I = \begin{bmatrix} \bar{\rho}\tilde{w} \\ \bar{\rho}\tilde{w}\tilde{u} \\ \bar{\rho}\tilde{w}\tilde{v} \\ \bar{\rho}\tilde{w}^2 + \bar{p} + \frac{2}{3}\bar{\rho}k \\ (\bar{\rho}\tilde{E} + \bar{p} + \frac{2}{3}\bar{\rho}k)\tilde{w} \end{bmatrix}. \quad (\text{A.13})$$

The turbulent viscous fluxes are:

$$F_x^V = \begin{bmatrix} 0 \\ \tau_{xx} \\ \tau_{yx} \\ \tau_{zx} \\ \tilde{u}\tau_{xx} + \tilde{v}\tau_{xy} + \tilde{w}\tau_{xz} - q_x \end{bmatrix}, \quad F_y^V = \begin{bmatrix} 0 \\ \tau_{xy} \\ \tau_{yy} \\ \tau_{zy} \\ \tilde{u}\tau_{yx} + \tilde{v}\tau_{yy} + \tilde{w}\tau_{yz} - q_y \end{bmatrix} \quad (\text{A.14})$$

and

$$F_z^V = \begin{bmatrix} 0 \\ \tau_{xz} \\ \tau_{yz} \\ \tau_{zz} \\ \tilde{u}\tau_{zx} + \tilde{v}\tau_{zy} + \tilde{w}\tau_{zz} - q_z \end{bmatrix}. \quad (\text{A.15})$$

The nondimensional stresses are:

$$\begin{aligned} \tau_{xx} &= \frac{\mu_T}{\hat{Re}_\infty} \left( 2 \frac{\partial \tilde{u}}{\partial x} - \frac{2}{3} \nabla \cdot \tilde{\mathbf{u}} \right) & \tau_{xy} = \tau_{yx} &= \frac{\mu_T}{\hat{Re}_\infty} \left( \frac{\partial \tilde{v}}{\partial x} + \frac{\partial \tilde{u}}{\partial y} \right), \\ \tau_{yy} &= \frac{\mu_T}{\hat{Re}_\infty} \left( 2 \frac{\partial \tilde{v}}{\partial y} - \frac{2}{3} \nabla \cdot \tilde{\mathbf{u}} \right) & \tau_{yz} = \tau_{zy} &= \frac{\mu_T}{\hat{Re}_\infty} \left( \frac{\partial \tilde{w}}{\partial y} + \frac{\partial \tilde{v}}{\partial z} \right), \\ \tau_{zz} &= \frac{\mu_T}{\hat{Re}_\infty} \left( 2 \frac{\partial \tilde{w}}{\partial z} - \frac{2}{3} \nabla \cdot \tilde{\mathbf{u}} \right) & \tau_{zx} = \tau_{xz} &= \frac{\mu_T}{\hat{Re}_\infty} \left( \frac{\partial \tilde{u}}{\partial z} + \frac{\partial \tilde{w}}{\partial x} \right), \end{aligned} \quad (\text{A.16})$$

and the heat flux vector is:

$$\mathbf{q} = - \frac{\mu_T}{\hat{Re}_\infty} \frac{\gamma(\mu Pr_T + \mu_E Pr)}{Pr Pr_T(\mu + \mu_E)} \nabla \tilde{e}, \quad (\text{A.17})$$

where  $\mu_T = \mu + \mu_E$ . Usually the turbulent kinetic energy term is included in the pressure. By defining that  $\hat{p} = \bar{p} + 2/3\bar{\rho}k$ , the form of the time-averaged equations returns to the original form of the equations for laminar flow with the coefficient of viscosity replaced by its total (laminar plus turbulent) value.

If the turbulent coefficient of eddy viscosity is known, these equations completely define the turbulent flow in terms of time-averaged and mass-weighted time-averaged flow variables. The turbulent coefficient of eddy viscosity is obtained from a turbulence modeling.





## APPENDIX B

# EIGENVALUES AND EIGENVECTORS OF EULER EQUATIONS

The eigenvalues and eigenvectors of the system of Euler equations are needed when Roe's approximate Riemann Solver is applied to discretize the inviscid flux terms. They are also needed to determine the boundary condition. In this appendix their derivation is presented to show the possible choices which can be made, for the sake of completeness and for future use elsewhere.

Consider first the Euler equations in a Cartesian coordinate system, written in conservation form:

$$\frac{\partial Q}{\partial t} + A_x^I \frac{\partial Q}{\partial x} + A_y^I \frac{\partial Q}{\partial y} + A_z^I \frac{\partial Q}{\partial z} = 0 \quad (\text{B.1})$$

which quasi-linear form reads:

$$\frac{\partial Q}{\partial t} + A_x^I \frac{\partial Q}{\partial x} + A_y^I \frac{\partial Q}{\partial y} + A_z^I \frac{\partial Q}{\partial z} = 0, \quad (\text{B.2})$$

where  $Q = [Q_1, Q_2, Q_3, Q_4, Q_5]^T = [\rho, \rho u, \rho v, \rho w, \rho E]^T$  is the vector of conservative variables,  $A_x^I, A_y^I, A_z^I$  are the Jacobian matrices. In the so-called primitive variables  $q = [q_1, q_2, q_3, q_4, q_5]^T = [\rho, u, v, w, p]^T$ , equation (B.1) reads:

$$\frac{\partial q}{\partial t} + a_x^I \frac{\partial q}{\partial x} + a_y^I \frac{\partial q}{\partial y} + a_z^I \frac{\partial q}{\partial z} = 0, \quad (\text{B.3})$$

where the flux Jacobian of the Euler equations, written in the conservative and primitive variables, are connected by a *similarity transformation*, e.g. in  $x$ -direction:

$$a_x^I = M^{-1} A_x^I M, \quad (\text{B.4})$$

with  $M = \partial Q / \partial q$ .  $M$  can be easily calculated by writing the conservative variables as functions of primitive variables,

$$M = \frac{\partial}{\partial q} \begin{bmatrix} \rho \\ \rho u \\ \rho v \\ \rho w \\ p/\bar{\gamma} + \rho k \end{bmatrix} = \begin{bmatrix} 1 & 0 & 0 & 0 & 0 \\ u & \rho & 0 & 0 & 0 \\ v & 0 & \rho & 0 & 0 \\ w & 0 & 0 & \rho & 0 \\ k & \rho u & \rho v & \rho w & 1/\bar{\gamma} \end{bmatrix},$$

where  $k$  is the kinetic energy per unit mass,  $\frac{1}{2}(u^2 + v^2 + w^2)$ , and  $\bar{\gamma} = \gamma - 1$ . In the same way  $M^{-1} = \partial q / \partial Q$  is obtained as:

$$M^{-1} = \frac{\partial}{\partial Q} \begin{bmatrix} Q_1 \\ Q_2/Q_1 \\ Q_3/Q_1 \\ Q_4/Q_1 \\ \bar{\gamma}[Q_5 - \frac{1}{2}(Q_2^2 + Q_3^2)/Q_1] \end{bmatrix} = \begin{bmatrix} 1 & 0 & 0 & 0 & 0 \\ -u/\rho & 1/\rho & 0 & 0 & 0 \\ -v/\rho & 0 & 1/\rho & 0 & 0 \\ -w/\rho & 0 & 0 & 1/\rho & 0 \\ \bar{\gamma}k & -\bar{\gamma}u & -\bar{\gamma}v & -\bar{\gamma}w & \bar{\gamma} \end{bmatrix},$$

Since  $a^I$  and  $A^I$  are *similar* according to the relation given in equation (B.4), they share the same eigenvalues. The eigenvectors of  $a^I$  and  $A^I$  diagonalize  $a^I$  and  $A^I$  into the same diagonal matrix  $\Lambda$ , which contains the eigenvalues at its diagonal. For example, in  $x$ -direction it follows:

$$\Lambda_x = l_x a_x^I r_x = L_x A_x^I R_x,$$

where the left and right eigenvectors are normalized in such a way that  $R_x L_x = r_x l_x = I$ . Using equation (B.4) one obtains:

$$\Lambda_x = l_x M^{-1} A_x^I M r_x = L_x A_x^I R_x,$$

which gives the relations between the eigenvectors in the primitive and conservative variables as:

$$L_x = l_x M^{-1} \quad \text{and} \quad R_x = M r_x. \quad (\text{B.5})$$

In deriving the eigenvalues and eigenvectors of the Euler equations, it is easier to work with the primitive variables rather than the conservative ones, because in this form many entries in the Jacobian matrix are zero. The flux Jacobian of the Euler equations in the primitive variables is, e.g. in  $x$ -direction:

$$a_x^I = \begin{bmatrix} u & \rho & 0 & 0 & 0 \\ 0 & u & 0 & 0 & 1/\rho \\ 0 & 0 & u & 0 & 0 \\ 0 & 0 & 0 & u & 0 \\ 0 & \rho a^2 & 0 & 0 & u \end{bmatrix}.$$

In a curvilinear coordinate system the flux normal to the cell surface is treated as in the one-dimensional case; for example in the  $\xi$ -direction:  $\hat{F}_\xi^I = [Q, F_x^I, F_y^I, F_z^I]^T \cdot [\hat{\xi}_t, \hat{\xi}_x, \hat{\xi}_y, \hat{\xi}_z]^T$ . The flux Jacobian of the transformed equations in the conservative and primitive variables become, respectively:

$$\begin{aligned} \hat{A}_\xi^I &= \hat{\xi}_t I + \hat{\xi}_x A_x^I + \hat{\xi}_y A_y^I + \hat{\xi}_z A_z^I, \\ \hat{a}_\xi^I &= \hat{\xi}_t I + \hat{\xi}_x a_x^I + \hat{\xi}_y a_y^I + \hat{\xi}_z a_z^I, \end{aligned}$$

where  $I$  is an identity matrix of  $(5 \times 5)$ .

The characteristic equation for the flux Jacobian of the Euler equations in primitive variables is:

$$|\lambda I - \hat{c}| = \begin{vmatrix} \hat{U} - \lambda & \rho \hat{\xi}_x & \rho \hat{\xi}_y & \rho \hat{\xi}_z & 0 \\ 0 & \hat{U} - \lambda & 0 & 0 & \hat{\xi}_x / \rho \\ 0 & 0 & \hat{U} - \lambda & 0 & \hat{\xi}_y / \rho \\ 0 & 0 & 0 & \hat{U} - \lambda & \hat{\xi}_z / \rho \\ 0 & \rho a^2 \hat{\xi}_x & \rho a^2 \hat{\xi}_y & \rho a^2 \hat{\xi}_z & \hat{U} - \lambda \end{vmatrix} = 0, \quad (\text{B.6})$$

where  $\hat{U} = \hat{\xi}_t + \hat{\xi}_x u + \hat{\xi}_y v + \hat{\xi}_z w$  is the contravariant velocity. The determinant is obtained by first expanding equation (B.6) using the first column, followed by the expansion using the first row of the reduced matrix:

$$(\hat{U} - \lambda) \left[ (\hat{U} - \lambda) \begin{vmatrix} \hat{U} - \lambda & 0 & \hat{\xi}_y / \rho \\ 0 & \hat{U} - \lambda & \hat{\xi}_z / \rho \\ \rho a^2 \hat{\xi}_y & \rho a^2 \hat{\xi}_z & \hat{U} - \lambda \end{vmatrix} - \hat{\xi}_x / \rho \begin{vmatrix} 0 & \hat{U} - \lambda & 0 \\ 0 & 0 & \hat{U} - \lambda \\ \rho a^2 \hat{\xi}_x & \rho a^2 \hat{\xi}_y & \rho a^2 \hat{\xi}_z \end{vmatrix} \right] = 0.$$

Finally the first row of the reduced matrices is used for expansion to obtain:

$$(\hat{U} - \lambda)^3 [(\hat{U} - \lambda)^2 - a^2(\hat{\xi}_x^2 + \hat{\xi}_y^2 + \hat{\xi}_z^2)] = 0, \quad (\text{B.7})$$

which can be solved easily for the eigenvalues:

$$\begin{aligned} \lambda_1, \lambda_2, \lambda_3 &= \hat{U} \\ \lambda_4 &= \hat{U} + a \sqrt{\hat{\xi}_x^2 + \hat{\xi}_y^2 + \hat{\xi}_z^2} \\ \lambda_5 &= \hat{U} - a \sqrt{\hat{\xi}_x^2 + \hat{\xi}_y^2 + \hat{\xi}_z^2}. \end{aligned} \quad (\text{B.8})$$

The left and right eigenvectors can be calculated from the relation (B.5), e.g. in  $\xi$ -direction:

$$l^j \hat{A}_\xi^I = \lambda_j l^j \quad \text{and} \quad \hat{A}_\xi^I r^j = \lambda_j r^j,$$

where  $l^j$  is the  $j^{\text{th}}$  line vector and  $r^j$  is the  $j^{\text{th}}$  column vector associated with the  $j^{\text{th}}$  eigenvalue of  $\hat{A}_\xi^I$ . The equation for the left eigenvector reads:

$$[l_1, l_2, l_3, l_4, l_5]^j \begin{bmatrix} \hat{U} & \rho \hat{\xi}_x & \rho \hat{\xi}_y & \rho \hat{\xi}_z & 0 \\ 0 & \hat{U} & 0 & 0 & \hat{\xi}_x / \rho \\ 0 & 0 & \hat{U} & 0 & \hat{\xi}_y / \rho \\ 0 & 0 & 0 & \hat{U} & \hat{\xi}_z / \rho \\ 0 & \rho a^2 \hat{\xi}_x & \rho a^2 \hat{\xi}_y & \rho a^2 \hat{\xi}_z & \hat{U} \end{bmatrix} = \lambda_j [l_1, l_2, l_3, l_4, l_5]^j,$$

or after reducing the left hand side:

$$\begin{aligned} l_1 \hat{U} &= \lambda_j l_1 \\ l_1 \rho \hat{\xi}_x + l_2 \hat{U} + l_5 \rho a^2 \hat{\xi}_x &= \lambda_j l_2 \\ l_1 \rho \hat{\xi}_y + l_3 \hat{U} + l_5 \rho a^2 \hat{\xi}_y &= \lambda_j l_3 \\ l_1 \rho \hat{\xi}_z + l_4 \hat{U} + l_5 \rho a^2 \hat{\xi}_z &= \lambda_j l_4 \\ l_2 \hat{\xi}_x / \rho + l_3 \hat{\xi}_y / \rho + l_4 \hat{\xi}_z / \rho + l_5 \hat{U} &= \lambda_j l_5. \end{aligned}$$

For  $\lambda_{1,2,3} = \hat{U}$  one obtains:  $l_1$  is arbitrary, thus define  $l_1 = \alpha_1^{(1,2,3)}$ . The remaining equations are:

$$l_1 + a^2 l_5 = 0$$

$$l_2 \hat{\xi}_x / \rho + l_3 \hat{\xi}_y / \rho + l_4 \hat{\xi}_z / \rho = 0,$$

which can be satisfied by taking  $l_5 = -\alpha_1^{(1,2,3)}/a^2$  and  $[l_2, l_3, l_4]^T = [\tilde{\kappa}_x^{(1,2,3)}, \tilde{\kappa}_y^{(1,2,3)}, \tilde{\kappa}_z^{(1,2,3)}]^T$  in which  $\tilde{\kappa} \cdot \nabla \hat{\xi} = 0$ . For  $\lambda_{4,5} = \hat{U} \pm a|\nabla \hat{\xi}|$  one obtains that  $l_1 = 0$ , leaving:

$$l_5 \rho a^2 \tilde{\xi}_x = \pm l_2 a$$

$$l_5 \rho a^2 \tilde{\xi}_y = \pm l_3 a$$

$$l_5 \rho a^2 \tilde{\xi}_z = \pm l_4 a$$

$$l_2 \tilde{\xi}_x / \rho + l_3 \tilde{\xi}_y / \rho + l_4 \tilde{\xi}_z / \rho = \pm l_5 a,$$

which is satisfied by an arbitrary  $l_5 = \alpha_2$ . Note that  $\nabla \tilde{\xi} = \nabla \hat{\xi} / |\nabla \hat{\xi}|$ . Summing up, the matrix of the left eigenvectors is:

$$l = \begin{bmatrix} \alpha_1^{(1)} & \tilde{\kappa}_x^{(1)} & \tilde{\kappa}_y^{(1)} & \tilde{\kappa}_z^{(1)} & -\alpha_1^{(1)}/a^2 \\ \alpha_1^{(2)} & \tilde{\kappa}_x^{(2)} & \tilde{\kappa}_y^{(2)} & \tilde{\kappa}_z^{(2)} & -\alpha_1^{(2)}/a^2 \\ \alpha_1^{(3)} & \tilde{\kappa}_x^{(3)} & \tilde{\kappa}_y^{(3)} & \tilde{\kappa}_z^{(3)} & -\alpha_1^{(3)}/a^2 \\ 0 & \alpha_2 \rho a \tilde{\xi}_x & \alpha_2 \rho a \tilde{\xi}_y & \alpha_2 \rho a \tilde{\xi}_z & \alpha_2 \\ 0 & -\alpha_2 \rho a \tilde{\xi}_x & -\alpha_2 \rho a \tilde{\xi}_y & -\alpha_2 \rho a \tilde{\xi}_z & \alpha_2 \end{bmatrix}. \quad (\text{B.9})$$

The matrix form of the equations for the right eigenvectors reads:

$$\begin{bmatrix} \hat{U} & \rho \hat{\xi}_x & \rho \hat{\xi}_y & \rho \hat{\xi}_z & 0 \\ 0 & \hat{U} & 0 & 0 & \hat{\xi}_x / \rho \\ 0 & 0 & \hat{U} & 0 & \hat{\xi}_y / \rho \\ 0 & 0 & 0 & \hat{U} & \hat{\xi}_z / \rho \\ 0 & \rho a^2 \hat{\xi}_x & \rho a^2 \hat{\xi}_y & \rho a^2 \hat{\xi}_z & \hat{U} \end{bmatrix} \begin{bmatrix} r_1 \\ r_2 \\ r_3 \\ r_4 \\ r_5 \end{bmatrix} = \lambda_j \begin{bmatrix} r_1 \\ r_2 \\ r_3 \\ r_4 \\ r_5 \end{bmatrix}$$

or

$$r_1 \hat{U} + r_2 \rho \hat{\xi}_x + r_3 \rho \hat{\xi}_y + r_4 \rho \hat{\xi}_z = \lambda_j r_1$$

$$r_2 \hat{U} + r_5 \hat{\xi}_x / \rho = \lambda_j r_2$$

$$r_3 \hat{U} + r_5 \hat{\xi}_y / \rho = \lambda_j r_3$$

$$r_4 \hat{U} + r_5 \hat{\xi}_z / \rho = \lambda_j r_4$$

$$r_2 \rho a^2 \hat{\xi}_x + r_3 \rho a^2 \hat{\xi}_y + r_4 \rho a^2 \hat{\xi}_z + r_5 \hat{U} = \lambda_j r_5.$$

For  $\lambda_{1,2,3} = \hat{U}$  one obtains:  $r_1$  is arbitrary, thus define  $r_1 = \beta_1^{(1,2,3)}$  and  $r_5 = 0$ . The only equation left is:

$$r_2 \hat{\xi}_x + r_3 \hat{\xi}_y + r_4 \hat{\xi}_z = 0,$$

which can be satisfied by taking  $[r_2, r_3, r_4]^T = [\tilde{\chi}_x^{(1,2,3)}, \tilde{\chi}_y^{(1,2,3)}, \tilde{\chi}_z^{(1,2,3)}]^T$ , in which  $\tilde{\chi} \cdot \nabla \tilde{\xi} = 0$ . For  $\lambda_{4,5} = \tilde{U} \pm a |\nabla \tilde{\xi}|$  the system of equations becomes:

$$\begin{aligned} r_2 \rho \tilde{\xi}_x + r_3 \rho \tilde{\xi}_y + r_4 \rho \tilde{\xi}_z &= \pm r_1 a \\ r_5 \tilde{\xi}_x / \rho &= \pm r_2 a \\ r_5 \tilde{\xi}_y / \rho &= \pm r_3 a \\ r_5 \tilde{\xi}_z / \rho &= \pm r_4 a \\ r_2 \rho a^2 \tilde{\xi}_x + r_3 \rho a^2 \tilde{\xi}_y + r_4 \rho a^2 \tilde{\xi}_z &= \pm r_5 a, \end{aligned}$$

which can be satisfied by an arbitrary value of  $r_1$ , defined as  $r_1 = \beta_2$ , and  $r_5 = r_1 a^2$ . The right eigenvectors can then be written in matrix form as:

$$r = \begin{bmatrix} \beta_1^{(1)} & \beta_1^{(2)} & \beta_1^{(3)} & \beta_2 & \beta_2 \\ \tilde{\chi}_x^{(1)} & \tilde{\chi}_x^{(2)} & \tilde{\chi}_x^{(3)} & \beta_2 a \tilde{\xi}_x / \rho & -\beta_2 a \tilde{\xi}_x / \rho \\ \tilde{\chi}_y^{(1)} & \tilde{\chi}_y^{(2)} & \tilde{\chi}_y^{(3)} & \beta_2 a \tilde{\xi}_y / \rho & -\beta_2 a \tilde{\xi}_y / \rho \\ \tilde{\chi}_z^{(1)} & \tilde{\chi}_z^{(2)} & \tilde{\chi}_z^{(3)} & \beta_2 a \tilde{\xi}_z / \rho & -\beta_2 a \tilde{\xi}_z / \rho \\ 0 & 0 & 0 & \beta_2 a^2 & \beta_2 a^2 \end{bmatrix}. \quad (\text{B.10})$$

It should be noted that the choice of  $\alpha$ 's and  $\beta$ 's is constrained by the normalization  $rl = I$ .

The left and right eigenvectors of the Euler equations in the conservative variables are obtained by transforming the left and right eigenvectors in the primitive variables through equation (B.4). The left eigenvectors in the conservative variables are:

$$\begin{bmatrix} \alpha_1^{(1)} \phi - \tilde{U}^{(1)} / \rho & \tilde{\kappa}_x^{(1)} / \rho + \alpha_1^{(1)} \tilde{\gamma} u & \tilde{\kappa}_y^{(1)} / \rho + \alpha_1^{(1)} \tilde{\gamma} v & \tilde{\kappa}_z^{(1)} / \rho + \alpha_1^{(1)} \tilde{\gamma} w & -\alpha_1^{(1)} \tilde{\gamma} \\ \alpha_1^{(2)} \phi - \tilde{U}^{(2)} / \rho & \tilde{\kappa}_x^{(2)} / \rho + \alpha_1^{(2)} \tilde{\gamma} u & \tilde{\kappa}_y^{(2)} / \rho + \alpha_1^{(2)} \tilde{\gamma} v & \tilde{\kappa}_z^{(2)} / \rho + \alpha_1^{(2)} \tilde{\gamma} w & -\alpha_1^{(2)} \tilde{\gamma} \\ \alpha_1^{(3)} \phi - \tilde{U}^{(3)} / \rho & \tilde{\kappa}_x^{(3)} / \rho + \alpha_1^{(3)} \tilde{\gamma} u & \tilde{\kappa}_y^{(3)} / \rho + \alpha_1^{(3)} \tilde{\gamma} v & \tilde{\kappa}_z^{(3)} / \rho + \alpha_1^{(3)} \tilde{\gamma} w & -\alpha_1^{(3)} \tilde{\gamma} \\ -\alpha_2(a \tilde{U}' + \tilde{\gamma} k) & \alpha_2(a \tilde{\xi}_x - \tilde{\gamma} u) & \alpha_2(a \tilde{\xi}_y - \tilde{\gamma} v) & \alpha_2(a \tilde{\xi}_z - \tilde{\gamma} w) & \alpha_2 \tilde{\gamma} \\ \alpha_2(a \tilde{U}' - \tilde{\gamma} k) & -\alpha_2(a \tilde{\xi}_x + \tilde{\gamma} u) & -\alpha_2(a \tilde{\xi}_y + \tilde{\gamma} v) & -\alpha_2(a \tilde{\xi}_z + \tilde{\gamma} w) & \alpha_2 \tilde{\gamma} \end{bmatrix}, \quad (\text{B.11})$$

where  $\tilde{\gamma} = \bar{\gamma} / a^2$ ,  $\phi = 1 + \bar{\gamma} k / a^2$ ,  $\tilde{U}^{(i)} = \tilde{\nabla} \kappa^{(i)} \cdot [u, v, w]^T$ , and  $\tilde{U}' = \tilde{\nabla} \xi \cdot [u, v, w]^T$  is the velocity normal to the fixed cell face. The right eigenvectors in the conservative variables are:

$$\begin{bmatrix} \beta_1^{(1)} & \beta_1^{(2)} & \beta_1^{(3)} & \beta_2 & \beta_2 \\ \beta_1^{(1)} u + \tilde{\chi}_x^{(1)} \rho & \beta_1^{(2)} u + \tilde{\chi}_x^{(2)} \rho & \beta_1^{(3)} u + \tilde{\chi}_x^{(3)} \rho & \beta_2(u + \tilde{\xi}_x a) & \beta_2(u - \tilde{\xi}_x a) \\ \beta_1^{(1)} v + \tilde{\chi}_y^{(1)} \rho & \beta_1^{(2)} v + \tilde{\chi}_y^{(2)} \rho & \beta_1^{(3)} v + \tilde{\chi}_y^{(3)} \rho & \beta_2(v + \tilde{\xi}_y a) & \beta_2(v - \tilde{\xi}_y a) \\ \beta_1^{(1)} w + \tilde{\chi}_z^{(1)} \rho & \beta_1^{(2)} w + \tilde{\chi}_z^{(2)} \rho & \beta_1^{(3)} w + \tilde{\chi}_z^{(3)} \rho & \beta_2(w + \tilde{\xi}_z a) & \beta_2(w - \tilde{\xi}_z a) \\ \beta_1^{(1)} k + \tilde{U}^{(1)} \rho & \beta_1^{(2)} k + \tilde{U}^{(2)} \rho & \beta_1^{(3)} k + \tilde{U}^{(3)} \rho & \beta_2(H + \tilde{U}' a) & \beta_2(H - \tilde{U}' a) \end{bmatrix}, \quad (\text{B.12})$$

where  $H = k + a^2 / \bar{\gamma}$  is the total enthalpy per unit mass and  $\tilde{U}^{(i)} = \tilde{\nabla} \chi^{(i)} \cdot [u, v, w]^T$ .

From these two matrices of the eigenvectors, the forms presented in the literature can be identified. For example, the form presented by Whitfield and Janus [174] and Pulliam [137], which were generated using the MACSYMA symbolic manipulator, can be obtained by setting:

$$\begin{aligned} \alpha_1^{(1)} &= \tilde{\xi}_x & \alpha_1^{(2)} &= \tilde{\xi}_y & \alpha_1^{(3)} &= \tilde{\xi}_z & \alpha_2 &= 1/(\rho a \sqrt{2}) \\ \beta_1^{(1)} &= \tilde{\xi}_x & \beta_1^{(2)} &= \tilde{\xi}_y & \beta_1^{(3)} &= \tilde{\xi}_z & \beta_2 &= \rho/(a \sqrt{2}) \end{aligned} \quad (\text{B.13})$$

$$\begin{bmatrix} \tilde{\kappa}_x^{(1)} & \tilde{\kappa}_y^{(1)} & \tilde{\kappa}_z^{(1)} \\ \tilde{\kappa}_x^{(2)} & \tilde{\kappa}_y^{(2)} & \tilde{\kappa}_z^{(2)} \\ \tilde{\kappa}_x^{(3)} & \tilde{\kappa}_y^{(3)} & \tilde{\kappa}_z^{(3)} \end{bmatrix} = \begin{bmatrix} \tilde{\chi}_x^{(1)} & \tilde{\chi}_y^{(1)} & \tilde{\chi}_z^{(1)} \\ \tilde{\chi}_x^{(2)} & \tilde{\chi}_y^{(2)} & \tilde{\chi}_z^{(2)} \\ \tilde{\chi}_x^{(3)} & \tilde{\chi}_y^{(3)} & \tilde{\chi}_z^{(3)} \end{bmatrix} = \begin{bmatrix} 0 & \tilde{\xi}_z & -\tilde{\xi}_y \\ -\tilde{\xi}_z & 0 & \tilde{\xi}_x \\ \tilde{\xi}_y & -\tilde{\xi}_x & 0 \end{bmatrix}. \quad (\text{B.14})$$

The forms presented by Morrison [113], which have a very simple form of the right eigenvectors, can be reproduced using:

$$\begin{aligned} \alpha_1^{(1)} &= 1 & \alpha_1^{(2)} &= 0 & \alpha_1^{(3)} &= 0 & \alpha_2 &= 1/(2a^2) \\ \beta_1^{(1)} &= 1 & \beta_1^{(2)} &= 0 & \beta_1^{(3)} &= 0 & \beta_2 &= 1 \end{aligned} \quad (\text{B.15})$$

$$\begin{bmatrix} \tilde{\kappa}_x^{(1)} & \tilde{\kappa}_y^{(1)} & \tilde{\kappa}_z^{(1)} \\ \tilde{\kappa}_x^{(2)} & \tilde{\kappa}_y^{(2)} & \tilde{\kappa}_z^{(2)} \\ \tilde{\kappa}_x^{(3)} & \tilde{\kappa}_y^{(3)} & \tilde{\kappa}_z^{(3)} \end{bmatrix} = \rho \begin{bmatrix} 0 & 0 & 0 \\ \tilde{\eta}'_x & \tilde{\eta}'_y & \tilde{\eta}'_z \\ \tilde{\zeta}'_x & \tilde{\zeta}'_y & \tilde{\zeta}'_z \end{bmatrix} \quad (\text{B.16})$$

$$\begin{bmatrix} \tilde{\chi}_x^{(1)} & \tilde{\chi}_y^{(1)} & \tilde{\chi}_z^{(1)} \\ \tilde{\chi}_x^{(2)} & \tilde{\chi}_y^{(2)} & \tilde{\chi}_z^{(2)} \\ \tilde{\chi}_x^{(3)} & \tilde{\chi}_y^{(3)} & \tilde{\chi}_z^{(3)} \end{bmatrix} = \frac{1}{\rho} \begin{bmatrix} 0 & 0 & 0 \\ \tilde{\eta}'_x & \tilde{\eta}'_y & \tilde{\eta}'_z \\ \tilde{\zeta}'_x & \tilde{\zeta}'_y & \tilde{\zeta}'_z \end{bmatrix}, \quad (\text{B.17})$$

where  $[\tilde{\eta}'_x, \tilde{\eta}'_y, \tilde{\eta}'_z]^T$  and  $[\tilde{\zeta}'_x, \tilde{\zeta}'_y, \tilde{\zeta}'_z]^T$  are unit vectors tangential to the cell face.

The form used in the present work is judiciously chosen to have the same right eigenvectors as those usually presented in accordance with Roe's scheme. For three-dimensional flow, the forms are almost the same as those presented in [137, 174], with slight different values of  $\alpha_2$  and  $\beta_2$ . The right eigenvectors are:

$$\begin{bmatrix} \tilde{\xi}_x & \tilde{\xi}_y & \tilde{\xi}_z & \alpha_2 & \alpha_2 \\ u\tilde{\xi}_x & u\tilde{\xi}_y - \rho\tilde{\xi}_z & u\tilde{\xi}_z + \rho\tilde{\xi}_y & \alpha_2(u + \tilde{\xi}_x a) & \alpha_2(u - \tilde{\xi}_x a) \\ v\tilde{\xi}_x + \rho\tilde{\xi}_z & v\tilde{\xi}_y & v\tilde{\xi}_z - \rho\tilde{\xi}_x & \alpha_2(v + \tilde{\xi}_y a) & \alpha_2(v - \tilde{\xi}_y a) \\ w\tilde{\xi}_x - \rho\tilde{\xi}_y & w\tilde{\xi}_y + \rho\tilde{\xi}_x & w\tilde{\xi}_z & \alpha_2(w + \tilde{\xi}_z a) & \alpha_2(w - \tilde{\xi}_z a) \\ k\tilde{\xi}_x + \rho\bar{U} & k\tilde{\xi}_y + \rho\bar{V} & k\tilde{\xi}_z + \rho\bar{W} & \alpha_2(H + \bar{U}'a) & \alpha_2(H - \bar{U}'a) \end{bmatrix},$$

where  $\alpha_2 = \rho/(2a)$  and  $[U^{(1)}, U^{(2)}, U^{(3)}]$  has been named  $[\bar{U}, \bar{V}, \bar{W}]$ , which using equation (B.14), can be expressed as:

$$\begin{aligned} \bar{U} &= v\tilde{\xi}_z - w\tilde{\xi}_y \\ \bar{V} &= w\tilde{\xi}_x - u\tilde{\xi}_z \\ \bar{W} &= u\tilde{\xi}_y - v\tilde{\xi}_x. \end{aligned}$$

The corresponding left eigenvectors for this set of arbitrary values are:

$$\begin{bmatrix} \tilde{\xi}_x \phi - \bar{U}/\rho & \tilde{\xi}_x u \tilde{\gamma} & \tilde{\xi}_x v \tilde{\gamma} - \tilde{\xi}_z/\rho & \tilde{\xi}_x w \tilde{\gamma} + \tilde{\xi}_y/\rho & -\tilde{\xi}_x \tilde{\gamma} \\ \tilde{\xi}_y \phi - \bar{V}/\rho & \tilde{\xi}_y u \tilde{\gamma} + \tilde{\xi}_z/\rho & \tilde{\xi}_y v \tilde{\gamma} & \tilde{\xi}_y w \tilde{\gamma} - \tilde{\xi}_x/\rho & -\tilde{\xi}_y \tilde{\gamma} \\ \tilde{\xi}_z \phi - \bar{W}/\rho & \tilde{\xi}_z u \tilde{\gamma} - \tilde{\xi}_y/\rho & \tilde{\xi}_z v \tilde{\gamma} + \tilde{\xi}_x/\rho & \tilde{\xi}_z w \tilde{\gamma} & -\tilde{\xi}_z \tilde{\gamma} \\ \beta_2(\bar{\gamma}k - \bar{U}'a) & -\beta_2(u \tilde{\gamma} - \tilde{\xi}_x a) & -\beta_2(v \tilde{\gamma} - \tilde{\xi}_y a) & -\beta_2(w \tilde{\gamma} - \tilde{\xi}_z a) & \beta_2 \tilde{\gamma} \\ \beta_2(\bar{\gamma}k + \bar{U}'a) & -\beta_2(u \tilde{\gamma} + \tilde{\xi}_x a) & -\beta_2(v \tilde{\gamma} + \tilde{\xi}_y a) & -\beta_2(w \tilde{\gamma} + \tilde{\xi}_z a) & \beta_2 \tilde{\gamma} \end{bmatrix},$$

where  $\beta_2 = 1/(\rho a)$ . The characteristic variable corresponding to these sets of eigenvectors can be calculated as  $\delta W = L\delta Q$  or  $\delta W = l\delta q$ . The latter has a much simpler form than the first one and thus it is used here:

$$\begin{aligned} \delta W &= \begin{bmatrix} \tilde{\xi}_x & 0 & \tilde{\xi}_z & -\tilde{\xi}_y & -\tilde{\xi}_x/a^2 \\ \tilde{\xi}_y & -\tilde{\xi}_z & 0 & \tilde{\xi}_x & -\tilde{\xi}_y/a^2 \\ \tilde{\xi}_z & \tilde{\xi}_y & -\tilde{\xi}_x & 0 & -\tilde{\xi}_z/a^2 \\ 0 & \alpha_2 \rho a \tilde{\xi}_x & \alpha_2 \rho a \tilde{\xi}_y & \alpha_2 \rho a \tilde{\xi}_z & \alpha_2 \\ 0 & -\alpha_2 \rho a \tilde{\xi}_x & -\alpha_2 \rho a \tilde{\xi}_y & -\alpha_2 \rho a \tilde{\xi}_z & \alpha_2 \end{bmatrix} \begin{bmatrix} \delta \rho \\ \delta u \\ \delta v \\ \delta w \\ \delta p \end{bmatrix} \\ &= \begin{bmatrix} \tilde{\xi}_x(\delta \rho - p/a^2) + \delta \bar{U} \\ \tilde{\xi}_y(\delta \rho - p/a^2) + \delta \bar{V} \\ \tilde{\xi}_z(\delta \rho - p/a^2) + \delta \bar{W} \\ \alpha_2(\rho a \delta \bar{U}' + \delta p) \\ \alpha_2(-\rho a \delta \bar{U}' + \delta p) \end{bmatrix}. \end{aligned}$$

For two-dimensional flow only  $[x, z]^T$  and  $[\xi, \zeta]^T$  coordinate directions are used. The left eigenvectors of the two-dimensional flow equations can be obtained by simply removing the second column and third row of the left eigenvectors for the three-dimensional flows, i.e. equations (B.9) and (B.11). In the same way the right eigenvectors of the two-dimensional flow equations are obtained by removing the third column and second row of the right eigenvectors for the three-dimensional flows, i.e. equations (B.10) and (B.12).

The form used in the present study gives a very simple expression for the right eigenvectors. The arbitrary values are:

$$\begin{aligned} \alpha_1^{(1)} &= 1 & \alpha_1^{(2)} &= 0 & \alpha_2 &= 1/(2a^2) \\ \beta_1^{(1)} &= 1 & \beta_1^{(2)} &= 0 & \beta_2 &= 1 \end{aligned} \quad (\text{B.18})$$

$$\begin{bmatrix} \tilde{\kappa}_x^{(1)} & \tilde{\kappa}_z^{(1)} \\ \tilde{\kappa}_x^{(2)} & \tilde{\kappa}_z^{(2)} \end{bmatrix} = \rho \begin{bmatrix} 0 & 0 \\ \tilde{\xi}_z & -\tilde{\xi}_x \end{bmatrix} \quad (\text{B.19})$$

$$\begin{bmatrix} \tilde{\chi}_x^{(1)} & \tilde{\chi}_z^{(1)} \\ \tilde{\chi}_x^{(2)} & \tilde{\chi}_z^{(2)} \end{bmatrix} = \frac{1}{\rho} \begin{bmatrix} 0 & 0 \\ \tilde{\xi}_z & -\tilde{\xi}_x \end{bmatrix}. \quad (\text{B.20})$$

The right eigenvectors are:

$$\begin{bmatrix} 1 & 0 & 1 & 1 \\ u & \tilde{\xi}_z & u + a\tilde{\xi}_x & u - a\tilde{\xi}_x \\ w & -\tilde{\xi}_x & w + a\tilde{\xi}_z & w - a\tilde{\xi}_z \\ k & \tilde{W} & H + a\tilde{U}' & H - a\tilde{U}' \end{bmatrix},$$

and the left eigenvectors are:

$$\begin{bmatrix} \phi & \tilde{\gamma}u & \tilde{\gamma}w & -\tilde{\gamma} \\ -\tilde{W} & \tilde{\xi}_z & -\tilde{\xi}_x & 0 \\ \alpha_2(\tilde{\gamma}k - a\tilde{U}') & \alpha_2(-\tilde{\gamma}u + a\tilde{\xi}_x) & \alpha_2(-\tilde{\gamma}w + a\tilde{\xi}_z) & \alpha_2\tilde{\gamma} \\ \alpha_2(\tilde{\gamma}k + a\tilde{U}') & \alpha_2(-\tilde{\gamma}u - a\tilde{\xi}_x) & \alpha_2(-\tilde{\gamma}w - a\tilde{\xi}_z) & \alpha_2\tilde{\gamma} \end{bmatrix},$$

where  $\alpha_2 = 1/(2a^2)$ . The characteristic variables corresponding to these sets of eigenvectors are:

$$\begin{aligned} \delta w &= \begin{bmatrix} 1 & 0 & 0 & -1/a^2 \\ 0 & \rho\tilde{\xi}_z & -\rho\tilde{\xi}_x & 0 \\ 0 & \alpha_2\rho a\tilde{\xi}_x & \alpha_2\rho a\tilde{\xi}_z & \alpha_2 \\ 0 & -\alpha_2\rho a\tilde{\xi}_x & -\alpha_2\rho a\tilde{\xi}_z & \alpha_2 \end{bmatrix} \begin{bmatrix} \delta\rho \\ \delta u \\ \delta w \\ \delta p \end{bmatrix} \\ &= \begin{bmatrix} \delta\rho - \delta p/a^2 \\ \rho\delta\tilde{W} \\ \alpha_2(\rho a\delta\tilde{U}' + \delta p) \\ \alpha_2(-\rho a\delta\tilde{U}' + \delta p) \end{bmatrix}. \end{aligned} \quad (\text{B.21})$$

This set of right eigenvectors, left eigenvectors and characteristic variables is used in the present study to calculate the flux and the flux Jacobian for the Roe's FDS according to equations (3.41) and (3.68).



## APPENDIX C

# TURBULENCE MODELS

After adopting the Bussinesq eddy-viscosity approximation to compute the Reynolds stresses, a turbulence model is required to calculate the turbulent eddy viscosity coefficient. Two types of turbulence model have been applied for the present CUA method, i.e. the Baldwin-Lomax algebraic turbulence model [18] and the Spalart-Allmaras one-equation turbulence model [157]. This appendix presents some descriptions of these turbulence models and discusses the implementation in the current CUA method.

### C.1 BALDWIN-LOMAX ALGEBRAIC MODEL

The Baldwin-Lomax algebraic turbulence model [18] is the most popular algebraic turbulence model. It is an improvement of the Cebeci-Smith model as far as ease of implementation is concerned, since the Baldwin-Lomax does not need the determination of the location of the boundary layer edge like in the Cebeci-Smith model. These algebraic turbulence models are based on Prandtl's mixing length hypothesis. At solid surfaces the Baldwin-Lomax turbulence model has a two-layer eddy viscosity model:

$$\mu_E = \begin{cases} (\mu_E)_{\text{inner}} & \bar{\zeta} \leq \bar{\zeta}_{\text{crossover}} \\ (\mu_E)_{\text{outer}} & \bar{\zeta} > \bar{\zeta}_{\text{crossover}} \end{cases}, \quad (\text{C.1})$$

where  $\bar{\zeta}$  is the normal distance from the wall and  $\bar{\zeta}_{\text{crossover}}$  is the smallest value of  $\bar{\zeta}$  at which values of  $\mu_E$  from the inner and outer models are equal. The normal distance  $\bar{\zeta}$  is implemented in the present study as the distance along the  $\zeta$ -coordinate direction, i.e. in general not perpendicular to the surface. At the wake region only the outer formulation is applied in which the normal distance is measured from the center of the wake.

For the inner region the classical Prandtl formulation, where the coefficient of eddy viscosity is a product of the turbulence length scale  $l$  and the turbulence velocity scale  $v = l|\omega|$ , corrected by Van Driest is used:

$$(\mu_E)_{\text{inner}} = \rho l^2 |\omega|, \quad (\text{C.2})$$

where  $|\omega| = |\nabla \times \mathbf{u}|$  is the magnitude of the vorticity and:

$$l = k\bar{\zeta}(1 - e^{-y^+/A^+}), \quad (\text{C.3})$$

in which  $k=0.41$  is the von Kármán constant; the parameter  $A^+$  is a damping constant and has been calibrated with boundary layer data to be  $A^+=26$ . The variable  $y^+$  is defined as:

$$y^+ = \frac{\sqrt{\rho_w \tau_w} \bar{\zeta}}{\mu_w}, \quad (\text{C.4})$$

where subscript  $w$  represents the solid wall condition and  $\tau_w$  is the wall shear stress. The formulation of the eddy viscosity for the outer region is:

$$(\mu_E)_{\text{outer}} = \rho K C_{CP} F_{\text{WAKE}} F_{\text{KLEB}}, \quad (\text{C.5})$$

where  $K=0.0168$ ,  $C_{CP}=1.60$ .  $F_{\text{WAKE}}$  is the product of the turbulent length scale and the turbulent velocity scale.  $F_{\text{WAKE}}$  is calculated as:

$$F_{\text{WAKE}} = \min(\bar{\zeta}_{\text{MAX}} F_{\text{MAX}}, C_{WK} \bar{\zeta}_{\text{MAX}} u_{\text{DIFF}}^2 F_{\text{MAX}}), \quad (\text{C.6})$$

where  $\bar{\zeta}_{\text{MAX}}$  and  $F_{\text{MAX}}$  are determined from the so-called Baldwin-Lomax  $F$ -function:

$$F(\bar{\zeta}) = \bar{\zeta} |\omega| (1 - e^{-y^+/A^+}). \quad (\text{C.7})$$

After calculating the  $F$ -function in a  $(\xi, \eta)$ -station,  $F_{\text{MAX}}$  is determined as the maximum value of  $F(\bar{\zeta})$  at that station and  $\bar{\zeta}_{\text{MAX}}$  is the  $\bar{\zeta}$ -value at which  $F_{\text{MAX}}$  occurs. To find  $F_{\text{MAX}}$  and  $\bar{\zeta}_{\text{MAX}}$  in a profile at a  $(\xi, \eta)$ -station a parabolic function approximation is applied for every three points starting at the solid surface. Each time the first derivative is checked for the presence of a stationary point, and when that is the case the second derivative is checked to determine whether or not the stationary point is a maximum. Subsequently  $\bar{\zeta}_{\text{MAX}}$  is used to calculate the Klebanoff intermittency factor,  $F_{\text{KLEB}}$ , given by:

$$F_{\text{KLEB}}(\bar{\zeta}) = \left[ 1 + 5.5 \left( \frac{C_{\text{KLEB}} \bar{\zeta}}{\bar{\zeta}_{\text{MAX}}} \right)^6 \right]^{-1}. \quad (\text{C.8})$$

This factor accounts for the intermittent behavior of the flow between laminar and turbulent condition in approaching the outer flow from inside the boundary layer. It should be noted that the exponential function in equation (C.7) is calculated only above solid surfaces, in the wake this quantity is set to zero. The quantity  $u_{\text{DIFF}}$  is the difference between the maximum and minimum of the magnitude of the velocity at an  $(\xi, \eta)$ -station:

$$u_{\text{DIFF}} = |u|_{\text{MAX}} - |u|_{\text{MIN}}, \quad (\text{C.9})$$

where  $|u|_{\text{MIN}} = 0$  on solid surfaces.

The calculation of the eddy viscosity in the wake region is started by first searching the center of the wake at a  $(\xi, \eta)$ -station. The search method is the same as that used to find the  $F_{\text{MAX}}$ , using a parabolic three-point approximation. The normal distance is then calculated with respect to this position. The calculation of  $F_{\text{WAKE}}$  always uses the second formula of equation (C.6).

## C.2 SPALLART-ALLMARAS ONE-EQUATION MODEL

The one-equation turbulence model of Spalart and Allmaras [157] is a method of modeling the turbulent eddy viscosity by using a transport equation with  $\tilde{\nu}$  as the variable. The turbulent eddy viscosity coefficient,  $\mu_E = \rho\nu_E$  can then be calculated from  $\tilde{\nu}$  using:

$$\rho\nu_T = \rho\tilde{\nu}f_{\nu1}, \quad (\text{C.10})$$

where:

$$f_{\nu1} = \frac{\chi^3}{\chi^3 + c_{\nu1}^3} \quad \text{and} \quad \chi = \frac{\tilde{\nu}}{\nu}.$$

The governing equation representing the transport of the turbulent variable  $\tilde{\nu}$  the production and destruction of  $\tilde{\nu}$  is:

$$\frac{\partial \tilde{\nu}}{\partial t} + (\mathbf{u} \cdot \nabla)\tilde{\nu} - M(\tilde{\nu}) - P(\tilde{\nu}) + D(\tilde{\nu}) + T = 0. \quad (\text{C.11})$$

This equation has to be solved simultaneously with the flow equations. The mixed advection diffusion terms are:

$$M(\tilde{\nu}) = c_{b3} \nabla \cdot [(\nu + \tilde{\nu})\nabla]\tilde{\nu} - c_{b4} (\nu + \tilde{\nu})\nabla^2\tilde{\nu}, \quad (\text{C.12})$$

where  $c_{b3} = (1 + c_{b2})/\sigma$  and  $c_{b4} = c_{b2}/\sigma$ , in which  $c_b$ 's and  $\sigma$  are constants of Spalart-Allmaras turbulence model. These constants are specified at the end of this section. The production of eddy viscosity in a free shear flow is related to the deformation tensor  $(\partial u_i/\partial x_j)$ . Spalart and Allmaras [157] suggest to use the vorticity strength as the norm of the deformation tensor. The other norms which can be used include the strain rate and the norm of the whole tensor  $(\sqrt{u_{i,j}u_{i,j}})$ . These norms should return to the usual  $|\partial u/\partial n|$  in a simple shear flow. The production term as suggested in [157] is:

$$P(\tilde{\nu}) = c_{b1}[1 - f_{t2}]\tilde{S}\tilde{\nu}. \quad (\text{C.13})$$

The norm used in the production term should satisfy the log-law behavior close to solid walls. The norm used in the present study is proposed by Edwards and Chandra [50], who claimed that their norm of the deformation tensor is more stable than the original norm of Spalart-Allmaras:

$$\tilde{S} = S\left(\frac{1}{\chi} + f_{\nu1}\right) \quad (\text{C.14})$$

The destruction term is present in the region close to the solid wall due to the blocking effect. The destruction term of the original Spalart-Allmaras model is:

$$D(\tilde{\nu}) = (c_{w1}f_w - \frac{c_{b1}}{\kappa^2}f_{t2})\left(\frac{\tilde{\nu}}{d}\right)^2, \quad (\text{C.15})$$

where:

$$f_w = g \left[ \frac{1 + c_{w3}^6}{g^6 + c_{w3}^6} \right]^{\frac{1}{6}}, \quad g = r + c_{w2}(r^6 - r) \quad \text{and} \quad r = \frac{\tilde{\nu}}{\tilde{S}\kappa^2 d^2}.$$

Following the statement in [157] that the wall-blockage function,  $f_w = f_w(\nu_T, d, S)$ , may be replaced by any function provided that the dimension is correct and behaves properly in the inner layer where the log law holds, Edwards and Chandra [50] also introduced another type of wall-blockage function. They claim that the new wall-blockage function behaves better numerically, which guarantees a positive destruction term. The modification replaces  $r$  in equation (C.15) by:

$$r = \frac{\tanh(\tilde{\nu}/(\kappa^2 d^2 \tilde{S}))}{\tanh(1)} \quad (\text{C.16})$$

The turbulent transition is incorporated in the model using a smooth function to prevent numerical difficulties. The transition function is:

$$T = f_{t1}(\Delta U)^2, \quad (\text{C.17})$$

where

$$f_{t1} = c_{t1} g_t e^{-c_{t2} \frac{\omega_t^2}{\Delta U^2} [d^2 + g_t^2 + d_t^2]}, \quad g_t = \min(0.10, \frac{\Delta U}{\omega_t \Delta x}) \quad \text{and} \quad f_{t2} = c_{t3} e^{-c_{t4} \chi^2}.$$

The transition point has to be defined a priori (e.g. in case a transition strip is present) or defined using other criteria (e.g. the position at which  $\mu_E$  reaches a certain value). This feature is not incorporated in the current study. The constants used in the Spalart-Allmaras turbulence model are:

$$\begin{array}{llll} c_{b1}=0.1355 & \sigma=2/3 & c_{b2}=0.622 & \kappa=0.41 \\ c_{w1} = c_{b1}/\kappa^2 + (1 + c_{b2})/\sigma & c_{w2}=0.30 & c_{w3}=2 & c_{\nu1}=7.1 \\ c_{t1}=1 & c_{t2}=2 & c_{t3}=1.1 & c_{t4}=2 \end{array}$$

Further,  $d$  is the distance to a nearest wall,  $S$  is the magnitude of the vorticity,  $d_t$  is the distance from the field to the position of the transition strip,  $\Delta U$  is the difference between the velocity at the field and at the velocity at the transition strip and  $\omega_t$  the the wall vorticity at the position of the transition strip.

### C.2.1 DISCRETIZATION

Equation (C.11) can be expressed in a conservation form by using the mass conservation equation to arrive at:

$$\frac{\partial \rho \tilde{\nu}}{\partial t} + \nabla \cdot \rho \tilde{\nu} \mathbf{u} + \rho Q = 0, \quad (\text{C.18})$$

where the source terms are:

$$Q(\nu) = -M(\tilde{\nu}) - P(\tilde{\nu}) + D(\tilde{\nu}) + T. \quad (\text{C.19})$$

Subsequently, transforming equation (C.18) from the Cartesian coordinate system to a curvilinear coordinate system results in:

$$\frac{\partial \rho h \tilde{\nu}}{\partial \tau} + \frac{\partial \rho \tilde{\nu} \hat{U}}{\partial \xi} + \frac{\partial \rho \tilde{\nu} \hat{V}}{\partial \eta} + \frac{\partial \rho \tilde{\nu} \hat{W}}{\partial \zeta} + \rho h Q = 0, \quad (\text{C.20})$$

where  $h = \partial(x, y, z)/\partial(\xi, \eta, \zeta)$  is the inverse Jacobian of the transformation and  $[U, V, W]^T$  are the contravariant velocity components. Following Spalart and Allmaras [157] a first-order upwind method is adopted to discretize equation (C.20). Borrowing the idea of Roe [145], a linearized equation,

$$\frac{\partial \rho h \tilde{\nu}}{\partial \tau} + \hat{U} \frac{\partial \rho \tilde{\nu}}{\partial \xi} + \hat{V} \frac{\partial \rho \tilde{\nu}}{\partial \eta} + \hat{W} \frac{\partial \rho \tilde{\nu}}{\partial \zeta} + \rho h Q = 0, \quad (\text{C.21})$$

is solved in which each coordinate direction is considered independently and  $[\hat{U}, \hat{V}, \hat{W}]^T$  is calculated using the Roe averaged variables. The flux at a cell face is calculated in the same manner as by equation (3.29), e.g. in the  $\xi$ -direction:

$$f_{\xi\ i+\frac{1}{2},j,k} = \frac{1}{2}(f_{\xi\ i+1,j,k} + f_{\xi\ i,j,k}) - \frac{1}{2}|\hat{U}|(\rho \tilde{\nu}_{i+1,j,k} - \rho \tilde{\nu}_{i,j,k}), \quad (\text{C.22})$$

where the flux function is  $f_{\xi} = \rho \tilde{\nu} \hat{U}$ . The time derivative is approximated as in the case of the flow equations:

$$\frac{\partial \rho h \tilde{\nu}}{\partial \tau} = h \frac{\partial \rho \tilde{\nu}}{\partial \tau} + \rho \tilde{\nu} \frac{\partial h}{\partial \tau}, \quad (\text{C.23})$$

with  $\partial h/\partial \tau$  calculated from the contravariant mesh speed using the GCL statement, i.e. equation (3.12), and  $\partial \tilde{\nu}/\partial \tau$  is approximated using a backward differencing with the same order of accuracy as that for the flow equations.

Following the approach for the flow equations, the thin-layer approximation is also applied to the advection diffusion terms. The first term in a curvilinear coordinate system is:

$$M_1(\tilde{\nu}) = c_{b3}[\zeta_x \frac{\partial}{\partial \zeta}(\bar{\nu} \zeta_x \frac{\partial \tilde{\nu}}{\partial \zeta}) + \zeta_z \frac{\partial}{\partial \zeta}(\bar{\nu} \zeta_z \frac{\partial \tilde{\nu}}{\partial \zeta})], \quad (\text{C.24})$$

where  $\bar{\nu} = \nu + \tilde{\nu}$  and discretized as:

$$\begin{aligned} M_1(\tilde{\nu}) = & c_{b3}[\bar{\nu}_{i,j,k+\frac{1}{2}}(\zeta_{x\ i,j,k} \zeta_{x\ i,j,k+\frac{1}{2}} + \zeta_{z\ i,j,k} \zeta_{z\ i,j,k+\frac{1}{2}})(\tilde{\nu}_{i,j,k+1} - \tilde{\nu}_{i,j,k}) \\ & - \bar{\nu}_{i,j,k-\frac{1}{2}}(\zeta_{x\ i,j,k} \zeta_{x\ i,j,k-\frac{1}{2}} + \zeta_{z\ i,j,k} \zeta_{z\ i,j,k-\frac{1}{2}})(\tilde{\nu}_{i,j,k} - \tilde{\nu}_{i,j,k-1})]. \end{aligned} \quad (\text{C.25})$$

The second term reads:

$$M_2(\tilde{\nu}) = -c_{b4} \bar{\nu} [\zeta_x \frac{\partial}{\partial \zeta}(\zeta_x \frac{\partial \tilde{\nu}}{\partial \zeta}) + \zeta_z \frac{\partial}{\partial \zeta}(\zeta_z \frac{\partial \tilde{\nu}}{\partial \zeta})], \quad (\text{C.26})$$

which is discretized as:

$$M_2(\bar{\nu}) = -c_{b4}\bar{\nu}_{i,j,k}[(\zeta_{x\ i,j,k}\zeta_{x\ i,j,k+\frac{1}{2}} + \zeta_{z\ i,j,k}\zeta_{z\ i,j,k+\frac{1}{2}})(\bar{\nu}_{i,j,k+1} - \bar{\nu}_{i,j,k}) \\ - (\zeta_{x\ i,j,k}\zeta_{x\ i,j,k-\frac{1}{2}} + \zeta_{z\ i,j,k}\zeta_{z\ i,j,k-\frac{1}{2}})(\bar{\nu}_{i,j,k} - \bar{\nu}_{i,j,k-1})]. \quad (C.27)$$

The production and destruction terms can be calculated at each volume cell directly from equations (C.13) to (C.16).

### C.2.2 GRADIENT OF PRODUCTION AND DESTRUCTION TERMS

The gradient of the production and destruction terms are required for an implicit solution of the Spalart-Allmaras one-equation turbulence model. The gradient of the production term is:

$$\frac{\partial P}{\partial \bar{\nu}} = c_{b1}(\bar{S} + \bar{\nu} \frac{\partial \bar{S}}{\partial \bar{\nu}}), \quad (C.28)$$

where

$$\frac{\partial \bar{S}}{\partial \bar{\nu}} = S(-\frac{1}{\chi^2 \bar{\nu}} + \frac{\partial f_{\nu 1}}{\partial \bar{\nu}}) \\ \frac{\partial f_{\nu 1}}{\partial \bar{\nu}} = \frac{3}{\bar{\nu}}(\frac{\bar{\nu}}{\bar{\nu}})^2[(\frac{\bar{\nu}}{\bar{\nu}})^3 + c_{\nu 1}^3]^{-1} - \frac{3}{\bar{\nu}}(\frac{\bar{\nu}}{\bar{\nu}})^5[(\frac{\bar{\nu}}{\bar{\nu}})^3 + c_{\nu 1}^3]^{-2}.$$

The gradient of the destruction term is:

$$\frac{D(\bar{\nu})}{\partial \bar{\nu}} = -c_{w1}[\frac{f_w}{d^2} + \frac{\bar{\nu}}{d^2} \frac{\partial f_w}{\partial \bar{\nu}}], \quad (C.29)$$

where

$$\frac{\partial f_w}{\partial \bar{\nu}} = \frac{\partial g}{\partial \bar{\nu}} \left\{ \left[ \frac{1 + c_{w3}^6}{g^6 + c_{w3}^6} \right]^{\frac{1}{6}} - \frac{g^6(1 + c_{w3}^6)}{(g^6 + c_{w3}^6)^2} \left[ \frac{1 + c_{w3}^6}{g^6 + c_{w3}^6} \right]^{-\frac{5}{6}} \right\} \\ \frac{\partial g}{\partial \bar{\nu}} = c_{w2}(6r^5 - 1) \frac{\partial r}{\partial \bar{\nu}} \\ \frac{\partial r}{\partial \bar{\nu}} = \frac{1 - \tanh(\bar{\nu}/(\bar{S}k^2d^2))^2}{\tanh(1)} \frac{1}{\kappa^2 d^2} \left[ \frac{1}{\bar{S}} - \frac{\bar{\nu}}{\bar{S}^2} \frac{\partial \bar{S}}{\partial \bar{\nu}} \right] \quad (C.30)$$

## APPENDIX D

# TRANSITION MATRIX METHOD

The transition matrix method is a method to solve a system of first-order ordinary differential equations in the form of:

$$\dot{X} = AX + BU, \quad (\text{D.1})$$

where matrices  $A$  and  $B$  are constant or time invariant,  $X$  is the state vector and  $U$  is the excitation vector. This type of equation is often used in flight mechanics for the analysis of the stability and control of aircraft.

To obtain the solution of equation (D.1) consider first the homogeneous part:

$$\dot{X} = AX. \quad (\text{D.2})$$

Applying the Laplace transform to equation (D.2) results in:

$$s\chi(s) - \chi(0) = A\chi(s),$$

and after reduction:

$$\chi(s) = [sI - A]^{-1}\chi(0). \quad (\text{D.3})$$

The time domain solution is obtained by applying the inverse Laplace transform to equation (D.3):

$$\begin{aligned} X(t) &= \mathcal{L}^{-1}[sI - A]^{-1}X(0) \\ &= e^{At}X(0). \end{aligned} \quad (\text{D.4})$$

The formal definition of the exponential function in equation (D.4) is obtained through the Taylor series expansion:

$$e^{At} = I + At + \frac{A^2t^2}{2} + \frac{A^3t^3}{3!} + \dots \quad (\text{D.5})$$

Consider now the particular solution of equation (D.1). First premultiply equation (D.1) by  $K$ :

$$K\dot{X} - KAX = KBU. \quad (\text{D.6})$$

Choosing  $K$  to be  $e^{-A(t-t_0)}$ , so that  $\dot{K} = -KA$ , then equation (D.6) can be written as:

$$d(KX) = KBU dt, \quad (D.7)$$

from which integration leads to:

$$KX - K_0X_0 = \int_0^t K(\tau)BU(\tau) d\tau. \quad (D.8)$$

Since  $K$  has always an inverse,  $X$  becomes:

$$\begin{aligned} X(t) &= K^{-1}K_0X_0 + \int_0^t K^{-1}K(\tau)BU(\tau) d\tau \\ &= e^{At}X_0 + \int_0^t e^{A(t-\tau)}BU(\tau) d\tau. \end{aligned} \quad (D.9)$$

Since equation (D.1) is linear, a recurrence formula can be developed:

$$X^{n+1} = e^{A\Delta t}X^n + \int_{t^n}^{t^{n+1}} e^{A\Delta t}BU(\tau) d\tau. \quad (D.10)$$

Since  $B$  is constant, equation (D.10) can be written as:

$$X^{n+1} = \Phi X^n + \Theta \bar{Q}, \quad (D.11)$$

where  $\Phi$  is called the transition matrix and  $\Theta \bar{Q}$  is the approximation to the nonhomogeneous part, where a constant value of  $Q$  throughout the time step is assumed.

In case matrix  $A$  is simple the exact form of the transition matrix can be calculated using equation (D.4). When matrix  $A$  is not simple, direct computation using equation (D.5) is preferred. Furthermore, direct computation of the transition matrix is more suited for computational implementation.

For equation (6.30), used in the three-dimensional CAS method, the exact form of the transition matrix can be derived as:

$$\Phi(\Delta\tau) = \frac{e^{-\zeta\omega\Delta\tau}}{\sqrt{1-\zeta^2}} \begin{bmatrix} \sin(\omega_d\Delta\tau + \psi) & \frac{1}{\omega} \sin(\omega_d\Delta\tau) \\ -\omega \sin(\omega_d\Delta\tau) & \sin(\omega_d\Delta\tau + \phi) \end{bmatrix}, \quad (D.12)$$

where

$$\begin{aligned} \psi &= \tan^{-1} \frac{\sqrt{1-\zeta^2}}{\zeta}, \quad \phi = \tan^{-1} \frac{\sqrt{1-\zeta^2}}{-\zeta} \\ \omega_d &= \omega \sqrt{1-\zeta^2} \end{aligned}$$

$\Theta$  can be easily obtained by integrating  $\Phi$ .



# FYSISCH EN NUMERIEKE ASPECTEN VAN AEROELASTISCHE SIMULATIES

## SAMENVATTING IN HET NEDERLANDS

Het proefschrift beschrijft onderzoek naar de ontwikkeling en toepassing van een numerieke aëro-elastische simulatiemethode (CAS=Computational Aero-elastic Simulation method). De behoefte aan zo'n CAS-methode, waarvan het wiskundig model gebaseerd is op de Euler- en Navier-Stokes-vergelijkingen, is recentelijk door de industrie en onderzoeksinstituten bij verschillende gelegenheden naar voren gebracht. Daarbij is een kloof geconstateerd tussen de mogelijkheden van bestaande Euler/N-S-methoden die hoofdzakelijk ontwikkeld zijn door de instituten, en de eisen die door de industrie worden gesteld. Daarom zijn de aspecten inzake de industriële toepassing in het hier beschreven onderzoek van bijzonder belang. Onder deze aspecten vallen: aanvaardbare turnaround-tijd, robuustheid, nauwkeurigheid en redelijke hardware-eisen.

Een fundamentele keuze in het onderzoek was de ontwikkeling van een losse aërodynamisch-elastomechanische koppelingsmethode die een betrekkelijk onafhankelijk gebruik toelaat van gewenste methoden voor de behandeling van de aërodynamische en elastomechanische delen. Als deel van het onderzoek is een methode ontwikkeld voor de numerieke simulatie van tweedimensionale instationaire stromingen (CUA= Computational Unsteady Aerodynamics). Zoals vaak in de vakliteratuur is opgemerkt, vereist de numerieke stabiliteit in aëro-elastische simulaties in de meeste gevallen het gebruik van een betrekkelijk kleine tijdstap. Daar een grote tijdstap essentieel is voor een efficiënte methode, is in het onderzoek een impliciete methode toegepast die het mogelijk maakt de tijdstap te laten bepalen door de fysica. Deze impliciete methode past in iedere tijdstap een lijnrelaxatie toe om de niet-lineaire instationaire stromingsvergelijkingen op te lossen. Om het relaxatieschema efficiënt te laten werken wordt van een upwind-methode gebruik gemaakt die een positieve Jacobiaan garandeert. Diverse upwind-methoden voor de niet-visceuze flux zijn onderzocht. De methode van Roe voor fluxdifferentiesplitsing is voor de hier beschouwde toepassingen het meest geschikt gebleken. De CUA-methode is aan de hand van standaard test-gevallen gevalideerd. Ook zijn nieuwe gevallen onderzocht.

Verder zijn losse aërodynamisch-elastomechanische koppelingsmethoden bestudeerd om de traditionele koppelingsmethode te verbeteren, die niet doeltreffend bleek te zijn voor aëro-elastische simulaties met grote tijdstappen. Twee nieuwe

aërodynamisch-elastomechanische koppelingsmethoden zijn geïntroduceerd: de aërodynamische extrapolatie methode en de elasto-mechanische extrapolatie methode. Testgevallen hebben de verbetering door de nieuwe koppelingsmethode aangetoond. Vervolgens is de methode toegepast op de aëro-elastische simulatie van een tweedimensionale vleugel met twee vrijheidsgraden. Nieuwe resultaten met de N-S-vergelijkingen zijn verkregen die kunnen dienen als toekomstige testgevallen voor andere numerieke methoden. Resultaten van een flutterberekening voor een tweedimensionale superkritieke vleugel bij een hoge invalshoek laten een tweede dip zien, die sterk lijkt op die in het SKV-5 experiment van het NLR.

Ten slotte is de CUA/CAS-methode voor tweedimensionale stromingen uitgebreid naar driedimensionale stromingen, bedoeld voor de toepassing op enkelvoudige vleugels en vleugel-rompcombinaties. De belangrijkste stap om rekentijden aanvaardbaar te maken is de toepassing van een methode voor parallel rekenen in combinatie met vele processoren. Een domeindecompositiemethode is gekozen die gebruik maakt van standaard portable communicatieprogrammatuur waardoor het mogelijk is de methode te draaien op een variëteit van computers. De driedimensionale methode is toegepast op verschillende standaard testgevallen, van enkelvoudige vleugels tot vleugel-rompconfiguraties van een transportvliegtuig en een gevechtsvliegtuig.

# ACKNOWLEDGMENT

There are many people who directly influenced the work presented in this thesis. The author would like to take a moment to thank them:

- Prof. R.J. Zwaan for the supervision during the course of this work and during the writing of the thesis. His willingness and enthusiasm in discussing the results, providing critical comments and transferring his knowledge were of great importance for the success of this research. For these, the author would like to express his gratitude. Prof. H.W.M. Hoeijmakers for the proper supervision concerning the unsteady CFD methods. His accurate comments, critical suggestions and pleasant discussions during the course of the study and during the writing of the thesis are greatly appreciated. Members of defense committee for giving very useful and interesting comments based on their own field of expertise.
- APERT Project Officers, Messrs. J.P. Klok and L. Sombroek of NLR, Amsterdam and prof. H. Djojodihardjo of ITB, Bandung, for taking care the author's fellowship during his stay in the Netherlands.
- Members of the Department of Aerodynamics Engineering and Aeroelasticity, NLR, Amsterdam, especially Mr. Michel Hounjet to whom the author is indebted for letting the author to use the AEVair, for his very interesting comments and the rich-in-idea discussions; Messrs. Bart Eussen, Jos Meijer, Bert Persoon and Roel Houwink for many discussions concerning system dynamics, identifications, mesh generation, flutter, experiment and analysis of computational results.
- Dr. R. Heinrich of the German's Deutsches Zentrum für Luft- und Raumfahrt (DLR) Institute of Aerodynamic Design, Braunschweig and Dr. R. Voss of DLR Institute of Aeroelasticity, Göttingen for providing a three-dimensional mesh of the LANN wing and some two-dimensional computational results.
- DUT Center for High Performance Applied Computing (HP $\alpha$ C) for the very generous grant of CPU time on the CRAY J910se PVP supercomputer and the CRAY T3E AC80-128 MPP supercomputer.
- Mr. Koen de Cock of the Department of Theoretical Aerodynamics, NLR, Amsterdam and Mr. E.M. Houtman of Chair Aerodynamics, DUT for various discussions concerning steady CFD methods.
- Members of the Chair Aerospace Structures and Computational Mechanics, especially Messrs. Jan Hol, Theo Douma and Raymundo Hordijk for the professional computing support and the very generous setup of computing accounts. Mr. Fons Klompé for general assistance and Mrs. Annemarie van Lienden-Datema for secretarial work and many things beyond that.
- Fellow PhD students of Chair Aerospace Structures and Computational Mechanics,

people who always give their hands to help each other: Eelco Jansen, Erwan Karyadi, Gert Rebel, the former room mates, Arjan Stam, Made Mahardika, Tom van Eekelen Patrick de Visser and Joris Remmer for providing ideal working environment, answering questions and sharing passion for research.

- Finally the author would like to thank his parents and relatives in Indonesia for their continuous moral support, his wife Cirilla who sacrificed her career in exchange of being a housewife in Holland, his son Mikael Luke and his daughter Kayla for the joy they bring to the author's life. This thesis is dedicated to them.

## CURRICULUM VITAE

The author of this thesis was born in Surakarta, Indonesia, on April 28, 1966. After finishing his high school in 1984 he studied Mechanical Engineering in the Institute of Technology Bandung. In 1990 he graduated from the Aerospace Engineering subdepartment after completing a final thesis work in the field of unsteady aerodynamics. After graduation he joined the Aerospace Engineering subdepartment as a research/teaching assistant. He also worked for IPTN on a part-time basis. For a period of one year, starting in November 1990, he carried out a training program sponsored by the APERT project in the Faculty of Aerospace Engineering, DUT and in the Department of Aeroelasticity and Unsteady Aerodynamics, National Aerospace Laboratory (NLR) in Amsterdam. The training covered transonic unsteady aerodynamics. During the second half of 1992 he stayed at the San Diego Supercomputer Center, University of California San Diego, La Jolla, USA as a visiting fellow. In this period he worked on the development of an unsteady full-potential flow solver and a hydrodynamic free-surface problem in high performance computing environment. The PhD study at the Faculty of Aerospace Engineering, DUT, which has resulted in this thesis, began in 1993 under the supervision of Prof. R.J. Zwaan of Chair Aerospace Structures and Computational Mechanics and Prof. H.W.M. Hoeijmakers of the Faculty of Mechanical Engineering, University of Twente. During the course of the research the author worked closely with the members of the Department of Aeroelasticity and Unsteady Aerodynamics, NLR, Amsterdam. Currently, the author is working at the Department of Theoretical Aerodynamics, NLR, Amsterdam.

Besides aeroelasticity, the author's passion goes also to: electronics, computing in general, hiking, geography, basket-ball and certainly his family.

